Development of a Hybrid Assist-as-need Hand Exoskeleton for Stroke Rehabilitation

Lachlan McKenzie

A thesis presented for partial fulfilment of the

requirements for the degree of Doctor of Philosophy

in

Mechanical Engineering

at the

University of Canterbury

Christchurch, New Zealand

May 2021

Abstract

Stroke is one of the leading causes of disability globally and can significantly impair a patient's ability to function on a daily basis. Through physical rehabilitative measures a patient may regain a level of functional independence. However, required therapy dosages are often not met. Rehabilitation is typically implemented through manual one-to-one assistance with a physiotherapist, which quickly becomes labour intensive and costly.

Hybrid application of functional electrical stimulation (FES) and robotic support can access the physiological benefits of direct muscle activation while providing controlled and repeatable motion assistance. Furthermore, patient engagement can be heightened through the integration of a volitional intent measure, such as electromyography (EMG). Current hybrid hand-exoskeletons have demonstrated that a balanced hybrid support profile can alleviate FES intensity and motor torque requirements, whilst improving reference tracking errors. However, these support profiles remain fixed and patient fatigue is not addressed.

The aim of this thesis was to develop a proof-of-concept assist-as-need hybrid exoskeleton for post-stroke hand rehabilitation, with fatigue monitoring to guide the balance of support modalities. The device required the development and integration of a constant current (CC) stimulator, stimulus-resistant EMG device, and hand-exoskeleton.

The hand exoskeleton in this work was formed from a parametric Watt I linkage model that adapts to different finger sizes. Each linkage was optimised with respect to angular precision and compactness using Differential Evolution (DE). The exoskeleton's output trajectory was shown to be sensitive to parameter variation, potentially caused by finger measurement error and shifts in coupler placement. However, in a set of cylindrical grasping trials it was observed that a range of movement strategies could be employed towards a successful grasp. As there are many possible trajectories that result in a successful grasp, it was deduced that the exoskeleton can still provide functional assistance despite its sensitivity to parameter variation.

The CC stimulator developed in this work has a part cost of USD $145 and allows flexible adjustment of waveform parameters through an on-board micro-controller. The device is designed to output current up to $\pm 30mA$ given a voltage compliance of $\pm 50V$. When applied across a 2kΩ load, the device exhibited a linear output transfer function, with a maximum ramp tracking error of 5%.

The stimulus-resistant EMG device builds on current designs by using a novel Schmitt trigger based artefact detection channel to adaptively blank stimulation artefacts without stimulator synchronisation. The design has a part cost of USD $150 and has been made open-source. The device demonstrated its ability to record EMG over its predominant energy spectrum during stimulation, through the stimulation electrodes or through separate electrodes. Pearson's correlation coefficients greater than 0.84 were identified between the normalised spectra of volitional EMG (vEMG) estimates during stimulation and of stimulation-free EMG recordings. This spectral similarity permits future research into applications such as spectral-based monitoring of fatigue and muscle coherence, posing an advantage over current same-electrode stimulation and recording systems, which cannot sample the lower end of the EMG spectrum due to elevated high-pass filter cut-off frequencies.

The stimulus-resistant EMG device was used to investigate elicited EMG (eEMG)-based fatigue metrics during vEMG-controlled stimulation and hybrid support profiles. During intermittent vEMG-controlled stimulation, the eEMG peak-to-peak amplitude (PTP) index was found to be inconsistent due to the recovery intervals between contractions. In constrast, the median frequency (MDF) had a negative correlation for all subjects with $R^2 > 0.62$ during stimulation-induced wrist flexion and $R^2 > 0.55$ during stimulation-induced finger flexion. During hybrid FES-robotic support trials, a 40% reduction in stimulus intensity resulted in an average 21% reduction in MDF gradient magnitudes. This reflects lower levels of fatigue during the hybrid support profile and indicates that the MDF gradient can provide useful information on the progression of muscle fatigue.

A hybrid exoskeleton system was formed through the integration of the CC stimulator, stimulus-resistant EMG device, and the hand exoskeleton developed in this work. The system provided assist-as-need functional grasp assistance through stimulation and robotic components, governed by the user's vEMG. The hybrid support profile demonstrated consistent motion assistance with lowered stimulation intensities, which in-turn lowered the subjects' perceived levels of fatigue.

Publications

Over the course of this research, a number of papers have been published. The research demonstrated in these papers is based on the work presented in this thesis.

Journal Papers

- **McKenzie, L.R.**, Pretty, C.G., Fortune, B.C., Chatfield L.T. (2021). "Low-cost Stimulation Resistant Electromyography." *HardwareX*, e00178. *Forming the contents of Chapter 7.*

Conference Papers

- **McKenzie, L.R.**, Pretty, C.G., Fortune, B.C., Chatfield L.T. (2021)."Evoked Electromyographic Fatigue Indices During Intermittent Stimulation Towards Dynamic Wrist Contractions." *IEEE/ASME International Conference on Mechatronic and Embedded Systems and Applications (MESA). Forming the contents of Chapter 8.*

Acknowledgments

I would like to express my sincere gratitude to my supervisory team consisting of Associate Professor Chris Pretty, Professor XiaoQi Chen, and Dr Brian Ruddy, for their invaluable contributions and support over the course of my research. To Julian Murphy and Scott Lloyd, thank you for your readiness to provide technical expertise during the hardware development of this work.

Special thanks to my primary supervisor, Chris Pretty, for his endless patience and guidance with my research. Also, thank you for your enthusiastic and frequent visits to the office, often leading to research meetings on anything but research.

To everyone in my office, thank you for creating a fantastic office dynamic, full of laughs and well needed procrastination. I truly hope to encounter similar work atmospheres in the future, the bar has been set high.

Finally, to my family, thank you for your endless support throughout all of life's endeavours, and the supply of food that kept finding its way to me in the past couple of months. Sarah, thank you for your interest in my work, your moral support, and your patience during busy times.

Contents

List of Figures

List of Tables

List of Abbreviations

ADC analog to digital converter

ADL activities of daily living

ARAT Action Research Arm Test

BCI Brain-Controlled Interface

BOM bill of materials

CAD computer-aided design

CC constant current

CI Co-Contraction Index

CMRR common-mode rejection ratio

COR center of rotation

CoV coefficient of variation

CV constant voltage

DAC digital to analog converter

DAQ data acquisition card

DE Differential Evolution

DIP distal interphalangeal joint

DOF degree of freedom

DPh distal phalanx

ED extensor digitorum

EEG electroencephalograph

eEMG elicited EMG

EMG electromyography

EMI electro-magnetic interference

FD flexor digitorum

FES functional electrical stimulation

FFT fast Fourier transform

FMA Fugl-Meyer Assessment

FMG force myography

HCS Howland current source

IC integrated circuit

IHCS Improved Howland current source

ILC iterative-learning-control

MAS Modified Ashworth Scale

MAV mean absolute value

MCP metacarpophalangeal joint

MDF median frequency

MNF mean frequency

NMES neuro-muscular electrical stimulation

PID proportional-integral-derivative

PIP proximal interphalangeal joint

PSD power spectral density

PTP peak-to-peak amplitude

RLD right leg driver

RMS root mean square

RMSE root mean square error

ROM range of motion

SCI spinal-cord-injury

SPI serial peripheral interface

vEMG volitional EMG

WMFT Wolf Motor Function Test

CHAPTER 1

Introduction

1.1 Motivation

Globally, stroke is the second most prominent cause of death and is one of the leading causes of disability (World Stroke Organisation, 2017). The World Stroke Organisation (WSO) defines stroke as an ischemic or hemorrhagic disruption to the brain's blood supply, resulting in oxygen starvation, brain damage, and loss of function (World Stroke Organisation, 2017). In New Zealand, stroke is the third largest killer, with approximately 9000 New Zealanders having a stroke each year and an estimated 60,000 stroke survivors (Stroke Foundation of New Zealand, 2017).

There are a broad variety of adverse physical effects that a stroke survivor may encounter, such as: paresis, abnormal muscle tone, muscular atrophy, abnormal motor synergies, and loss of somatosenstaion. Stroke patients typically suffer from hemiparesis, a condition that manifests as weakness of the contralesional side of the body. Such physical deficits can prevent a patient from performing basic activities of daily living (ADL), having a substantial

impact on their quality of life. Stroke can also have large financial and psychological effects on society, the patients' families, and the healthcare system (Strong, Mathers, & Bonita, 2007). The predicted cost of stroke in New Zealand is expected to be $1.7 billion by 2038, with the cost over five years approximated at $105,000 per stroke patient (Stroke Foundation of New Zealand, 2016).

Functional recovery after stroke is facilitated by learning-related neural plasticity, both at synaptic and cortical levels (Krakauer, 2005). Research has long indicated that therapy should begin as soon as possible after stroke (Cifu & Stewart, 1999). Additionally, therapy delivered in high dosages, high intensity, and of a task-orientated nature, have been linked to more extensive functional recovery (Bayona, Bitensky, Salter, & Teasell, 2005; H. C. Huang, Chung, Lai, & Sung, 2009; Popović & Popović, 2006). Despite these findings, traditional therapy is not delivered at the required dosages. This is due to a restriction of rehabilitation resources. Therapy is often implemented through manual assistance and in a one-to-one manner, which can easily become labor-intensive and expensive (Nef, Quinter, Müller, & Riener, 2009).

Through the introduction of alternative rehabilitation technologies, common therapy restrictions may be alleviated. Two forefront technologies are robotic devices and functional electrical stimulation (FES). Robotic devices are able to provide reliable, accurate motion at high intensities. FES is the application of electrical pulses, which generates muscle contractions towards functional movements. FES directly activates the patients' muscles and can therefore be used to prevent impairments such as muscle atrophy. However, the isolated use of FES and robotic support is limited by their inherent limitations. The most prominent issues with FES are early onset of patient fatigue, and control difficulty due to the muscles' non-linear and time-varying responses to stimulation. Robotic devices often become cumbersome in the pursuit of adequate torque levels, and cannot elicit the muscle activation that FES provides.

The conjunction of robotic and FES modalities holds promise to improve rehabilitation outcomes. A hybrid device can provide the physiological benefits from FES muscle activation while utilising the robotic structure's reliable motion. Through balanced hybrid support the requirements on robotic torque and stimulation intensity can be reduced. In turn, this can lead to enhancement of robotic-device portability and alleviation of FES-based discomfort and fatigue. Furthermore, patient focus may be improved by incorporating their bioelectric signals, such as electromyography (EMG), to deliver support in an assist-as-need manner.

A limited number of existing upper-limb devices apply FES and robotic support for hybrid assistance of the same joint. These devices have demonstrated that a balanced FES-robotic support profile can reduce the patients' reference tracking errors and improve their volitional muscle activity. However, little concern is given to the patients' fatigue levels and the hybrid support profiles remain fixed. In addition to this, current hybrid hand-exoskeletons are limited to tasks which involve the simultaneous flexion or extension of all fingers. This can be attributed to a lack of space when applying electrodes on the forearm, limiting the selectivity of both FES delivery and EMG recording. In some cases, mismatch between robotic and FES supported degree of freedom (DOF) results in excess device weight that does not serve a functional purpose.

1.2 Goals of this thesis

The aim of this thesis is the development of a hybrid exoskeleton for post-stroke hand rehabilitation. This aim requires the development and integration of the following system components:

1. *Exoskeleton:* A hand-exoskeleton will be developed to support pinch and power grasp functional movements. Key design processes include the dimensional synthesis of a parent model exoskeleton and the subsequent formation of a parametric model to adapt to different finger sizes.

2. *Stimulator:* Development of a constant current (CC) stimulator with flexible control of stimulation waveform parameters.

3. *EMG device:* Development of a stimulus resistant EMG device that can record concurrently to stimulation through separate or through common electrodes.

Further objectives of this work are the application of the hybrid exoskeleton to provide assist-as-need support, and the investigation of stimulation induced fatigue during these dynamic contraction periods.

Contributions to the Field

The main contributions of this thesis lie in the development of a novel stimulus-resistant EMG device and the investigation of EMG-based fatigue indices during assist-as-need supported dynamic movements. The device can record from stimulation electrodes with band-pass characteristics spanning the predominant usable energy of the EMG spectrum. This feature removes the limitations of current same-electrode FES-EMG systems which use elevated high-pass filter cut-off frequencies to reduce artefact transient times. The device hardware and design decisions are made open-source to provide a tool for future researchers (McKenzie, Pretty, Fortune, & Chatfield, 2021).

EMG fatigue indices are studied during volitional-based stimulation and hybrid support protocols. This builds on current fatigue studies which typically deliver stimulation with fixed timings. The results of the study provide insight on the applicability of EMG fatigue indices during hybrid assist-as-need support. Ultimately, this provides a step towards the integration of fatigue monitoring and management in hybrid hand-exoskeleton devices, which, to my knowledge, current systems are lacking (Mckenzie, Fortune, Chatfield, & Pretty, 2021).

A minor contribution lies in the optimisation procedure of the finger exoskeleton, which includes a cost function to promote device compactness. The inclusion of a compactness cost function holds promise to reduce exoskeleton volume and overall weight. To my knowledge, device compactness has not been addressed in the current optimisation procedures for hand-exoskeleton linkages.

1.3 Overview

An overview of this thesis is outlined below:

Chapter 2 provides background on the effects of stroke and the state of current rehabilitation practices. Chapter 2 also introduces the concept and potential benefits of a hybrid rehabilitation tool with FES and robotic support components.

Chapter 3 provides a review of current literature of hybrid devices that apply FES and robotic components to support the same joint, simultaneously. The review predominately focusses on devices intended for stroke rehabilitation of the hand, but also covers hybrid devices applied to other areas.

Chapter 4 details background on hybrid exoskeleton components identified in Chapter 3. This includes background on rehabilitation robotics and FES, as well as EMG recording and fatigue of stimulated muscle, as they are relevant to hybrid exoskeleton development.

Chapter 5 outlines the kinematic and dimensional synthesis of a scalable one DOF finger exoskeleton model. The chapter also covers experimental testing of the parent model and investigates the phalanx trajectories of five subjects during a series of cylindrical grasping trials.

Chapter 6 details the design and testing of a CC stimulator. The stimulator is used in the

testing of the EMG design and hybrid-exoskeleton application in later chapters.

Chapter 7 outlines the hardware design for an open-source stimulus resistant EMG device and adaptive filter for residual artefact removal. Experimental testing of the device is provided when using separate electrodes for EMG recording and FES, and when EMG is recorded from the stimulation electrodes.

Chapter 8 investigates the efficacy of EMG peak-to-peak amplitude (PTP) and median frequency (MDF) as fatigue indicators during isometric constant stimulation and during volitional intent driven stimulation.

Chapter 9 details the integration of CC stimulator, EMG device, and exoskeleton, applied towards assist-as-need hybrid support during a functional grasping task. The EMG MDF is investigated during this period to determine the MDF's efficacy as a fatigue indicator during hybrid assist-as-need support.

Chapters 10 and 11 provide a summary of this thesis and highlights a selection of possible future-work avenues to extend the work presented in this thesis.

CHAPTER 2

Stroke Background

2.1 Introduction

A stroke is the hemorrhagic or ischemic interruption of oxygen-rich blood to the brain, leading to the damage of brain cells and loss of function (Norouzi-Gheidari, Archambault, & Fung, 2012). Stroke can happen to anyone, regardless of age, however predominately occurs in the elderly population. In 2009, 66% of people hospitalised for stroke were aged 65 and over (Hall, Levant, & DeFrances, 2012). With an ageing population, the number of people affected by stroke is increasing.

2.2 Physical Effects of Stroke

Stroke can have an overwhelming influence on a patient's physical capabilities and their ability to function on a daily basis. From patient to patient, the type, severity, and recovery from physical deficits can vary considerably. For the upper-extremities, common physical impairments can include paresis, abnormal muscle tone, loss of fractionated movement,

muscular atrophy, and changes in somatosensation.

2.2.1 Paresis and Plegia

Paresis is a reduced ability to voluntarily activate motor units caused by damage to the corticospinal system, and is the most common physical impairment post-stroke (Sathian et al., 2014). Paresis is often seen as an inability to activate muscles with sufficient force, in a coordinated and timely manner. Depending on severity, paresis may manifest as slight deficits and inefficiencies in a patient's movements, or a patient may not be able to move at all (Lang, Bland, Bailey, Schaefer, & Birkenmeier, 2013). Stroke commonly causes paresis in the contralesional side of the body, known as hemiparesis. Severe paresis, known as plegia (Sathian et al., 2014), and hemiplegia, are also common after a stroke.

2.2.2 Abnormal muscle tone

Two different forms of abnormal muscle tone occur after a stroke.

- *Hypertonicity (spasticity):* Hypertonicity manifests as an increased resistance to passive movement and increased stretch reflex response.

- *Hypotonicity (flaccidity):* Hypoponicity manifests as muscular weakness and a decrease in muscle tone.

A combination of hypotonicity and hypertonicity in muscle groups may contribute to the impairement of function (Gregson et al., 2000). Hypertonicity develops due to loss of inhibitory control to upper motor neurons (Watkins et al., 2002), whilst hypotonicity develops due to injury of lower motor neurons and therefore weakness of neuronal signals.

2.2.3 Muscular Atrophy

Muscle atrophy of the paretic limb is a common problem after stroke, seen as a decrease of muscle mass and volume (Ryan, Dobrovolny, Smith, Silver, & Macko, 2002). Atrophy in stroke patients is caused through the disuse of the paretic limb, which may arise through impaired motor recruitment and learned non-use. Disuse atrophy can exacerbate post-stroke hemiparesis, and in-part has been associated with post-stroke abnormalities and strength deficits (Prado-medeiros et al., 2012; Triandafilou & Kamper, 2012). Prevention and reversal of muscle atrophy can be achieved through passive movement of the patient's arm. However, electrical stimulation and exercises that require volitional effort are more effective.

2.2.4 Abnormal Motor Synergies

According to Dewald et al., abnormal motor synergies are the primary cause of movement dysfunction in many hemiparetic stroke patients (Dewald, Sheshadri, Dawson, & Beer, 2001). Abnormal motor synergies can be defined as typical whole-limb movements which, in humans, are indicative of neurological deficits and result in the loss of fractionated joint control (Dipietro et al., 2007). Fractionation of movement is the ability to selectively activate individual muscles, and is particularly crucial for upper extremity function. Loss of independent movement has been demonstrated across both distal and proximal upper extremities. For example, there can be extensor synergy, characterised by concurrent shoulder adduction, elbow extension, and forearm pronation; and there can be flexor synergy, characterized by concurrent shoulder abduction, elbow flexion, and forearm supination (Kung, Lin, & Ju, 2010).

2.2.5 Loss of Somatosensation

Sensation affiliated with the skin, muscles, or joints are often referred to by the term somatosensation. Information is transmitted and processed by ascending peripheral nerves

and the cortical regions of the somatosensory system, respectively (Kessner, Bingel, & Thomalla, 2016). Through stroke, the somatosensory system may be damaged, causing deficits of modalities such as light touch and proprioception (Meyer, Karttunen, Thijs, Feys, & Verheyden, 2014). Sensory damage appears to magnify the impact of motor impairments, with somatosensation reported to be a predictor for motor recovery and long-term functional outcomes post-stroke (Sullivan & Hedman, 2008). In addition to this, the loss of sensory feedback can be potentially dangerous to the patient as they may be unaware of what their limb interacts with; for example, a patient may burn their hand if it rests on a hot surface but limited pain or temperature feedback is available.

2.3 Post-Stroke Upper Extremity Evaluation

Stroke guidelines and policies strongly encourage monitoring of rehabilitation intervention effectiveness (Alt Murphy, Resteghini, Feys, & Lamers, 2015). There are many metrics used to evaluate post-stroke upper extremity performance. These assessment measures have been used to monitor patient progress, assist with clinical decision making, and ultimately to optimise the rehabilitation process for maximal functional recovery. Clinical tests may take many forms, from interviews/questionnaires to manual and observational assessments (Johansson, 2015). The focus of these tasks may range from simple joint movement to functional ability for activities of daily living (ADL). A variety of outcome measures have been well established in clinical settings and in rehabilitation trials; however, these methods are often reviewed and new protocols developed. New quantitative measures are becoming readily available with the introduction of alternative rehabilitation modalities such as electromyography (EMG) and rehabilitation robotics. Evaluation metrics are vital to the assessment of new rehabilitation techniques and technologies. Evaluation metrics will therefore be very important if the research reaches a clinical trial phase, as they assess the studies' practical outcomes.

2.4 Upper-Extremity Stroke Rehabilitation

The effects of a stroke can have an immense adverse impact on a person's ability to function on a daily basis. The upper-extremities, in particular the hand, are used extensively in ADL, from washing dishes and cooking, to more sensitive tasks such as toileting and showering. Rehabilitation can restore functional independence for simple ADL and have considerable impact on mental well-being: this in turn will lessen a patient's reliance on carers and return a quality of life that may have been deprived.

It is recommended that rehabilitative measures be taken soon post-stroke, with the most extensive improvements observed in the first 30 to 90 days post-stroke. However, it has been found that cortical reorganisation can occur well into chronic stages of recovery (Byl et al., 2003). Therefore, rehabilitative measures are often continued past the acute phase of recovery.

Depending on environmental and societal factors, a patient's motivation, involvement, and focus may vary during rehabilitation (Pollock et al., 2013). This engagement can often be modulated by the setting in which the therapy is delivered. Sessions can occur in a number of settings. In early stages of recovery, rehabilitation sessions mostly occur in a clinical setting, with a physiotherapist or occupational therapist likely to administer the treatment. As the rehabilitation progresses, it is more likely to transition into a community or home-based setting, either externally monitored or self-monitored. In addition, rehabilitation sessions can be done in both individual and group sessions. Note, treatment may be confined to particular settings due to limited resources, such as trained staff, equipment, and facilities.

The delivery and nature of rehabilitation can have significant impacts on patient outcome. Factors such as corticospinal tract damage, lesion location, degree of impairment, and time

after stroke, cause heterogeneity in the effects of rehabilitative interventions. Therapy intensity can impact on rehabilitation outcomes. The Australian Clinical Guidelines for Stroke Management (Stroke Foundation, 2017) recommend for rehabilitation structure to provide as much therapy as possible and that patients be encouraged to continue task practice outside of monitored sessions. There is a growing body of evidence that there is a dose-response relationship in rehabilitation: better functional outcomes arise from a higher rehabilitation intensity and more practice time (Kwakkel, 2009a). Currently, there is a mismatch between the dose-response evidence and actual therapy time being provided through healthcare systems (Kwakkel, 2009b). More efficient use of resources such as group therapy, or assistance modalities that allow for home-based rehabilitation, may help to reduce this mismatch.

Post-stroke rehabilitation covers a broad range of areas. Upper-extremity rehabilitation may include the strengthening of the limb and limb movements, lessening of impairments, and improvement of motor performance during functional activities. Adjacent interventions can range from physical therapy to electrical stimulation and pharmacological treatments. Physical rehabilitation will often involve repetitive movements in conjunction with assistive or resistive devices. Devices used in stroke therapy may be passive or active in nature.

- *Active:* Active devices are capable of moving the patient's limb without their assistance, and may use electrical stimulation and/or actuation.

- *Passive:* Passive devices often use mechanical stoppers and components that are elastic in nature (such as springs or rubber lengths) and are primarily used in resistive training or to set motion limits.

"Repeated motor practice and sensory motor coupling is important for motor learning

and recovery" (Woldag, Waldmann, Heuschkel, & Hummelsheim, 2003). However, repetitive movements without any meaningful skill learning is unlikely to induce any significant cortical changes (Bayona et al., 2005). Consequently, high repetition is often applied in intervention strategies that focus on functional motions in a meaningful context. This rehabilitation profile is known as *task specific training*, is the gold standard for rehabilitation post-stroke (Dimyan & Cohen, 2011), and has higher functional outcomes than rote exercises or passive modalities (Winstein et al., 2004). There are a vast range of techniques/devices available to assist with upper-extremity stroke rehabilitation, such as: Constraint-Induced Movement Therapy (CIMT), bilateral training, mental imagery, mirror therapy, Virtual Reality (VR), Functional Electrical Stimulation (FES), robotics, and neuroprosthetics (Pollock et al., 2013).

2.5 Alternative Rehabilitation Technologies

Successful rehabilitation can depend on a range of factors. As detailed in Section 2.4, functional rehabilitation requires high repetitions of task-related movements. Current evidence suggests that more significant response is generated with high therapy dosages, that rehabilitation should begin as soon as possible after stroke, and that a patient remains motivated and involved in their therapy. Environmental setting can impact largely on therapy. Home-based and community therapies can provide context to rehabilitation, improve patient involvement, and can be substantially more cost effective than clinical alternatives. A patient practising 20 minute blocks of tasks each day in a home based setting is more likely to improve than if they merely stop rehabilitation outside of clinical settings (Dobkin, 2004).

Despite evidence that links high intensity rehabilitation to improved outcomes, patients in general receive little contact time with therapists (Dewey, Sherry, & Collier, 2007; Teasell & Kalra, 2005). This can be due to a lack of rehabilitation resources. Therapy is often implemented through manual assistance and in a one-to-one manner, which can easily become

labor-intensive and expensive (Nef et al., 2009). The economic burden of stroke and stroke related interventions is significant (Rajsic et al., 2019). The cost of stroke rehabilitation in New Zealand is predicted to be $1.1 billion NZD in 2020 and is expected to increase to $1.7 billion by 2038 (Stroke Foundation of New Zealand, 2020). In New Zealand, 70-75% of strokes occur in people 65 years or older. With an ageing population, the demand on stroke rehabilitation resources is only going to increase, as will the potential savings associated with the optimisation of stroke rehabilitation (Hogan & Siddharth, 2018).

Through the introduction of alternative rehabilitation technologies. therapy may be delivered in a more efficient manner than conventional modalities. This can help to reduce the mismatch between recommended rehabilitation dosages and its actual delivery. Functional electrical stimulation (FES) and robotic assistance hold considerable potential when applied in rehabilitation efforts. Robotic devices are able to provide assistance to task related movements in a repeatable and reliable way, and can enhance patient autonomy and motivation (Keller & Veneman, 2012). Additionally, robotic devices are able to provide quantitative performance analysis measures. FES devices are typically light-weight, compact, and discrete. Electrical stimulation directly activates the user's muscles, providing both physiological and psychological benefits to the impaired user, including: improved muscle strength, decreased muscle impairment, improved bone density, decreased spasticity, and improved cardiographic health (Ha, Murray, & Goldfarb, 2016).

Despite the numerous benefits of robotic or FES therapy, FES to their use are also present. Typical problems in the application of FES include discomfort, lack of selectivity, and fatigue (Shao, Li, Yokoi, & Zhang, 2016). Perhaps the predominant limiting factor of FES is the early onset of muscle fatigue and pain/discomfort felt by the user. There are a number of theories suggesting the mechanisms behind FES evoked fatigue, as discussed in Section 4.4.1. In addition to this, functional movements are difficult to produce: In the hand this is largely due to a lack of finger control through ordinary self-adhesive electrodes (Tu

et al., 2017). Control complexity is further heightened due to non-linear and time-varying characteristics of FES-induced motion (Freeman, 2016). This contrasts to the use of robotic support, which is able to provide control in a reliable and repeatable way. Robotic support provides an external torque to generate user motion: as opposed to electrical stimulation, robotic support does not directly activate the user's muscles and therefore lacks most physiological benefits associated with FES.

There are few powered devices that support basic ADL outside a clinical environment, mainly due to design challenges and economic restrictions (Maciejasz, Eschweiler, Gerlach-Hahn, Jansen-Troy, & Leonhardt, 2014). To increase a device's force output, more actuators and stronger materials are required. Due to limitations of actuator power to weight ratio and material strength to weight ratio, robotic support and exoskeletons typically become cumbersome in the pursuit of adequate force levels (Iqbal & Baizid, 2015; Tu et al., 2012). Consequently, issues with portability, user fatigue, energy consumption, and device acceptance arise. This effect is especially profound when the device targets distal regions (e.g. hand exoskeletons): actuation placed on distal regions tend to quickly fatigue the user and more complex mechanical structures are required, resulting in higher set-up times and typically a more 'bulky' appearance.

In this context, a hybrid system is a device in which FES is applied in conjunction with electromechanical/robotic support on the same joints. Through integration of FES and robotic therapies, the disadvantages of each technique may be mitigated while their inherent advantages remain, maximising therapeutic effect (Rong et al., 2015). Robotic support in conjunction with the physiological benefits of FES can reduce muscle impairment and improve functional ability for a range patients. The system can be applied to patients of all voluntary capacities. The repeatability and reliability of robotic assistance can account for the non-linear and time-varying characteristics of FES elicited motion. Robotic support also allows for lower stimulation intensities to be used, therefore decreasing any potential

discomfort felt at the electrode sites, potentially allowing FES application on patients who are particularly sensitive to electrical stimulation. In a similar manner, the use of FES can reduce the force output requirements of the robot. Smaller actuation units can be used, therefore reducing the overall weight and volume of the device, as well as lessening strength requirements of the materials used. This in turn may increase portability, enhance user acceptance, and increase user comfortability. The ability to dynamically adjust robotic and FES support can allow for more advanced and smarter control algorithms. For instance, with the use of bioelectric information such as EMG, an assist-as-need control can be implemented, helping to incorporate the patient's voluntary capacity. The use of EMG also allows for detection of fatigue. With this information a balanced control of FES and robotic assistance can be implemented, aimed to combat early onset and high levels of fatigue induced through the FES.

2.6 Summary

Stroke is one of the global leading causes of disability. The economic and societal impacts of stroke and stroke-related interventions are significant. The cost of stroke rehabilitation in New Zealand is expected to be $1.7 billion by 2038. In New Zealand, 70-75% of strokes occur in people aged 65 years or older (Stroke Foundation of New Zealand, 2020). As our population ages the burden of stroke will only escalate. If new technologies are not produced to counteract this increased demand, the lives of many people will be severely negatively affected.

Functional post-stroke rehabilitation is facilitated through learning-related neural plasticity. Research has long indicated that therapy, delivered in high dosages, high intensity, and of a task-orientated nature, have been linked to more extensive functional recovery. Despite these findings, traditional therapy is still not delivered accordingly: this is due to a restriction of rehabilitation resources.

Introduction of alternative rehabilitation technologies can make therapy more accessible, helping to reduce mismatch between its recommended and actual delivery. Two forefront technologies are robotic devices and FES, both proven beneficial to stroke rehabilitation. Inherent limitations, however, restrict the isolated usage of these technologies. Combination of robotic devices and electrical stimulation holds promise to generate more effective rehabilitation technologies.

CHAPTER 3

Review of Hybrid Exoskeleton Devices

This review primarily focuses on hybrid exoskeletons for post-stroke hand rehabilitation. In this context, a hybrid exoskeleton refers to an exoskeleton device that uses both functional electrical stimulation (FES) and active mechanical actuation for the control of the same joint, simultaneously. Although the review predominately focuses on post-stroke centred devices, systems built for other purposes, such as post-spinal-cord-injury (SCI) rehabilitation, will be included. Technology that fits the aforementioned 'hybrid exoskeleton' definition, but not applied to the hand, will be briefly covered.

3.1 Applicable Device Summary

Twelve devices were found to use a hybrid of active mechanical actuation and FES for control of the same joint. Four devices were found which use a hybrid exoskeleton for finger control. A further four upper-limb and four lower-limb devices were found to use

Table 3.1: Summary of the reviewed hybrid exoskeleton devices and their implementations of some key requirements for a hybrid exoskeleton rehabilitation device.

System	Supported Joints	Actuation	FES Device	User Intention Method	Portable	Fatigue monitor
Systems where actuation and FES are applied to the fingers						
Tendon-Driven FES Robotic Glove (Neto, Fajardo, Ferman, Fujiwara, & Rohmer, 2019)	Fingers	Servo motor	STIMSHIELD	FMG sensor	No	No
Intelligent Haptic Robotic Glove (Hartopanu & Poboroniuc, 2015)	Fingers	DC linear	MotionStim 8	Flex sensor	No	No
EMG-driven NMES Robotic Hand (Rong et al., 2015)	Fingers	DC linear	Unspecified	EMG	No	No
Wearable Rehabilitation Robot (Tu et al., 2012)	Shoulder (actuator only) Elbow (actuator only) Wrist Fingers	Pneumatic muscle	Beurer EM41	N/A	No	No
Systems where actuation and FES are applied to the upper limb						
Exoslim (Irimia, Poboroniuc, Serea, Baciu, & Olaru, 2016)	Shoulder (actuator only) Elbow Wrist	DC motor	MotionStim 8	EEG	No	No
EMG-Driven NMES Robot (Hu & Tong, 2014)	Wrist	Servo motor	Unspecified	EMG	No	No
NMES-Robot System (Rong et al., 2017)	Elbow Wrist	Servo motor	Unspecified	EMG	No	No
Systems where actuation and FES are applied to the lower limb						
Hypo (Obinata et al., 2007)	Hip, Knee	DC motor	Unspecified	User interface	No	No
Kinesis (Del-Ama, Gil-Agudo, Pons, & Moreno, 2014)	Knee	DC motor	Rehastim	Interaction force	Yes	Yes
Powered Hybrid FES System (Ha et al., 2016)	Hip (actuator only) Knee	Servo motor	Unspecified	Pressure Position	Yes	Yes
Hybrid Assistive System (Popovic, Tomovic, & Schwirtlich, 1989)	Hip (FES only) Knee Ankle	Cybernetic actuator (Linear Actuation)	Unspecified	Pressure Position	Yes	Yes

a hybrid exoskeleton for joint control. Table 3.1 summarises the reviewed devices with respect to some key specifications for a hybrid exoskeleton rehabilitative device.

3.2 Hybrid Exoskeletons Towards Finger Control

3.2.1 Intelligent Haptic Robotic Glove, IHRG

The Intelligent Haptic Robotic Glove (IHRG) is a hybrid device specifically designed for upper limb rehabilitation of stroke patients (Hartopanu & Poboroniuc, 2015), Figure 3.1.

Figure 3.1: Intelligent Haptic Robotic Glove (Hartopanu & Poboroniuc, 2015).

The IHRG mechanical actuation is comprised of a metal tendon per finger that is driven by linear actuators (Firgelli L12) to achieve finger flexion and extension. The metal tendons are routed on the dorsal side of the hand via leather glove, and linear actuators placed remotely. The forces generated by the tendon system were deemed to be harmless, and the fingers could move freely while attached to the exoskeleton. Issues were found, however, with the elasticity of the leather and the limited adjustability of the tendons, causing the system to not support the fingers full range of motion (ROM).

The neurostimulator, MotionStim8, is used to apply FES to the hand extensor and interosseous muscles (one channel each). Stimulation is delivered as 50Hz biphasic pulses,

with a pulse width varying between 150us and 300us, and intensity between 15mA and 30mA.

User intent and positional feedback is given via bend sensors on a separate right-handed glove. This information is fed into the microcontroller and MATLAB host PC, subsequently used to control actuation of the left-hand glove. This control-base represents a form of bilateral training. Visual feedback is given through a PC display. The power source for the linear actuators and controller were not specified.

A clinical trial was undertaken by Grigoras et al. (Grigoras, Irimia, Poboroniuc, & Popescu, 2016), where post-stroke patients with left-side hemiparesis were asked to take part. The trial consisted of a group of 12 for conventional therapy and 13 people for robotic therapy. It was found that both groups experienced reduction in motor impairment and improved affected limb functionality. However, there were no significant differences between the experimental and control groups' outcomes. It was noted that the trial only spanned over two weeks and that a statistically significant improvement may be made over a longer duration.

3.2.2 EMG-driven NMES Robotic Hand

The EMG-driven NMES Robotic Hand Robotic Hand is an electromyography (EMG) driven robotic system coupled with neuro-muscular electrical stimulation (NMES) (Rong et al., 2015), Figure 3.2. The system is primarily produced to investigate its effect on post-stroke rehabilitation.

A mechanical linkage system is applied to provide finger flexion/extension through coupled metacarpophalangeal joint (MCP) and proximal interphalangeal joint (PIP) joint rotations. Each finger linkage is individually actuated through linear servo motors (Firgelli), mounted on a dorsal hand orthosis. Firgelli linear actuators are lead-screw driven so are likely not

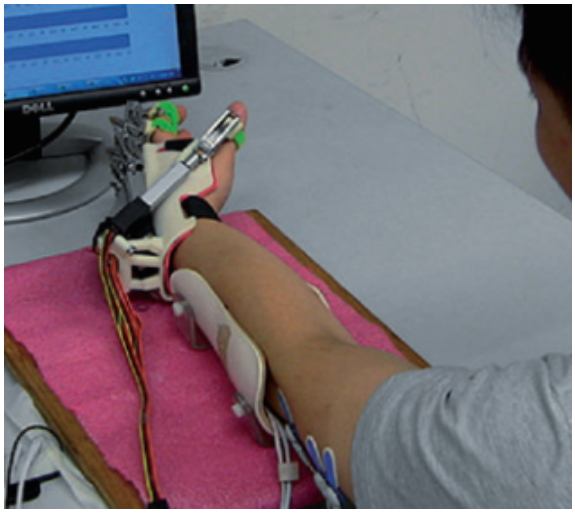

Figure 3.2: EMG driven robot aided hand with NMES (Rong et al., 2015).

backdriveable.

The NMES component is a two-channel stimulator that directly stimulates the extensor digitorum (ED) and the flexor digitorum (FD). Stimulation is provided in a square pulse pattern with frequency of 40Hz, amplitude of 100V, and an adjustable pulse width from 0 to 300us.

EMG levels of the ED and FD were sampled by a data acquisition card (DAQ)(National Instruments). The normalised EMG envelope was used to provide an estimate of user intent, scaling the force input and finger angular velocities. Separate proportional control algorithms are used for stimulator and motor based assistance. The algorithms both consist of a gain factor, manually set between 0 and 100 percent, and a scaling factor determined by the EMG signal level. Motor position sensors are used to measure the finger position. LabVIEW is used as a control platform, providing visual feedback and command signals.

An initial system evaluation was conducted on five chronic stroke subjects (Rong et al., 2015). Eight assistance profiles were tested, ranging from no input (FES or mechanical) to full assistance. The subjects were asked to complete finger tracking motions under each of these profiles. The root mean squared error (RMSE) between the MCP joint and

the target angle, the maximal ROM during tracking, EMG activation levels, and EMG Co-Contraction Index (CI) were used to evaluate the system performance. It was found that a 50-50 assistance profile was optimal.

A 20-session pilot study was subsequently conducted on the four of the five subjects, with the 50-50 robot-NMES assistance (Rong et al., 2015). In each session, lateral and vertical reaching-grasping tasks were performed in ten-minute intervals. Training effects were evaluated by a training-blinded assessor, using the EMG CI and activation levels pre and post training, as well as the Fugl-Meyer Assessment (FMA), Action Research Arm Test (ARAT), Wolf Motor Function Test (WMFT), and Modified Ashworth Scale (MAS) clinical scores. It was found that the MAS (for finger and elbow joints),FMA, and WMFT scores, significantly increased after the 20-session training. Significant decrease in EMG activation and CI levels were also observed over the 20-session period. It was concluded that the NMES assistance mainly reduced excessive elbow muscle activity and increased voluntary finger movement, while the robotic support component improved the movement accuracy of the fingers. Due to the limited sample-size of this study, it was recommended the a large-scale randomised control experiment should be conducted to confirm the positive effects of the system in stroke rehabilitation.

The system was then applied in a 20-session single-group design clinical trial, conducted on 15 chronic stroke subjects (Nam et al., 2017). Training effects were evaluated using the clinical scores of the FMA, Wolf Motor Function Test, ARAT, Motor Functional Indendance Measure, and MAS, at pre-training, post-training, and 3-month follow-up assessments. EMG activation levels and co-contraction indexes were also investigated at these stages. Significant improvements were observed post-training and at the 3-month follow-up in the FMA wrist/hand and shoulder/elbow scores, the ARAT, and in the MAS. Significant reduction in CI and decrease in muscle activation levels were also observed. It was concluded that EMG-driven NMES-robotic assistance facilitates improvements in muscle coordination and

voluntary motor function in patients with chronic stroke.

A randomised controlled trial with 3-month follow-up was then conducted on 30 chronic stroke patients, with the objective to compare the rehabilitation effects of the EMG-driven NMES Robotic Hand Robotic Hand and of EMG-driven robotic support (Y. Huang et al., 2020). Subjects were randomly assigned to receive 20 training sessions with either the EMG-driven NMES-Robotic Hand (n=15) or the EMG-driven Robotic Hand (n=15). The NMES-robotic support group achieved significantly better EMG activation levels and CIs than the robotic support group over the training sessions. ARAT and FMA scores increased significantly for both groups, and improved significantly more for the NMES-robotic support group. It was concluded that both systems were effective in improving long term motor functions, while the NMES-robotic support achieved better voluntary motor recovery, muscle coordination, and release in muscle spasticity.

3.2.3 Tendon-Driven FES Robotic Glove

The Tendon-Driven FES Robotic Glove makes use of a robotic glove and FES (Neto et al., 2019), Figure 3.3. The system is intended for hand rehabilitation post-stroke or SCI.

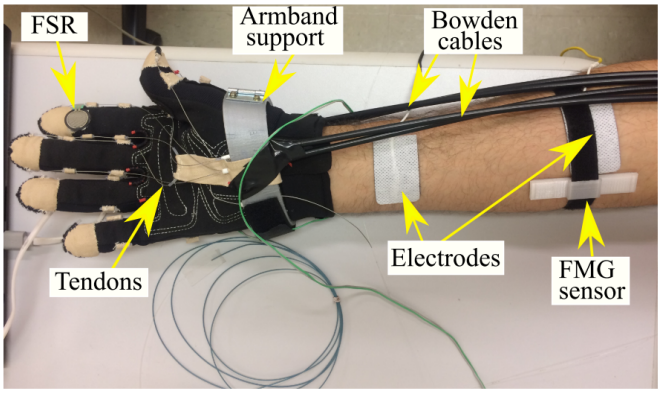

Figure 3.3: Tendon Driven Robotic Glove with FES (Neto et al., 2019).

The mechanical component of the system is comprised of a robotic glove that is driven by a servo-actuated tendon system. The tendons are routed through glove-mounted sheaths

to control thumb, index, and middle finger movements. Power supplies were not specified.

An open-source two-channel stimulator, STIMSHIELD, was used to provide biphasic stimulation through rectangular surface electrodes. Biphasic stimulation was applied to flexor and extensor muscle groups (one channel each) at 25Hz, pulse width of 150us, and magnitude up to 80V.

User intent is detected through an optical force myography (FMG) sensor placed on the FD. The optical FMG sensor measures light attenuation between two corrugated plates, which is modulated by the muscle's activity (Fajardo et al., 2019). Additionally, a force sensing resistor (FSR) is placed on the index fingertip to detect contact with an object. The closing, grasp, and opening of the hand is triggered by the FMG and FSR signal levels. A hybrid control strategy is implemented where FES and tendon systems are active in opening and closing sequences, but only the tendon system is active during passive grasp. The prototype has been tested on one healthy subject and showed the successful grasp of a glue stick and roll of tape 3.3.

3.2.4 Wearable Rehabilitation Robot

The Wearable Rehabilitation Robot is catered towards repetitive therapy in upper-limb stroke rehabilitation (Tu et al., 2012). The group note that many issues found in conventional rehabilitation robots and FES may be alleviated through the hybrid design. Pneumatic artificial muscles and FES enable five degrees of freedom (DOFs) to realise active reach-to-grasp trainings. The five DOF include finger flexion/extension, wrist flexion/extension, elbow flexion/extension, shoulder flexion/extension, and shoulder abduction/adduction.

The pneumatic muscles provide unidirectional mechanical actuation, while FES is applied to the corresponding antagonistic muscles. A commercial current-controlled stimulator, the Beurer EM41, provides two channels for FES. Stimulation pulses are set at a frequency

of 35Hz, pulse duration of 300us, and intensity between 10mA and 25mA. The intensity is tuned by the user through a computer GUI. The power sources for the stimulator and the pneumatic system were not mentioned.

User intent was not considered in the control architecture, instead a predefined sinusoidal trajectory was to be followed. Joint angle sensors provides positional feedback that guides the pneumatic and FES actuation FES is controlled in an on/off manner depending on the robot's angle and angle rate of change. The pneumatic muscles are regulated using positional error based incremental PID.

Experiments were conducted on one healthy subject (Tu et al., 2012). The pneumatic system output was limited so that the desired motion could not be achieved. FES was then introduced and the performance in regards to the reference trajectory was measured. It could be seen that with FES applied, the trajectory was achieved with less motion error. It was concluded that integration of FES can reduce the demand of robotic actuation force for a given movement.

3.3 Hybrid Exoskeleton Devices Applied to Other Areas

Hybrid systems with FES and active mechanical actuation have been developed for both upper and lower extremities. Although not directly relevant, systems that do not focus on the hand contain similar design concepts. A selection of these devices will be briefly discussed.

3.3.1 Upper-limb

Four upper-limb devices are covered: The ExoSlim (Irimia et al., 2016); EMG-Driven NMES Robot (Hu & Tong, 2014); and the NMES-Robot System (Rong et al., 2017).

The Exoslim is a hybrid FES-exoskeleton system for post stroke upper limb rehabilitation.

A combination of FES and DC-motor actuation are applied at the shoulder and elbow. The elbow forms a hybrid component as it is supported by both FES and motor. Control was implemented through MATLAB-generated commands. Angular position and acceleration feedback was provided to the user, while control was based off reference trajectories and positional data (Serea, 2014). An experiment was performed on one healthy subject (Rong et al., 2017). Electroencephalograph (EEG) signals were recorded and used to control the system through a Brain-Controlled Interface (BCI).

The EMG-Driven NMES Robot is designed for post-stroke wrist rehabilitation. A servomotor-based rehabilitation robot is combined with NMES to perform wrist flexion/extension. The wrist is strapped in place on a bench-top surface for the entirety of the exercises. An on-screen cursor is displayed; the cursor provides visual feedback and a target to track for the patients. EMG based proportionate control is implemented for both NMES and robotic components.

The NMES-Robot System is intended for coordinated multi-joint upper limb training. Both the wrist and elbow use a combination of NMES and servo motor actuation. Visual feedback is provided via PC display and EMG intention estimation is used. NMES and servo motors are proportionately controlled via a normalised EMG function.

3.3.2 Lower-limb

A review of lower-limb hybrid exoskeletons has been composed by Del-Ama et al (Del-Ama, Moreno, Koutsou, & de los Reyes-Guzman, 2013). The review identified two classes of hybrid exoskeleton: joint power dissipation (through braking or clutching) and active joint actuation. Only the active joint class is deemed applicable to this review. Four lower-limb hybrid exoskeletons are detailed below: HyPo (Obinata et al., 2007); Kinesis (Del-Ama et al., 2014); Powered Hybrid FES System (Ha et al., 2016); and the Hybrid Assistive System (Popovic et al., 1989).

The Powered Hybrid FES System uses cooperative control of FES with a powered exoskeleton for gait restoration of paraplegic persons. The system consists of a four-channel stimulator and the Vanderbilt lower limb exoskeleton. Electrical actuation is applied at the hips and knee of the exoskeleton and FES is applied to the quadriceps and hamstrings. The system follows predefined trajectories based upon joint-angle feedback. A PD controller is used for the exoskeleton, with the FES activation set as a disturbance to the control loop. FES activation is based upon exoskeleton torque from the previous iteration. Fatigue monitoring is included, using joint torque and FES amplitude readings for identification.

Kinesis is a hybrid leg exoskeleton for post-SCI rehabilitation. The device's knee forms a hybrid component: A Maxon DC-motor is combined with FES (via Rehastim commercial stimulator) of the knee flexor/extensor muscles. Impedence control is used for the DC-motor, applying a torque field around a reference trajectory. FES of extensor and flexor muscles are controlled by proportional-integral-derivative (PID) and iterative-learning-control (ILC), respectively, to minimise leg/exoskeleton interaction forces. Positional and force feedback are used as inputs to these control systems. Muscle fatigue was detected when the subject's torque-time integral generated under constant stimulation parameters decreased by 19%.

The hybrid leg exoskeleton, HyPo, is developed for motor function rehabilitation of SCI patients. DC motors are placed on parallel structures for hip and knee joint actuation. Functional neuromuscular stimulation (FNS) is applied to the quadriceps. Voluntary motion is cued via user interface. Actuator encoders are used to provide joint position and velocity information; motor torque control is based on these readings. FNS effort is included as a disturbance to the control system.

Popovic et al. designed a Hybrid Assistive System for motor rehabilitation of paralysed lower limbs. The system was tested on one subject with quadriplegia resulting from in-

complete spinal cord severance. The Self Fitting Modular Orthosis (SFMO) (Popovič & Schwirtlich, 1993), through cybernetic actuators, drove the patient's knees and ankles. A six channel stimulator was applied to the gluteus medius, quadriceps, and peroneal muscles. A qualitative control method, artificial reflex control, was applied. Potentiometers are used to give joint angle feedback, and force transducers give pressure feedback. The control system uses these readings to evaluate a set of boolean rules. Muscle fatigue resistance was tested before the experiment, however no measurements were made in real time and fatigue did not factor into the control system.

3.4 Discussion

3.4.1 Portability

Most hand exoskeleton rehabilitation devices lack portability (Iqbal, Khan, Tsagarakis, & Caldwell, 2014). Portability of the reviewed systems appears to restrict them to more conventional rehabilitation rather than ADL assistance. Lack of portability can be attributed to the device's weight and size, as well as their dependence on PC and power supply connections:

- *Weight and size:* Devices such as the EMG-Driven NMES Robot, Wearable Rehabilitation Robot, and EMG-driven NMES Robotic Hand Robotic Hand are all bulky in nature: power-supplies and computers are supported by an external structure such as a bench-top, rather than the subject themselves. This set-up suits a conventional rehabilitation setting where the patient is stationary. If the systems were to be used for ADL, the externally supported items would have to be transferred to the patient and exoskeleton. Although this may improve the manoeuvrability of the device, the additional weight of each component will contribute significantly to user fatigue, thus reducing the time in which the system can be donned.

- *External power supply and PC connection:* Reliance on a PC connection or external power supply can also have a large effect on device portability. Most of the reviewed exoskeletons are tethered to a PC, either for data acquisition or control processing. This inhibits the motion range of the user, ultimately hampering ADL. Connection to external power or air supplies will achieve the same effect. Additionally, power sources such as an air supply may be hard to acquire for an outpatient setting: most of the reviewed devices do not disclose the energy source used.

- *Specialised Software:* Specialised software can hinder both ADL and rehabilitation systems, as the system's compatibility with outpatient settings is subject to the software's availability to the patient. The IHRG, Exoslim, and Powered Hybrid FES System, all use MATLAB. The EMG-driven NMES Robotic Hand Robotic Hand and NMES-Robot System both use LabVIEW.

Each of the reviewed devices seem appropriate for the delivery of conventional rehabilitation and for rehabilitation-based research. Additionally, they all appear to be compact enough to be transferred to outpatient environments; however, the reliance on external power supplies, computer connections, and specialised software, mean that many of the reviewed devices are not appropriate for outpatient use.

3.4.2 Intention Recognition

There are a number of methods used for intention sensing in hybrid exoskeleton systems. Perhaps the simplest approach is a computer interface where the user is required to press a button to initiate movement. Two upper-limb exoskeleton systems have used this method: The Wearable Rehabilitation Robot and the earlier prototype of the Exoslim. The simplicity of this approach is advantageous. However, the button press occupies one hand and therefore may limit this intention method and the spontaneity of movements (e.g. scenarios without a physiotherapist present that requires two hands). The next simplest

approach may be bilateral control, as used by the IHRG, where the unimpaired hand is used to guide the assistance of the impaired hand.

The use of bioelectric signals for intention estimation is becoming increasingly commonplace in exoskeleton technology. EMG and EEG signals are the most typically applied. Both EMG and EEG require volitional effort, increasing the degree of participation from the subject (Frisoli, Solazzi, Loconsole, & Barsotti, 2016). Through the subject's intention and ensuing sensation of the intended movement, the re-establishment of neural pathways may be enhanced. However, the use of EMG for intention estimation often requires more complex control systems and calibrations due to time-varying responses and high inter-subject variability (Trigili et al., 2019).

Of the reviewed exoskeletons only the upper-limb designs use bioelectric signals, with EMG signals the most commonly monitored. EMG signals tend to be used as opposed to EEG as they are most easily acquired and processed, and tend to be more reliable (Lalitharatne, Teramoto, Hayashi, & Kiguchi, 2013). EMG can be used to provide an 'assist-as-need' actuation control. The EMG-Driven NMES Robot, EMG-driven NMES Robotic Hand Robotic Hand, and NMES-Robot System use the normalised EMG profile to regulate robot/FES assistance. It is important to note that the use of EMG in the presence of FES requires careful placement of electrodes and additional processing steps to filter stimulation artefacts. To avoid these conditions, Neto et al use FMG: FMG can be considered as a mechanical counterpart to EMG and is insensitive to electromagnetic noise. For some subjects, muscle spasms can often cause disturbances to EMG and FMG readings. In addition to this, EMG and FMG signals may be hard to capture, or may not be present in some individuals (Ferreira et al., 2008). In these situations the use of an alternative method such as EEG may be desired.

The reviewed lower-extremity devices do not utilise bioelectric signals for intention estima-

tion, rather relying on external measures such as interaction force, pressure, and positional feedback. Of the four lower-limb exoskeletons, three use similar intention estimation systems: whilst in a 'stance' phase, force sensors are used to detect shifts of pressure and initiate the leg swing movement. The HyPo lower limb exoskeleton uses an interface to cue voluntary movement; however this interface is yet to be fully developed.

3.4.3 Control

There are a number of ways that a user's movement intention can be measured and recognised, from a button push to bioelectric signals. Subsequent control of actuation can be implemented through various methodologies.

Of the reviewed systems, control loops are most commonly applied to track a predefined reference trajectory. This control methodology is considered passive as little attention is given to the subject's voluntary effort post-triggering. For the lower-extremity devices, reference trajectories are integrated between stance and swing phases. Upper-limb devices typically apply reference trajectories towards reach-to-grasp movements.

Control systems such as ILC, impedance control, and variations of PID control have been implemented in the reviewed devices. Joint angle feedback is typically the main controller input to regulate motor actuation and FES efforts. Lower-extremity devices such as HyPo, the Powered Hybrid FES System, and Kinesis also regulate FES efforts to minimise motor torque and person-exoskeleton interaction forces.

Control procedures that incorporate the patient's voluntary capacity and engagement throughout rehabilitation are increasingly important. Due to the strong component of user intent in these control techniques, reliable real-time user intention estimation is critical. Four of the reviewed exoskeletons utilise a continuous measure of user intent to guide robotic and FES assistance. The IHRG, designed for bilateral rehabilitation, uses the non-paretic hand to

provide a continuous measure of user intent. This is perhaps the most simple approach for continuous control. The EMG-Driven NMES Robot, NMES-Robot System, and EMG-driven NMES Robotic Hand Robotic Hand each use normalised EMG of the stimulated muscle to control their assistance profiles. Each design demonstrates the importance of a balanced support ratio for the reduction of tracking error. However, it should be noted that the support ratios were fixed for the duration of each trial. A coupled control scheme would take better advantage of the hybrid nature of the system and allow dynamic adjustment of support levels. This dynamic behaviour will allow a better response to occurrences such as muscular fatigue and help to maximise the 'assist as need' functionality of the device.

3.4.4 Fatigue

Health benefits obtained through FES-evoked exercise are limited by rapid muscle fatigue (Ibitoye, Hamzaid, Hasnan, Wahab, & Davis, 2016). The rate of fatigue through FES driven contractions has been seen to be greater than through voluntary contraction. A number of causes have been identified such as simultaneous stimulation of motor units, and the unnatural recruitment order (Doucet, Lam, & Griffin, 2012).

Muscular fatigue is rarely monitored in exoskeleton systems, with only three of the reviewed hybrid systems making any measurements. Only Kinesis and the Powered Hybrid FES System monitor fatigue in real time and apply this information in the exoskeleton control. The Powered Hybrid FES System uses joint torque output with respect to stimulation intensity as a measure of fatigue. Kinesis monitors the leg-exoskeleton interaction torque time integral (TTI). Subsequent to fatigue detection, the Powered Hybrid FES System simply halts stimulation for a two minute period, while Kinesis modifies the FES parameters through frequency and intensity modulation (del Ama Servicio, Gómez-Soriano, Bravo-Esteban, & Moreno, 2013). Both the Kinesis and the Powered Hybrid FES System seek to remedy fatigue after a threshold has been breached, and only do so through the adjustment of FES parameters.

Although no upper-extremity devices monitor fatigue, two consider reduction mitigation in their design. Neto et al (Neto et al., 2019) apply FES and mechanical actuation during hand opening/closing, but only use mechanical actuation to provide object grasping forces. Rong et al (Rong et al., 2017, 2015) provide a two minute rest between trials.

Very few exoskeleton designs have the capacity for fatigue detection or monitoring, and the few that do only focus on reduction/remedial efforts, rather than use it as an active control component. Fatigue based dynamic adjustment of FES-robotic support may allow for better patient adaptability, comfort, and ultimately performance.

3.4.5 Actuation and Electrical Stimulation

Actuation

Across reported dynamic hand orthoses, electrical actuation is the most commonly used, such as DC or servo motors (Bos et al., 2016). This trend is reflected in the reviewed devices, which utilise electric motors for their high torque capabilities, small package size, and for their ease of control. However, care needs to be taken in their placement. The actuator needs to provide sufficient force levels for effective functional movements, but cannot be so heavy that the patient is uncomfortable or rapidly fatigues.

The closer a weight is placed towards the core of the user's body, the more easily supported. Consequently, devices that support the shoulder and elbow joints, such as the Exoslim, are able to directly couple the motor to the DOF of interest. Appropriate actuator placement is crucial for hand exoskeletons. The EMG-driven NMES Robotic Hand Robotic Hand uses DC linear motors for each finger, placed on the dorsum of the hand. The device was shown to improve a subject's movement accuracy, however, some subjects reported difficulty with the weight of the device (Rong et al., 2015). The initial design for the IHRG also planned actuators on the dorsum of the hand, but encountered difficulty in their mounting. Cabled transmission as seen in the updated IHRG design and the Tendon-Driven FES Robotic

Glove, allowed for the actuators to be placed more proximally on the body (or elsewhere). In these designs the constraints on actuator weight could be alleviated at the price of degraded transmission efficiency and varying friction loads.

The Wearable Rehabilitation Robot uses pneumatic muscle actuation due to their higher power to weight ratio and inherently compliant nature. The designers have noted however that the pneumatic actuators have limited stretch distance and have a slower response due to compressed air. The use of pneumatic actuation may be further limited due to their control complexity and the need for an air supply. Other actuation options include the use of hydraulics, and materials such as shape memory alloy and electro-active polymers. These technologies are not yet commonly applied in rehabilitation exoskeleton technologies.

The actuator supported movements depend on the joint of interest. For instance, a knee exoskeleton will typically support one DOF whilst a shoulder exoskeleton often supports multiple. Amongst the hand-exoskeletons reviewed, there are a range of supported DOF. The IHRG and FES/Robotic Hand actuators support independent flexion/extension of each finger and thumb. The designers of the Tendon-Driven FES Robotic Glove chose only to actuate the flexion/extension of the index and middle fingers (one actuator), and thumb.

Electrical Stimulation

A range of electrical stimulators are adopted by the reviewed devices. Commercial systems such as Motionstim 8 and Rehastim 2 are used by the IHRG, Exoslim, Kinesis, and Wearable Rehabilitation Robot. For the other devices, it was unclear whether the stimulation boards were custom designed or commercial. During the application of FES, three parameters are predominately controlled: Pulse frequency, width, and intensity. The respective levels of each parameter varies between each patient and movement focus. Stimulation frequency typically remains fixed whilst pulse width and/or amplitude are varied.

The DOF supported by stimulation are limited by the relative size of the electrodes and muscles of interest. Typical electrode sizes range from 25x25mm to 40x90mm. For lower-extremity and upper-arm DOF, stimulation can achieve selective movement due to the larger size of the target muscles. Muscle selectivity becomes an issue for the hand DOF due to the size and spacing of forearm muscles. This is reflected in reviewed hand-exoskeletons where stimulation only provides gross hand opening/closing motions.

3.5 Device Limitations

3.5.1 Outpatient suitability

With the exception of the Exoslim and the Tendon-Driven FES Robotic Glove, the reviewed devices are designed for conventional rehabilitation purposes. The majority of devices could be made portable for home-based rehabilitation, however, mobility restrictions limit them to clinic-based therapy settings. Such restrictions include the need for a PC, specialised software, and external power/air supplies. The designers also do not appear to consider the cost of their device or ease of production. This presents another factor limiting access to their technology.

Environmental setting can have a large impact on the effectiveness of therapy. In particular, home-based or community settings can provide context to rehabilitation and improve patient engagement. The development of portable robotic rehabilitation devices can enable access to high-dosage rehabilitation outside of the hospital (Keller & Veneman, 2012). Design for ease of production would also be beneficial towards more accessible, meaningful therapy.

3.5.2 Intention Recognition and Cooperative Control

Most devices do not take the user's voluntary capacity into account, instead passively following a joint trajectory using PID control or ILC. Only the FES-Robot rehabilitation system

and designs by Rong et al base their control on a continuous measure of user intention. Creating an assist-as-need control base can help maximise therapeutic effects, and when associated with bio-electric signals such as EMG, these effects can be further enhanced.

The reviewed devices have not fully exploited the availability of robotic support in conjunction with FES. In association with hybrid systems, the benefit most referred to is the ability to reduce energy consumption and device weight/volume; however, there are further potential benefits in the combination of FES and robotic support. Early onset of fatigue significantly limits the application of FES in rehabilitation. With the addition of robotic compensation in a dynamic control approach, this fatigue may be delayed and minimised. However, all of the reviewed upper-limb exoskeletons do not monitor fatigue nor manage it. A selection of lower-limb devices provide fatigue monitoring/management, yet only the FES assistance is adjusted after fatigue detection.

Cooperative/compensatory control of robotic and FES assistance can also be applied to present a more customised therapy for the patient; for instance, more precise movements or higher muscular activation may be more suited depending on the patient's abilities and stage of rehabilitation. With the robotic support's ability to generate precise movement and stimulation-elicited muscle activation, tuning of the support ratio can be used to achieve the desired assistance profile. Furthermore, a dynamic control base could be especially useful where a patient becomes uncomfortable due to stimulation effects.

3.5.3 Supported Movements

The DOFs supported by the reviewed devices are a function of both FES and robotic DOFs. Of the reviewed hand exoskeletons, robotic supported DOFs ranges from independent flexion/extension of the fingers and thumb to simple one-DOF hand opening/closing. In all devices, FES only supports one-DOF hand opening/closing; consequentially the use of hybrid FES-robotic control is limited to functional movements that involve whole-hand

grasp and release. Lack of FES selectivity can be attributed to the electrode sizes and lack of space on the forearms. This effect is magnified when EMG based intention is used, requiring a further three electrodes.

FES support is currently the limiting factor behind achievable movements in hybrid hand exoskeletons. Higher resolution FES is required to improve their functionality past one-DOF. Of the reviewed devices, those which apply an actuator per finger currently sacrifice exoskeleton weight for no functional gain. It is also important to note that typical activities of daily living (ADL) movements do not require independent flexion/extension of each finger. In current hybrid hand devices, imbalance of FES and robotic DOFs can create excess weight and limit movements to full hand opening/closing. It is therefore important to develop a more balanced DOF support to enable functional movements without redundant device weight.

3.6 Summary

Conjunction of robotic and FES modalities holds promise to generate more effective rehabilitation technologies. The reviewed hybrid systems present a step in the right direction towards more effective and efficient rehabilitation resources. The devices' application of hybrid FES robotic support has been shown to improve patient tracking error and reduce the demand of robotic torque for a given movement. Design limitations, however, reduce the devices' effectiveness and wider application. In order to maximise the therapeutic impact of hybrid robotic FES support, further developments are still required. Key developements include improved compatability with outpatient settings, cooperative control of FES/robotic efforts, and function balance of DOF support between FES and robotic actuation.

The hybrid exoskeleton developed in this thesis aims to improve portability through the coupling of the index-middle and ring-little fingers, reducing the required number of actuators while supporting functional pinch and grasp movements. In order to promote DOF

balance between FES and robotic components, an EMG device will be developed which can record through the stimulation electrodes, facilitating higher resolution EMG and FES. The device will be used to provide volitional-intent estimates concurrent to stimulation, in-turn used to guide FES and robotic support in an assist-as-need nature. EMG-based fatigue metrics will be investigated during these assist-as-need supported dynamic movements. These studies aim to provide insight on the potential for EMG-based fatigue indices to be integrated into hybrid-exoskeleton devices, ultimately towards fatigue compensation through dynamic balance of FES and robotic modalities.

CHAPTER 4

Hybrid Exoskeleton Component Background

4.1 Rehabilitation Robotics

Robotics have potential for stroke rehabilitation and are gradually replacing manual therapies (Iqbal & Baizid, 2015). Rehabilitation robotics have a number of benefits over conventional therapy. They are able to provide consistent, high intensity, and interactive rehabilitation, with performance measures that can be more specific and reliable (Norouzi-Gheidari et al., 2012). Robotic training is based on exercise therapy modalities such as passive movement, where the robot fully controls the patient's arm, and active assistance, where movement is partially supported (or resisted) by the device. Therefore, robotic assistance can be applied regardless of the patient's voluntary function (Prange, Jannink, Groothuis-Oudshoorn, Hermens, & IJzerman, 2006).

Physical therapy and activities of daily living (ADL) assistance are two main post-stroke ap-

plications for robotic devices. Devices providing physical therapy are often made complex in the attempt to support many degrees of freedom (DOFs). Consequently, these robots tend to be heavy, expensive, and have limited portability. Physical therapy robots tend to be used in clinical settings rather than for home-based rehabilitation. Devices for ADL assistance will be worn for extended periods of time during the day. The usability of ADL systems are therefore dictated by factors such as weight, portability, ease of use, comfort, and safety (Maciejasz et al., 2014). The devices should also be cost effective to extend availability to a wide range of users. To improve the aforementioned qualities and to simplify the design, ADL based devices will often support fewer degrees of freedom.

End-effector and exoskeleton-based mechanisms are used in robotic devices. End-effector based devices attach to the distal end of the limb, Figure 4.1a. For the hand, the device would attach and manipulate from distal end of the fingers, Figure 4.1b. Due to the nature of the coupling, end-effector devices have the advantage of not constricting joint motion and keeping the palmar side of the hand free. However, they are less suitable for home-based rehabilitation or ADL due to poor portability (Bos et al., 2016). Exoskeleton devices are fitted closely to the body, and the mechanisms tend to be more complicated than end-effector devices. Device complexity is elevated by issues such as limited spacing, joint alignments, and user compatibility. Safety issues such as pressure and pinching of the skin also need to be well managed. Exoskeleton devices, however, are more portable and can more closely mimic human movement due to direct control of more DOFs.

Robotic devices apply external torque to generate patient motion, however, cannot directly activate muscle. Robot-based therapy therefore lacks the physiological benefits inherent to stimulation therapy. Consequently, isolated application of these devices may not drive desired patient outcomes.

The majority of robotic designs are developed for hospital use, often focussing on a high

(a) Hand end-effector (Ranzani et al., 2020)

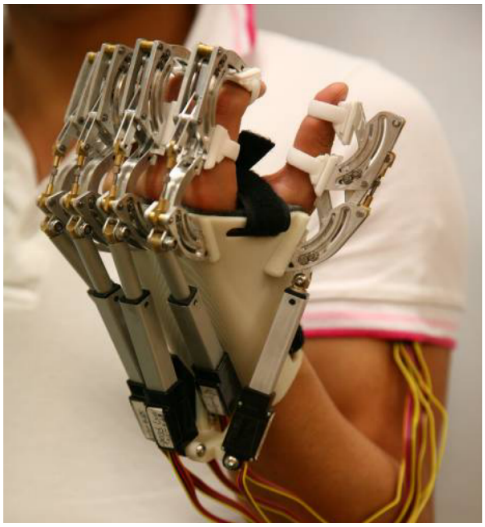

(b) Hand exoskeleton (Tong et al., 2010)

Figure 4.1: Hand exoskeleton and end-effector devices.

number of actuated DOFs and neglecting portability. Among the designs for ADL/outpatient settings, many still suffer from issues of portability, user fatigue, power consumption, and device acceptance. These issues may stem from the number of DOFs supported and required manipulation forces, which define specifications on design structure and actuation. For instance, in a hand-exoskeleton that independently moves each phalanx, a minimum of five actuators are required. Each actuator needs to provide sufficient manipulation forces whilst the device structure needs to support the finger DOFs and withstand loading forces. When applied to the distal regions of the body such as the hands, careful management of device weight and size is especially critical to ensure patient comfort.

4.1.1 Hand Exoskeleton Supported DOF

The hand is a complex structure consisting of many DOFs. This nature allows the hand to produce the broad spectrum of movements used in everyday life. Accounting for the full complexity of the hand, however, would give rise to convoluted and cumbersome exoskeleton designs. Consequently, hand exoskeleton designers often take steps to simplify the anatomical model, such as approximating finger joints as a series of revolute joints, and omitting certain DOF depending on intended function. The most common finger model adopted in hand exoskeleton design is a 4-DOF revolute chain (Sarakoglou et al.,

2016), as seen in Figure 4.2. Flexion/extension movements of the metacarpophalangeal joint (MCP)-proximal interphalangeal joint (PIP)-distal interphalangeal joint (DIP) chain are represented by a planar 3-revolute chain (red joints) while MCP abduction/adduction is represented by a perpendicular revolute joint (blue joint).

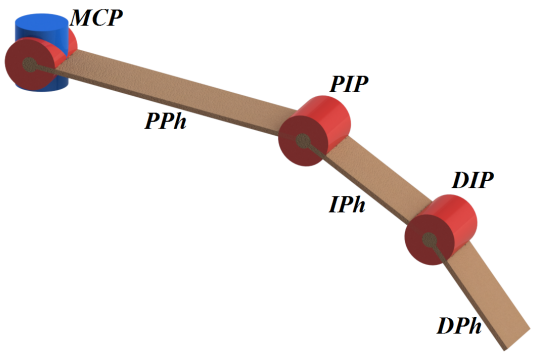

Figure 4.2: Simplified finger model 4-R chain. MCP, PIP, and DIP are the Metacarpophalangeal, Proximal Interphalangeal, and Distal Interphalangeal joints. PPh, IPh, and DPh, are the corresponding Proximal, Inter, and Distal phalanxes

In current exoskeleton technologies, there is diversity in the support of finger joints and DOFs. Any movement that is controlled by an exoskeleton is seen as a supported movement. In finger exoskeletons flexion/extension movements are most often supported whilst the abduction/adduction of the MCP joint is left passive, reducing the finger model to a 3-revolute planar chain. Active support of the MCP ab/adduction, such as in works by Fontana et al (Fontana, Fabio, Marcheschi, & Bergamasco, 2017) and Kawasaki et al (Kawasaki, Ito, & Ishigure, 2007), achieve a higher degree of controllability, but result in a more complex device.

Actuators: The number of used actuators can vary considerably. Considering the basic three-revolute (three-DOFs) planar finger model, there are a range of options for actuation. Firstly, a designer may use an actuator per DOF, obtaining independent control of the MCP, PIP, and DIP joints (Jones, Wang, Morrison, Sarkar, & Kamper, 2014; Kawasaki et al., 2007; J. Li, Zheng, Zhang, & Yao, 2011). The resulting exoskeleton will be highly controllable and have a large reachable workspace. However, the device is likely to be

cumbersome and complicated. Reducing the number of actuators will help to alleviate issues of weight, complexity, and size. There are two main ways to feasibly reduce the number of exoskeleton actuators:

- Underactuation: In underactuated devices there are fewer driving sources than DOFs, often relying on passive elements such as springs to achieve desired motion. Underactuation of a finger-exoskeleton can result in a simpler device without constraining the finger workspace. However, complete control of finger joint posture cannot be achieved (Chiri et al., 2012; Sarac, Solazzi, Sotgiu, Bergamasco, & Frisoli, 2017). Despite the lack of fully constrained motion, underactuated exoskeletons have been shown to produce natural flexion/extension grasping motions (Ertas, Hocaoglu, & Patoglu, 2014; Sarac et al., 2017). The AssistOn-Finger applied elastic elements to ensure motion coordination (Ertas et al., 2014), whilst Sarac et al. showed that intrinsic finger-joint mechanical impedance is sufficient to produce natural motion (Sarac et al., 2017).

- Reducing exoskeleton DOFs: Reducing the exoskeleton DOFs lessens the requirements for actuation. DOF reduction can be achieved by neglecting a finger phalanx (most often distal) (Schabowsky, Godfrey, Holley, & Lum, 2010; Taheri et al., 2014; Takagi et al., 2009). However, reduction is more commonly accomplished through coupling of joint motions. Existing dynamic intra-finger constraints allow for DOF reduction without losing natural finger motion. The strongest intra-finger constraint is between the PIP and DIP joints: a coupling ratio of $\theta_{DIP} = 2\backslash 3\ \theta_{PIP}$ has been found in a variety of studies (Chen Chen et al., 2013; Cobos, Ferre, Sánchez-Urán, & Ortego, 2007; Rijpkema & Girard, 1991) and successfully applied in exoskeleton/prosthetic technologies (Lin, Wu, & Huang, 2000; Liu & Zhang, 2007). Weaker correlation between MCP and PIP/DIP joint movements have been noted (Lucas, Dicicco, & Matsuoka, 2004; Yili, Wang, Wang, Liu, & Zhang, 2007). However, Chen et al. reported

that the $\theta_{PIP} = 3\backslash 4\ \theta_{MCP}$ relationship proposed by Cobos et al. is faithfully respected under normal flexion/extension motions (Chen Chen et al., 2013; Cobos et al., 2007). Infact, linear MCP-PIP coupling ratios have been applied in a number of exoskeleton/prosthetic designs to produce acceptable natural motion (Sidher, 2017; Taheri et al., 2014; Takagi et al., 2009). In other works Jo et al. and Yang et al. estimated the MCP-PIP coupling with higher order polynomials (Jo, Park, Lee, & Bae, 2019; Yang, Xie, & Shi, 2016).

The choice of supported movements and DOFs depend largely on the intended application of the exoskeleton. Through independent actuation of multiple DOF or the use of underactuation, an exoskeleton can move throughout a workspace. Conversely, a highly constrained mechanism is spatially limited. For instance, a one-DOF finger mechanism in which all phalanx rotations are coupled, can only follow one trajectory. Logically, an exoskeleton with a larger workspace can be used for a broader range of tasks/hand poses, whilst a one-DOF system can only be used for simple motion. Basic curling motion, however, is the predominant finger movement incorporated into most ADL (Taheri et al., 2014). Accordingly, Yang et al. recommends that recovery of the hand's normal curling function should have priority over more complex movement (Yang et al., 2016). Refour et al. note that the finger essentially behaves as a one-DOF system during common grasping motions due to inherent joint couplings (Refour et al., 2018). This is reinforced by the findings of Kamper et al (Kamper, Cruz, & Siegel, 2003). The index fingertip follows a stereotypical logarithmic trajectory during a grasp, and different-sized objects only effect the trajectory portion in which the fingers follow. Kamper et al. suggests that hand function could be significantly improved with the recovery of a small sector of the finger workspace.

Robotic exoskeletons can provide consistent high-intensity motion assistance. However, the devices typically become cumbersome through the actuation of many DOF. Towards post-stroke hand rehabilitation, the recovery of basic finger curling is often recommended

over more complex movements. This suggests that an exoskeleton with coupled-DOFs may be useful in rehabilitation settings, as it can support the recovery of functional grasping motions whilst reducing actuation requirements. By reducing the number of actuators, a coupled-DOF exoskeleton can lower device volume, weight, and component cost. Ultimately, these factors can lead to lesser-rates of patient fatigue and higher levels of user acceptance.

4.2 Electrical Stimulation

Neuro-muscular electrical stimulation (NMES) is electrical stimulation of paralysed muscles, applied through intact lower motor neurons (LMN). Functional electrical stimulation (FES) is a class of neuro-muscular electrical stimulation (NMES) with the objective of accomplishing functional tasks. To these ends, FES can either assist or replace a person's voluntary ability, and does so through precise sequences and magnitudes of activation (Sheffler & Chae, 2007). Through FES, two mechanisms are hypothesised to promote neuro-plastic change leading to regained functionality. Firstly, FES stimulates afferent peripheral nerves. Plasticity may be promoted through this feedback, coupled with task-related movements. Secondly, the application of FES with voluntary effort could cause antidromic firing of motor nerve fibres, in-turn causing remodelling of the Hebb-type pyrimidal tract - anterior horn synapses (Piast, Kustrzeba-Wójcicka, Matusiewicz, & Banaś, 2005; Quandt & Hummel, 2014). Other physical benefits may arise from the use of FES such as muscular strengthening, reduction of muscle atrophy, and sensory recovery. These effects are induced by the stimulation of motor and sensory neurons (Chantraine, Baribeault, Uebelhart, & Gremion, 1999; Doucet et al., 2012).

FES may be applied transcutaneously, subcutaneously, or through implanted electrodes. Typically, surface electrodes are used as they are non-invasive and can be easily applied/removed. In typical FES devices, current is passed through surface electrodes, placed on the skin over the motor points or nerves of the target muscle. The passing current generates

an electric field, localised around the electrodes, which has a depolarising effect on the cell membrane of neurons within its vicinity, Figure 4.3. If the applied current is above a nerve's stimulation threshold, voltage gated sodium ion channels will activate, eliciting an action potential in the innervating axon. The action potential is conducted in both directions from afflicted area. The distal impulse travels to the neuromuscular junction and elicits contraction of muscle cells. Note that neuronal action potentials have stimulation thresholds 100 to 1000 times lower than producing muscle fibre action potentials. Therefore it can be deduced that the LMN and neuromuscular junction need to be intact for FES to be effective (Peckham & Knutson, 2005; Sheffler & Chae, 2007).

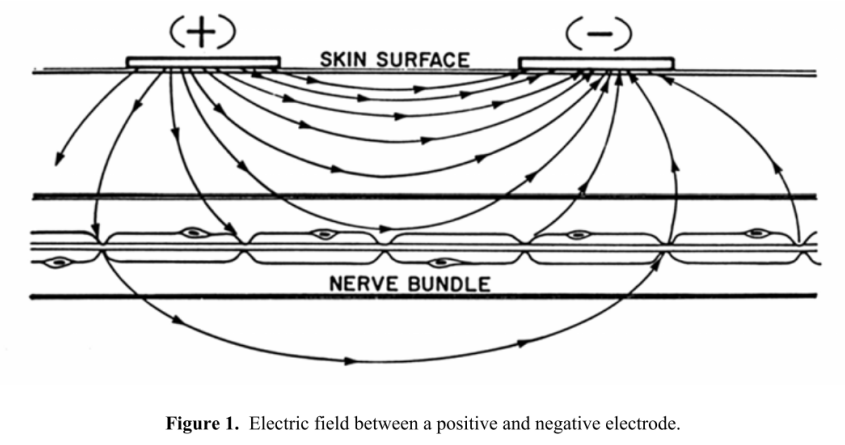

Figure 4.3: Electric field between FES electrodes (Bajd & Munih, 2014).

4.2.1 FES configurations and parameters

Pulse waveform configuration

Stimulation is predominately delivered as a chain of pulse waveforms, Figure 4.4. Commonly, monophasic or biphasic square waves are applied. Monophasic waveforms consist of a unidirectional pulse. Biphasic pulses consist of a repeating current pulse of positive phase combined with a negative phase (Peckham & Knutson, 2005). The initial phase is used to activate axon action potentials, and the second phase is used to balance electrode-skin charge. This configuration reduces charge accumulation that could potentially cause damage to the skin and electrode. It is important to note that waveform amplitudes may

not be symmetrical, and there may be an interphase delay.

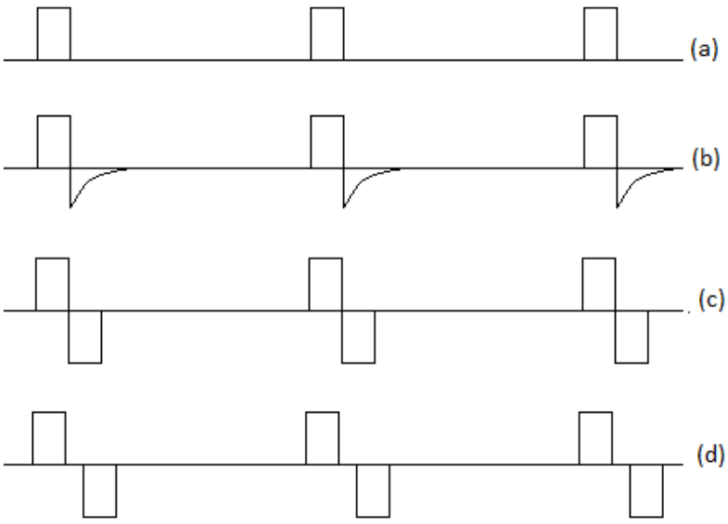

Figure 4.4: Typical FES pulse waveforms(a) Monophasic (b) Asymmetric biphasic (c) Symmetric biphasic (d) Symmetric biphasic with Interphase delay (Stewart et al., 2016).

Electrode configuration

Two electrode configurations can be used for electrical stimulation, bipolar and monopolar. In both configurations an active electrode is usually placed near the motor point. In a monopolar configuration an inactive/indifferent electrode is placed remotely from the active electrode. For a multichannel set-up the inactive electrode will act as a current return route for all active channels. Bipolar configurations use an indifferent electrode per active electrode, often placed in near proximity to the active contact. Consequently, a bipolar multichannel system will have many more leads/connections than a corresponding monopolar system. However, bipolar arrays allow for greater activation selectivity due to a more localised electric field between each electrode pair (Peckham & Knutson, 2005).

Constant current, constant voltage

There are two main types of electrical stimulators, constant current (CC) and constant voltage (CV). CC devices tend to be more complex and expensive than CV, however consistent physiological response is more achievable in CC devices due to their independence from

electrode-skin impedance. CV devices are not typically able to produce stimulation with the same repeatability and reliability as CC stimulators, however they are inherently more safe. With a CC output, incorrect electrode contact can cause current densities to increase to uncomfortable and dangerous levels (Krenn & Löfler, 2013).

FES parameters

Through altering of stimulation parameters, induced contractile force can be regulated. Figure 4.5 depicts a typical biphasic stimulus square waveform. The waveform can be characterised by four attributes: pulse amplitude (PA), pulse width (PW), inter-pulse duration (IPD), and pulse frequency (f).

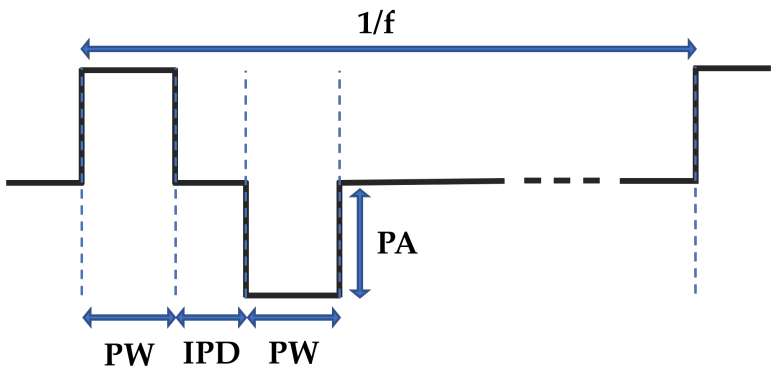

Figure 4.5: Typical biphasic square-wave stimulation waveform with pulse frequency (f), pulse amplitude (PA), pulse-width (PW) and inter-pulse delay (IPD).

The pulse frequency refers to the number of pulses per second during stimulation (Doucet et al., 2012). Strength of contraction increases as the applied pulse frequency increases. Above a certain frequency known as the fusion frequency, the temporal summation of stimuli does not allow the muscle to return to its resting state, producing smooth contraction. Below this frequency, the stimuli will result in twitching of the target muscle. Elevated muscle fatigue is associated with higher stimulus frequencies and the increase of stimulus frequency will only increase contraction strength up to a limit. In the application of FES, near-fusion frequencies that result in smooth contraction are typically applied, helping to minimise patient fatigue and discomfort (Eser, Donaldson, Knecht, & Stüssi, 2003). Most systems use stimulation frequencies in the range of 10-50 Hz (Sheffler & Chae, 2007)

The time span of a stimulation pulse is known as the pulse width (Doucet et al., 2012). Pulse widths of 0-300us are commonly applied in upper-limb FES therapy, and up to 500us for lower-limb applications. For biphasic stimulation waveforms, the period between phases is known as the inter-pulse duration. Pulse amplitude is the strength of the stimulus, typically in milliAmperes (CC devices) or volts (CV devices). Stimulation current of up to 150mA and voltage up to 150V are commonly provided. Stimulus amplitude and pulse width are analogous to stimulation intensity (Wood & Swain, 2013). As previously mentioned, if the applied stimulus is above a nerve fibre's stimulation threshold, an action potential is triggered and consequentially muscle fibre contraction occurs. Conversely, if the stimulus is below the stimulation threshold, no contraction occurs. As pulse width or amplitude are increased the effective intensity of the stimulus is elevated. Consequently, the range of the produced electric field is expanded, depolarising a broader range of nerve fibres, and activating a larger number of motor units. This phenomenon is known as spacial summation. At higher intensities, the electric field ranges further into the muscle and begins to activate deeper motor units (Mesin, Merlo, Merletti, & Orizio, 2010).

FES is an important tool for stroke-rehabilitation as it can directly activate a patient's muscles and promote neuro-plastic change. Modulation of stimulation parameters such as pulse frequency, pulse width, and pulse amplitude, can influence physiological responses such as the strength of muscle contractions as well as the rate of muscle fatigue. Therefore, control over stimulation parameters is essential to provide effective motor-unit recruitment whilst minimising patient discomfort and fatigue. Towards these requirements, a stimulator that allows user adjustment of its waveform parameters would be a useful tool in therapy and research applications.

4.3 Electromyography

Bioelectric signals are becoming increasingly common-place in stroke rehabilitation technology: electromyography (EMG) is perhaps the most frequently utilised. An EMG device

is used to study skeletal muscle contraction, detecting the electrical activity in muscle cells (Suhaimi, A.R, Adnan, Shahriman, & Bakar, 2014). When applied in neuroprosthetic technology, EMG is commonly used as a measure of movement intention, either controlling or triggering the induced motion. Additional information can be extracted from EMG signals, such as fatigue and muscle-contraction estimates. This information may help direct the assistance of rehabilitation tools.

There are a range of benefits in using EMG to control movement generation. As voluntary effort is required, EMG-based control can be provided in an assist-as-needed manner and increases patient engagement in their rehabilitation (Giggins, Persson, & Caulfield, 2013). In hemiplegic patients, there is likely still a detectable EMG signal, even if their resulting contraction is weak. Due to electro-mechanical delay EMG signals can be detected 2-3 ms before muscular contraction. Therefore, EMG-based assistance can be provided synchronously with the patients voluntary effort (Basmajian & De Luca, 1979). Furthermore, EMG intention (as opposed to inputs such as buttons or joysticks) allow the patient to use both hands whilst the device is operating. The ability to use both hands can greatly increase functionality and the range of tasks that can be participated in. Robotic and electrical stimulation systems have progressively began to integrate EMG.

4.3.1 Electromyography of stimulated muscle

Due to the low amplitude of the bio-potential signal, EMG can be contaminated by several forms of interference, such as mains supply interference and movement artefact. In stroke rehabilitation use, EMG is often used alongside functional electrical stimulation (FES). However, due to the nature of FES, the user's volitional EMG (vEMG) signal becomes contaminated with interference. Such interference is elicited by two predominant artefact sources: stimulation artefacts and the elicited EMG (eEMG) (Luo, 2013; Reaz, Hussain, & Mohd-Yasin, 2006). If an EMG device does not account for or manage such artefacts, meaningful data will be lost and the device components can be damaged.

Stimulation artefact is generated by the stimulator's current output and takes the form of a voltage spike, followed by an exponential decay (Megill et al., 1982). Stimulation pulses are several orders larger than a typical vEMG signal and can easily saturate a recording amplifier if not accounted for, causing component damage and long duration artefacts (Megill et al., 1982). The stimulator used in this work can output voltage up to $\pm 40V$, while vEMG is typically within $\pm 10mV$. The eEMG is the synchronous contraction of multiple motor units, elicited by electrical stimulation (Luo, 2013). The eEMG is decidedly smaller than the stimulation artefact, in the range of milliVolts; however, it's typically still orders of magnitude larger than vEMG. On top of this, the eEMG can superpose the vEMG for the entire stimulation period. Close proximity of recording electrodes to the stimulation point can cause super-position of the eEMG and stimulation artefacts (Mandrile, Farina, Pozzo, & Merletti, 2003). Both artefacts are dependant on a number of factors such as the electrode-skin interface, stimulation type, and amplifier design. Figure 4.6 shows an example waveform of the vEMG superimposed with the stimulation artefact and eEMG.

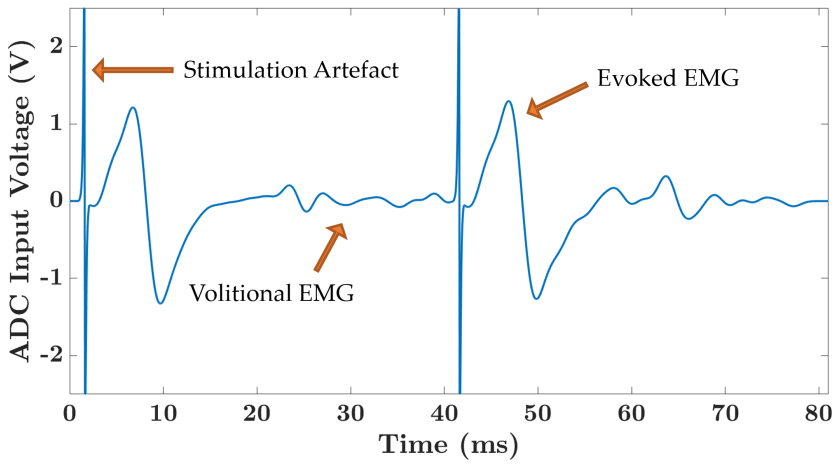

Figure 4.6: Superposed stimulation artefact, eEMG, and vEMG over two stimulation periods.

Artefact reduction techniques

The main obstacle to recording from stimulated muscle are large-scale artefacts due to the stimulation that corrupt the vEMG signal; therefore, artefact reduction techniques are necessary. To the authors knowledge, there are very few commercial devices that contain

protection against large stimulation voltages or measures to reduce artefact transient times. In the presence of electrical stimulation, typical EMG designs will therefore be damaged and vEMG recordings saturated. Techniques for amplifier protection and artefact suppression have been explored in literature. A number of hardware and software techniques are discussed in this section.

Hardware

Blanking is perhaps the most widely applied artefact reduction method. Disconnection of the amplifier front-end is the most common form of blanking (Futami et al., 2005; Taylor & Chappell, 2003). Alternatively, the system gain can be reduced during stimulation to prevent amplifier saturation. Most blanking windows are synchronised with the stimulation via microcontroller, not updated in accordance with the electrode potentials. This is a significant disadvantage of current hardware blanking solutions. The inability for the blanking to adapt to dynamic artefact conditions can lead to residual artefacts or unintended removal of the desired signal (Heffer & Fallon, 2008; Mandrile et al., 2003; Yochum & Binczak, 2015).

The isolated use of a blanking period can cause further artefacts to enter the system. A discharge curve is generated as the systems exit the blanking phase, due to a sharp change in signal level, seen as a step by the systems' filtering amplifiers (Brown et al., 2008; Taylor & Chappell, 2003). Some authors have applied sample-and-hold circuitry to help minimise this signal shift, holding the system at pre-stimulation levels prior to reconnection (Hottowy et al., 2012; Langzam, Isakov, & Mizrahi, 2006). In other works, a non-linear feedback loop is used to accommodate sharp changes in the input signal level (DeMichele & Troyk, 2004; Ilić, Jorgovanović, Antić, Morača, & Ungureanu, 2016; Thorsen, 1999). Note that no pre-amplifier disconnection is used in these designs, and the pre-amplifier gains are kept low to avoid saturation. Due to the low gain, the common-mode rejection properties of the designs' pre-amplifiers are not fully exploited.

Depending on stimulator type, the artefact shape changes. CV stimulators tend to evoke shorter transient times than CC outputs, due to their lower output impedance (Mclean, Scott, & Parker, 1996). However, the muscle response from CV stimulation will not be as reliable. The designs presented in Mandrile et al. and Knaflitz et al. use a hybrid module to obtain reliable stimulation with low discharging transient durations (Knaflitz, Knaflitz, Merletti, & Merletti, 1988; Mandrile et al., 2003). During stimulation a constant current output is used. The stimulator is then switched to a constant voltage output in-between stimulation pulses.

Artefact transient times have also been reduced through electrode shorting. Shorting electrodes provides a low impedance path to ground, therefore allowing fast discharge of the energy stored by tissue capacitance (Brown et al., 2008). Chester et al found that electrode discharging reduced artefact time from 25ms to 7ms (Chester & Durfee, 1997). Furthermore, techniques common to standard stimulation systems can help reduce artefact effects. Bipolar stimulation prevents long-term build-up of electrode-tissue charge (Knaflitz et al., 1988), while proper skin preparation reduces the electrode-skin impedance and minimises electrode impedance mismatch.

Software

Software techniques can be used as an alternative to hardware solutions, or in conjunction with them. The main advantage of software implementations is the possibility for adaptation to different artefact and recording situations (Hoffmann, Cho, Ramos-Murguialday, & Keller, 2011). There is a vast array of code-based approaches that have been applied for suppression of both stimulation and eEMG.

Although predominately applied in hardware, artefact blanking can be implemented in software. Hardware blanking is often preferred due to fast IC responses. Additionally,

the lack of blanking or signal limiting hardware may allow amplifier saturation. However, software blanking is more customisable due to the ability to set flexible thresholds at low voltages (O'Keeffe, Lyons, Donnelly, & Byrne, 2001).

In addition to blanking, conventional digital filters have been frequently applied towards artefact removal. Comb filtering is often used to remove stimulation artefacts. Authors usually stimulate at a factor of the local power-line frequency as the comb-filter will remove both spectra (Frigo, Ferrarin, Frasson, Pavan, & Thorsen, 2000). Digital high-pass filters may also be applied 20-30ms post-stimulation to remove the remaining low frequency artefact such as the eEMG tail and stimulation discharging curve (Shalaby et al., 2011).

The use of conventional digital filters has been shown to be less accurate than other filtering techniques due to temporal and spectral overlap of artefact and vEMG, and the non-stationary nature of the eEMG (Al-ani, Cazettes, Palfi, & Lefaucheur, 2011; Ambrosini et al., 2014). Researchers have used methods such as adaptive algorithms (Sennels, Biering-Sorensen, Hansen, & Andersen, 1996), Gram-Schmidt prediction filters (Yeom & Chang, 2011), and wavelet analysis (Yochum & Binczak, 2015), as they are more able to accurately predict non-stationary signals. There is a large number of artefact estimation techniques. A subtraction template can be generated through the sub-threshold method, off-nerve method, or double-pulse method (Megill et al., 1982), often followed by linear scaling. Other estimation techniques, such as singular value decomposition, ensemble averaging, and curve fitting, have also been used.

Existing devices for same-electrode stimulation and recording

Existing devices have managed to record vEMG of stimulated muscles using the aforementioned techniques. However, these devices often require separate electrode pairs for recording and stimulation. With an additional reference, a total of five electrodes are required for a single channel. This configuration is spatially inefficient and the optimal

positioning of stimulation and recording electrodes can be difficult (Muraoka, 2002).

A number of authors have speculated that EMG measurement from stimulation electrodes would provide technological advantages over the separate electrode configuration (Schauer, 2017; Valtin, Werner, & Schauer, 2016). In addition to being spatially efficient, the consistency between recording and stimulation sites has potential to provide more intuitive and practical use of the modalities (Nishida & Suzuki, 2016). However, there are several challenges in recording EMG from stimulation electrodes (Schauer, 2017). Significant discharging transients can be introduced to the EMG recordings due to residual capacitive charge on the electrodes. These transients are accentuated due to the large size of the stimulation electrodes (Shalaby et al., 2011). Furthermore, direct measurement from stimulation electrodes means that the EMG front-end will be subjected to the full stimulation voltage.

There are a limited number of designs that support concurrent EMG recording from stimulation electrodes. Initial work completed by Muraoka et al. demonstrated that artefact cancellation could be achieved through a combination of electrode discharging, pre-amplifier blanking, and amplifier gain-switching (Muraoka, 2002). The design was then miniaturised by Kamono et al., who then applied the device in gait training experiments (Kamono et al., 2003). Similar techniques were implemented by Shalaby et al. in a four-channel device that was then applied towards FES cycling biofeedback (Shalaby et al., 2011). A selection of key design features are detailed in Table 4.1.

Table 4.1: Key parameters of same electrode systems (Muraoka, 2002; Shalaby et al., 2011)

Parameter	***(Muraoka, 2002)***	***(Shalaby et al., 2011)***
Number of Channels	1	4
System Gain (dB)	68-108	71
Preamplifier Gain (dB)	28	10
System Bandwidth (Hz)	330-460	170-700
Blanking/ Muting Period (ms)	7	30
Stimulation Frequency (Hz)	20	20

Both designs used fixed blanking/ muting periods to remove part of the stimulation artefact and eEMG. Additionally, narrow band-pass filter characteristics and low pre-amplifier gains

were used to reduce artefact transient times and to avoid saturation, respectively. Although these techniques were successful in suppressing the stimulation artefact and eEMG, they could have a negative impact on the quality of vEMG extraction. For instance with gains as low as 10dB the pre-amplifier common-mode rejection ratio (CMRR) is not fully exploited, compromising the output signal-to-noise ratio. With high-pass cutoff frequencies as high as 330Hz, the energy of the extracted vEMG is also likely reduced (Osuagwu, Whicher, & Shirley, 2020).

A more recent design by Muraoka et al. (Integrated Volitional-control Electrical Stimulator, IVES) uses the CMRR of the recording pre-amplifier for artefact reduction (Muraoka, Tanabe, Yamaguchi, & Takeda, 2013). The IVES uses both recording electrodes as a virtual stimulation electrode and the reference electrode as a current return path. In this configuration the stimulation voltage is seen as a common-mode signal. A similar concept is introduced by Nag et al. who uses a tripolar amplifier configuration to suppress the stimulation artefact (Nag, Sikdar, Thakor, Rao, & Sharma, 2015). The main advantage of these systems is the suppression of artefact without the need for any switching circuitry. However, performance of artefact suppression is dependant on the balance of electrode impedances (Nag et al., 2015). Even with abrasive skin preparation, the electrode-skin impedance imbalance can be large (B. C. Fortune et al., 2021). Additionally, the design may suffer from a lack of stimulation selectivity due to the activation of three electrodes. Extension to multi-channel applications could also become problematic as cross-talk would create a differential voltage on the recording electrodes.

The IVES uses minimal hardware after the pre-amplifier stage, directly sampling the pre-amplifier output with an analog to digital converter (ADC). By minimising the device's hardware footprint its portability is enhanced. An alternative low-hardware approach was introduced by Valtin et al. (Valtin et al., 2016) who utilised a four-channel analogue front-end for biopotentials (Texas Instruments, ADS1294). Front-end disconnection and electrode dis-

charging were also used. The front-end provides a compact four-channel EMG monitoring solution. However, its 24-bit range is not fully used due to a maximum amplifier gain of twelve. The front-end may be limited to low gains due to the lack of compensation for electrode offset potentials. For residual artefact removal, a non-causal high-pass filter with 200Hz cut-off frequency was applied. To minimise the filter transients, optimal initial filter states were calculated. Without such optimisation the filter transients were misinterpreted as vEMG (Valtin et al., 2016).

When applied in stroke rehabilitation, EMG can be a useful tool for directing support modalities and providing biofeedback. However, recording EMG of a stimulated muscle is challenging due to the presence of large-scale stimulation-elicited artefacts. Most stimulus-resistant EMG designs rely on separate recording and stimulation electrodes, and the limited number of existing same-electrode designs typically use elevated high-pass cut-off frequencies. An EMG device that can record from stimulation electrodes whilst maintaining the band-pass characteristics of typical EMG devices ($\sim 20 - 480Hz$) would yield an improvement over current designs as it can record the predominant energy spectra of EMG in a space-efficient manner. Additionally, the use of adjustable-threshold blanking, based on electrode potentials rather than fixed timings, would allow the system to avoid the potential removal of useful recordings.

4.4 Fatigue

A significant limitation of FES-based rehabilitation is rapid onset of patient fatigue. However, with the guided application of external support, such as rehabilitation robotics, this fatigue can be managed. In order to direct a balanced scheme of FES and robotic support, reliable tracking of muscular fatigue is needed.

4.4.1 Stimulation Elicited Fatigue

Performance differences between electrically stimulated and voluntary muscular contractions have been linked to discrepancies in the spatial, temporal, and order of motor unit recruitment. There are two main classes of motor unit: slow, oxidative type; and fast, glycolytic type. Fast motor units tend to have lower excitation thresholds due to large axon diameters. Slow motor units have smaller diameter axons and therefore have higher stimulation thresholds. In addition to this, fast motor units are capable of exerting larger forces, however are less fatigue-resistant.

Henneman's size principle suggests that the normal motor-recruitment order during voluntary contractions is in a geometrical order: smaller motor units tend to be activated before larger ones (Hennemen, Somenm, & Carpenter, 1965). Through electrical stimulation, alteration of the natural recruitment order occurs. The nature of these alterations appear to be a matter of controversy in literature. A common and long-established theory is that early onset of muscular fatigue and therefore lower capacity for contractile force, is due to a reversal of Henneman's size principle during electrically stimulation. The reversal principle suggests that larger motor units are activated before smaller ones during electrical stimulation, due to their larger axon diameters and therefore lower stimulation thresholds. The early activation of these motor units in conjunction with less fatigue resistance (than smaller motor units) is used to support the reversal theory. In other literature, such as in (Dumitru et al., 2014) and (Gregory & Bickel, 2005), it is contested that the reversal theory only applies in direct stimulation of the motor unit. Through cutaneous or surface electrical stimulation, at high or low force levels, it is speculated that the recruitment of motor units is a randomised, non-selective process regardless of fibre type. Instead it is suggested that during electrical stimulation a higher metabolic demand is the predominant factor behind early fatigue onset. This is mainly due to spatial fixation of motor unit recruitment (Maffiuletti, 2010).

Delay of muscular fatigue during voluntary contraction can be achieved in two ways, through modulation of active motor unit firing rates or through alternate recruitment patterns to activate additional motor units(Gregory & Bickel, 2005; Jubeau et al., 2008). Frequency and intensity factors can be modulated during electrical stimulation in an attempt to mimic these means and delay fatigue onset. Frequency modulation to alter motor unit firing rates, and intensity modulation to activate deeper muscle fibres as superficial layers fatigue. In addition to this, multichannel stimulation applied at low frequencies has been shown to activate different muscle units, increasing muscle resistance without decreasing contraction force (Malesevic, Popovic, Schwirtlich, & Popovic, 2010). Electrically elicited contractions also differ from voluntary contractions in a temporal manner. Temporal motor unit recruitment during voluntary action is asynchronous in nature whilst synchronous recruitment is imposed through electrical stimulation.

4.4.2 Fatigue Monitoring

As mentioned in Section 3.4.4 most hybrid exoskeletons do not monitor fatigue. The hybrid exoskeletons that do monitor fatigue all target lower-limb gait assistance for spinal-cord-injury (SCI) patients. External torque sensors and exoskeleton interaction forces were used for monitoring. However, external torque sensors can be affected by voluntary motion and other disturbances, and can be impractical for daily use (Q. Zhang, Hayashibe, & Guiraud, 2011).

Outside of exoskeleton-based fatigue monitoring, EMG is perhaps the most widely applied biopotential signal for the assessment of muscular fatigue (Ibitoye, Estigoni, Hamzaid, Wahab, & Davis, 2014; Shair, Ahmad, Marhaban, Tamrin, & Abdullah, 2017). The evoked EMG signal (eEMG) is particularly used for assessing stimulation induced fatigue. The eEMG is produced by the synchronous contraction of multiple motor units, elicited by electrical stimulation (Luo, 2013). Changes of the eEMG properties have been used to track muscle force decay over the course of fatigue. Such changes include the increase of eEMG am-

plitude features due to temporal dilation as well as the decrease of spectral features due to reduction of muscle fiber conduction velocity (Merletti & Farina, 2016a). Typical eEMG amplitude indices include the mean absolute value (MAV), root mean square (RMS), and peak-to-peak amplitude (PTP) (Tepavac & Schwirtlich, 1997). The mean frequency (MNF) and median frequency (MDF) of the power spectrum are commonly used as spectral indices. Alternative indices have also been applied such as wavelet coefficients to characterise the temporal dilation of the eEMG (Yochum & Binczak, 2015).

Most studies of FES-evoked fatigue are performed during isometric contractions with constant stimulation (Ibitoye et al., 2014). Under these conditions it is suggested that eEMG characteristics are reliable indices for muscle fatigue (Chester & Durfee, 1997; Tepavac & Schwirtlich, 1997). However, many practical applications of FES generate dynamic muscle contractions and continuous stimulation is not common in rehabilitation practices (Miura & Watanabe, 2016; Yu, Chen, & Ju, 1999). Under dynamic conditions, cross-talk and muscle movement under the electrodes can influence the EMG signal (Merletti & Farina, 2016b). In (Yu et al., 1999) Yu et al. investigated eEMG features during isokinetic knee movements, elicited by constant stimulation. It was found that fatigue trends could be identified over repetitive movements, although the eEMG features oscillated concurrently with the knee position.

During dynamic movements elicited through intermittent stimulation, the relationship between eEMG parameters and muscle torque output, and therefore the relationship between eEMG parameters and muscle fatigue, may be less evident. In (Estigoni, Fornusek, Smith, & Davis, 2011), Estigoni et al. suggested that the eEMG is not a good proxy for muscle torque during FES-evoked cycling. Within each session, the relative magnitudes of change between eEMG indices and torque were different. However, a potential connection was suggested as their direction of change was consistent. Further work was completed by Miura et al. who investigated the efficacy of doublet elicited M-waves to estimate fatigue during

intermittent stimulation (Miura & Watanabe, 2016). Under dynamic conditions, the eEMG PTP of the doublet's second pulse was observed to decrease with fatigue. Conversely, the eEMG PTP of single-pulses were not sensitive to muscle fatigue during stimulation intervals of one second.

Current studies provide useful insights for the estimation of muscular fatigue from eEMG properties. Research of dynamic movements during intermittent stimulation provides a step towards the use of fatigue indices in practical rehabilitation settings. However, the current protocols for intermittent stimulation are limited to isokinetic cyclic movements. Stimulation trains are delivered with fixed timings and the subjects' volitional intents are not considered. The integration of eEMG-based fatigue metrics into functional stroke-rehabilitation requires their investigation under more practical assistance protocols. One such protocol is vEMG-controlled stimulation towards functional dynamic movements.

Overall, technologies such as robotic-exoskeletons, FES devices, and EMG devices, have potential to improve patient outcomes when incorporated into rehabilitation practices. The integration of these technologies into a hybrid device can yield further improvements through the balance of FES and robotic support profiles, guided by EMG biofeedback. The following chapters focus on the development of a coupled DOF hand-exoskeleton, CC stimulator, and stimulus resistant EMG device that can record from stimulation electrodes. The developed exoskeleton, stimulator, and EMG device are then integrated to provide vEMG-controlled assist-as-need hybrid support during dynamic movements. eEMG-based fatigue metrics are monitored during these trials to assess their potential for future integration with the hybrid-exoskeleton system.

CHAPTER 5

Hand Exoskeleton

5.1 Introduction

Robotics and exoskeletons are being integrated into stroke rehabilitation due to their ability to provide high intensity, consistent, and interactive therapy. Exoskeletons can be portable and typically fit close to the body. However, device complexity can become an issue when applied to areas with limited spacing and higher degree of freedom (DOF). This issue is especially prominent in hand exoskeletons. In current hand exoskeletons there is diversity in the support of finger joints and DOF. Exoskeleton kinematic designs are often simplified to improve portability and user comfort. By doing so, the exoskeletons application range is limited. However, recovery of basic curling motion is often recommended over more complex movements. For more information, see Section 4.1. This chapter presents a one-DOF hand exoskeleton. The exoskeleton is linkage-based and is readily 3d printed. A parametric model has been formed which sizes the exoskeleton according to the users finger measurements.

5.2 Design Requirements

There are a number of factors that influence a hand exoskeletons usability, availability, and functional capacity towards stroke rehabilitation. To create an effective exoskeleton device, such factors need to be kept in mind during the design process.

- **Safety**: The exoskeleton must ensure the user's safety at all times. The exoskeleton must respect the users natural finger range of motion (ROM) and should ensure that the linkage centres of rotation (CORs) coincide with the rotation axis of the human body joint (Moreno-SanJuan, Cisnal, Fraile, Pérez-Turiel, & De-la Fuente, 2021; Sarac, Solazzi, & Frisoli, 2019).

- **Availability**: To promote wide-spread usage of the exoskeleton, it must be affordable to the patients and the clinicians. Furthermore, the exoskeleton should be functional for a range of patients hand sizes. (du Plessis, Djouani, & Oosthuizen, 2021; Sarac et al., 2019).

- **Usability**: There are a number of factors that lead to the device's practical usability and user acceptance. The device should be comfortable to wear and lightweight to prevent user fatigue. In a 2021 review of hand exoskeletons for assistance and rehabilitative purposes, device weight on hand ranged between 80g and 1kg (du Plessis et al., 2021). Device compactness should also be considered, as a large device may interfere with activities of daily living (ADL) and impact the users willingness to interact with the system. Device set-up and configuration times will also impact the practicality of the system.

- **Functionality**: The exoskeleton should promote flexion and extension movements similar to a natural finger's trajectory and ROM (M. Li et al., 2019; Moreno-SanJuan

et al., 2021). Additionally, the exoskeleton should provide enough torque to actuate the hand (Ferguson, Dimapasoc, Shen, & Rosen, 2019).

- Finger trajectory: The finger's trajectory is characterised by its interjoint couplings. A coupling ratio of 2/3 between the proximal interphalangeal joint (PIP) and distal interphalangeal joint (DIP) has been generally accepted; However, a range of metacarpophalangeal joint (MCP)-PIP coupling definitions have been used by exoskeleton designers (See Section 4.1.1). Based on the large variety of MCP-PIP coupling definitions, it has been argued that a constant coupling could result in a comfortable grasping motion (Rätz, Conti, Müri, & Marchal-Crespo, 2021).

- Joint ROM: Only a small percentage of active joint ROM are required to perform functional tasks. Over a range of 11 ADL, Hume et al. recorded functional ROM for the MCP, PIP, and DIP, of 33°-73°, 33°-73°, and 20°-61° , respectively (Hume, Gellman, McKellop, & Brumfield, 1990). Over 20 activities, Bain et al. recorded similar ROM for the MCP, PIP, and DIP, of 19°–71°, 23°–87°, and 10°–64°, respectively (Bain, Polites, Higgs, Heptinstall, & McGrath, 2015).

- Force output: The torque output of the exoskeleton should enable finger flexion-extension movements and generate the grasping forces required to manipulate objects in ADL. Li et al. recommend a minimum continuous fingertip force of 30N given values ranging from 15N to 25N recorded in literature (Kamper, Fischer, Cruz, & Rymer, 2006; M. Li et al., 2019). Boser et al. recommended a lower force output (10N of pinch grip) given that some individuals with impaired hand function may be able to generate force independently (Boser, Dawson, Schofield, Dziwenko, & Hebert, 2020).

5.3 Mechanism Structure

A one-DOF linkage system with output links corresponding to the finger phalanx is desired. This structure allows the flexion/extension motion of the finger to be fully characterised via a single actuator. The design will solely use revolute joints (as opposed to slider) for ease of prototype manufacture.

For a one-DOF parallel mechanism with revolute joints, an alternate form of Grubler's mobility equation is (Mozaffari, 2013):

$$J = \frac{3}{2}N - 2 \tag{5.1}$$

Where J represents the number of joints in the mechanism, and N represents the number of links. There must be a integer number of joints in the mechanism. Therefore, an even number of linkages is needed to achieve one-DOF.

The simplest one-DOF structure with revolute joints is a four-bar mechanism. However, a four-bar structure cannot properly control MCP, PIP, and DIP angles, whilst avoiding interference between between exoskeleton and finger. With the trade-off of added complexity, mechanisms with a higher number of linkages provide more design flexibility and are more able to achieve the desired system behaviour.

After the four-bar, the next to explore is the six-bar mechanism. Mozaffari (Mozaffari, 2013) attempted to use a six-bar topology attached to the distal phalanx. The authors reported difficulties in synthesising a linkage that did not interfere with the fingers or encounter kinematic singularities. Bataller et al (Bataller, Cabrera, Clavijo, & Castillo, 2016) produced a six-bar mechanism that successfully controls all finger phalanx. However, the linkage is placed lateral to the finger, leading to spatial issues if a multi-fingered device is required.

The eight-bar structure has been successfully utilised as a one-DOF finger exoskeleton by a number of authors. Wolbrecht et al (Wolbrecht, Reinkensmeyer, & Perez-Garcia, 2011) utilised an eight-link structure with all revolute joints and two end-effectors, controlling the poses of finger proximal-phalanx and inter-phalanx. In a pilot test conducted by Taheri et al (Taheri et al., 2014), the device was shown to promote natural grasping patterns.

The exoskeleton design in this chapter focusses on mechanism adaptability to different finger sizes. Specifically, the objective is to create a parametric model that defines the exoskeleton dimensions, given input finger measurements. In order to simplify the model identification a six-bar linkage topology is utilised. Control of the distal phalanx is omitted to allow more design flexibility. The Watt I and Stephenson II six-bar linkage topologies are considered, Figure 5.1. These topologies were selected as the linkages can be solved as cascaded four-bar linkages. This feature allows for a fast and simple process to solve the mechanism kinematics.

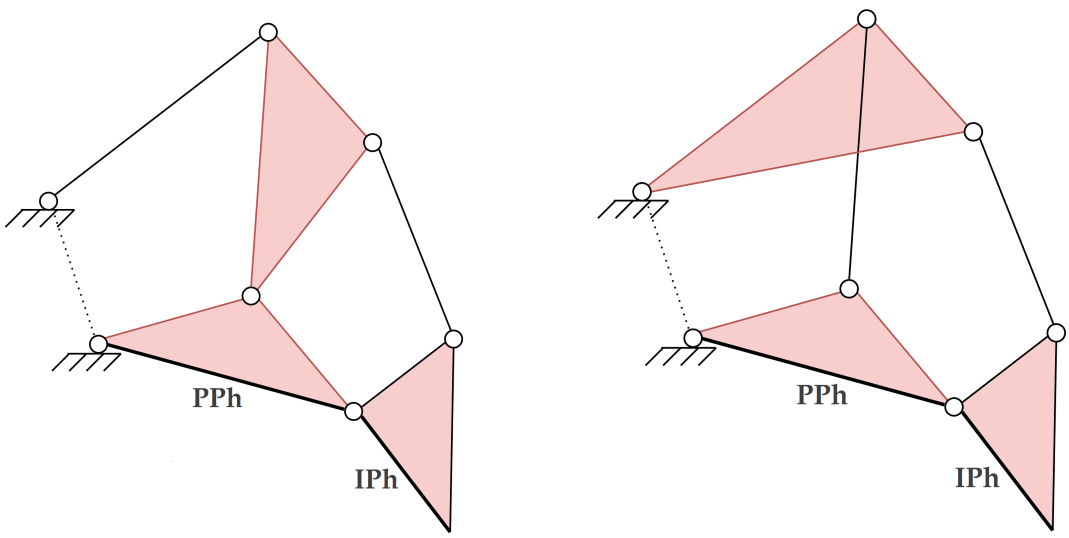

(a) Watt I linkage topology

(b) Stephenson II linkage topology

Figure 5.1: Watt I and Stephenson II linkage topologies. PPh and IPh denote the proximal-phalanx and inter-phalanx respectively

5.4 Dimensional Synthesis

Dimensional synthesis is the process of sizing link dimensions and configuring the mechanism assembly to achieve the desired system outputs. The exoskeleton dimensional synthesis process can be broken into two tasks; mechanism kinematic analysis, and mechanism parameter selection.

5.4.1 Kinematic Analysis

Kinematic analysis is used to solve the exoskeleton's configuration at each task position, given its link and coupler parameters. The Watt I and Stephenson II six-bar topologies are considered for the exoskeleton, as their kinematics can be solved as cascaded four-bar mechanisms.

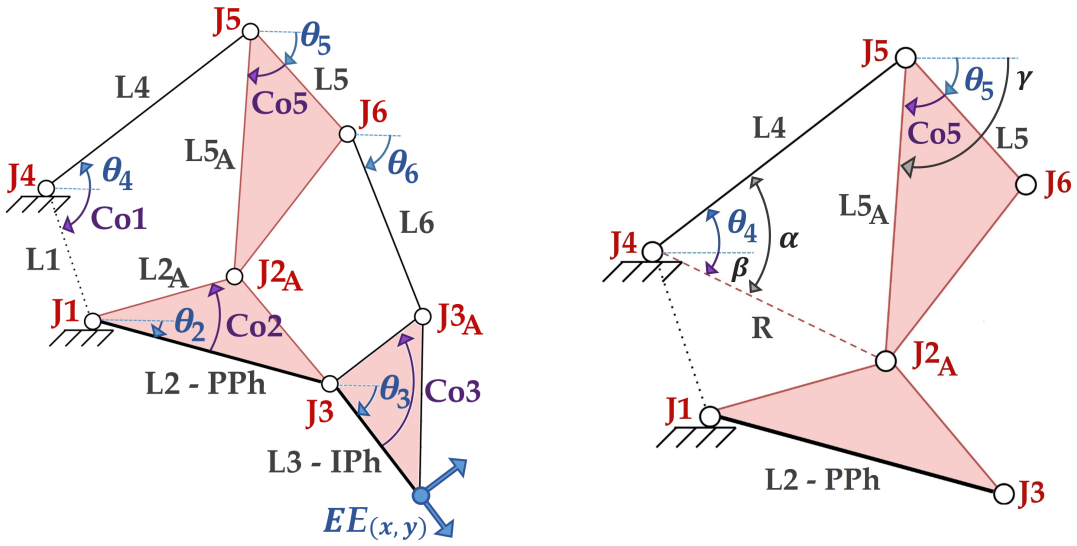

(a) Watt I linkage kinematic parameters.

(b) Watt I input four-bar kinematic parameters.

Figure 5.2: Watt I linkage kinematics. PPh and IPh denote the proximal-phalanx and inter-phalanx respectively.

The following kinematic analysis is shown for the Watt I mechanism. Figure 5.2a shows the Watt I topology and its properties. The link lengths and coupler angles are assumed to be known, denoted by the grey and purple labels, respectively. The properties denoted by the blue labels are unknown variables. Kinematic analysis is used to define these properties

and therefore solve for the mechanism's configuration.

Input Four-bar

For the following kinematic analysis, the angular position of the PPh, θ_2, is treated as the input crank of the mechanism. The crank position θ_2 therefore coincides with the desired θ_2 at each task position. Figure 5.2b depicts the input four-bar geometry. Joint 1 (J1) represents the MCP, and is treated as the origin [0,0]. Joint 4 (J4) represents the fixed-base coupler. The position of J4 remains fixed throughout all task-positions. Joint 2A (J_{2A}) represents the PPh coupler position, which is defined by the coupler definition and crank position. The positions for J1, J4, and J_{2A} can be calculated through equation set 5.2.

$$\begin{aligned} J1 &= [0,\ 0] \\ J4 &= [J1_x - L1\cos Co1, J1_y - L1\sin Co1] \\ J2_A &= [J1_x + L2_A\ cos\theta_2 + Co2, J1_y + L2_A\ sin\theta_2 + Co2 \end{aligned} \tag{5.2}$$

The distance (R) and orientation (β) between joints J4 and J_{2A} can be defined, Equation 5.3.

$$\begin{aligned} R &= \sqrt{(J4_x - J2_{Ax})^2 + (J4_y - J2_{Ay})^2} \\ \beta &= \arctan\frac{J4_y - J2_{Ay}}{J4_x - J2_{Ax}} \end{aligned} \tag{5.3}$$

The law of cosines of the triangle R-L4-$L5_A$ can then be used to determine the orientation of Link 4 (θ_4), Equation 5.4. Note, only the elbow up configuration of the L4-$L5_A$ linkage is considered, as an elbow down configuration would likely interfere with the finger workspace.

$$\begin{aligned} \cos\alpha &= \frac{R^2 + L4^2 - L5_A}{2\ R\ L4} \\ \sin\alpha &= +\sqrt{1 - \cos\alpha^2} \\ \alpha &= \arctan\frac{\sin\alpha}{\cos\alpha} \\ \theta_4 &= \alpha - \beta \end{aligned} \tag{5.4}$$

The position of J5 can now be solved, Equation 5.5

$$J5 = [J4_x + L4\cos\theta_4, J4_y + L4\sin\theta_4] \tag{5.5}$$

The orientation of link 5, θ_5, is the remaining unknown in the input four-bar linkage. θ_5 can be solved through the relative positions of J5 and $J2_A$ and the known coupler angle Co5, Equation 5.6

$$\begin{aligned} \gamma &= \arctan\frac{J5_y - J2_{Ay}}{J5_x - J2_{Ax}} \\ \theta_5 &= \gamma - Co4 \end{aligned} \tag{5.6}$$

Output Four-bar

The output four-bar problem is defined between joints J_{2A}, J6, J3, and J_{3A}, with unknowns θ_3 and θ_6, Figure 5.2a. The positions of J3 and $J2_A$ can be determined via Equation 5.7

$$\begin{aligned} J3 &= [L2\cos\theta_2,\ L2\sin\theta_2] \\ J2_A &= [L2_A\cos\theta_2 + Co2,\ L2_A\sin\theta_2 + Co2] \end{aligned} \tag{5.7}$$

The position of J6 can be determined from the position of J5 and θ_5, as solved from the input four-bar problem.

$$J6 = [J5_x + L5\cos\theta_5,\ J5_y + L5\sin\theta_5] \tag{5.8}$$

The process to solve for angles θ_6 and θ_3 is analogous to the input four-bar solution process (i.e. the law of cosines is used on the triangle J6-J3-$J3_A$). The end effector position is then determined via Equation 5.9

$$EE = [J3_x + L3\cos\theta_3,\ J3_y + L3\sin\theta_3] \tag{5.9}$$

5.4.2 Exoskeleton Parameter Selection

The definition of mechanism linkage parameters is an integral part of the dimensional synthesis process. The dimensional synthesis requires definition of the eleven linkage parameters shown in Figure 5.3. The lengths of the PPh, IPh, and distal phalanx (DPh) are measured parameters.

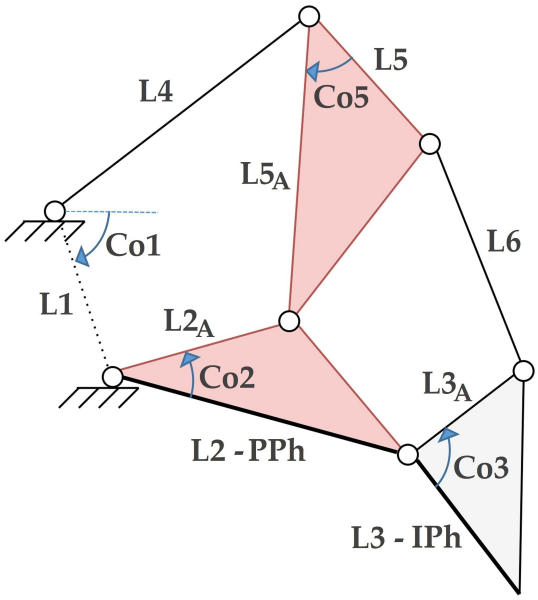

Figure 5.3: Six-bar dimensional synthesis problem. PPh and DPh denote the proximal and inter phalanx, respectively

Sonawale et al. (Sonawale & McCarthy, 2014) mention that the selection of the 3-R chains is challenging, requiring the designer's intuition: the synthesis of a useful eight-bar design is heavily dependant on correct parameter selection. This was also found by Mozaffari et al. (Mozaffari, 2013) who used the synthesis process to design a six-bar mechanism: through a trial and error process, it took hundreds of code executions before parameter selection gave rise to an acceptable solution. Integrating an optimisation scheme into the mechanism synthesis process gives rise to useful linkages whilst alleviating the reliance on designer intuition.

5.5 Differential Evolution Parameter Optimisation

A number of optimisation schemes have been successfully applied towards mechanism dimensional synthesis, such as genetic algorithms, particle swarm optimisation, and Differential Evolution (DE) (Cabrera, Ortiz, Nadal, & Castillo, 2011; Connor, Douglas, & Gilmarti, 1995; Pertuz, Llanos, & Muñoz, 2016; Shete & Kulkarni, 2015; Shiakolas, Koladiya, & Kebrle, 2005). Simplicity and low computational cost are significant advantages in the implementation of such algorithms (Bataller et al., 2016; Cabrera, Nadal, Muñoz, & Simon, 2007). Additionally, numerical optimisation schemes have no limit on the number of synthesis precision points (Connor et al., 1995). Differential evolution and genetic algorithms have both been successfully applied for exoskeleton dimensional synthesis. Bataller et al. used differential evolution for the angular and positional optimisation of a 6-bar linkage, while Orlando et al. used a genetic algorithm to path-optimise three 4-bar linkages (Orlando, Akolkar, Dutta, Saxena, & Behera, 2010).

A DE algorithm has been implemented to optimise Watt I and Stephenson II mechanisms. The exoskeleton is optimised with respect to angular error and novel compactness error cost functions, detailed in Section 5.5.1. The following sections outline the procedure for the exoskeleton optimisation through DE.

5.5.1 Problem Definition

DE, like any other optimisation scheme, requires a problem definition. The problem definition consists of the the scheme's input data, design variables, and cost function.

Input Data and Design Variables

Table 5.1 shows the DE input data and design variables for Watt I and Stephenson II linkages. The input data is comprised of finger phalanx length and width measurements. Design variables relate to the mechanism structure, Figure 5.3.

Table 5.1: DE synthesis input data and design variables

Input Data	**Design Variables**
L2 - PPh length	*L1, L4, L5, L6* - Link lengths
L3 - IPh length	$L2_A$, $L3_A$, $L5_A$ - Coupler link lengths
W1 - MCP thickness	*Co2, Co3, Co5* - Coupler link angular position
W2 - PIP thickness	*Co1* - Base link fixed angular position
W3 - DIP thickness	

Finger measurements are performed manually with a vernier calliper. Measurement definitions are outlined in Figure 5.4. These measurement definitions are similar to those used by Kuo et al. and Sandoval-Gonzalez et al(Kuo, Kung, Wu, & Wang, 2020; Sandoval-Gonzalez et al., 2016).

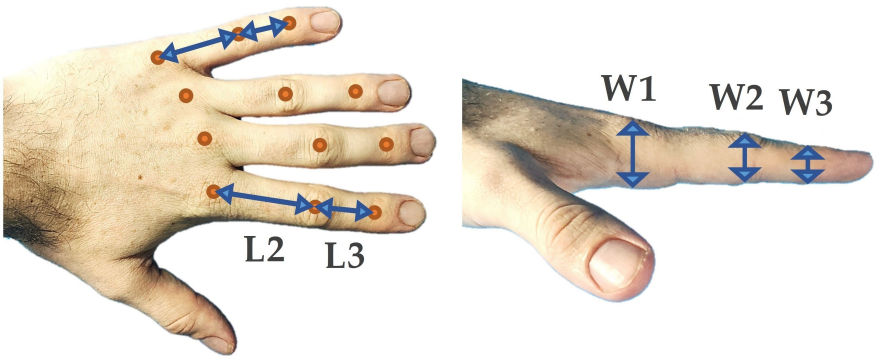

Figure 5.4: Hand measurement definitions. L_2 and L_3 represent the PPh and IPh length measurement definitions, respectively. W_1, W_2, and W_3, represent the width measurement definitions for the MCP, PIP, and DIP, respectively.

Cost Function

A range of parameters can be used to quantify the suitability of an exoskeleton solution, such as phalanx output angle, position, and velocity. Two evaluation functions have been used in this work: angular error and a compactness cost. The combination of these metrics are tailored towards a device that follows the finger-trajectory and is small in profile. To the author's knowledge, a compactness function has not been included in the optimisation

scheme of existing finger exoskeletons.

In addition to the cost function, a penalty function is introduced to represent design failure during the synthesis process. The following conditions are used to indicate design failure:

1. The exoskeleton joints interfere with the finger

2. The exoskeleton linkage cannot be solved with the link parameters given

3. The rotation of the crank (length L4) is not continuous in one direction

4. The output configuration causes PIP joint hyper-extension

Angular cost function

As mentioned in Section 4.1.1 basic curling motion is the main motion used during ADL and stroke rehabilitation. Cobos et al (Cobos et al., 2007) report that a linear coupling ratio between θ_{MCP} and θ_{PIP} of 3/4 is representative of a natural grasp, and linear coupling ratios have been successfully utilised by several other exoskeleton designs (Díez et al., 2018; Fang, Xie, & Liu, 2009; Schabowsky et al., 2010). For these reasons a linear coupling ratio between θ_{MCP} and θ_{PIP} of 3/4 has been selected for this design, Equation 5.10.

$$\theta_{PIP} = \frac{3}{4}\theta_{MCP} \tag{5.10}$$

The MCP and PIP angle can be calculated from the kinematic procedure detailed in Section 5.4.1 and using Equation 5.11.

$$\begin{aligned} \theta_{MCP} &= \theta_2 \\ \theta_{PIP} &= \theta_3 - \theta_3 \end{aligned} \tag{5.11}$$

The desired MCP angles for this design have been split into twenty task-positions in the range $\theta_{MCP} \in [0°, 80°]$. This range represents the functional ROM of the MCP joint (Bain et al., 2015). The MCP task-positions and equivalent DIP task-positions are listed in Table 5.5 under Section 5.6.1.

Angular error is defined as the root mean square error (RMSE) between desired and actual PIP joint angles (θ_{PIP}). As the proximal phalanx (θ_{MCP}) is used as an input crank in the kinematic analysis (Section 5.4.1), there will always be zero error between the desired and actual MCP angles.

$$f_{angular} = \sqrt{\frac{1}{M}\sum_{j=1}^{M}[(\theta_{PIP\ des,j} - \theta_{PIP\ act,j})^2]} \tag{5.12}$$

Compactness cost function

The height of each exoskeleton joint above the finger, perpendicular to the link, is used as the basis for the compactness metric, Figure 5.5. The compactness cost is defined as the squared height terms, summed over all task positions.

$$f_{comp} = \sqrt{\sum_{j=1}^{M}[(J2_{Ay})^2 + (J3_{Ay})^2 + (J4y)^2 + (J5y)^2 + (J6y)^2]} \tag{5.13}$$

The optimisation problem is defined as the sum of weighted cost functions. Favourable parameter-sets minimise the optimisation problem

$$\begin{aligned} f_{cost} &= W_{ang} \cdot f_{ang} + W_{comp} \cdot f_{comp} + M \\ objective &\rightarrow min\{f_{cost}\} \end{aligned} \tag{5.14}$$

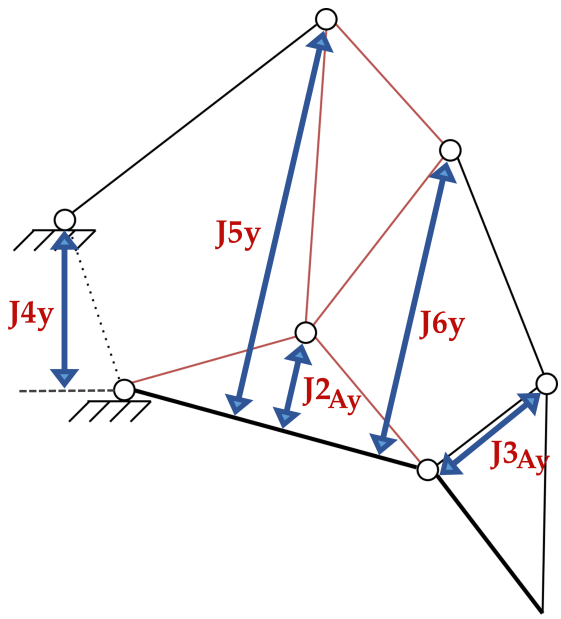

Figure 5.5: Exoskeleton joint heights definitions.

Where W_{ang} and W_{comp} are cost-function weightings: adequate selection of $W_{ang,comp}$ will give a solution that is both compact in size and follows an acceptable trajectory. Weighting values were manually refined in an iterative manner. W_{ang} and W_{comp} values of 0.85 and 0.15, respectively, were found to produce acceptable exoskeletons. M represents the penalty function for design failure. A high value of M ($M = 100,000$) ensures that infeasible mechanisms are rejected.

Cost function range normalisation

The cost function terms f_{ang} and f_{comp} typically vary on different scales.

$$f_{ang} \rightarrow \{0, 360\}$$

$$f_{comp} \rightarrow \{300, 700\}$$

Normalisation of the cost function terms allows for easier refining of the weighting functions W_{ang} and W_{comp}. Each cost function is range normalised as follows, Equation 5.15.

$$f_i^{norm} = \frac{f_i(x) - f_i^o}{f_i^{max} - f_i^o} \tag{5.15}$$

Where f_i^{norm} is the normalised form of the cost function $f_i(x)$, f_i^o is the utopia point, and f_i^{max} is the maxima. The utopia and maxima points are determined by optimising for each cost function separately (Arora, 2012). Table 5.2 details the weightings used to find the maxima and utopia points for the angular and compactness cost functions.

Table 5.2: Definitions for setting the maxima and utopia points of the angular and compactness cost functions. The utopia points are found by optimising for each cost-function separately, setting all other cost-function weightings to zero.

Cost function weightings	f_{ang}^o	$f_{angular}^{max}$	$f_{compact}^o$	$f_{compact}^{max}$
$\{W_{ang}, W_{comp}\} \rightarrow \{0, 1\}$	-	f_{ang}	f_{comp}	-
$\{W_{ang}, W_{comp}\} \rightarrow \{1, 0\}$	$f_{angular}$	-	-	f_{comp}

5.5.2 Differential Evolution Process

Initial population formation

The design variables to be optimised are recorded in Table 5.1. These parameters are organised into parameter vectors of form.

$$x = \begin{bmatrix} L1 \; L4 \; L5 \; L6 \; L2_A \; L3_A \; L5_A \; Co1 \; Co2 \; Co3 \; Co5 \end{bmatrix}^T_{DX1} \tag{5.16}$$

Where D is the size of each parameter vector x. An initial population χ_1 of size N is defined. A choice for $N \in [5D, 10D]$ is recommended (Storn & Price, 1997b).

$$\chi_1 = \begin{bmatrix} x_1, x_2, ..., x_N \end{bmatrix}_{DXN} \tag{5.17}$$

Each element of x_i is allocated a random value within their upper and lower bounds $x_{i,j} \in [Lim_{j,lower}\ ,\ Lim_{j,upper}]$, Equation 5.18.

$$x_{i,j} = Lim_{j,lower} + Rand(0,1) \cdot (Lim_{j,upper} - Lim_{j,lower}) \qquad \begin{array}{l} j = 1, ..., D \\ i = 1, ..., N \end{array} \tag{5.18}$$

Where $Rand(0,1)$ returns a single uniformly distributed random number in the interval (0,1).

Formation of subsequent generations

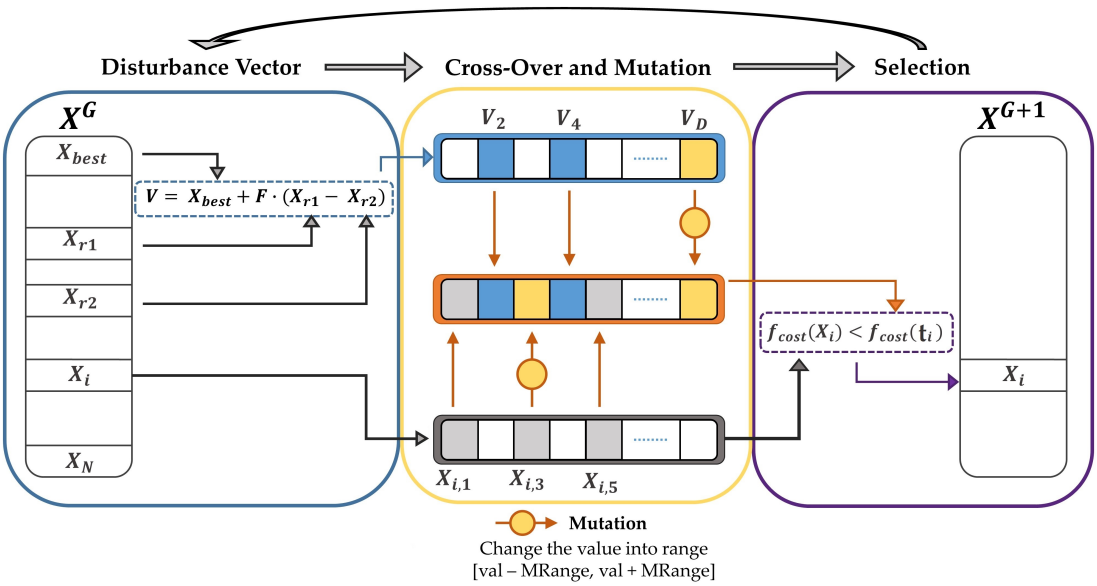

Figure 5.6: Overview of the applied DE algorithm's mutation, cross-over, and selection schemes. Note: the depicted process is repeated for every member of χ_G to fully populate χ_{G+1}

A parameter vector's evolution between generations is controlled by four processes: disturbance, cross-over, mutation, and selection. A version of Storn et al's DE2 scheme (Storn & Price, 1997a) is applied, depicted in Figure 5.6.

Disturbance

In Storn et al's scheme, random variation is added to x_i forming the mutant vector v_i

$$v_i = x_i + \lambda \cdot (x_{best} - x_i) + F \cdot (x_{r1} - x_{r2}) \qquad i = 1, ..., N$$
$$\{r_1, r_2 \in \mathbb{Z} \mid 1 \leq r_1, r_2 \leq N, r_1, r_2 \neq i, r_1 \neq r_2\} \tag{5.19}$$

Where x_{best} is the best solution of the current generation, and x_{r1}, x_{r2} are randomly selected parameters vectors (with r_1, r_2 independent real integers in the range $1 \rightarrow N$, both different from the index i). Constants λ and F moderate bias towards the best solution and random variation contributed by $(x_{r1} - x_{r2})$, respectively. A weighting $\lambda = 1$ was chosen, making Equation 5.19 take the form used in Cabrera et al's MUMSA algorithm (Bataller et al., 2016; Cabrera et al., 2011)

$$v_i = x_{best} + F \cdot (x_{r1} - x_{r2}) \qquad i = 1, ..., N \tag{5.20}$$

This equation form adds a weighted disturbance vector to the best parameter vector in the current generation. Larger values of F (e.g. 0.9 - 1) are often more useful here to avoid becoming trapped in local minima.

Out of range: Components of v_i may be outside its respective upper or lower limit: in this situation, the parameter value is shifted to a position half-way between its current value and the limit.

$$if \quad v_{i,j} > Lim_{j,upper} \qquad v_{i,j} \rightarrow \frac{x_{i,j} + Lim_{j,upper}}{2}$$
$$if \quad v_{i,j} < Lim_{j,lower} \qquad v_{i,j} \rightarrow \frac{x_{i,j} + Lim_{j,lower}}{2}$$

Cross-over

Cross-over is the process of taking components of v_i and x_i to form a new trial vector.

The conditions for cross-over are:

$$t_{i,j} = \begin{cases} v_{i,j} & if \quad C_{rand} \leq CR \quad or \quad j = j_{rand} \\ x_{i,j} & else \end{cases} \qquad j = 1, ..., D \tag{5.21}$$

Where CR is the cross-over probability constant ($CR \in [0, 1]$), C_{rand} is a randomly generated number in the range [0,1], and j_{rand} is a randomly generated integer in the range [1,D]. Use of the $j = j_{rand}$ criterion ensures that at least one parameter is taken from the mutant vector (Storn & Price, 1997b).

Mutation

Mutation is the process of adding random variation to members of the trial vector t_i. The mutation process is used to avoid solution stagnation in local minima. The conditions for mutation are:

$$t_{i,j} = \begin{cases} t_{i,j} + W_{rand} \cdot MRange & if \quad M_{rand} \leq MP \quad and \quad S_{rand} < 0.5 \\ t_{i,j} - W_{rand} \cdot MRange & if \quad M_{rand} \leq MP \quad and \quad S_{rand} \geq 0.5 \\ t_{i,j} & else \end{cases} \qquad j = 1, ..., D \tag{5.22}$$

Where MP is the mutation probability constant ($MP \in [0, 1]$). A MP much lower than CP is recommended (Ortiz, Cabrera, Nadal, & Bonilla, 2013). $M_{rand}, W_{rand}, S_{rand}$ are randomly generated numbers in the range [0,1], and MRange is the specified maximum mutation range, $MRange \in [0, Lim_{j,upper} - Lim_{j,lower}]$.

Out of range: If trial vector member $t_{i,j}$ is mutated out of range $[Lim_{j,lower}, Lim_{j,upper}]$, the parameter value is shifted to a position half-way between its current value and the limit.

$$if \quad t_{i,j}\ (mutated) > Lim_{j,upper} \qquad t_{i,j} \rightarrow \frac{t_{i,j} + Lim_{j,upper}}{2}$$

$$if \quad t_{i,j}\ (mutated) < Lim_{j,lower} \qquad t_{i,j} \rightarrow \frac{t_{i,j} + Lim_{j,lower}}{2}$$

Selection

The selection process simply decides if x_i or the trial vector t_i becomes a member of the next generation χ_{G+1}. Greedy criterion with respect to the cost function (Section 5.5.1) is used

$$\chi_{G+1_i} = \begin{cases} t_i & if \quad f_{cost}(t_i) \leq f_{cost}(x_i) \\ x_i & else \end{cases} \qquad i = 1, ..., N \tag{5.23}$$

Given the problem definition in Section 5.5.1, the DE process is used to optimise Watt I exoskeleton linkage parameters for angular accuracy and height compactness. The algorithm is initially used to optimise a parent-model exoskeleton and then further applied in the identification of a parametric exoskeleton model.

5.6 Exoskeleton Model Formation

There are two stages of exoskeleton models applied in this work. The first stage is the formation of a parent exoskeleton model. This model is based off one set of finger measurements and is optimised with the full set of design variables listed in Table 5.1. The second stage is the formation of a parametric exoskeleton model, which is adapted to the individual based on the input finger measurements provided. The parametric model is based off the parent model, where some of the design variables are held consistent with the parent model and a smaller subset are allowed to vary throughout the optimisation process.

5.6.1 Parent Model

The DE process detailed in Section 5.5 was carried out in MATLAB (R2019b,MathWorks) to form a parent exoskeleton model. The utilised DE parameters and measurement input data are listed in Tables 5.3 and 5.4, repectively.

Table 5.3: DE parameter values used in the generation of the parent model

F	***CR***	***MP***	M_{Range}	W_{ang}	W_{comp}
0.9	0.8	0.1	0.5	0.85	0.15

Table 5.4: Input data for the DE process based on finger measurements

L2 (mm)	*L3 (mm)*	*W1 (mm)*	*W2 (mm)*	*W3 (mm)*
48.7	27.0	26.0	17.0	12.0

The output task-positions are listed in Table 5.5. As mentioned in Section 5.5.1 the target MCP angles (θ_{MCP}) are split into twenty task-positions in the range $\theta_{MCP} \in [0°, 80°]$, and the target PIP angles (θ_{PIP}) are a 3/4 ratio of these MCP angles.

Table 5.5: Angular task-positions for the MCP (θ_{MCP}) and PIP (θ_{PIP})

Task Position	***1***	***2***	***3***	***4***	***5***	***6***	***7***	***8***	***9***	***10***
θ_{MCP} *(deg)*	0	4.21	8.42	12.6	16.8	21.1	25.3	29.5	33.7	37.9
θ_{PIP} *(deg)*	0	3.16	6.32	9.47	12.6	15.8	18.9	22.1	25.3	28.4
Task Position	***11***	***12***	***13***	***14***	***15***	***16***	***17***	***18***	***19***	***20***
θ_{MCP} *(deg)*	42.1	46.3	50.5	54.7	59	63.2	67.4	71.6	75.8	80
θ_{PIP} *(deg)*	31.6	34.7	37.9	41.1	44.2	47.4	50.5	53.7	56.8	60

Table 5.6 shows the output values of the DE design variables. These values characterise the parent model exoskeleton structure, Figure 5.3. Figure 5.7 depicts the MATLAB and computer-aided design (CAD) models (SolidWorks 2019, Dassault Systems). The CAD model represents the physical exoskeleton structure. Curvature of the links is used to avoid their interference with the finger.

Table 5.6: Output values of the DE design variables

L1	***L4***	***L5***	***L6***	$L2_A$	$L3_A$	$L5_A$	***Co1***	***Co2***	***Co3***	***Co5***
38.0	51.7	28.6	41.5	38.1	17.1	26.9	-37.9	48.9	61.9	-18.9

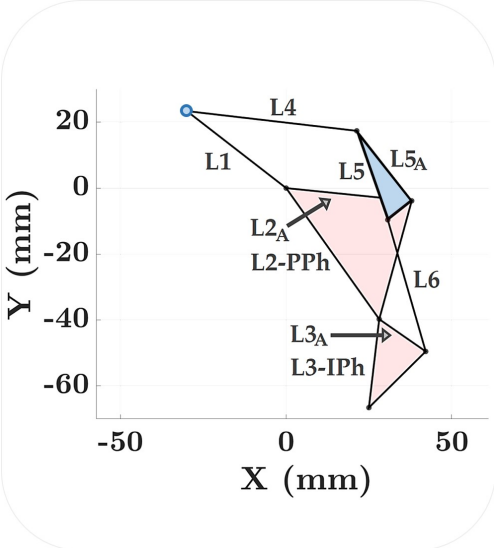

(a) Matlab representation of the parent model

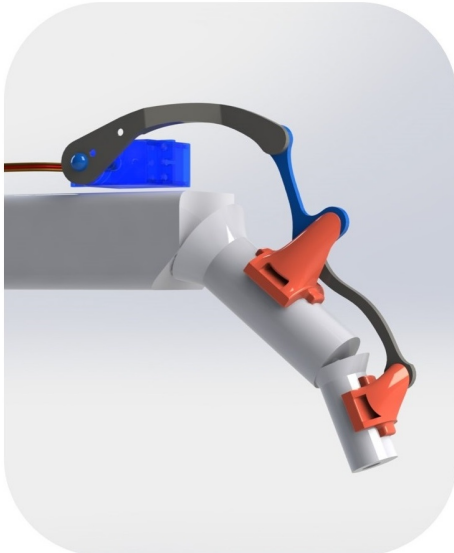

(b) CAD parent model render

Figure 5.7: Representation of the parent model in Matlab and Solidworks, characterised by the design variables in Table 5.6

The mechanism structure characterised by Table 5.6 achieves the cost function error terms shown in Table 5.7. Figure 5.8 shows the trajectory of the parent model against the target linear trajectory. The convergence plots for the DE process are shown in Figure 5.9, including plots for the weighted total error (f_{cost}), angular error (f_{ang}), and compactness error (f_{comp}). From Figures 5.9b and 5.9c it can be seen that there is some fluctuation in the angular error and compactness error terms. However, Figure 5.9a shows that the objective function consistently trends downwards during the evolution process. The effect of the weighting terms W_{ang} and W_{comp} can be observed when comparing Figure 5.9b and Figure 5.9c trends. The angular error term has much less fluctuation than the compactness error, as a change in the angular error term is weighted significantly more highly ($W_{ang} = 0.85$, $W_{comp} = 0.15$).

Table 5.7: Residual error terms of the DE process for the parent model.

f_{cost}	f_{ang}	f_{comp}
0.08979	0.9252 deg	435.9 mm

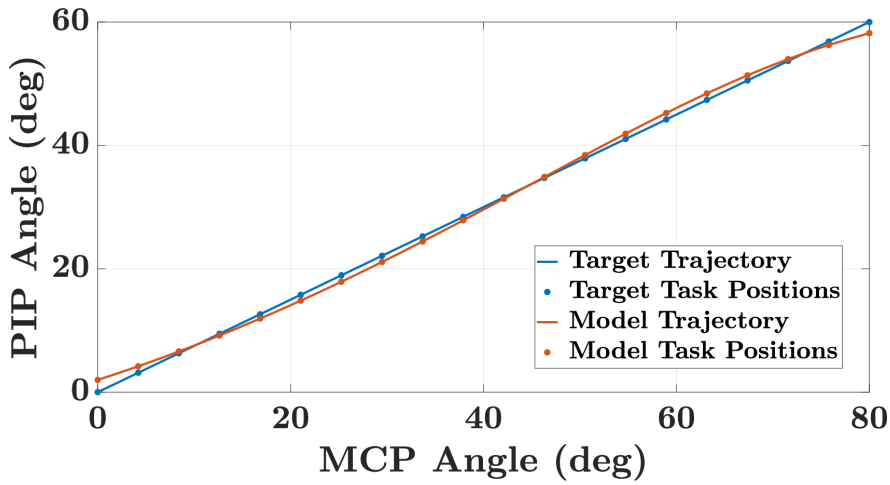

Figure 5.8: Parent model trajectory against the target trajectory. The solid blue circles indicate the 20 task-positions used in the optimisation problem. The solid orange circles indicate the task-positions reached by the parent model exoskeleton

5.6.2 Parametric Model

The one-DOF exoskeleton presented in Section 5.6.1 is optimised with respect to one specific finger measurement set. For users with different sized fingers, application of this exoskeleton can be uncomfortable and will result in significantly different kinematic profiles. This section presents the adaptation of the parent model into a parametric model that adapts based on the measurements outlined in Figure 5.4.

The process to obtain the parametric model involves exoskeleton DE optimisation for a number of different finger measurement sets. For each measurement set, DE is performed where only a subset of the initial design variables (Table 5.1) are allowed to vary. The parametric model can then be formed by identifying relationships between each of the variables' optimal value and their adjacent finger measurements.

When selecting which characteristics are adopted from the parent model, the main deciding factor was ease of production, with the intention to reduce exoskeleton fabrication lead-times. The exoskeleton is intended to be 3d printed. Observing Figure 5.7b, the MCP and PIP couplers are irregularly shaped and are more complex than the other exoskeleton

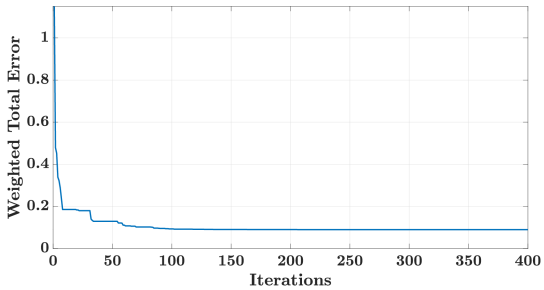

(a) Convergence of the weighted total error

(b) Convergence of angular error

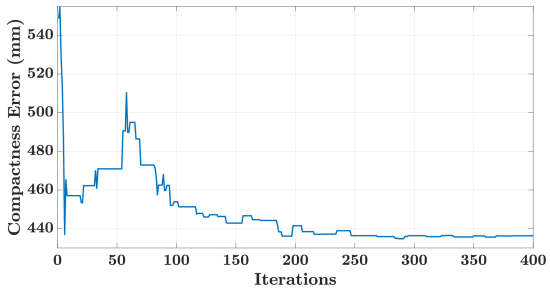

(c) Convergence of compactness error

Figure 5.9: Convergence plots (a) Total weighted error (b) Angular error (c) Compactness error

links. The print times for these components are therefore longer than the other links. For these reasons, the MCP\PIP coupler characteristics are kept consistent for all finger sizes. The MCP\PIP couplers can be mass printed and stored, reducing the time to produce the exoskeleton. The location of the servo-actuator is also kept consistent to enable easier exoskeleton placement on the hand.

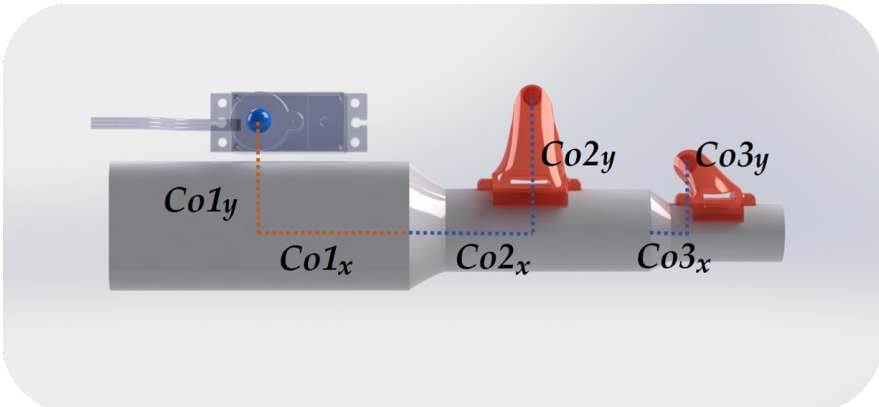

Figure 5.10: X and Y components of the hand-base and finger couplers.

As the geometry of the couplers and their placement on the hand remains consistent, a change in finger geometry will change the effective location of the coupler joints. To more

easily characterise this effect, the coupler variables $\{L1, L2_A, L3_A, Co1, Co2, Co3\}$ are split into their x and y components, Figure 5.10. Equation 5.24 details how these x and y shift with a change in finger size. Note $Co1_x$ remains unchanged.

$$\begin{aligned} Co1_y &= Co1_{y,orig} - \frac{W1_{orig} - W1_{new}}{2} \\ Co2_x &= Co2_{x,orig} - \frac{L2_{orig} - L2_{new}}{2} \\ Co2_y &= Co2_{y,orig} - \frac{W2_{orig} - W2_{new}}{2} \\ Co3_x &= Co3_{x,orig} - \frac{L3_{orig} - L3_{new}}{2} \\ Co3_y &= Co3_{y,orig} - \frac{W3_{orig} - W3_{new}}{2} \end{aligned} \tag{5.24}$$

Identifying the parametric functions

Hand measurements were collected from eighteen subjects, detailed in Appendix B. For each set of measurements, the DE process was carried out where three design variables $\{L4, Co5, L6\}$ were allowed to change. Parametric functions were fitted for each variable by finding a combination of four elements from F that formed the best linear correlation with each variable, where

$$F \in \{L2, L3, W1, W2, W3, Co1_x, Co1_y, Co2_x, Co2_y, Co3_x, Co3_y\}$$

The identified functions for L4, Co5, and L6 are detailed in Equation 5.25 and take the general linear form of $y = \alpha\ X_i\ +\ \beta$. Figure 5.11 shows the linear fit for each variable, and Table 5.8 details their adjacent coefficients.

$$Function\ (X_i) \begin{cases} L4 & X_{L4} = \frac{L2-L3}{Co2_y - W1} \\ Co5 & X_{Co5} = \frac{Co3_x - W1}{Co2_y + Co3_y} \\ L6 & X_{L6} = \frac{L2+L3}{Co1_x + Co1_y} \end{cases} \tag{5.25}$$

Table 5.8: Linear coefficients for each of the parametric functions (α, β) and their coefficient of determination (R^2).

Parametric Function	α	β	R^2
X_{L4}	0.642	46.521	0.93
X_{Co5}	3.606	11.256	0.87
X_{L6}	0.008	8.844	0.99

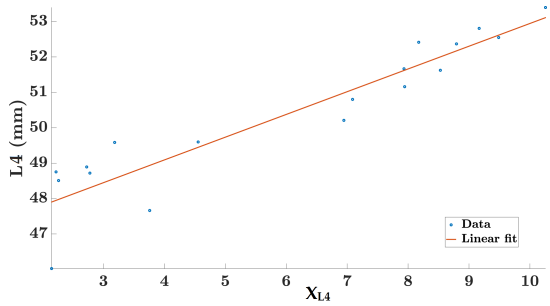

(a) Linear fit between parametric function A and L4.

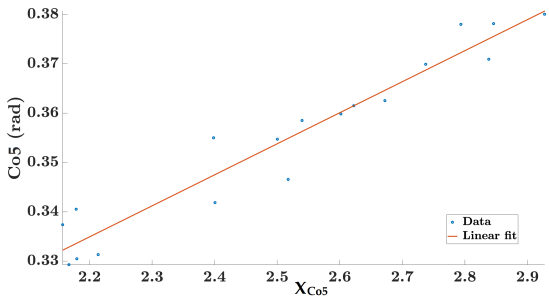

(b) Linear fit between parametric function B and Co5.

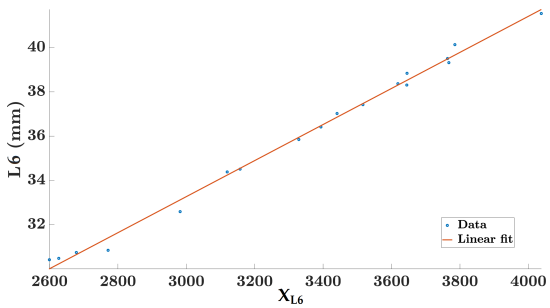

(c) Linear fit between parametric function C and L6.

Figure 5.11: Linear fits between parametric functions and optimal values for L4, Co5, and L6.

5.7 Methods

Experimental testing can be broken into two sections. The first section evaluates the parent model exoskeleton when applied to a 3d printed finger, accurate to the model dimensions. The exoskeleton is then applied to its intended human finger and a Monte Carlo analysis is introduced to study the effect of model/implementation inaccuracies. The second section focuses on human finger trajectories employed during a set of cylindrical grasping trials. This study was approved by the Human Ethics Committee, University of Canterbury (HEC2020/68) and informed consent was obtained from each participant prior the experiment.

5.7.1 Experimental Protocol

Exoskeleton Trial

The exoskeleton was fitted onto the 3d printed finger and to one human subject. Hook and loop fasteners were used to couple the exoskeleton to the human finger and zip ties were used on the 3d printed finger, Figure 5.15. Finger movements were tracked using a motion tracking system with reflective markers, as the subject performed four flexion-extension movements, Section 5.7.2. The 3d printed finger and exoskeleton dimensions were consistent with the parent model finger measurements detailed in Table 5.4 and the parent model DE output parameters detailed in Table 5.6, respectively. Movement of the 3d printed finger was actuated by servo motor.

Grasping Trial

Seven healthy subjects participated in a series of grasping trials. The subjects were five male and two female, aged 26 ± 1 years. Subjects were seated at a table with two cylindrical objects placed in front of them. The objects had diameters of 62.45mm and 47.75mm, respectively, and were orientated in an upright configuration, Figure 5.12. Throughout the trial, the subjects were instructed to reach, grasp, and lift an object with their dominant hand. There were no specific instructions given on how to grasp the object, in an attempt to promote a natural grasping motion. Between grasping motions, the subject's hand rests in a comfortable posture on the table.

Ten grasping trials per object were completed, with the order of grasping instructions randomised. Every five grasps, the subject was given thirty seconds of rest. Each subject's index finger was tracked throughout the trial using reflective markers and optical tracking system, Section 5.7.2.

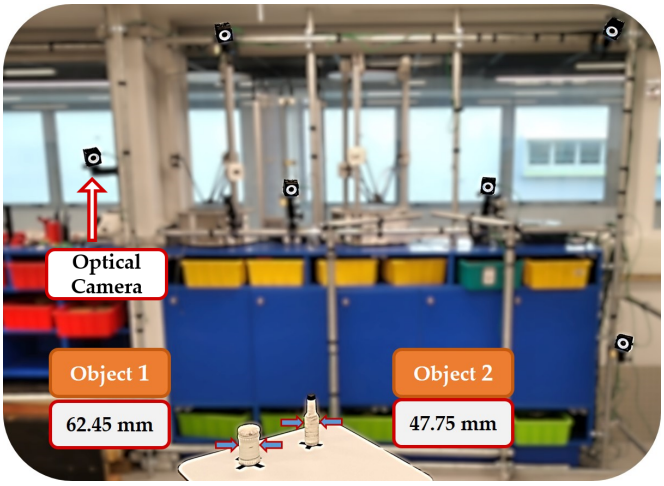

Figure 5.12: Experimental set-up with optical cameras and cylindrical objects

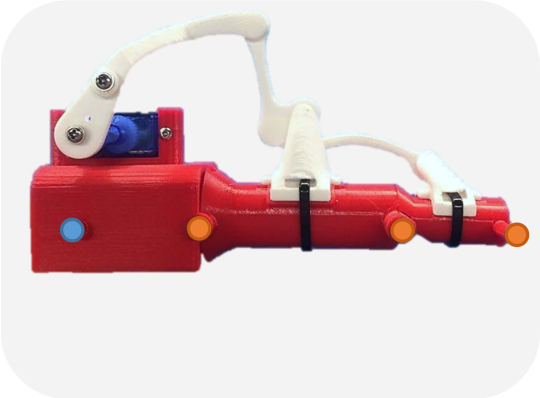

(a) Marker placement on 3d printed finger

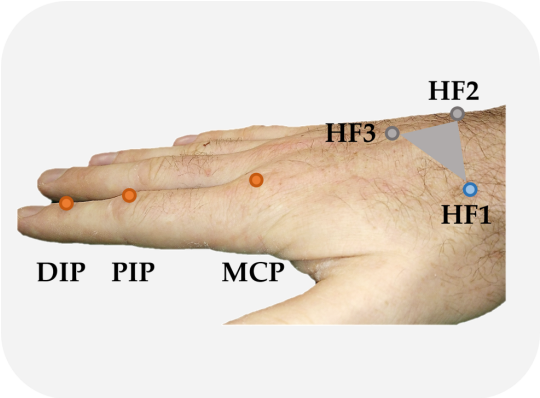

(b) Marker placement on human hand.

Figure 5.13: Marker placements on the finger. Orange markers represent the MCP,PIP, and DIP finger joints. The blue markers represent the index finger proximal MCP, HF1. Markers HF1, HF2, and HF3 form the human hand's rigid body (a) Placement on 3d printed finger model (b) Placement on human hand

5.7.2 Instrumentation and Data Processing

A motion capture system with eight cameras (Prime 13, Optitrack) recorded the position of reflective markers at 240Hz, Figure 5.12. Eight markers were placed on the subjects' hands and four markers were placed on the 3d printed finger, shown in Figure 5.13b and Figure 5.13a respectively. The trajectory of each marker was smoothed through Optitrack Motive by a 4th order low-pass Butterworth filter with frequency cutoff of 6Hz.

The orange markers in Figure 5.13 represent the MCP, PIP, and DIP finger joints. The

blue markers represent the hand-base location used in Figure 5.14. The hand-base marker is vertically aligned with the MCP joint on the 3d printed model and is placed on the proximal MCP joint on the human hand. Markers HF1 HF2, and HF3 form the rigid body frame used to track the position and orientation of the hand throughout the experimental protocol. HF1 and HF2 are positioned on the carpometacarpal joints of the index and ring fingers, respectively. HF3 is placed halfway along the middle finger's metacarpal bone.

The following process is used to obtain continuous MCP and PIP angles throughout the grasping process.

1. Transform all marker positions from the global camera frame into local coordinates using the transform based on plane HF1-HF2-HF3 with HF1 used as the origin. Note, as the position and orientation of the 3d printed finger-base remains fixed, no rigid-body tracking is necessary.

2. The trajectories of the MCP, PIP, and DIP joints can be assumed to lie along the same plane. A least-squares plane is fit to the trajectories of the MCP, PIP, and DIP markers. The marker coordinates are then projected onto the plane, to reduce the problem space to two dimensions (X. Zhang, Lee, & Braido, 2003), Figure 5.14.

3. MCP and PIP angles are obtained using the equation sets 5.26 and 5.27 with respect to Figure 5.14.

$$\begin{aligned} \theta_{Base} &= atan2(MCPy, MCPx) \\ \alpha &= atan2(MCPy - PIPy, MCPx - PIPx) \\ \theta_{MCP} &= \alpha - \theta_{Base} \end{aligned} \tag{5.26}$$

$$\beta = atan2(PIPy - DIPy, PIPx - DIPx)$$
$$\theta_{PIP} = \beta - \alpha \tag{5.27}$$

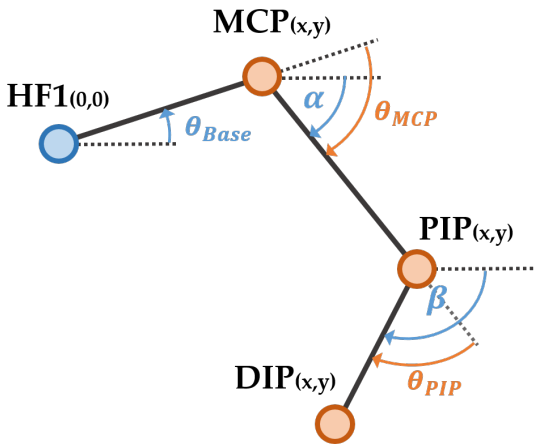

Figure 5.14: Reflective markers representation in 2D after being projected into the plane of best fit.

5.8 Results

5.8.1 Exoskeleton

Figure 5.15a and Figure 5.15b shows the exoskeleton applied to the 3d printed finger and on the human hand, respectively.

The MCP and PIP trajectories recorded over four flexion-extension movements are shown in Figure 5.16a for the 3d printed finger and in Figure 5.16b for the human finger. The parent model trajectory is included in both figures and the trajectories for the human finger are split into flexion and extension movements.

In Figure 5.16b the optical data shows hyper-extension of the human finger's MCP joint by $\sim 6°$. This motion can be produced by the human finger, as depicted in Figure 5.17. However, the parent model indicates design failure due to hyper-extension of the PIP joint.

(a) Exoskeleton mounted on finger model

(b) Exoskeleton placed on human hand

Figure 5.15: Exoskeleton placement on a 3d printed finger model and on a human finger.

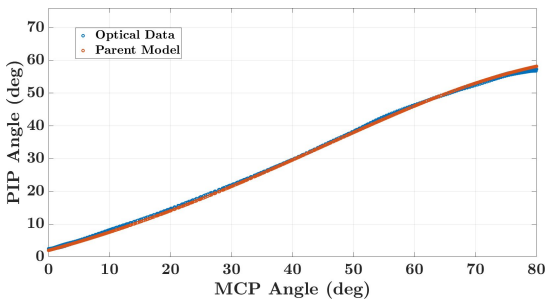

(a) 3d printed finger data

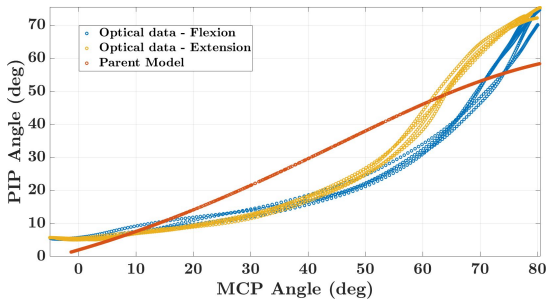

(b) Human finger data

Figure 5.16: Optical data for MCP and PIP angles against the parent model when applied on a 3d printed finger and when applied on a human finger.

The joint trajectories of the human finger and parent model can only be compared in the range of $\theta_{MCP} \in [-1°, 80°]$ where modelled PIP hyper-extension does not occur.

Table 5.9 details the RMSE between the parent model trajectory and the trajectories recorded over four flexion-extension movements for the 3d printed finger and the human finger.

Table 5.9: RMSE between the simulated exoskeleton PIP trajectory and the trajectories recorded when applied on a 3d printed finger and on a human finger.

	3d printed finger	***Human finger***
RMSE (deg)	0.46	10.3

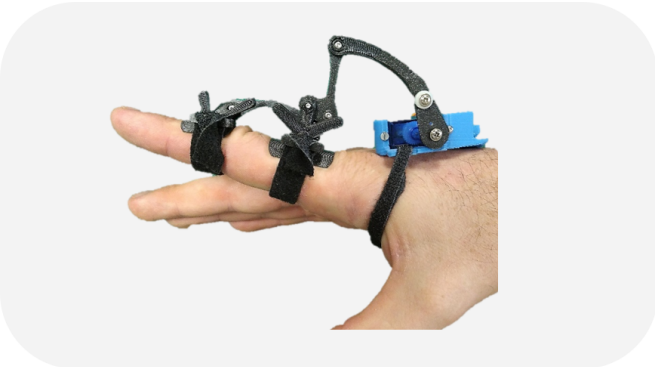

Figure 5.17: Hyper-extension of the MCP joint.

A Monte Carlo analysis was implemented to observe the effect of parent model parameter variation on the output MCP-PIP trajectories. The mean PIP angle range for each MCP angle ($\theta_{MCP} \in [0°, 80°]$) was monitored to determine the number of iterations needed to fully capture output trajectory variation. The mean PIP variation over the MCP range was used, as opposed to PIP variation at one specific MCP angle, because any subset of the MCP range may be used in a grasping task. Figure 5.18a shows the convergence of the mean PIP angle range as the number of iterations approaches 500,000.

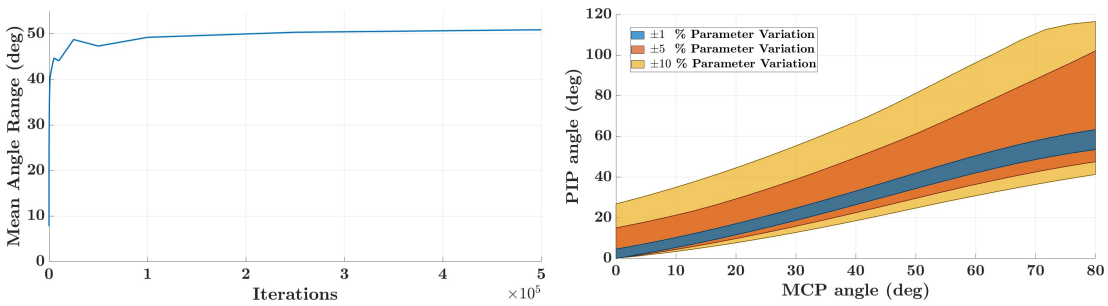

(a) Mean PIP angle range generated over iterations with ten percent parameter variation.

(b) Angle range generated with parameter variation of ±1%, ±5%, and ±10%, over 500,000 iterations.

Figure 5.18: PIP angle range over parent model parameter variation for iterations up to 500,000.

Figure 5.18b depicts the range of MCP-PIP trajectories generated over 500,000 iterations with parameter variation of ±1%, ±5%, and ±10%. The corresponding minimum, maximum, and mean PIP range variations are detailed in Table 5.10.

Table 5.10: Minimum, maximum, and mean PIP variation range for parent model variation of ±1%,±5% and ±10% over 500,000 iterations.

Variation	±1%	±5%	±10%
Minimum Range (deg)	4.6	15.0	26.8
Maximum Range (deg)	9.8	54.5	75.9
Mean Range (deg)	7.0	29.7	50.9

5.8.2 Grasping Trials

A selection of grasp trajectories are depicted in Figure 5.19, where orange data represents the grasping of Object 1 (62.45mm diameter) and blue data represents the grasping of Object 2 (47.75mm diameter). Figure 5.19a and Figure 5.19b shows data collected from Subject 5 and Subject 7, respectively, where their MCP-PIP trajectories are reasonably consistent over the ten grasping trials. Figure 5.19c and Figure 5.19d shows data from Subject 1 and Subject 2, respectively, whose grasp patterns are more diverse.

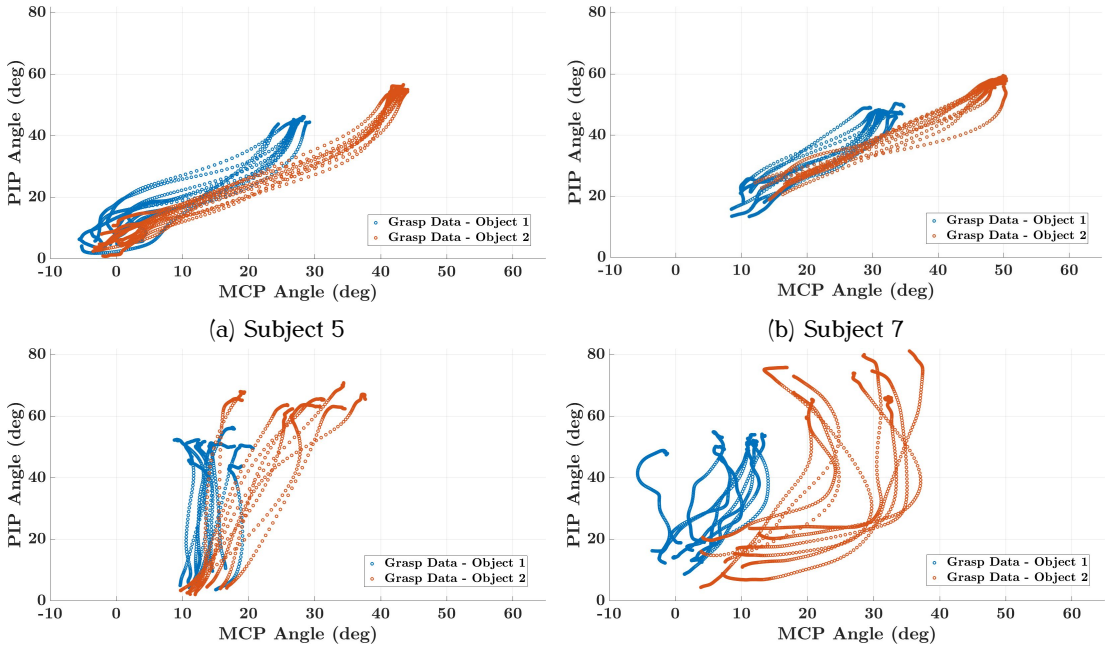

(a) Subject 5 (b) Subject 7

(c) Subject 1 (d) Subject 2

Figure 5.19: Subject grasp trajectories. Blue data represents Object 1 grasp trials and orange data represents Object 2 grasp trials.

Figure 5.20 depicts the envelope of MCP-PIP trajectories used by each subject over the grasping trials. Figure 5.20a shows the grasp envelopes employed during the grasping of Object 1 and Figure 5.20b shows the corresponding envelopes for Object 2.

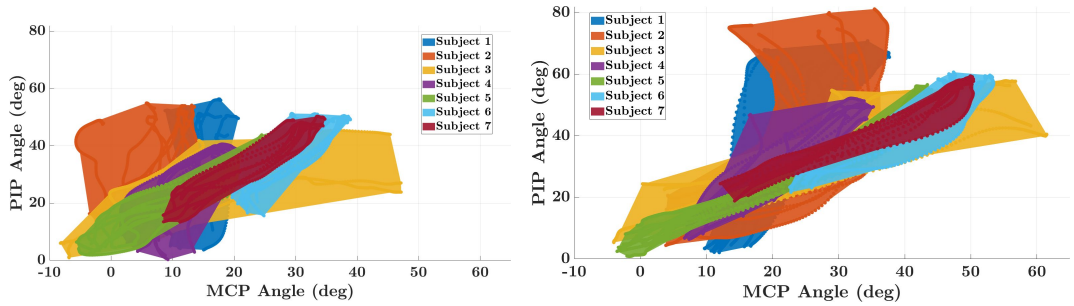

(a) Trajectory envelopes used in the grasping of Object 1.

(b) Trajectory envelopes used in the grasping of Object 2.

Figure 5.20: MCP-PIP trajectory envelopes for all subjects over ten grasping trials.

5.9 Discussion

A six-bar exoskeleton has been designed for finger motion guidance towards stroke rehabilitation. The exoskeleton links are designed to scale using finger measurement based parametric functions, Equation 5.25. Each parametric fit is based on eighteen measurement sets and have correlation of determination greater than 0.87. Using these models the exoskeleton can adapt to different finger sizes and can be quickly produced. To reduce the dependence on designer intuition a differential evolution process was used to dimension the exoskeleton's linkage properties. Exoskeleton optimisation was directed by an angular cost function f_{ang}, and a height compactness term f_{comp}. The synthesised exoskeleton achieved final cost function values for f_{ang} of 0.92°. This corresponds to an RMSE of 0.93° between the PIP output trajectory and the task positions detailed in Table 5.5. The compactness cost function f_{comp}, is weighted much lower than f_{ang} (W_{ang} = 0.85, $W_{compact}$ = 0.15). Consequently the height of the exoskeleton may not be as optimised as it could be. The input four-bar linkage appears to be the limiting factor behind the exoskeleton's compactness, as it needs to avoid interference with the finger in its most flexed position, Figure 5.15. Compactness may be improved by using a linear actuator rather than a servo, as the effective length of the input crank (L4) can change throughout the flexion-extension process.

The parent model exoskeleton was experimentally tested under two conditions. Firstly, the

exoskeleton is applied to a 3d printed finger consistent with the parent model input measurements (Table 5.4), Figure 5.15a. The measured joint trajectories track the parent model well with an RMSE of 0.46° over four flexion-extension movements. The exoskeleton is then applied to the human finger in which the parent model measurements were based, Figure 5.13b. The discrepancy between the parent model and the human finger's motion is larger with an RMSE of 10.3°, Figure 5.16b. A number of factors may contribute to this phenomenon, including the accuracy of the original finger measurements, accuracy of exoskeleton placement, and any shifting of the exoskeleton with respect to the hand during operation due to the flexible hook-and-loop fastening of the exoskeleton.

The 3d printed finger is accurate to model dimensions and includes indicators to accommodate proper placement of the exoskeleton. Furthermore, the exoskeleton couplers are zip-tied to the finger to prevent any shifting throughout flexion-extension movements. Human finger dimensions were determined manually using vernier callipers, due to the wide availability of callipers (or rulers) to the community. This method introduces human error and lacks the accuracy of more specialised equipment such as radiography or ultrasound to locate the precise position of the joint. The design of the exoskeleton includes the finger phalanx as the base kinematic chain, Figure 5.1a. This property avoids alignment issues between the finger and the exoskeleton joints. However, the kinematic accuracy of the exoskeleton is dependant on the couplers' placement on the finger. User comfort is of importance when applying an exoskeleton. Opposed to the 3d printed finger, the exoskeleton cannot be coupled tightly to a human finger. Consequently, the exoskeleton couplers are more prone to move and tilt with respect to the human finger. This effect can be observed in Figure 5.16b through the difference between flexion and extension trajectories. This suggests that the exoskeleton may not achieve full posture control of the finger joints. However, the intrinsic mechanical impedance of finger joints have been shown to produce natural motion in underactuated exoskeletons (Sarac et al., 2017). Through Monte Carlo analysis of the parent model's design variables, it can be seen that the exoskeleton trajec-

tory is sensitive to deviation in hand measurements and coupler placements, Figure 5.18. With ten percent variation in exoskeleton design variables the mean range of PIP angles for any given MCP angle is 50.9°, and the maximum range is 75.8°, Table 5.10. This effect may prove useful, as small alterations in coupler position could allow the exoskeleton to produce a number of grasp topologies.

There are a range of MCP-PIP trajectories that may be employed towards the successful grasp of an object. This effect was observed throughout trials where healthy subjects were instructed to reach, grasp, and lift, cylindrical objects with diameters of 62.45mm and 47.75mm, Figure 5.12. From inspection of Figure 5.19, Subjects 5 and 7 display consistent grasping patterns, with larger ROM used when grasping Object 2, due to its smaller diameter. Subject 1 and Subject 2 also use larger ROM for Object 2. However, variation in grasping trajectories can be observed. PIP motion appears to dominate the grasp trajectories for Subject 1. This is particularly evident during their grasp of Object 1, where almost no MCP flexion occurs throughout the grasp. Grasping trajectories displayed by Subject 2 differ again, where MCP joint flexion is used in the early stages of the grasp, but PIP joint flexion completes the movement. In a number of grasps, Subject 2's MCP joint extends during the second phase of motion.

The envelopes in Figure 5.20 depict the workspaces that were used during the grasping of Objects 1 and 2. It is important to note that all movements within the envelopes resulted in the successful grasp and lift of the cylindrical objects. This shows that there are a large number of strategies that can be employed towards a successful grasp. Variation in such strategies can be caused by an individuals grasping habits as well as the finger's adaptation to an object's size and shape (Jo et al., 2019). The grasping patterns utilised by Subject 1 and Subject 2 are of particular interest as they show that a person may use different strategies within a short amount of time. The results from these trials indicate that the functional capacity of an exoskeleton may not rely on a high degree of positional accuracy. The

exoskeleton presented in this chapter, although sensitive to coupler placement, possesses the potential to assist with functional grasping movements.

5.10 Summary

Robotic exoskeletons show potential for stroke rehabilitation due to their ability to provide high-intensity and reliable therapy. In the design of hand exoskeletons there are a range of independent finger DOF that may be supported. However, the recovery of basic curling motion is often recommended over more complex movements. In this chapter the kinematic and dimensional synthesis of a parametric one-DOF finger exoskeleton was outlined. Dimensional synthesis was guided by DE optimisation with cost functions for angular precision and height compactness. The parent model reached twenty task-positions with an RMSE of 0.92° and its height appears to be reduced towards the minimum that the Watt I topology and fixed servo motor allows.

Experimental testing showed that the exoskeleton's kinematic trajectory is sensitive to the accuracy of finger measurements and the coupler placements on the finger. The exoskeleton's trajectory RMSE increased from 0.46° when applied to a model dimensioned 3d printed finger, to 10.3° when applied to the modelled human finger. A Monte Carlo analysis showed that with ±10% variation in parameter value a mean PIP angle range of 54.4° can be generated for a given MCP angle. This variation may prove to be useful as a small change in coupler placement can result a different grasp topology. Through a series of cylindrical grasping trials, it was observed that a large range of movement strategies may be employed towards a successful grasp. This suggests that exoskeleton presented in this chapter could possess the capacity for functional grasp assistance, despite the difficulty in achieving tight coupling and accurate finger measurements required for accurate kinematics.

CHAPTER 6

Stimulator Design

Functional electrical stimulation (FES) is the application of electrical current to generate ordered muscle contractions, facilitating movement towards a functional task (McIlroy & Verrier, 2005). There are a number of ways in which FES can be applied towards stroke rehabilitation. Perhaps the most implemented and acknowledged approach is through motion assistance: FES is often applied to support high-intensity functional training.

FES may be applied transcutaneously, subcutaneously, or through implanted electrodes. Surface electrodes are typically used as they are non-invasive and can be easily applied/removed. Stimulation-elicited muscle contractions are generated through the passing of electrical current between stimulation electrodes. Stimulation current is typically applied as a set of pulse waveforms. A basic stimulation waveform can be characterised through four parameters: pulse width, inter-pulse duration, pulse amplitude, and pulse frequency. For more information, see Section 4.2.

There are many FES devices available on the market. However, these devices are often

expensive and do not offer flexibility in control of waveform parameters. This chapter presents a low part-cost (~$145 USD, bill of materials (BOM) provided in Appendix A) constant-current stimulator that allows user adjustment of stimulation waveform parameters. The device is powered from a 12V battery or power supply to provide biphasic stimulation of intensities up to 30mA at low-voltage ±40V rails.

6.1 Stimulator Design

The stimulator design is centred around the Improved Howland current source (IHCS) with a set of analogue switches to form an h-bridge multichannel output. Current sensing and emergency-off hardware is integrated into the design to ensure user safety.

6.1.1 Howland Current Converter

The Howland current source (HCS) and its variations are a well known op-amp topology which forms a linear differential voltage-to-current converter (Pouliquen, Etienne-cummings, & Vogelstein, 2008). This converter topology has been widely applied in technology as it can output bidirectional, arbitrary current waveforms, and exhibits high output impedance (Mottaghi & Hofmann, 2015).

An IHCS topology has been applied in this work, Figure 6.1, and forms the core of the stimulator design. The IHCS was chosen as it can provide higher efficiency and output compliance than the basic Howland topology (Pease, 2013).

Care needs to be taken in selecting components as the HCS and IHCS topologies are sensitive to component mismatch. Resistor mismatch will degrade the common-mode rejection and output impedance of the current source (Burr-Brown, 1990). Hong et al (Hong, Rahal, Demosthenous, & Bayford, 2007), state that for good performance, resistors need to be matched below 0.1% tolerance. Resistors with these specifications can be expensive and limited in availability.

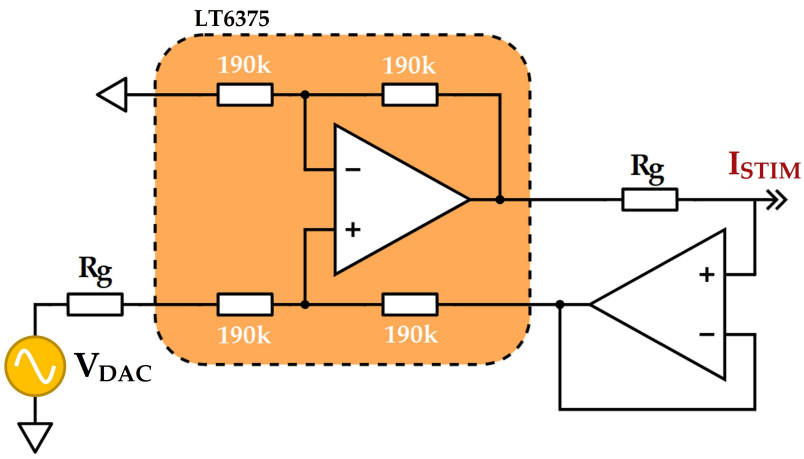

Figure 6.1: IHCS topology.

A high output impedance can be achieved through the use of differential amplifiers as their on-chip resistors are closely matched (Cornman, Akhtar, & Bretl, 2017). In this work, the LT6375 differential amplifier forms the main body of the stimulator. The current output of the IHCS is defined by the gain resistor, R_G, and input voltage, Equation 6.1.

$$I_L = \frac{V_{DAC}}{R_g} \tag{6.1}$$

V_{DAC} is set in the range $V_{DAC} \in [0, 3.3]$V by a 12-bit digital to analog converter (DAC), Equation 6.2. Through control of the DAC output voltage, the stimulation frequency, pulse width, inter-phase delay, and pulse amplitude can be adjusted.

$$V_{DAC} = \left(3.3 \frac{DAC_{CODE}}{4095}\right) \tag{6.2}$$

With R_g set to 110Ω, the output current $I_{STIM} \in [0, 30mA]$. As the IHCS is powered by a single rail 40V, it can only output monophasic waveforms. To produce biphasic current waveforms, the stimulator relies on output switching circuitry.

6.1.2 Stimulator Output Switching Circuitry

An overview of the IHCS output switching circuitry is depicted in Figure 6.2. The system consists of the IHCS, switches to disable the IHCS output (SW1, SW2), high-side current

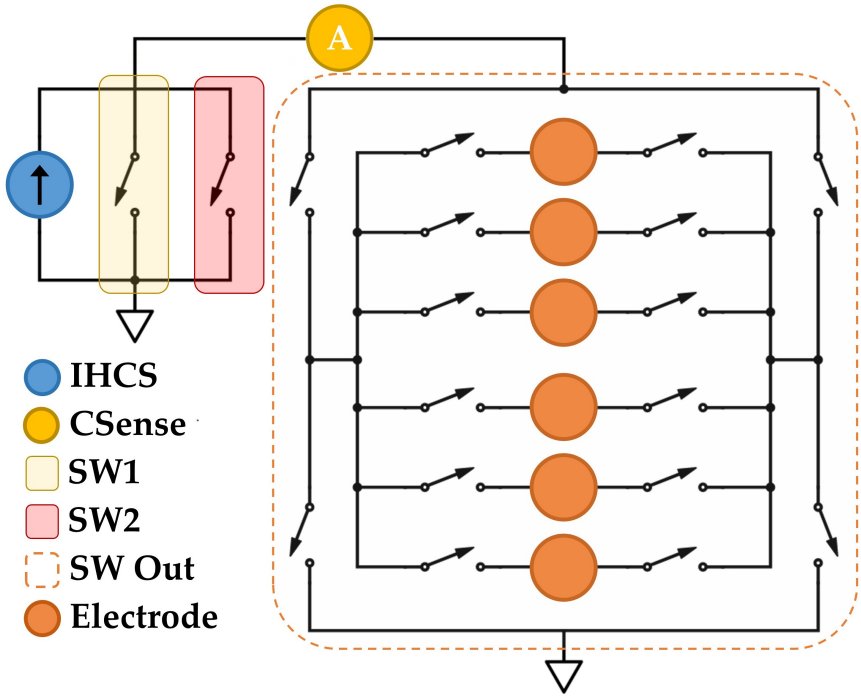

Figure 6.2: Overview of the stimulator switching output circuitry. IHCS refers to the current source, discussed in Section 6.1.1. CSense refers to the high-side current sensing system, SW1 and SW2 refer to stimulation disable switches, SW Out refers to the output switching circuitry, and Electrode refers to the electrode output channels.

sensing (CSense), and an h-bridge multichannel output (SW Out).

IHCS

The IHCS provides a mono-phasic constant-current waveform proportional to the DAC output voltage. See Section 6.1.1.

High-side current sensing

The output current of the IHCS is tracked by a high-side current monitor (AD8211). The current monitor outputs a voltage proportional to the IHCS output current. This voltage is used to detect an over-current fault, Section 6.2.2.

Output switching circuitry

A high-voltage 16 channel analogue switch integrated circuit (IC), MAX14802, is used to form the stimulation output switching circuitry. The MAX14802 is controlled by a micro-

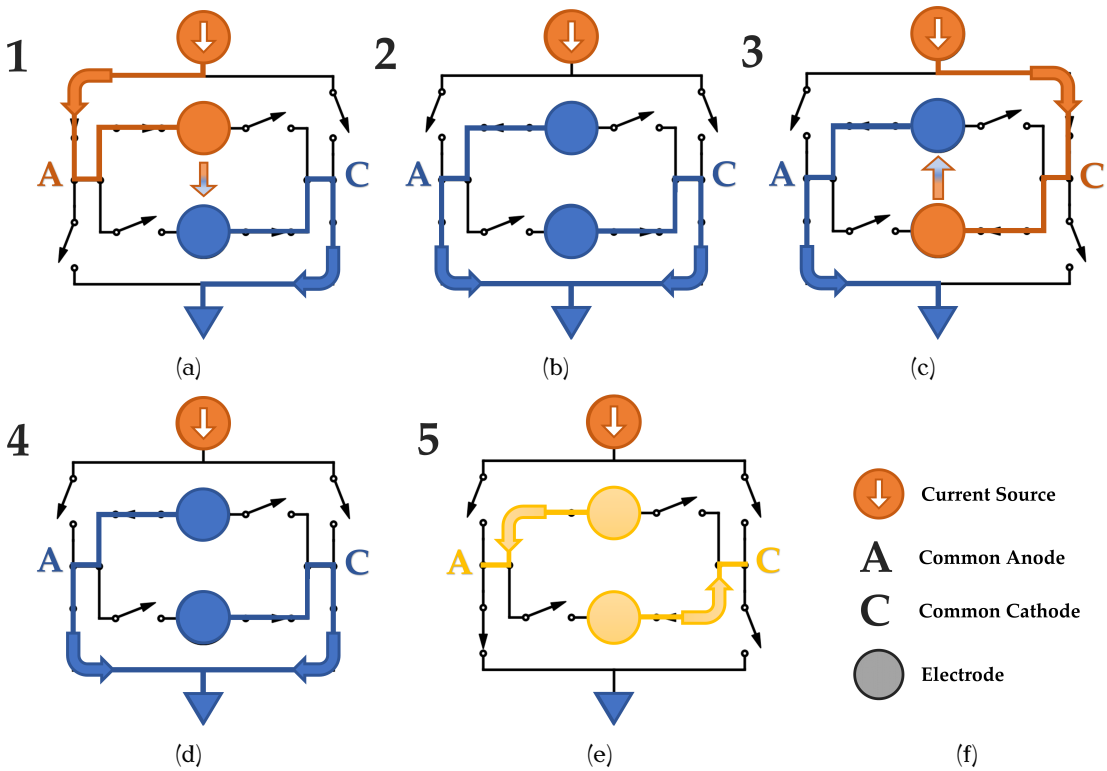

Figure 6.3: H-bridge switching sequence overview. Transitions from configuration *a* through to *d* represents typical biphasic stimulation delivery. Corresponding numberings *1-5* represent waveform states in Figure 6.4. (a,c) Active stimulation where current is passed between electrodes. (b,d) Passive electrode discharge. (e) Electrodes floating.

controller via serial peripheral interface (SPI). Four switches are used to form an h-bridge topology and the remaining 12 switches used to connect stimulation electrodes, Figure 6.2.

The h-bridge output is used to manipulate the IHCS monophasic output current into a biphasic current waveform. The h-bridge switching sequence is depicted in Figure 6.3. Figure 6.3a and Figure 6.3c show the active portions in which current is driven across the electrodes. In Figure 6.3b and Figure 6.3d, the system provides a low impedance path to ground to passively discharge the electrodes. Figure 6.3e shows the electrodes disconnected from the IHCS and system ground. To avoid h-bridge shoot-through, only one switch-state is altered at any one time. Therefore, two SPI commands are required to transition between states in Figure 6.3.

The timings between sequence transitions determine the stimulation pulse width (PW),

inter-phase delay (IPD), shorting duration (SD), and frequency (f), Figure 6.4.

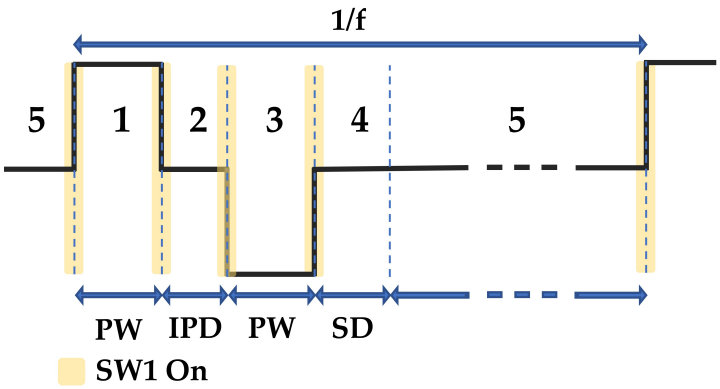

Figure 6.4: Stimulation timing diagram, with pulse width (PW), inter-phase delay (IPD), discharge duration (SD), and frequency (f). The yellow shaded areas indicate the times where SW1 (Figure 6.2) is active.

IHCS output disable switches

SW1 and SW2 are used to disable the output of the IHCS, Figure 6.2. When closed, SW1 and SW2 provide a low-impedance path to ground. In doing so, SW1 and SW2 can divert the IHCS output current away from the stimulation output circuitry and therefore away from the stimulation electrodes.

SW1: SW1 is enabled/disabled by a micro-controller. The timing for SW1 activation is indicated by the yellow shaded areas in Figure 6.4. SW1 is activated to avoid an infinite IHCS load, which would cause IHCS amplifier saturation.

SW2: SW2 is activated by the over-current emergency hardware to divert current away from the electrodes, Section 6.2.

6.2 Health and Safety

The possibility of electric shock and/or tissue damage of a patient is a hazard inherent to electrical stimulators (Huamani et al., 2019). Safety measures must be implemented in the stimulator design to mitigate any chances of patient harm. Several safety measures are implemented in the design of this stimulator.

6.2.1 Stimulator Characteristics

The stimulator presented in this work delivers low-voltage constant-current stimulation. The charge injected into the electrode-skin interface can therefore be controlled to be within safe bounds. Safety standard IECC 60601-2-10 requires user attention when RMS current density exceeds $2mA/cm^2$ (O'Connor, Lennon, Minogue, & Caulfield, 2020). However, lower current densities are often applied in practice. O'Conner et al. suggests limiting RMS current densities to be less than $0.5mA/cm^2$ in situations where skin sensation is impaired (O'Connor et al., 2020). This aligns with Patriciu et al (Patriciu et al., 2005) who note that average electrode current densities below $0.5mA/cm^2$ can be considered safe during human iontophoretic treatment.

The stimulator in this work can deliver a maximum current of 30mA. The stimulation pulse-width is limited to a maximum of 500us and the frequency is limited to 50Hz. Velloso et al (Velloso & Souza, 2007) calculate the RMS current density for a monophasic waveform with Equation 6.3

$$I_{RMS} = \frac{\sqrt{f \cdot \int_0^{PW} i(t)^2 dt}}{A} \tag{6.3}$$

Where f is the waveform frequency (Hz), PW is the pulse width (s), i is the current amplitude (A), and A is the area of the electrode (cm^2). When stimulation is applied to round 3cm diameter electrodes, the maximum current density is $0.67mA/cm^2$. This current density exceeds the limits suggested by O'Conner et al and Patriciu et al, but is well within the IECC 60601-2-10 standard. Additionally, a biphasic stimulation waveform is used and the electrodes are passively discharged every stimulation cycle, Section 6.1.2. These processes are useful to prevent charge accumulation in the electrode-skin interface which may lead to tissue damage (Ortmanns, 2007). Note, skin preparation and electrode gel is applied to promote even current density under the electrodes.

6.2.2 Emergency Shut-Off Hardware

Emergency shut-off hardware is incorporated in the stimulator design. An overview of the emergency shut-off hardware is provided in Figure 6.5. The emergency shut-off signal is used to control SW2, Section 6.1.2.

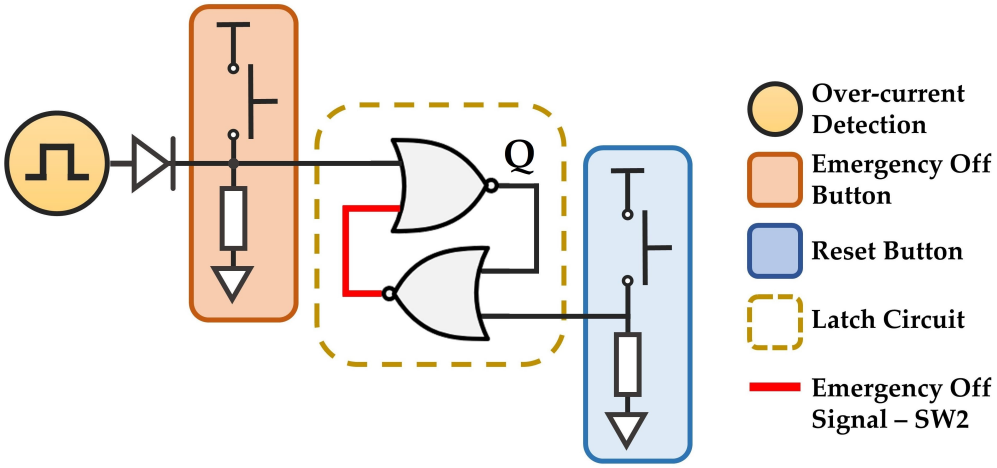

Figure 6.5: Emergency shut-off hardware.

The main body of the emergency off hardware consists of an SR latch formed from two NOR gates, with inputs: emergency-off button, reset button, and over-current detection. The over-current detection signal is generated from the high-side current sensing system, Section 6.1.2. When an output current larger than 50mA is detected, an output high signal is produced, which in turn latches the emergency-off signal high, SW2, Figure 6.5. The emergency-off button also activates the emergency-off signal. The button is made available to the user so that stimulation can be disabled when any discomfort is felt. The reset button is used to reset the latch and restore the stimulator's functionality. Table 6.1 details the emergency-off signal output logic. Note, Q is the output logic of the first NOR gate, and is not an externally generated input signal.

Table 6.1: Overview of the emergency shut-off hardware circuit logic.

Over-Current	EOff Button	Reset Buttom	Q	EOff Signal - SW2
0	0	0	1	0
0	0	0	0	1
1	0	0	0	1
0	1	0	0	1
0	0	1	1	0
1	0	1	0	0
0	1	1	0	0

6.3 Experimental Data and Testing

The performance of the stimulator was tested on a set of resistive loads, and on one subject. This study was approved by the Human Ethics Committee, University of Canterbury (HEC2020/68), and informed consent was obtained from the participant prior to the experiment. For the test depicted in Figure 6.6 the stimulator is applied across a resistive load of $2k\Omega$ while the DAC output voltage is swept from $0V$ to $3.3V$. The blue trace shows the ideal current output, characterised by Equation 6.2. The orange trace shows the measured current output. The maximum output current into the load can be determined using Equation 6.4.

$$I_{L\ (MAX)} = \frac{V_{OUT\ (MAX)}}{R_L + R_{SW}} \tag{6.4}$$

Where $V_{OUT\ (MAX)}$ is the voltage compliance of the stimulator, R_L is the load resistance, and R_{SW} is the combined switch resistances of the h-bridge. For this system, $V_{OUT\ (MAX)}$ is limited to 40V, and the combined on-resistance of the h-bridge switches is $\sim 30\Omega \cdot 4 = 120\Omega$. For a $2k\Omega$ load resistance, the theoretical maximum output current is 18.87mA, Equation 6.5.

$$I_{L\ (MAX)} = \frac{40V}{2000 + 120} = 18.87mA \tag{6.5}$$

The measured maximum output current is $18.70mA$, represented by the high-end plateau in Figure 6.6. The lower-end plateau is caused the current monitor's output bias at low input common-mode voltages, and is not representative of the stimulator's output current.

Between the two plateau areas, the stimulator's operation is notably linear. However, the measured gradient is steeper than the target gradient. The resulting RMSE between the target and measured currents, given DAC output voltages between the plateaus, is 0.25mA. Referring to Equations 6.1 and 6.2, this discrepancy is likely caused by the tolerancing of the IHCS gain resistor and DAC output voltage error.

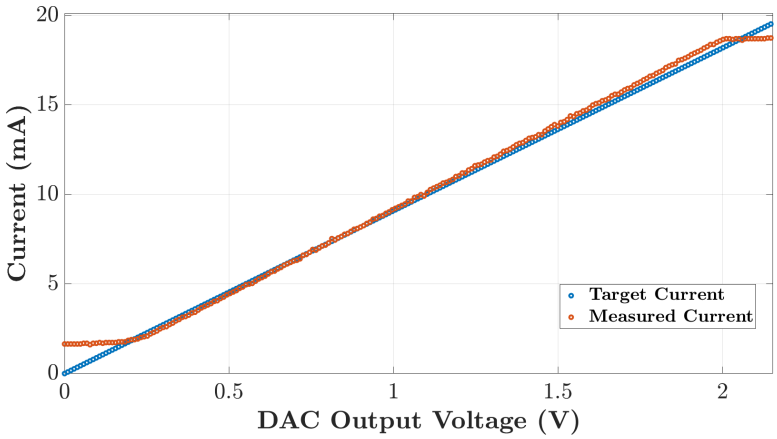

Figure 6.6: Current output levels for given DAC output voltages, ideal (blue) and measured (orange)

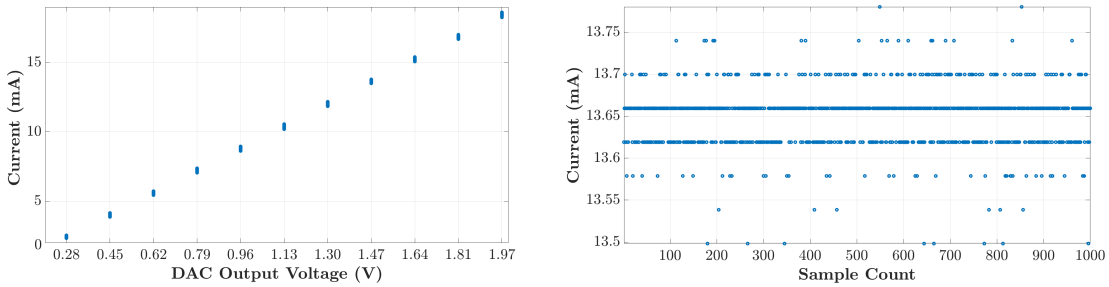

(a) Measured current output variation for a given set of DAC output voltages.

(b) Measured current output variation over 1000 samples, given a DAC output voltage of 1.47V.

Figure 6.7: Current output variation.

For the test depicted in Figure 6.7, the DAC output is swept between a subset of evenly spaced voltages. This subset is taken within the measured linear region from Figure 6.6. Each voltage is held for one second while the stimulator output is sampled at 1kHz. Figure 6.7a shows the stimulator output measurements collected for each of the DAC output voltages. Figure 6.7b shows the measurements for a DAC output voltage of 1.47V. It can be seen that the stimulator output remains between 13.6mA and 13.7mA for the majority of the sampling period, however there is also wider spread variation.

Table 6.2: Mean, standard deviation, and CoV of the stimulator output current for a given DAC output voltage.

DAC output voltage (V)	**0.28**	**0.45**	**0.62**	**0.79**	**0.96**	**1.13**	**1.30**	**1.47**	**1.64**	**1.81**	**1.97**
Mean (mA)	2.44	4.01	5.60	7.22	8.82	10.43	12.04	13.65	15.26	16.88	18.49
Standard Deviation (mA)	0.13	0.15	0.16	0.16	0.17	0.19	0.19	0.18	0.18	0.18	0.18
Coefficient of Variation (%)	5.26	3.74	2.86	2.28	1.92	1.78	1.59	1.30	1.20	1.05	0.95

The stimulator's mean output, standard deviation, and CoV are detailed in Table 6.2 for each DAC output voltage. The standard deviation ranges from 0.13mA to 0.18mA over all the current outputs, generally increasing as the current output increases. The CoV is the ratio of the standard deviation to the mean. The CoV can be seen to increase from 0.95% at 18.5mA mean current output, to 5.26% at 2.44mA. This is due to the relatively consistent nature of the standard deviation over all currents.

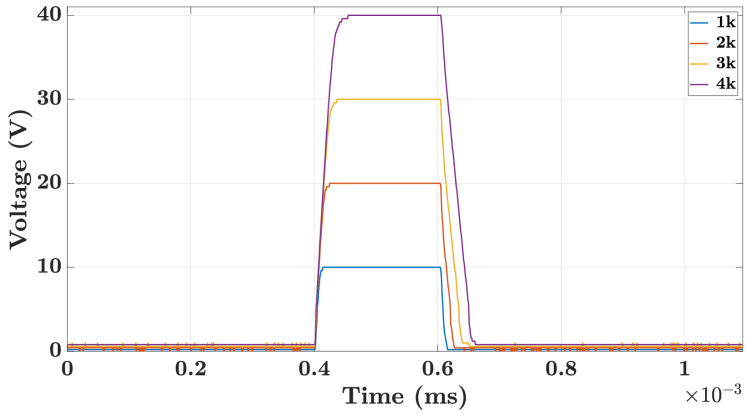

(a) Stimulator voltage across four resistive loads

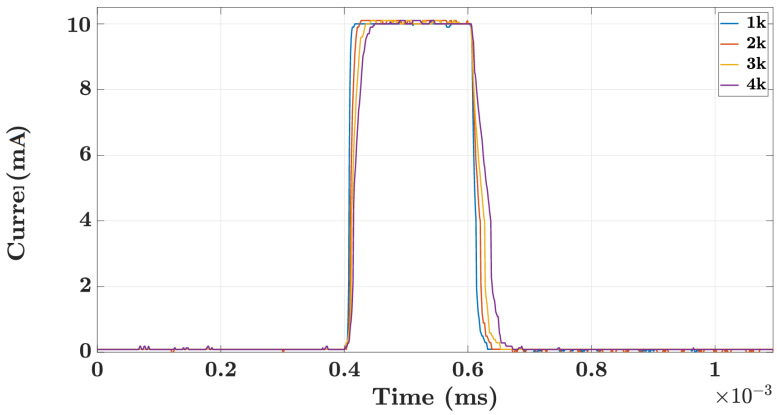

(b) Stimulator current across four resistive loads

Figure 6.8: Stimulator output voltage and current across four resistive loads, for a set 200us pulse of 10ma.

Figure 6.8 depicts the response of the stimulator's output across resistive loads in the set $R = \{1k,\ 2k,\ 3k,\ 4k\}$, for an input pulse of 200us and amplitude $V_{DAC} = 1.1V$ ($I_{StimDesired}$ = 10mA). From Figure 6.8b, the stimulator's steady-state output current converges to 10mA, and from Figure 6.8a, the output voltage rises proportionately with the increase of resistance. There is a noted increase in rise-fall times for voltage and current as the resistive

load increases from 1k to 4k. This phenomenon can be attributed to the slew-rate of the differential and buffer amplifiers (lt9375 - 2.4V/us, MCP6V51T - 1.2V/us), as well as an RC time-constant due to parasitic capacitance of the h-bridge output circuitry.

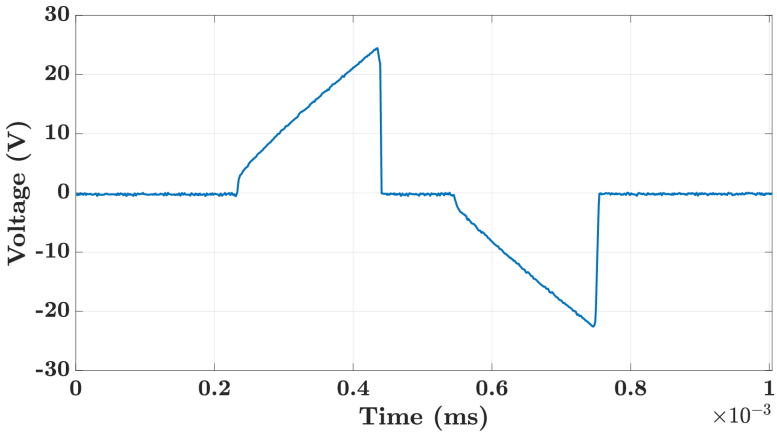

(a) Stimulator voltage across the subject's skin interface

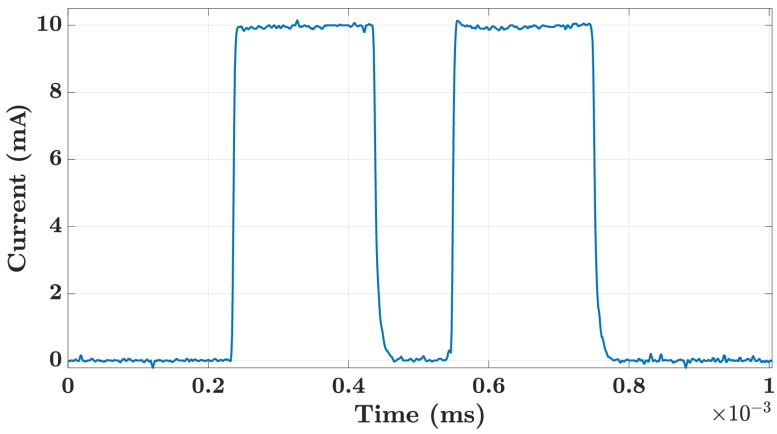

(b) IHCS output current

Figure 6.9: Stimulator output current and voltage applied to the forearm of one subject. Biphasic waveform with amplitude 10ma, pulse-width 300us, and inter-phase delay of 60us. Note, the second phase of the IHCS output current is reversed through h-bridge commutation.

For testing on the human subject, square, 30mm x 30mm stimulation electrodes were placed on the forearm. The stimulator input received square waveforms with pulse-width of 300us and amplitude of 1.1V from the DAC ($I_{StimDesired}$ = 10mA). The h-bridge circuitry was used to commute the IHCS output to a biphasic waveform with pulse-width 300us and an inter-phase delay of 60us. From Figure 6.9b, the stimulation current output quickly converges to the 10mA target and achieves the desired biphasic square waveform. Note,

Figure 6.9b shows two current pulses of positive magnitude, despite biphasic current being applied across the electrodes. This is due to the placement of the current sense circuitry, Figure 6.2. Figure 6.9a shows the voltage across the stimulation electrodes. In comparison to the resistive load, the stimulation output voltage exhibits a much slower rise time due to the electrode-tissue impedance. Consequently, the slew-rates of the stimulator amplifiers do not impede functionality of the device.

6.4 Summary

FES has been applied towards post-stroke rehabilitation as it can offer high-intensity practice with meaningful context. The widespread of FES based rehabilitation, however, is limited due to the high-cost and inflexibility of current commercial devices. The device detailed in this work presents a low part-cost constant-current stimulator with flexible stimulation waveform parameters. The stimulator can provide biphasic stimulation up to $\pm 30mA$ at low-voltage ($\pm 40V$), and includes emergency shut-off hardware to ensure user safety. When applied to a $2k\Omega$ load, the stimulator demonstrated a linear output transfer function, with a maximum ramp tracking error of 5%. Across resistive loads and one subject, the stimulator demonstrated its ability to output a square current-pulse of amplitude 10mA, regardless of the load impedance.

CHAPTER 7

Stimulus Resistant EMG Amplifier Design

7.1 Introduction

Bioelectrical signals are widely used throughout commercial technology as well as in research. One such signal is electromyography (EMG), a non-invasive technique applied to study skeletal muscle contraction, detecting the electrical activity in contracting muscle cells (Suhaimi et al., 2014). The electrical activity captured by EMG is a bipolar signal with amplitude $\leq 10mV$ pk-pk and usable energy within 0-500Hz, but predominantly within the 50-150Hz range (Basmajian & De Luca, 1979).

EMG is frequently used alongside FES in stroke rehabilitation. For applications such as monitoring (e.g. muscular torque, muscular fatigue) and control (e.g. neuro-prosthetic control), the volitional or stimulation elicited EMG signal is often used. In order to facilitate these applications in a space-efficient manner, there is a requirement for same-muscle

EMG recording and stimulation. The main obstacle to recording from stimulated muscle are large-scale electrical artefacts due to the stimulation that corrupt the EMG signal. Therefore, artefact reduction techniques have become increasingly paramount. Further background on EMG and artefact reduction is outlined in Sec 4.3.

Most commercial, research-level EMG devices are not open source hardware and can be costly. Their amplification and filtering stages are typically not divulged, despite having a significant impact on the resulting output signal. In this manner, most commercial EMG devices are effectively black boxes. For users, this means that these devices are generally inflexible and may not be suitable for their intended application. In addition, to the authors knowledge very few EMG devices are compatible with electrical stimulation, or can concurrently record EMG from a stimulated muscle.

Techniques for amplifier protection and artefact suppression have been explored in literature; however, these designs often rely on fixed timings for artefact suppression (Futami et al., 2005; Shalaby et al., 2011) or use low-gains to avoid amplifier saturation (Ambrosini et al., 2011; Yi et al., 2013). Furthermore, the designs are typically not open-source, with little more than high-level system overviews provided (Nishida & Suzuki, 2017; Taylor & Chappell, 2003; Yeom & Chang, 2011). Stimulation resistant EMG devices are predominately designed for separate stimulation and EMG electrodes. This electrode configuration is spatially inefficient and lacks consistency between the recording and stimulation sites(Muraoka, 2002). Only a limited number of devices have been designed for stimulation and recording through common electrodes. These designs typically avoid saturation through low pre-amplifier gains and reduce artefact transient times by raising the system's high-pass filter cut-off frequencies. For more information, see Section 4.3.1.

There is a need for low-cost, flexible, and open-hardware EMG designs, that can record from a stimulated muscle. This chapter presents a low-cost (USD $145, BOM in Appendix

D), open source EMG design, with hardware to detect and to minimise stimulation artefact transients. In this manner, the presented documentation allows future researchers and developers to more effectively use the design towards their intended application, saving time and money. Hardware design files are included in Appendix C

7.2 System Overview

The EMG device outlined in this chapter consists of an input protection stage, artefact detection channel, and EMG recording channel. The EMG recording channel is based on the design by Fortune et al. (B. Fortune, Pretty, Chatfield, McKenzie, & Hayes, 2019), modified to include input protection, artefact suppressing hardware, and to accommodate $\pm 15V$ rails on its pre-amplification stage.

The system utilises pre-gelled, conductive carbon-film surface electrodes. A high-level system overview is depicted in Figure 7.1.

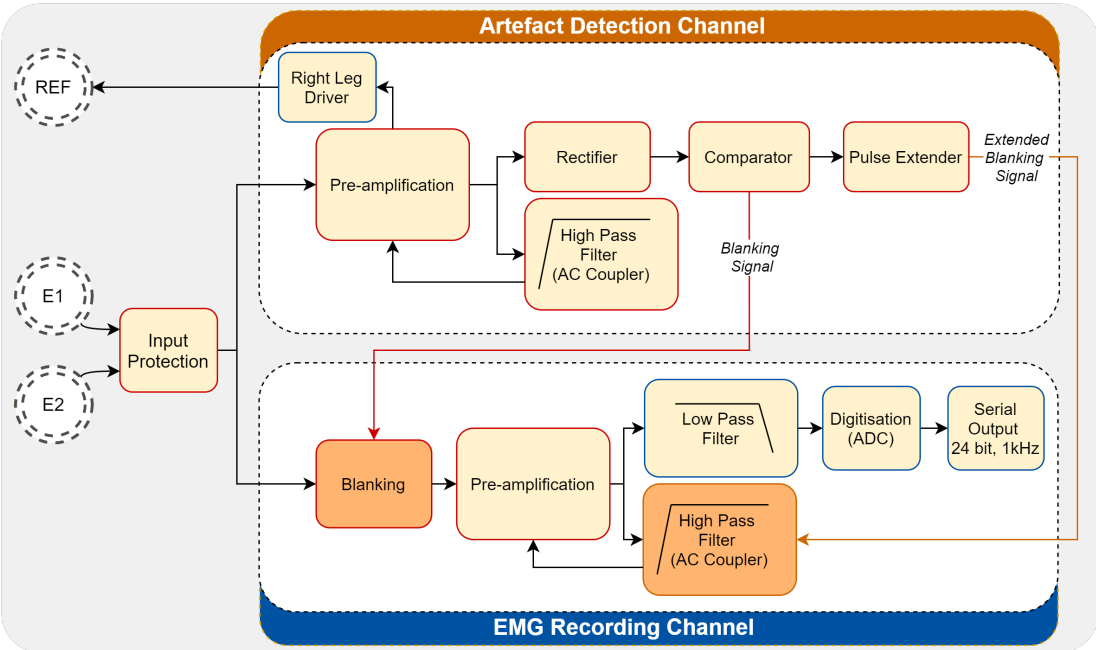

Figure 7.1: System overview block diagram. Blocks with dark orange fill contain artefact suppressing features. Blocks with a blue outline represent sections designed by Fortune et al (B. Fortune et al., 2019). E1, E2, and REF are the electrodes placed on the user for measurement.

7.3 Design Decisions

7.3.1 Power Supply

The device presented in this work, unlike that described by Fortune et al (B. Fortune et al., 2019), is not designed to have active electrodes (i.e. the recording device is not built into the electrodes): the PCB board size is therefore less restricted. Given the extra PCB board space, the design can include isolated power supplies and accommodate larger voltage rails.

The device is designed to operate from a single 12V supply. The input regulators for the design differ from those in (B. Fortune et al., 2019): an isolated 5V supply (U9:PDM1-S12-S5-S) and an isolated $\pm 15V$ supply (U10:PQP3-D12-D15-D) are used. The isolated nature of the on-board regulators allow the device to be safely powered by battery or an AC-powered bench-top supply.

The $\pm 15V$ rails are utilised for a number of reasons. Higher rail voltages allow for a larger pre-amplifier gain, taking advantage of the instrumentation amplifier's common-mode rejection ratio (CMRR) without causing saturation. Higher rails are also useful as the AC-coupler can account for larger electrode DC offsets: this is often an issue when stimulation is present on the recorded muscle. The low-pass filter and ADC stages are powered by the +2.5V regulator (U12, REG710) and -2.5V regulator (U11, LTC1550) as in (B. Fortune et al., 2019).

7.3.2 System Components Adapted from Fortune et al.

A number of system components have been adopted from Fortune et al (B. Fortune et al., 2019), with minor alterations. These components are represented by the blocks with a blue outline in Figure 7.1: adjustable gain low-pass filter, 24-bit sigma-delta analog to digital converter (ADC), and right leg driver (RLD). The adjustable-gain band-pass filer provides

flexibility towards varying application environments. The RLD attenuates electro-magnetic interference (EMI) in real-time and the ADC outputs high-accuracy digitised EMG. The minor alterations are as follows:

- RLD supply rails: The RLD rails are powered through a $\pm 15V$ supply. This alteration follows as the recording pre-amplifier and AC-coupler are also powered off the $\pm 15V$ supply.

- Op-amp selection: Two dual op-amp package OPA1602 (U1, U4) are used instead of the quad op-amp LT6204 for RLD and filtering sections. This substitution was made to allow cleaner routing of the PCB. The OPA1602 allows for $\pm 2.25V to \pm 18V$ supplies, is rail-to-rail input and output, unity gain stable, and has a gain bandwidth product of 35MHz.

- Low-pass filter adjustable gain: Adjustable gain of the low-pass anti-aliasing filter is still achieved through the AD5222 digital potentiometer (U17): However, control of the digital potentiometer is achieved through the micro-controller GPIO pins, rather than the ADC GPIO pins. This alteration is made for ease of PCB routing.

7.3.3 Input Protection

Amplifier inputs are clamped to $\pm 2.5V$ rails through resistor-diode shunt networks, depicted in Figure 7.2. This feature protects the amplifier from voltage transients above its rails. Input protection is especially necessary when the amplifier is not synchronised with the stimulator, and is regularly subjected to high-voltage stimulation pulses.

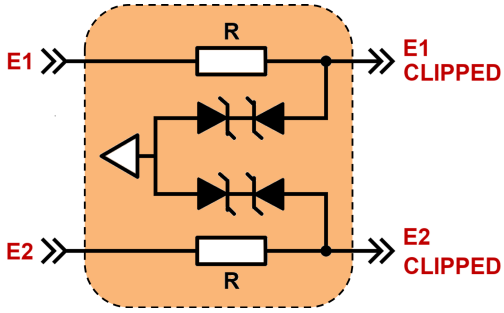

Figure 7.2: Resistor-diode shunt network to clamp the pre-amplifier input voltages to $\pm 2.5V$.

7.3.4 Artefact Detection Channel

The artefact detection channel is responsible for producing artefact suppression signals for the design. The signal timings are characterised through threshold detection of the artefact contaminated signal.

Pre-amplifier (U2: INA828)

An instrumentation amplifier is used to amplify the differential electrode voltage with respect to a reference. This is performed by the INA828, as depicted in Figure 7.3. Note, the INA828 is the second generation of the INA128 instrumentation amplifier used in Fortune et al (B. Fortune et al., 2019).

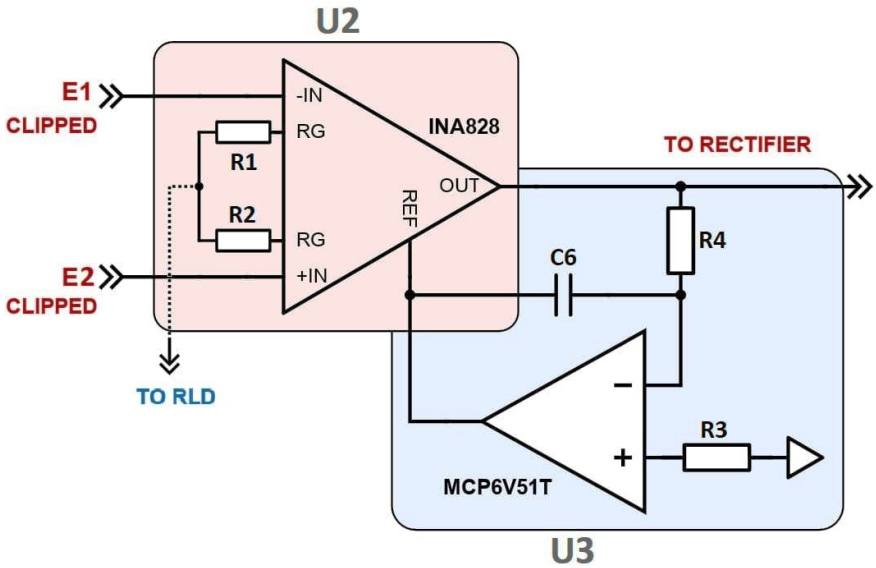

Figure 7.3: Basic pre-amplifier topology. The red section indicates the instrumentation amplifier and gain resistor. The blue section indicates the AC-coupler

The INA828 was chosen for its high common-mode rejection ratio (minimum of 130dB over the pass-band) and low noise (7nV/Hz). The output of the INA828 is AC coupled to remove any DC offset within $\pm 15V$ rails. The amplifier gain is set by an external resistor by equation $G = 1 + \frac{50k\Omega}{R_G}$. The gain of the instrumentation amplifier is set to ~369V/V via gain resistance of 136Ω. The gain resistance is formed by two 68Ω resistors (R1, R2), allowing the common-mode voltage to be accessed by the right leg driver (RLD).

AC Coupler (U3: MCP6V51T-E/OT)

The AC coupler is an integrating op-amp circuit that provides closed-loop feedback to the instrumentation amplifier's reference pin, Figure 7.3. The AC coupler acts to remove DC offset and attenuate low-frequency noise from the instrumentation amplifier's output. The frequency response of the AC coupler is the same as a first-order low-pass RC filter, $F_C = \frac{1}{2\pi RC}$. A ~325Hz frequency cut-off is obtained by using a 47nF (C6) capacitor and 10kΩ resistor (R4). The frequency cut-off is set above the main EMG spectra to avoid triggering of artefact detection thresholds by volitional contractions. A compensation resistor (R3) equal to the integrator resistor (R4) is applied.

Rectifier

As the EMG signal is bipolar in nature, the output of the instrumentation amplifier needs to be rectified before the Schmitt trigger stage. A precision full-wave rectifier topology is utilised, as outlined in (Ye, 2013). This design topology is used for its ability to output with minimal distortion near transition regions.

Schmitt trigger (U6: TLV1701)

The rectified EMG signal is passed to a Schmitt trigger to generate the blanking signal for the EMG recording channel. The Schmitt trigger's reference is set by an external voltage divider. Stimulation artefact is prone to vary with changes such as electrode configuration and electrode-skin interface. As such, it is desirable to have an adjustable threshold for artefact detection. The reference is manually adjustable via a 20 turn trimmer potentiometer

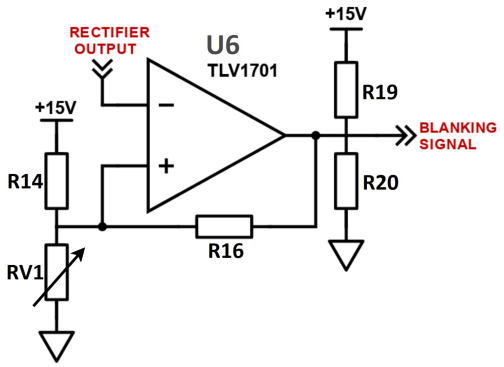

(a) Schmitt trigger topology

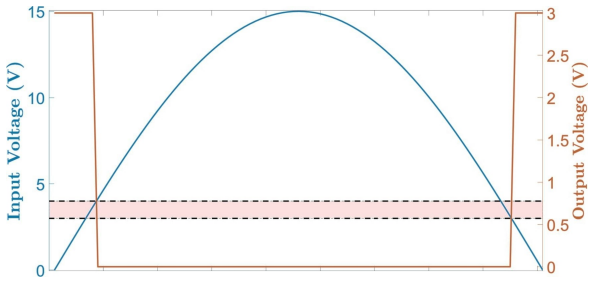

(b) Example: Blue represents the input voltage, and orange represents the Schmitt trigger output. The black dashed lines represent the high and low triggering voltages

Figure 7.4: Schmitt trigger topology and output waveform.

RV1, see Figure 7.4a.

The response of the Schmitt trigger is illustrated in Figure 7.4b. The blanking signal is pulled low when stimulus is detected (when the rectifier output exceeds the high trigger threshold). The blanking signal will return high once the rectifier output falls below the lower threshold. The red shaded section in Figure 7.4b represents the hysteresis region of the Schmitt trigger, which is useful for avoiding output jitter. The Schmitt trigger output passes through a voltage divider (R19, R20) to shift the output level to the +3.3V pulse extender and switching logic levels. The Schmitt trigger output signal is fed as a blanking signal for the EMG recording channel, see Section 7.3.5

Pulse Extender (U5: LTC6994)

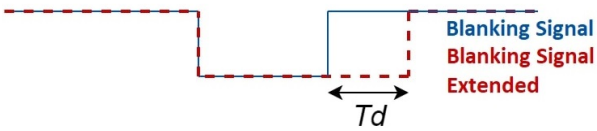

Figure 7.5: Delay block output: Blue line represents Schmitt trigger output. Red dashed line represents the delay block output. Td is the delay time, adjustable from 512us to 8ms

A programmable delay block is used to delay the rising edge of the Schmitt trigger signal by ~0.5-8 msec, Figure 7.5. The extended signal is used to alter the recording channel's AC-coupler time constant during stimulation. The extension time is set manually via trimmer potentiometer. More information is provided in Section 7.3.5.

7.3.5 EMG Recording Channel

The EMG recording channel is responsible for recording the user's volitional EMG. The channel contains elements for stimulation artefact suppression that are controlled by blanking signals, Section 7.3.4.

Pre-amplifier (U15: INA828)

The EMG recording pre-amplifier is similar to the artefact detection pre-amplifier, with modifications for stimulation artefact suppression. An overview of the pre-amplifier is depicted in Figure 7.6. Alterations to the detection pre-amplifier topology are highlighted by the orange-filled sections, U14 and U16.

The gain is nominally set to ~418 through an external 120Ω resistor (R24). DC electrode offset-voltages of up to ~36mV can be tolerated at this gain, before a DC offset is generated at the pre-amplifier output.

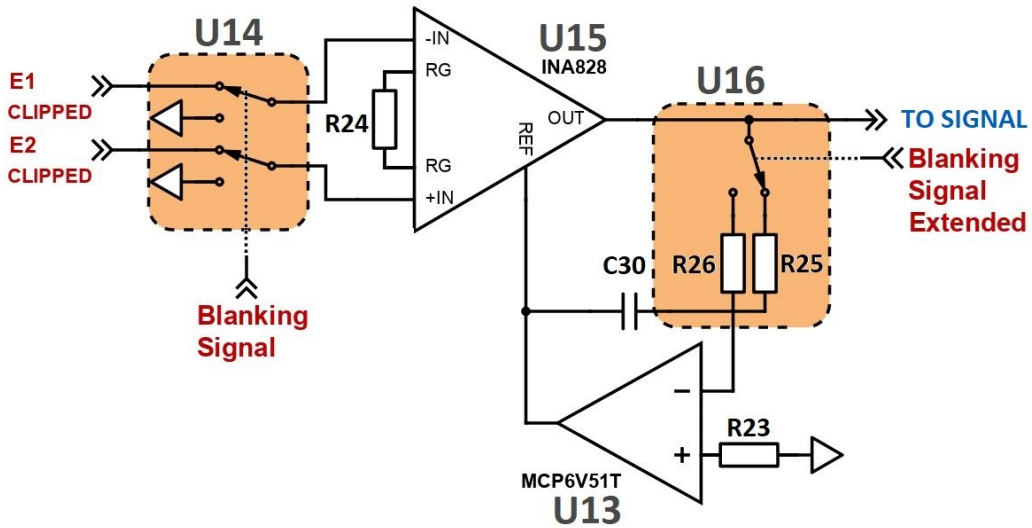

Figure 7.6: EMG recording pre-amplifier chain.

Artefact Suppression Hardware

Single-pole dual-throw switches, U14 and U16, are placed in the EMG recording pre-amplifier chain to suppress stimulation artefact, see Figure 7.6. The switches are controlled via the blanking signals generated by the artefact detection chain, Section 7.3.4.

Amplifier Input Blanking Switches (U14: TMUX6136)

The pre-amplifier can be easily saturated by stimulation artefacts, thus lengthening the recovery time in which volitional EMG cannot be measured (Chester & Durfee, 1997; Minzly, Mizrahi, Hakim, & Liberson, 1993). Switches U14, depicted in Figure 7.6 , are used to shunt the pre-amplifier inputs to ground during stimulation. The switches protect the pre-amplifier from the stimulation artefact pulses, and therefore allow higher pre-amplifier gains without output saturation. The TMUX6136 dual analog switch is chosen due to it's low leakage current (0.5pA), fast transition times (66ns), and low charge injection (-0.4pC).

The switch timing is determined by the detection-Schmitt trigger stage which outputs a blanking signal whenever the electrode differential voltage exceeds a set threshold, Section 7.3.4.

Integrator Time Constant Switch (U16: TMUX6119)

The isolated use of pre-amplifier input blanking can cause further artefacts to enter the system: a discharge curve is generated as the system exits the blanking phase, due to a sharp change in signal level, seen as a step by the system's filtering amplifiers (Brown et al., 2008; Megill et al., 1982; Taylor & Chappell, 2003).

In particular, the AC-coupler is of interest as it defines the high-pass characteristics of the pre-amplifier. When recording with no stimulation present,the AC coupler is configured to have a 20Hz corner frequency. In this configuration, the AC coupler will remove DC offset and movement artefacts; however, the low corner frequency will introduce a slow exponential tail in response to a step input or impulse.

Switch U16, depicted in Figure 7.6, is used to switch the AC coupler time-constant, giving

it an approximate ~10kHz low-pass corner frequency. Essentially, the AC-coupler will track the output of the pre-amplifier and feed it back into the reference pin, giving the pre-amplifier fast recovery from step input or impulse. The TMUX6119 analog switch is chosen, again for low leakage currents (0.5pA), low charge injection (0.19pC), and fast transition times (68ns).

An extended blanking signal (see Section 7.3.4) is used to control switch U16. As the extended signal is used, the AC-coupler can absorb the voltage step and transients as pre-amplifier blanking finishes.

7.4 Residual Artefact Suppression

Conventional digital filtering techniques such as a comb or high-pass filter can be applied to isolate the residual artefact (RA) from volitional EMG. However, these techniques are often unreliable due to non-stationary nature of the artefact, as well as the temporal and spectral overlap between artefact and volitional EMG (vEMG) (Al-ani et al., 2011; Heffer & Fallon, 2008). Alternative techniques such as wavelet analysis and adaptive filtering have been successfully applied as they are more able to represent the non-stationary nature of the RA (Ambrosini et al., 2012; Osuagwu et al., 2020).

7.4.1 Algorithm

The adaptive filter developed by Sennels et al. is implemented in this work to isolate the vEMG from the RA (Sennels et al., 1996). The filter estimates the artefact as a weighted combination of EMG recordings over a number of previous stimulation frames, equation 8.1.

$$RA(n) = \sum_{i=1}^{M} b_i \; EMG(n - iL) \quad , n \in [1, L] \tag{7.1}$$

Where L is the amount of EMG samples in one stimulation period, M is the number of previous stimulation frames (filter order), and b are the adaptive filter coefficients. Filter

weightings are least-square optimised to minimise the energy of the present frame. This assumes that vEMG can be modelled as band-limited Gaussian noise de Luca (1979). For more information, see Sennels et al. (Sennels et al., 1996).

To obtain an estimate of vEMG, the adaptive filter output is simply subtracted from the raw EMG signal, Eqn. 7.2.

$$vEMG = EMG - RA \tag{7.2}$$

7.4.2 Choice of filter order

In choosing the filter order there is a trade-off between achieving sufficient artefact suppression, having a non-critical time delay, and avoiding elimination of vEMG (Sennels et al., 1996). In order to examine this effect we compare the vEMG extraction under filter orders of one, three, and six, Figure 7.7 The vEMG extraction is performed on one subject's dataset during stimulation, obtained during common-electrode experimental testing, Section 7.5.

Figure 7.7a and Figure 7.7b shows the raw EMG recording and the corresponding signal spectra, respectively. No control signal can be obtained from the raw EMG and the underlying vEMG spectra is contaminated with large 25Hz harmonic artefacts. Figure 7.7c and Figure 7.7d depict the vEMG estimate from a first order adaptive filter and the corresponding spectra, respectively. From Figure 7.7c the subject's volitional intent is more apparent than from the raw EMG, albeit with a noisy baseline. It can be seen in Figure 7.7d that the 25Hz harmonics have been removed. However, the filter appears to distort the amplitude of the spectra, almost doubling the amplitude of the underlying vEMG from Figure 7.7b.

As the filter order increases, the power reduction between the raw EMG and the vEMG estimate also increases. This can be observed through Figures 7.7c, 7.7e, and 7.7g, where

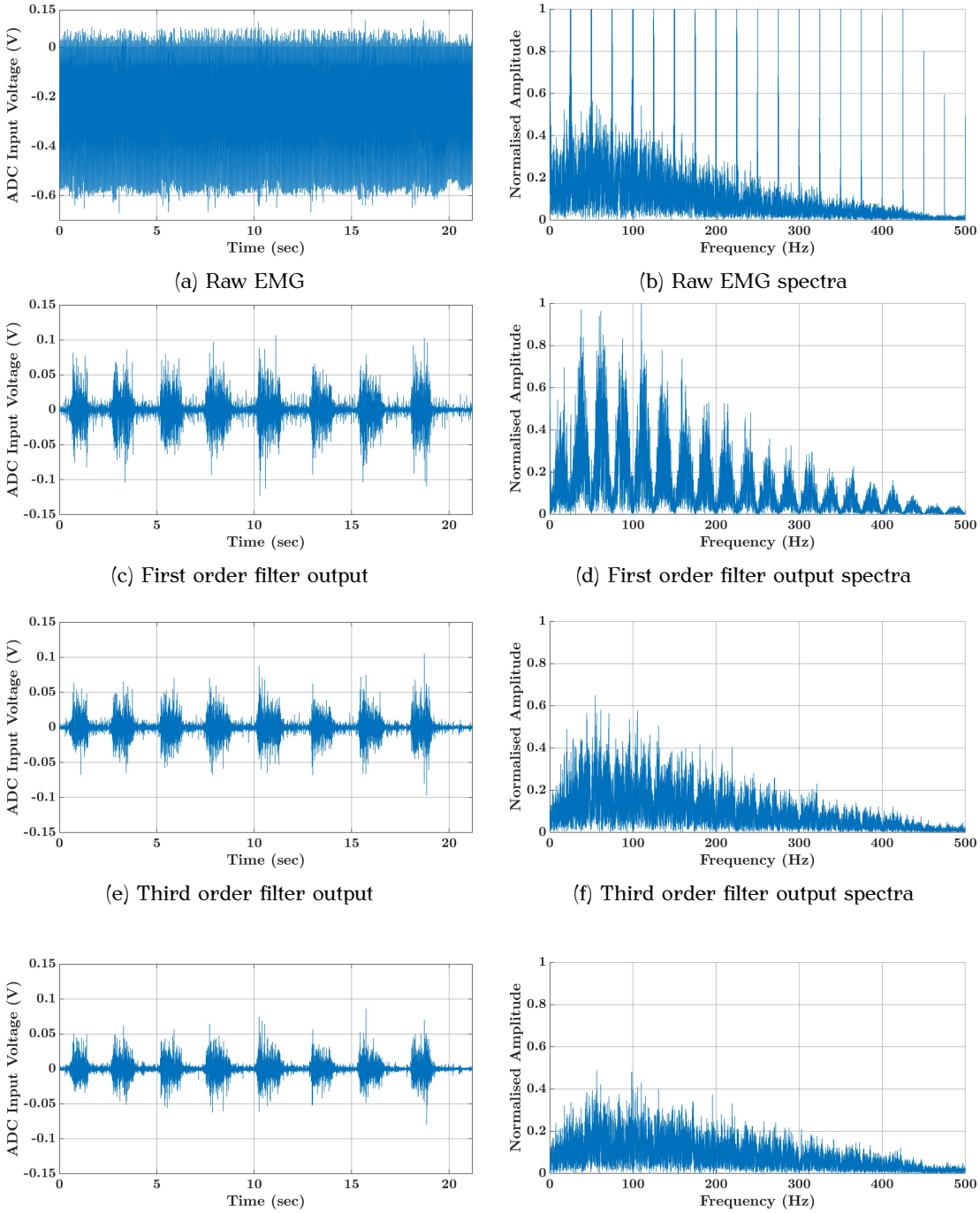

(a) Raw EMG

(b) Raw EMG spectra

(c) First order filter output

(d) First order filter output spectra

(e) Third order filter output

(f) Third order filter output spectra

(g) Sixth order filter output

(h) Sixth order filter output spectra

Figure 7.7: Raw EMG recording and corresponding spectra (a,b). vEMG estimate and corresponding spectra from adaptive filters of order one (c,d), three (e,f), and six (g,h).

an increase in filter order results in a cleaner baseline signal. However, the amplitude of the vEMG estimate during contractions also decreases. This is due to the assumption that vEMG can be characterised as band-limited Gaussian noise. The filter will adapt to any

cross-correlation between the vEMG in the present frame and the vEMG in any other filter frames (Sennels et al., 1996). As the number of filter frames increases, the cross-correlation is also likely to increase. This effect can also be observed through the decrease in amplitude from signal spectra in Figure 7.7f to the spectra in Figure 7.7h.

The choice of filter order is dependant on the intended application for the vEMG estimate. Towards control applications it is important that the RA is not mistaken for vEMG. A clean signal baseline can also improve the robustness of control thresholds. Therefore, higher filter orders may be preferable for control purposes. This finding is consistent with Sennels et al. and other authors who use a sixth-order adaptive filter towards stimulation control (Ambrosini et al., 2012; Osuagwu et al., 2020; Sennels et al., 1996). For vEMG spectra based applications such as fatigue and muscular torque estimation, a lower-order filter may be more appropriate. From visual inspection of Figure 7.7f and Figure 7.7h, the third-order filter's vEMG spectra achieves a good trade-off between maintaining the underlying vEMG signal and removing stimulation artefacts, Figure 7.7b.

7.5 Experimental Testing

This study was approved by the Human Ethics Committee, University of Canterbury (HEC2020/68) and informed consent was obtained from each participant prior to the experiments. The EMG device was tested under two conditions. Firstly, separate electrodes were used for EMG recording and FES delivery. Four able-bodied male individuals, aged 25-26 years, participated in this trial. The second experiment involves the use of common electrodes for both devices. Five able-bodied subjects participated in the trial, aged 25-27. The subjects were four male and one female.

7.5.1 Instrumentation

The instrumentation used during testing includes the presented stimulus resistant EMG design and the constant current (CC) stimulator detailed in Chapter 6. The EMG recording

device samples at 1kHz through an on-board 12-bit ADC and possesses band-pass characteristics of 20-480Hz. Pre-amplifier gains of 52dB and 41dB were utilised for the separate electrode and same electrode trials, respectively.

The CC stimulator provides biphasic stimulation with controllable pulse-width, frequency, and amplitude characteristics. Stimulation amplitude is controllable within $I \in [0, 30]$mA given a maximum voltage compliance of $\pm 40V$. When common electrodes are used for EMG recording and stimulation, a three millisecond electrode shorting period is introduced after each stimulus delivery. This shorting period is used to quickly discharge capacitive energy stored by the tissue.

7.5.2 Electrode Placement

Pre-gelled, conductive carbon-film surface electrodes were used throughout testing (Verity Medical, VS25). EMG was recorded through round 30mm diameter electrodes during both trials. Stimulation was delivered through the same electrodes or through separate 40mm x 40mm square electrodes. Figure 8.2 shows the electrode placements on the forearm.

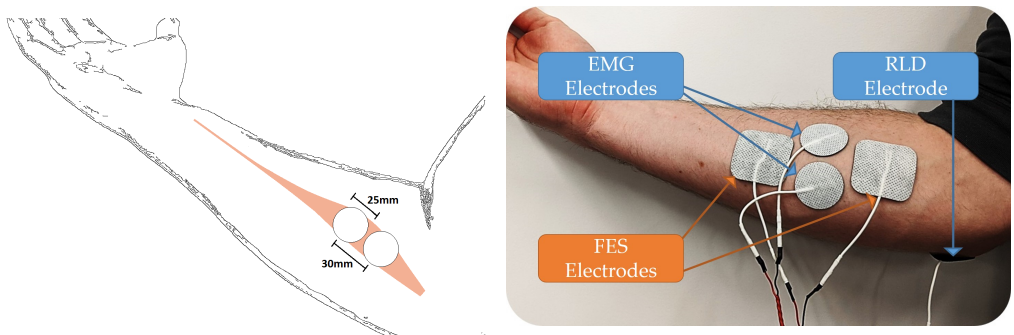

(a) Same electrode configuration: Round electrodes (30mm x 30mm) for stimulation and EMG are placed on the forearm longitudinally. The RLD electrode is placed on the elbow.

(b) Separate electrode configuration: Square stimulation electrodes (40mmx40mm) are placed on the forearm longitudinally, with round EMG electrodes (30mmx30mm) placed in-between. The RLD electrode is placed on the elbow.

Figure 7.8: Electrode configurations for separate electrode and same electrode trials.

In Figure 7.8a the same electrodes are used for recording and stimulation. The electrodes are placed longitudinally along the Flexor Carpi Radialis (FCR), with the RLD on the elbow.

In Figure 7.8b separate electrodes are used for recording and stimulation. The electrode configuration has the EMG electrodes perpendicular to the muscle fibre direction between the stimulation electrodes. As the EMG electrodes are perpendicular to the muscle fibre direction, there is slight reduction in EMG signal strength (Widjaja, Shee, Poignet, & Ang, 2009). However, the stimulation artefact and elicited EMG (eEMG) posses much higher common mode components and can be more easily rejected by the pre-amplifiers with this configuration (Frigo et al., 2000; Schauer, Seel, Bunt, Müller, & Moreno, 2016; D. Zhang & Ang, 2007). Additionally, the perpendicular orientation of the EMG electrodes creates a more compact configuration than if they were placed along the muscle fibre direction. This is especially useful when applied to small muscle groups such as the forearm.

7.5.3 Experimental Protocol

The same experimental protocol was followed for both trials. The subjects were seated with their elbow at a 90° angle and their forearm position neutral. Data was recorded as the subjects performed 80% maximum voluntary contractions of the wrist over twenty-second periods. Each dataset was collected with and without the presence of stimulation.

Stimulation was delivered with a fixed pulse-width of 300us and frequency of 25Hz. The stimulation amplitude was adjusted to a level that was comfortable for each subject and induced tetanic contraction of the wrist. These amplitudes were typically in the range $I \in [7.5, 10]$ mA.

7.5.4 Data Processing

Data were captured through the recording device presented with a sampling rate of 1kHz. For the estimation of vEMG under stimulation the adaptive algorithm described in Section 7.4 was utilised. The algorithm was implemented in real-time through the on-board microcontroller.

Further data processing used MATLAB (2019b, MathWorks). The frequency content of each signal was found by calculating the squared magnitude of the fast Fourier transform (FFT). Prior to FFT the signal mean was subtracted, followed by the application of a symmetric Hamming window and zero-padding with a factor of eight (Chester & Durfee, 1997). Power spectral density (PSD) estimates were produced using Welch's averaged modified periodogram method (Stoica & Moses, 2005).

The median frequency (MDF) divides the power spectral density into two parts of equal powers (Mizrahi, Levin, Aviram, Isakov, & Susak, 1997), Eqn. 8.4.

$$\int_0^{MDF} PSD(f)\ df = \int_{MDF}^{\infty} PDF(f)\ df = \frac{1}{2}TSP \tag{7.3}$$

Where TSP is the total spectral power. The MDF for each PSD was calculated using the MATLAB function medfreq.

7.6 Results

7.6.1 Separate Electrodes

A selection of raw EMG data recordings are depicted in Figure 7.9. Figure 7.9a shows the device output signal for each subject over three contractions. Figure 7.9b shows segments of Figure 7.9a, corresponding to three stimulation periods (highlighted by the yellow shaded sections).

The adaptive filter (sixth order) proposed by Sennels et al (Sennels et al., 1996) was applied to the raw EMG data from Figure 7.9 to provide an estimate of the subject's vEMG. Figure 7.10 (top) depicts the raw EMG from one subject, superposed with their eEMG. Figure 7.10 (bottom) depicts the equivalent adaptive filter output, in which the subject's estimated eEMG artefact has been removed.

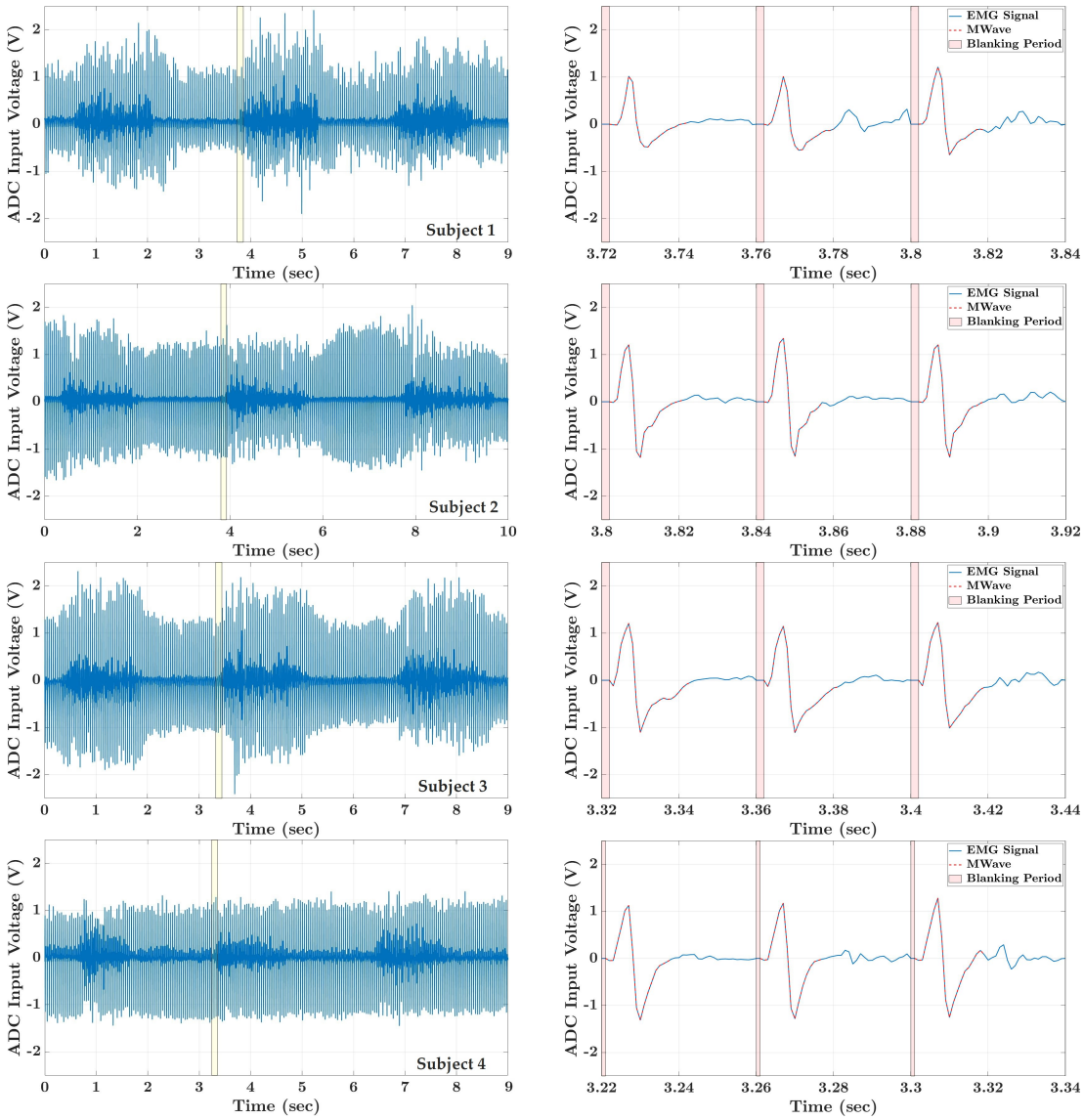

(a) Raw EMG recorded during stimulation

(b) Raw EMG over three stimulation cycles.

Figure 7.9: Raw EMG data recorded from four subjects with the separate electrode configuration. (a) EMG captured over three isotonic contractions. (b) Segments of the subject's data at the start of isotonic contraction, highlighted in yellow, spanning three stimulation periods.

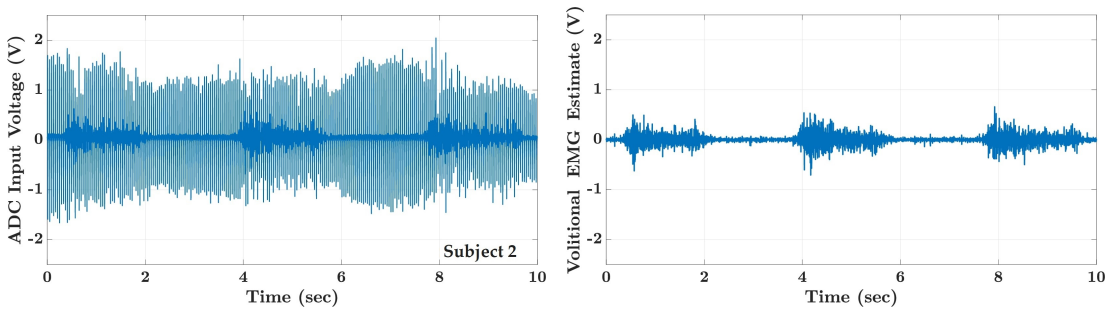

(a) EMG recorded during stimulation

(b) Adaptive filter vEMG estimate.

Figure 7.10: (a) Raw EMG recorded during stimulation for one subject. (b) Corresponding vEMG estimate using adaptive algorithm (Sennels et al., 1996) with six epochs.

Table 7.1: EMG blanking timings during separate electrode stimulation and recording

Blanking Durations				
	Subject 1	*Subject 2*	*Subject 3*	*Subject 4*
Min (ms)	2	2	2	2
Max (ms)	3	3	3	3

Table 7.1 details the system blanking durations when separate electrodes are used for stimulation and recording. The blanking durations are dictated by the output of the artefact detection channel and pulse extender, Figure 7.1.

7.6.2 Common Electrodes

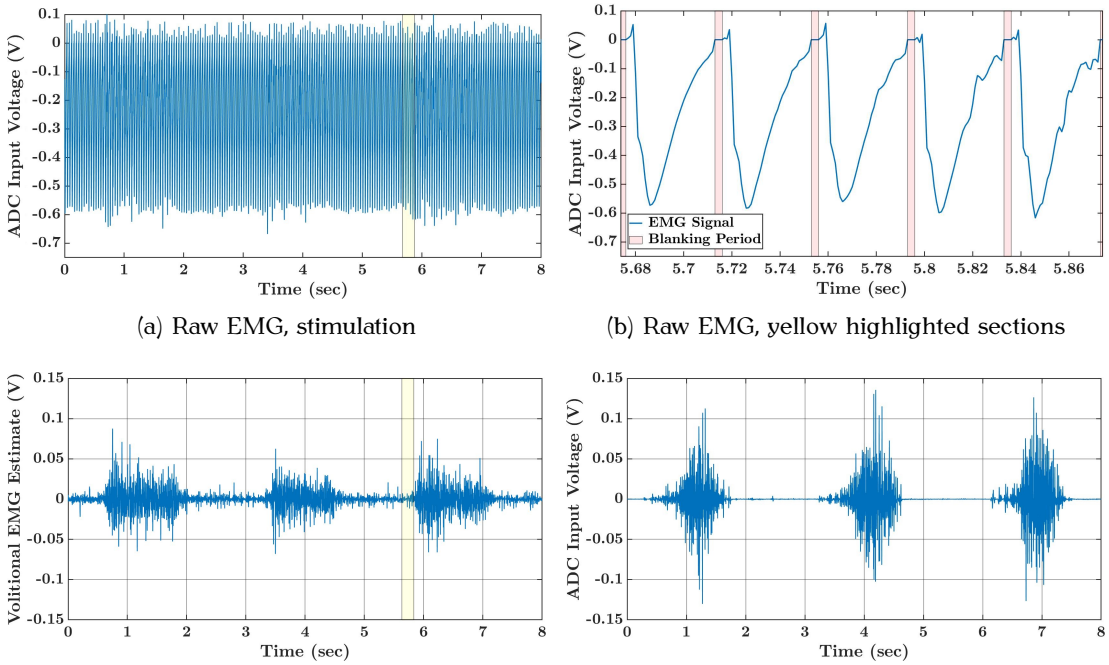

(a) Raw EMG, stimulation

(b) Raw EMG, yellow highlighted sections

(c) vEMG estimate

(d) Raw EMG, no stimulation

Figure 7.11: EMG data recorded through common stimulation and recording electrodes. (a) Raw EMG captured without stimulation present. (b) Raw EMG captured during stimulation. (c) A selection of raw EMG corresponding to yellow highlighted sections in (b,d). Red highlighted sections indicate the device's blanking periods. (d) Estimate of vEMG using a third-order adaptive filter with signal (b,c) as the input.

A selection of data recorded through common stimulation and recording electrodes is shown in Figure 7.11. Figure 7.11d depicts the raw EMG recorded over three contractions, without any stimulation present. Figure 7.11a shows the raw EMG recorded with stimulation present, and Figure 7.11c shows the corresponding vEMG estimate using a third-order adaptive filter, Section 7.4. An excerpt of the raw EMG over five stimulation

periods is shown in Figure 7.11b. This selection corresponds to the yellow highlighted sections in Figures 7.11a and 7.11c. The system's blanking durations are detailed in Table 7.2 for the common electrode trials.

Table 7.2: EMG blanking timings during same electrode stimulation and recording

Blanking Durations					
	Subject 1	*Subject 2*	*Subject 3*	*Subject 4*	*Subject 5*
Min (ms)	5	4	3	4	3
Max (ms)	5	4	4	4	4

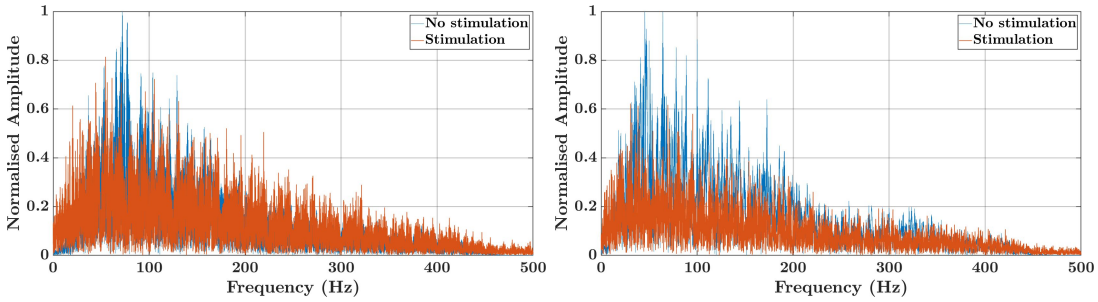

(a) Subject 1: vEMG spectra.

(b) Subject 2: vEMG spectra.

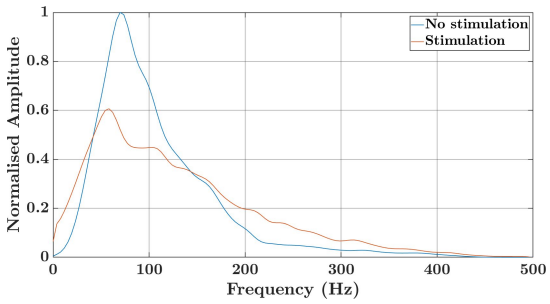

(c) Subject 1: vEMG Welch PSD estimate.

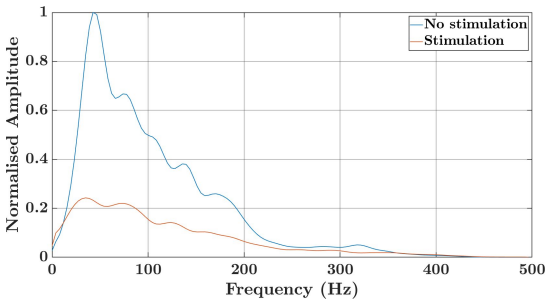

(d) Subject 2: vEMG Welch PSD estimate.

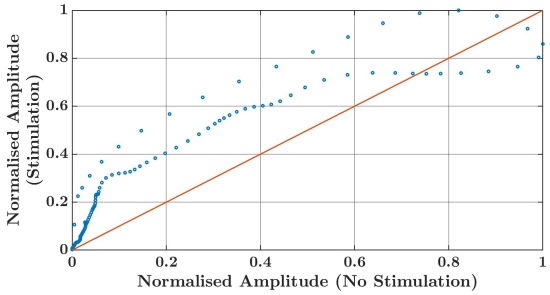

(e) Subject 1: Normalised vEMG PSD without stimulation against PSD during stimulation.

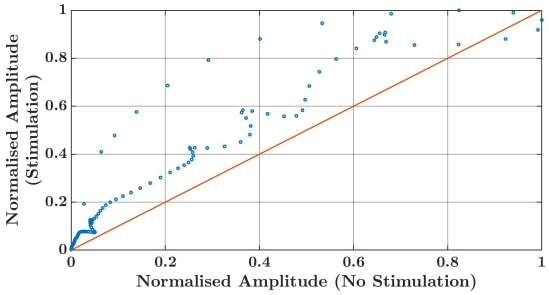

(f) Subject 2: Normalised vEMG PSD without stimulation against PSD during stimulation.

Figure 7.12: Comparison between the vEMG without stimulation and the vEMG estimates during stimulation, for Subjects one and two. For Figures (a,b,c,d) the blue waveforms represent vEMG spectra or PSD without stimulation and the orange waveforms represent the vEMG spectra or PSD with stimulation present. (e,f) Normalised PSD for vEMG under no stimulation and the normalised PSD of vEMG estimates under stimulation

For comparison between the vEMG without stimulation and the 3rd order adaptive filter vEMG estimates during stimulation, the signal spectra, PSD, and MDF are calculated, as detailed in Section 7.5.4. Figure 7.12a and 7.12b show the signal spectra for Subjects One and Two, respectively. Figures 7.12c and 7.12d show the equivalent Welch PSD. The blue waveforms represent the spectra or PSD of the vEMG without stimulation and the orange waveforms represent the spectra or PSD of the vEMG estimates under stimulation. Figures 7.12e and 7.12f provide comparison between the normalised PSD with and without stimulation.

Table 7.3: Pearson's correlation coefficient (R) and the MDF difference between subjects' vEMG PSD (no stimulation) and vEMG estimate PSD (stimulation).

Subject	***1***	***2***	***3***	***4***	***5***
R	0.95	0.92	0.93	0.93	0.84
Raw vEMG PSD MDF(Hz)	84.2	91.6	115.8	85.6	85.5
Estimate vEMG PSD MDF(Hz)	75.5	103.7	118.5	101.7	109.1
$\triangle$*MDF(Hz)*	-8.7	12.1	2.7	16.1	23.6

For each subject the similarity between PSDs for stimulation and no-stimulation data-sets is quantified using Pearson's correlation coefficient and the difference between their MDF, Table 7.3.

7.7 Discussion

Experimental testing of the EMG device was conducted using separate electrode and common electrode configurations, Section 7.5. Under both conditions, the device demonstrated the ability to record EMG concurrently to stimulation without saturation. System blanking was based on the electrode potentials and had maximum durations of 3ms and 5ms for separate electrode and common electrode configurations, respectively. The RA waveforms superposed with vEMG are depicted in Figures 7.9b and 7.11b for separate and common electrode configurations, respectively. When EMG is recorded through separate electrodes the stimulation artefact is blanked and the subjects' eEMG is preserved. This can be useful for applications where the eEMG is commonly used such as monitoring of stimulation induced torque and fatigue. As can be seen in Figure 7.11b the subject's eEMG is lost when

using common electrodes, due to longer lasting stimulation artefacts. Alternative indicators of muscle fatigue and torque may need to be developed for common-electrode systems.

The predominant limitations of existing common electrode designs are their low pre-amplifier gains ($<$ 25dB) and the elevated cut-off frequencies of their high-pass filters ($>$ 170Hz), compared to devices using separate electrodes for stimulation and recording, see Section 4.3.1. The elevated cut-off frequencies prevent existing common electrode devices from sampling the dominant frequency range of the EMG spectra ($f \in [50, 150]$Hz). This may limit the designs to conventional control purposes as alternative applications, such as the assessment of muscle fatigue and analysis of motor-unit recruitment, often use EMG spectral-domain features (Phinyomark, Thongpanja, Hu, Phukpattaranont, & Limsakul, 2012). The design presented in this work utilises a minimum gain of 41dB and possesses band-pass characteristics of 20-480Hz. These attributes represent a 16dB increase in pre-amplifier gain and 150Hz more bandwidth within the usable energy of EMG. From Figure 7.12 it can be observed that the vEMG obtained from the device, both with and without stimulation, possess energy content throughout the typical EMG spectral range. The device's potential applications may extend past vEMG-based control tasks due to its higher preservation of vEMG energy and therefore access to more information of the muscles' state.

The PSD amplitudes of vEMG estimates during stimulation are smaller than the equivalent amplitudes for vEMG recordings without stimulation, Figure 7.12. A number of factors may contribute to this effect such as the vEMG power reduction caused by the adaptive filter, discussed in Section 7.4, or the inhibition of vEMG caused by the stimulation current (Taylor & Chappell, 2003, 2004). Discrepancy also lies between the subjects' normalised PSD amplitudes during stimulation. For instance, the maximum normalised PSD amplitudes during stimulation are ~0.6 (Figure 7.12c) and ~0.2 (Figure 7.12d) for Subject 1 and Subject 2 respectively. These discrepancies may be explained by the subjects' ability to perform

80% maximum volitional contraction (MVC) under stimulation and the differing levels of stimulation applied. Subject 2 reported difficulty in performing voluntary contractions under stimulation, leading to a reduction of vEMG power during the stimulation protocol.

Despite the evident power reduction between the PSD without stimulation and the PSD during stimulation, the shape of the PSD are similar. The shape of the PSD is important as it strongly influences frequency-based metrics, such as the MDF, which are used for muscle-state assessments. The PSD collected from Subject 5 show the weakest correlation with a Pearson's correlation coefficient of 0.84, Table 7.3. The spectra collected from Subjects 1-4 all result in Pearson's correlation coefficients greater than 0.92. The EMG device presented in this work can preserve the vEMG spectral waveform during same electrode stimulation and recording. This capability creates potential applications for the device beyond the vEMG-based stimulation that current same-electrode systems have implemented, such as the monitoring of fatigue and muscle coherence.

Stimulation-induced fatigue is usually monitored using the eEMG through separate stimulation and recording electrodes. In Chapter 8 and Chapter 9 the efficacy of eEMG-based fatigue metrics are investigated under these conditions, during dynamic movements with assist-as-need support. However, when using common-electrodes, assessment of the eEMG is not feasible due to longer lasting stimulation artefacts (Schauer, 2017). This can be observed in Figure 7.11b where the RA takes the form of a slow-decaying tail rather than a typical eEMG. An alternative option could be to monitor vEMG properties which have been used for fatigue estimation with no stimulation present. The MDF is an example of such a metric. The differences between MDF calculated for stimulation-free vEMG spectra and the vEMG spectra during stimulation are detailed in Table 7.3 for each subject. These differences range from 30Hz for Subject 5 to 6.9Hz for Subject 2. Further investigation into vEMG PSD fatigue metrics during stimulation is warranted, given the similarity between the PSD waveforms and MDF over stimulation and stimulation-free protocols.

7.8 Conclusion

Recording EMG of a stimulated muscle can prove particularly difficult due to large scale and long lasting stimulation-induced artefacts that can saturate measurements and damage system components. There are very few commercial sEMG devices that contain protection against large stimulation voltages or measures to reduce artefact transient times. Furthermore, most commercial or research level designs are not open source. In this manner the devices are effectively an inflexible black box to researchers and developers. Even fewer devices are designed for stimulation and recording through the same electrodes. These designs utilise elevated high-pass cut-off frequencies to provide fast suppression of artefact transients. However, in doing so the main energy spectrum of the EMG signal cannot be obtained.

This chapter has outlined a low part-cost (USD $145) open source EMG design that can record muscle bio-potentials concurrently to stimulation. The device was tested using both separate and common electrodes for recording and stimulation. Using the separate electrode configuration the system demonstrated suppression of the stimulation artefact whilst preserving the eEMG shape and vEMG. The device is applied towards vEMG stimulation control and fatigue estimation in Chapter 8 and Chapter 9 using the separate electrode configuration.

The device possesses band-pass characteristics that span the predominant usable energy of the EMG spectrum. This feature may allow applications beyond vEMG control in which the current same-electrode systems are limited. Under the common electrode configuration the device was able to preserve the vEMG spectra during stimulation. Correlation coefficients greater than 0.84 were identified between the normalised PSD of stimulation-free vEMG recordings and of vEMG estimates during stimulation, demonstrating that the frequency spectra were very similar. This gives confidence that the stimulation-artefact

suppression hardware and RA filtering processes are not distorting the underlying signal of interest, warranting further investigation into alternative vEMG applications during common electrode stimulation and recording.

CHAPTER 8

Muscular Fatigue

8.1 Introduction

Functional Electrical Stimulation (FES) is the application of electrical pulses which elicit muscle contractions towards a functional movement (McIlroy & Verrier, 2005). FES has been extensively applied as a modality for training and rehabilitation (Marchis, Monteiro, Simon-Martinez, Conforto, & Gharabaghi, 2016). Towards post-stroke rehabilitation, it is typically implemented to facilitate high-intensity functional training with the objective of enhancing motor recovery and promoting neural plasticity (Sheffler & Chae, 2007). Another use for FES is to prevent non-use muscle atrophy as it directly activates the muscles (Ha et al., 2016). However, health benefits obtained through FES evoked exercise are limited by rapid muscle fatigue (Ibitoye et al., 2016). The rate of muscle fatigue during FES driven contractions is greater than through voluntary contractions. A number of causes have been identified such as simultaneous stimulation of motor units, and unnatural motor unit recruitment order (Doucet et al., 2012). The assessment and management of muscular fatigue is therefore crucial for the development of more effective rehabilitation strategies.

Muscular fatigue is often assessed using electromyography (EMG) (Shair et al., 2017). To assess stimulation-induced fatigue, changes of the elicited EMG (eEMG) properties are particularly useful, see Chapter 4. Such changes include the increase of eEMG amplitude features as well as the decrease of spectral features (Merletti & Farina, 2016a). Typical eEMG amplitude indices include the peak-to-peak amplitude (PTP), root mean square (RMS), and mean absolute value (MAV) (Tepavac & Schwirtlich, 1997). The eEMG spectra median frequency (MDF) and mean frequency (MNF) are commonly used as spectral indices.

Most studies of functional electrical stimulation (FES) evoked fatigue are performed during constant stimulation periods and under isometric conditions. Studies performed during intermittent stimulation and dynamic movements reflect more of a practical rehabilitation setting. However, the stimulation trains delivered in these studies have fixed timings regardless of the subject's volitional intent. Integration of volitional intent into rehabilitation practices can heighten patient engagement, leading to enhanced therapeutic outcomes. The purpose of this study is to investigate whether the eEMG can be used as an indicator of fatigue during volitional EMG (vEMG) based stimulation. In particular, the eEMG is monitored during dynamic flexion of the wrist, elicited by vEMG controlled stimulation.

8.2 Methods

Five healthy individuals participated in this study. The subjects were four male and one female. This study was approved by the Human Ethics Committee, University of Canterbury (HEC2020/68).

8.2.1 Instrumentation

Instrumentation used throughout this trial include a stimulator and an EMG recording device. Both devices are applied through pre-gelled, conductive carbon-film surface elec-

trodes (Verity Medical, VS25). The stimulation electrodes are square, 40mm by 40mm in dimension. The EMG and RLD electrodes are round, 30mm by 30mm.

Biphasic electrical stimulation was provided by a constant current stimulator with controllable frequency, pulse-width, and amplitude characteristics. The stimulator can deliver current of $I \in [0, 30]$ mA and has a maximum compliance voltage of ± 40 V. For the purposes of this study, stimulation frequency was fixed at 25Hz.

The main difficulty in recording EMG from stimulated muscle are the large-scale stimulation artefacts that can damage system componentry and corrupt the EMG signal. A stimulation resistant EMG amplifier device is used to obtain readings for the eEMG and vEMG (McKenzie et al., 2021), Chapter 7. The design utilises input blanking and a non-linear feedback stage to minimise stimulation artefact transients. A right-leg driver circuit is used to reduce common-mode interference. The device has bandpass characteristics of 20-480Hz and is sampled at 1kHz. A typical output waveform over three stimulation cycles is shown in Figure 8.1. Note that the vEMG and eEMG are present but the stimulation artefact has been blanked.

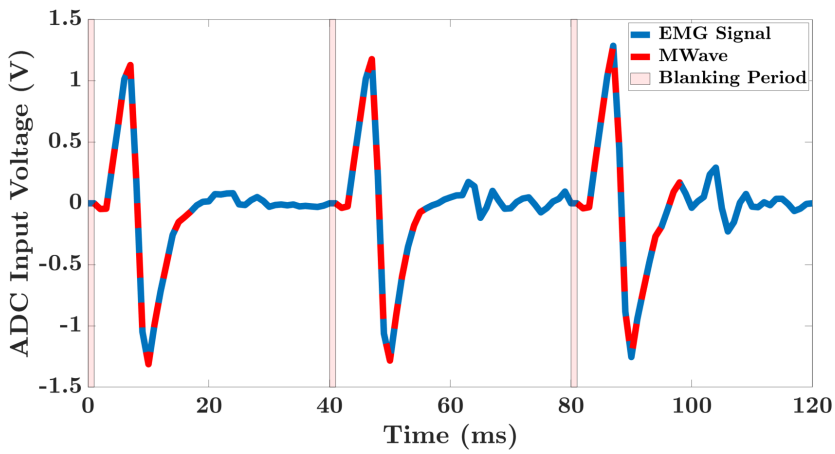

Figure 8.1: Typical EMG output waveform over three stimulation cycles.

8.2.2 Experimental protocol

Stimulation and EMG electrodes are placed on the forearm of each subject, Figure 8.2. The EMG electrodes are placed between the stimulation electrodes, perpendicular to the muscle fibre direction. In this configuration the sizes of the stimulation artefact and eEMG are reduced (D. Zhang & Ang, 2007). In addition to this, the perpendicular arrangement of the electrodes may help to minimise the effects of dynamic wrist movements, as the shift of muscle under the skin will be common to both electrodes. No skin-preparation or shaving was done prior to the electrode placement.

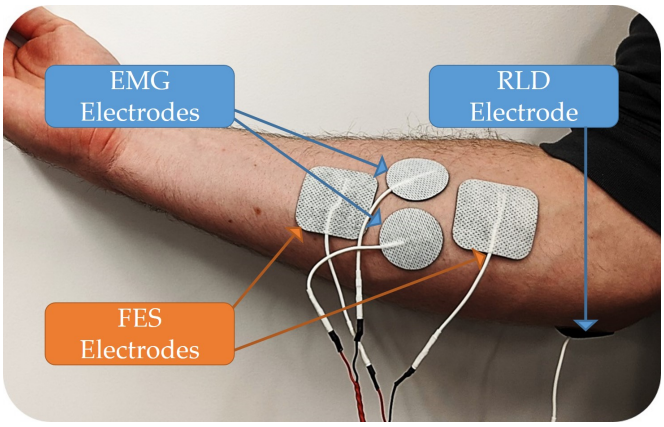

Figure 8.2: Electrode configuration: Stimulation electrodes (40mm x 40mm) are placed on the forearm longitudinally. Round EMG electrodes (30mm x 30mm) are placed perpendicular to the muscle fibres between the stimulation electrodes. The RLD electrode is placed on the elbow.

Subjects were given ten minutes to familiarise themselves with the sensation of electrical stimulation (Chester & Durfee, 1997). Following this period, two experimental protocols were implemented. During the protocols, subjects were seated upright with their elbow at a 90° angle and their forearm in a neutral position. The stimulation amplitude was adjusted to a level that provided tetanic contaction and was comfortable for each subject. This amplitude was typically in the range of $I \in [7.5, 10]$mA. Pulse-width and frequency parameters were fixed at 300us and 25Hz repectively.

Isometric Constant Stimulation

During this protocol, constant stimulation was delivered. The subjects were instructed to relax and to allow the stimulation to elicit wrist flexion. The wrist was held in the flexed position until the subject reported that their arm felt fatigued or the stimulation became uncomfortable. As the wrist was held in the flexed position for the entirety of this trial, we consider the contraction to be isometric.

vEMG Control

During this protocol, trains of stimulation were delivered. Stimulation train durations and the intervals between trains were dictated by the subjects' vEMG. The stimulation control follows a dual-threshold control system(Ambrosini et al., 2014), based on a volitional intent metric (vINT). vINT is calculated from measured vEMG using the process outlined in the EMG data processing section.

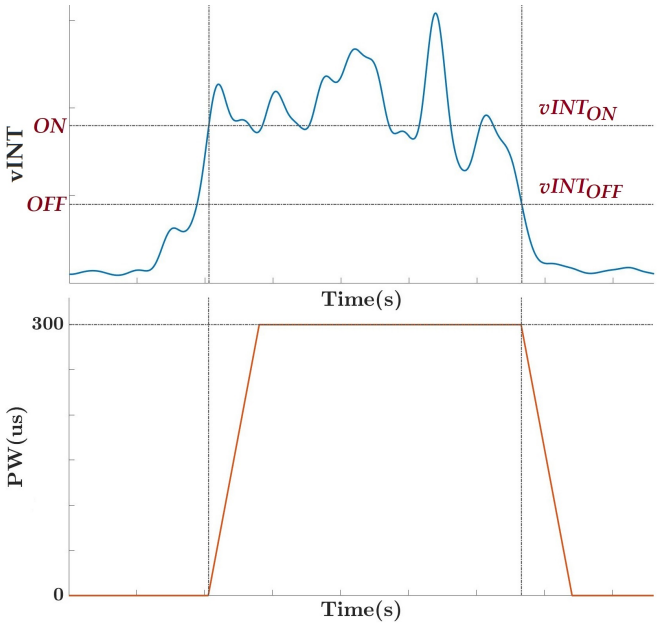

Figure 8.3: Overview of the vEMG based control method used. When the vInt rises above the threshold $vINT_{ON}$, the stimulation PW is ramped up to 300us. When the vInt falls below $vINT_{OFF}$, the PW is ramped down again.

An overview of the control is depicted in Figure 8.3. When the vInt estimate exceeds the threshold $vINT_{ON}$ the pulse-width is ramped up to 300us. The pulse-width is held at 300us

until the vInt drops below $vINT_{OFF}$. The thresholds $vINT_{ON}$ and $vINT_{OFF}$ were subject specific.

8.2.3 EMG data processing

Several EMG data processing stages were needed in order to generate the stimulation control signals and to generate the fatigue indices investigated.

Estimation of vEMG, eEMG, and vINT

The raw EMG is comprised of a superposition of the eEMG and vEMG, Figure 8.1. It is assumed the vEMG can be modelled as band-limited Gaussian noise (de Luca, 1979). An adaptive filter was used to isolate the eEMG and vEMG components (Sennels, Biering-Sorensen, Andersen, & Hansen, 1997). The filter estimates eEMG as a linear combination of EMG recordings over a number of previous stimulation frames. In accordance with (Sennels et al., 1997), a filter length of six epochs was applied, Equation 8.1.

$$eEMG(n) = \sum_{i=1}^{6} b_i \; EMG(n - iL) \quad , n \in [1, L] \tag{8.1}$$

Where L is the amount of EMG samples in one stimulation period and b are the adaptive filter coefficients. With a stimulation frequency of 25Hz, there are 40 samples in each period.

To obtain an estimate of vEMG, the adaptive filter output is simply subtracted from the raw EMG signal. vINT is calculated from vEMG using a moving average filter, Equation 8.2.

$$\begin{aligned} vEMG &= EMG - eEMG \\ vINT &= \frac{1}{N} \sum_{i=1}^{N} vEMG_{RMS}(i) \end{aligned} \tag{8.2}$$

Where N is the filter size (corresponding to the amount of stimulation periods) and $vEMG_{RMS}$ is the RMS value of the last 20 vEMG samples per stimulation period.

Fatigue Indices

For the purposes of this study, the PTP amplitude and MDF of each eEMG were monitored. Calculation for the eEMG PTP follows Equation 8.3

$$PTP = eEMG_{MAX} - eEMG_{MIN} \tag{8.3}$$

Where $eEMG_{MAX}$ is the eEMG maxima and $eEMG_{MIN}$ is the eEMG minima.

The MDF divides the power spectral density into two parts of equal powers (Mizrahi et al., 1997), Equation 8.4.

$$\int_0^{MDF} PSD(f)\ df = \int_{MDF}^{\infty} PDF(f)\ df = \frac{1}{2}TSP \tag{8.4}$$

Where power spectral density (PSD) is the power spectral density and TSP is the total spectral power. The frequency content of each eEMG segment is found by calculating the squared magnitude of the Fast Fourier Transform (FFT). Prior to FFT the eEMG's mean is subtracted, followed by the application of a Hamming window and zero-padding to N samples (Chester & Durfee, 1997).

Under the constant stimulation trials, the PTP amplitudes and the FFT specra were averaged over epochs of ten eEMGs (Mizrahi et al., 1997). Under the vEMG control trials, the PTP amplitudes and the FFT spectra were averaged over epochs of two contraction sets

(stimulation pulse trains). This averaging was used to mitigate the effects of intermittent stimulation and changing muscle length (Chen & Yu, 1997).

8.3 Results

The MDF and PTP amplitudes are collected from each subject during isometric constant stimulation and vEMG control protocols. For each dataset a line of best fit is applied, Equation 8.5.

$$y = \alpha X + \beta \tag{8.5}$$

Where y represents either the MDF or the PTP amplitudes, α represents the gradient of the linear fit, and β represents the y-axis intercept. For the constant stimulation datasets X represents the elapsed time in seconds. For the vEMG control datasets, the stimulation periods are intermittent and are reliant on the subject's volitional intent. Therefore the number of contractions is considered a more suitable X axis than elapsed time. The gradient α and coefficient of determination R^2 are recorded for each linear fit as these metrics give an indicator of the general trend and of the goodness-of-fit, respectively.

8.3.1 Isometric Constant Stimulation

A typical eEMG waveform during approximately one minute of constant stimulation is shown in Figure 8.4a. This particular waveform was captured from Subject 2. The corresponding MDF and PTP amplitudes with their linear estimates are shown in Figure 8.4b. Figure 8.4c shows the MDF and PTP amplitudes of Subject 4, where the PTP waveform behaves unexpectedly.

Table 8.1 details the α and R^2 for each subject's MDF during constant stimulation. Table 8.2 details the corresponding α and R^2 for the PTP amplitude. Note that the gradients for MDF and PTP are in $Hz \cdot s^{-1}$ and $V \cdot s^{-1}$ respectively.

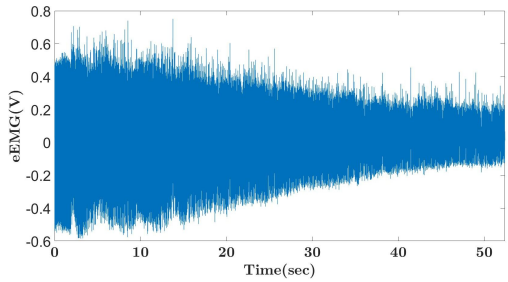

(a) eEMG waveform from Subject 2 during 60 seconds of constant stimulation.

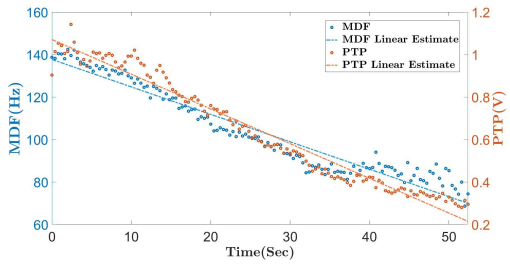

(b) MDF and PTP amplitudes calculated from Subject 2 during 60 seconds of constant stimulation.

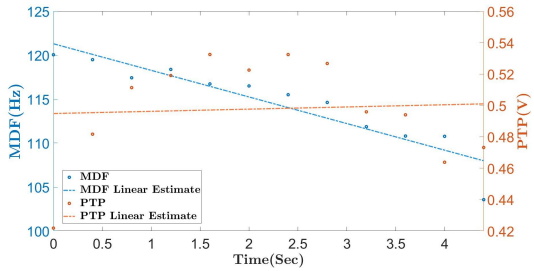

(c) MDF and PTP amplitudes calculated from Subject 4 during four seconds of constant stimulation.

Figure 8.4: Typical eEMG waveforms captured, as well as MDF and aPTP amplitudes calculated during isometric constant stimulation.

Table 8.1: Gradient (α) and coefficient of determination (R^2) for each subject's MDF linear fit during constant stimulation.

Subject	***1***	***2***	***3***	***4***	***5***
α $(Hz \cdot s^{-1})$	-1.90	-1.30	-2.70	-3.00	-3.60
R^2	0.96	0.93	0.98	0.87	0.98

Table 8.2: Gradient (α) and coefficient of determination (R^2) for each subject's PTP linear fit during constant stimulation.

Subject	***1***	***2***	***3***	***4***	***5***
α $(V \cdot s^{-1})$	-0.014	-0.016	-0.016	0.0014	-0.013
R^2	0.83	0.96	0.95	0.0036	0.83

8.3.2 vEMG Control

A typical eEMG waveform during intermittent vEMG controlled stimulation is depicted in Figure 8.5a. The figure represents four wrist contractions from Subject 1. Figure 8.5b depicts the MDF and PTP amplitudes calculated per contraction set for Subject 3. This dataset represents the highest MDF and lowest PTP linear correlations. Figure 8.5c depicts the MDF and PTP amplitudes calculated for Subject 5, where the MDF linear fit has the lowest R^2 value of all the subjects.

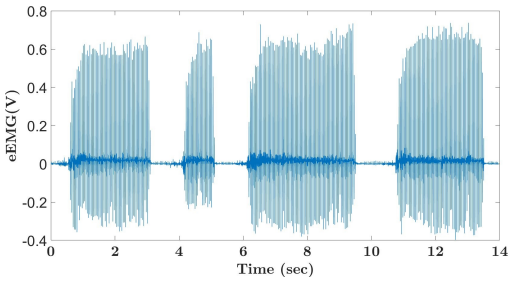

(a) eEMG waveform captured from Subject 2 during vEMG controlled stimulation coinciding with four contractions.

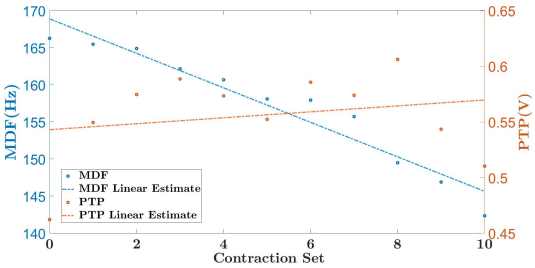

(b) MDF and PTP amplitudes calculated from Subject 3 per contraction set.

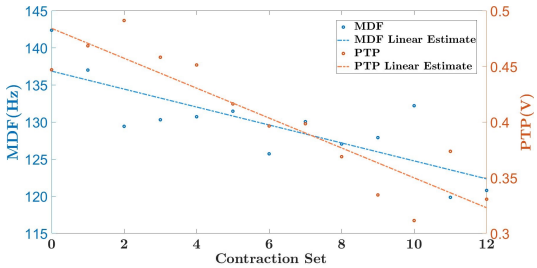

(c) MDF and PTP amplitudes calculated from Subject 5 per contraction set.

Figure 8.5: Typical eEMG waveforms captured, as well as MDF and aPTP amplitudes calculated during vEMG controlled stimulation.

Table 8.3: Gradient (α) and coefficient of determination (R^2) for each subject's MDF linear fit during vEMG controlled stimulation.

Subject	***1***	***2***	***3***	***4***	***5***
α $(Hz \cdot Cont^{-1})$	-3.30	-9.00	-5.80	-2.40	-3.00
R^2	0.83	0.90	0.93	0.89	0.62

Table 8.4: Gradient (α) and coefficient of determination (R^2) for each subject's PTP linear fit during vEMG controlled stimulation.

Subject	***1***	***2***	***3***	***4***	***5***
α $(V \cdot Cont^{-1})$	0.0070	-0.019	0.0027	-0.0091	-0.013
R^2	0.17	0.35	0.047	0.63	0.82

For each subject α and R^2 of the MDF and PTP linear fits are calculated. Table 8.3 details the α and R^2 for each subject's MDF during vEMG controlled stimulation. Table 8.4 details the corresponding α and R^2 for the PTP amplitude. Note that the gradients for MDF and PTP now are in $Hz \cdot Cont^{-1}$ and $V \cdot Cont^{-1}$ respectively.

8.4 Discussion

During isometric contractions under constant stimulation, the MDF and PTP fatigue indices exhibited negative gradients in the ranges -1.3 $Hz \cdot s^{-1}$ to -3.6 $Hz \cdot s^{-1}$ and -0.013 $V \cdot s^{-1}$ to -0.016 $V \cdot s^{-1}$ respectively. This trend is consistent with previous studies (Chester & Durfee, 1997; Tepavac & Schwirtlich, 1997), Tables 8.1 and 8.2. Linear regression fits were able to capture the general fatigue trend in both MDF and PTP datasets, most with R^2 values greater than 0.8. Linear estimation is the simplest approach to observe a general fatigue trend. However, if higher accuracy is required curvilinear fitting functions such as a hyperbolic or exponential fit may be more suitable to capture the indices' decay waveform (Chen & Yu, 1997; Yu et al., 1999). For example, a curvilinear function would be better able to capture the end of the waveform in Figure 8.4b where the MDF and PTP level out.

During the vEMG control trials, the MDF possessed a negative gradient for each subject in the range -2.4 $Hz \cdot Cont^{-1}$ to -9.0 $Hz \cdot Cont^{-1}$, Table 8.3. Linear regression fits were able to capture the fatigue trends in these datasets. The R^2 values for subjects 1-4 were all upwards of 0.83. The lowest MDF R^2 value was 0.62 for Subject 5. However, observing Figure 8.5c a general fatigue relationship can still be obtained. Compared to the MDF, trends in the PTP amplitude data are not as evident. The PTP linear fits show inconsistent gradients, with subjects 1 and 3 displaying positive gradients in the range 0.0027 $V \cdot Cont^{-1}$ to 0.0070 $V \cdot Cont^{-1}$ and subjects 2,4, and 5 displaying negative gradients in the range -0.0091 $V \cdot Cont^{-1}$ to -0.019 $V \cdot Cont^{-1}$. Low R^2 values for subjects 1, 2, and 3 demonstrates poor correlation between the PTP amplitudes and number of contractions, Table 8.4. Figure 8.5b depicts this effect where there is a large spread of data about the PTP linear fit. The corresponding R^2 value for Figure 8.5b is 0.047. These findings are similar to Miura et al. who found the PTP amplitude of single-pulse eEMGs to be insufficient for the detection of muscle fatigue (Miura & Watanabe, 2016). The intervals between contractions allow for recovery of eEMG variables and are thought to be the cause of this inability (Estigoni et

al., 2014, 2011). Recovery intervals have been found to have less of an impact on frequency based indices than amplitude indices (Yochum, Bakir, Lepers, & Binczak, 2012). This may be the reason why clear trends were identified for the MDF index and not the PTP index.

EMG based fatigue measures have been researched under a range of different conditions, including isometric and dynamic contractions during continuous or intermittent stimulation. Most studies appear to focus on spinal chord injury (SCI) patients, delivering stimulus trains of fixed amplitude and timings rather than vEMG based protocols. The reasoning behind this may be due to the patient's limited residual vEMG capabilities. Another reason may be the variability in fatigue indices caused by vEMG (Chester & Durfee, 1997). This effect is especially pronounced in healthy subjects with unhindered vEMG. If a patient possesses residual capabilities, the application of vEMG towards an 'assist as need' stimulation control can increase their engagement in rehabilitation (Giggins et al., 2013). For this reason we chose to investigate the eEMG parameters during vEMG based stimulation control. The controller modulates the duration of the stimulation trains based on a dual threshold method. Although the controller is not fully proportional such as in (Osuagwu et al., 2020) and (Sennels et al., 1996), its simplicity makes it more robust when applied to weak muscles (Ambrosini et al., 2014; Sennels et al., 1997). Additionally, the modulation of stimulation intensity can alter the eEMG properties, adding variability to fatigue indices such as the MDF (Farina, Blanchietti, Pozzo, & Merletti, 2004).

The constant stimulation waveform for Subject 4 is an anomaly, Figure 8.4c. Subject 4 was the most sensitive to stimulation, quickly fatiguing and becoming uncomfortable during the constant stimulation trial. Consequently their constant stimulation trial only lasted five seconds, compared to the other trials' 20-60 second durations. In this dataset the MDF waveform behaves as expected, but the PTP linear fit shows a slight positive gradient with a a low correlation R^2 value of 0.0036. This suggests that the MDF may be a more sensitive fatigue index than the PTP under constant stimulation.

The objective of this study was to investigate whether the eEMG PTP or MDF could be used as a fatigue indicator during isometric constant stimulation and dynamic vEMG controlled stimulation of the forearm. External torque measurements were not collected, therefore we can only comment on the general trend of the fatigue indices. Similar to Tepavac et al our goal was to recognise the event of fatigue, rather than the accurate estimation of muscle force or torque (Tepavac & Schwirtlich, 1997). In order to use the eEMG to estimate muscle torque, more sophisticated algorithms are required. For instance, Li et al. applied a recurrent neural network model towards accurate torque estimation (Z. Li, Hayashibe, Fattal, & Guiraud, 2014). Torque estimations were provided up to a 30-second prediction horizon, however, external torque sensors were required for model identification and model updates. Any external torque support, such as an exoskeleton, could therefore reduce the accuracy of their prediction method.

8.5 Summary

In this study the efficacy of eEMG PTP amplitude and MDF as fatigue indicators were investigated during isometric constant stimulation and vEMG controlled stimulation of the forearm. During isometric constant stimulation the PTP amplitude and the MDF both exhibited negative gradients. This effect is consistent with the findings of existing literature. During dynamic vEMG controlled stimulation the MDF was found to decrease linearly for each subject with $R^2 > 0.62$, while the PTP amplitude was inconsistent. This suggests that the MDF may be used as a fatigue indicator under such stimulation conditions, but the the PTP amplitude could prove unreliable. PTP amplitude inconsistency is thought to be generated by eEMG recovery during the intervals between contractions.

CHAPTER 9

Hybrid Robotic-FES Support

9.1 Introduction

Robotics and functional electrical stimulation (FES) possess great potential as support modalities for post-stroke rehabilitation. FES is able to directly stimulate the patients muscles, and robotic support can provide high-intensity, reliable movements. However, the isolated usage of these technologies is restricted due to their inherent limitations. FES induced motion is difficult to control and usage-time is constrained by patient fatigue. Robotic devices are often confined to clinical settings due to portability issues, and cannot achieve the direct muscle activation that FES can provide.

The hybrid application of robotic and FES support holds promise to improve rehabilitation. A hybrid device can utilise the robotic structure's controlled and repeatable motion, with additional physiological benefits from FES direct muscle activation. Balanced hybrid support can reduce requirements on both stimulation intensities and robotic forces. Furthermore, patient engagement can be improved with the integration of bioelectric signals such as

electromyography (EMG) for intention estimation. Current upper-limb hybrid technologies, such as the NMES-Robot System developed by Rong et al. (Rong et al., 2017), have demonstrated that a balanced support profile between FES and robotic assistance can yield improvements in reference tracking errors and voluntary muscle activations, see Section 3. However, these support profiles remain fixed and patient fatigue is not addressed. Patient fatigue is of particular importance in stroke rehabilitation as it can limit session times and therefore reduce the therapeutic outcomes. Hybrid devices have the potential to manage fatigue through dynamic adjustment of FES and robotic support, given an appropriate fatigue measure.

In this chapter, the constant current (CC) stimulator, stimulus resistant EMG device, and finger exoskeleton design that were independently developed, are integrated to form a hybrid hand-exoskeleton. The device is applied towards volitional EMG (vEMG) driven FES-robotic support to assist in functional grasping movements. In Chapter 8, elicited EMG (eEMG)-based fatigue indices were investigated during vEMG controlled forearm stimulation. The eEMG power spectral density (PSD) median frequency (MDF) was identified as a suitable fatigue indicator due to its negative gradient, which is consistent with existing literature. This chapter expands on the work in Chapter 8 to investigate the eEMG MDF during vEMG controlled hybrid-exoskeleton support.

9.2 Methods

Five healthy individuals participated in this study, four male and one female, aged 25-42 years. This study was approved by the Human Ethics Committee, University of Canterbury (HEC2020/68) and informed consent was obtained from each participant prior to the experiments. Two protocols were followed in this work. The first protocol involved sets of finger flexion, induced using only stimulation. The second protocol involved sets of finger flexion-extension using both stimulation and exoskeleton assisted motion. The control and timing of the flexion-extension sets were controlled by the subjects' vEMG.

9.2.1 Instrumentation

Instrumentation used throughout this study includes the CC stimulator detailed in Chapter 6, the stimulus resistant EMG device detailed in Chapter 7, and a hand exoskeleton based on the finger exoskeleton design in Chapter 5.

Stimulator and Recording Device

Stimulation and EMG recording devices are applied through separate pre-gelled carbon-film surface electrode pairs (Verity Medical, VS25). The FES device can provide biphasic CC stimulation with controllable pulse-width, amplitude, and frequency. Stimulation amplitude is delivered within $I \in [0, 30]$mA given the device's maximum voltage compliance of $\pm$50V. The EMG device has a pre-amplifier gain of 52dB, bandpass characteristics of 20-480Hz, and is sampled at 1kHz through an on-board 24-bit analog to digital converter (ADC). Separate electrodes are used for stimulation and EMG recording to enable assessment of the eEMG waveform. When recorded from stimulation electrodes, the eEMG shape is obscured due to longer lasting stimulation artefacts, Chapter 7.

Hand Exoskeleton and Wrist Brace

Chapter 5 presented a finger exoskeleton design and a parametric model which scales the exoskeleton to different finger lengths. Using the parametric model, index and pinky finger exoskeletons were created for a 'small', a 'medium', and a 'large' hand, using the finger measurements detailed in Table 5. The measurement definitions are depicted in Chapter 5, Figure 5.4

Table 9.1: Finger measurements (mm) used to generate small, medium, and large exoskeleton models.

		L2(mm)	*L3(mm)*	*W1(mm)*	*W2(mm)*	*W3(mm)*
Small	*Index*	38.8	20.0	26.8	17.9	13.1
	Pinky	28.6	16.5	20.0	15.9	13.5
Medium	*Index*	42.9	25.4	26.0	15.5	11.2
	Pinky	33.0	21,4	21.3	12.9	10.5
Large	*Index*	48.6	27.0	26.0	17.1	12.2
	Pinky	37.8	20.0	22.5	14.0	10.8

Figure 9.1: Mounting of the hand exoskeleton and wrist brace.

Figure 9.1 depicts an assembled exoskeleton and its fitting on the hand. The exoskeleton linkages were fixed onto a 3d-printed base which is secured to the dorsal side of the hand using hook-and-loop tape. Exoskeleton couplers were also fastened to the fingers using hook-and-loop tape. The movements of the index and middle fingers are coupled, as well as the movements of the ring and pinky fingers, by binding the fingers' distal phalanx. Each exoskeleton linkage is actuated through a servo motor (TowerPro, SG-90). The crank position of the servo motors are sampled at 1kHz with 8-bit resolution through the EMG device's on-board micro-controller. In addition to the exoskeleton, a 3d-printed wrist brace is used to prevent excessive wrist flexion during stimulation.

9.2.2 Experimental Protocol

The stimulation and recording electrodes were placed on the subject's right arm. The FES electrodes were placed longitudinally down the forearm with the EMG electrodes placed in between and orientated perpendicular to the muscle fibre direction. This layout is consistent with the study in Chapter 8. Biphasic stimulation was delivered with a constant pulse-width of 300us and frequency of 25Hz. Subjects were given ten minutes to familiarise themselves with the sensation of electrical stimulation. The wrist-brace and hand exoskeleton were then mounted to the subject.

Two experimental protocols were implemented in this work, vEMG-controlled stimulation, and vEMG-controlled hybrid support. The vEMG control method is detailed in Section 9.2.2. During both protocols the subjects were seated with their right arm's wrist neutral and their elbow at a 90° angle. Their left hand was used to hold a peanut-shaped object in place, Figure 9.2a. Object dimensions are provided in Figure 9.2b For both protocols the subjects were instructed reach and grasp the object fifteen times. No timing instructions were given for the frequency of the grasps.

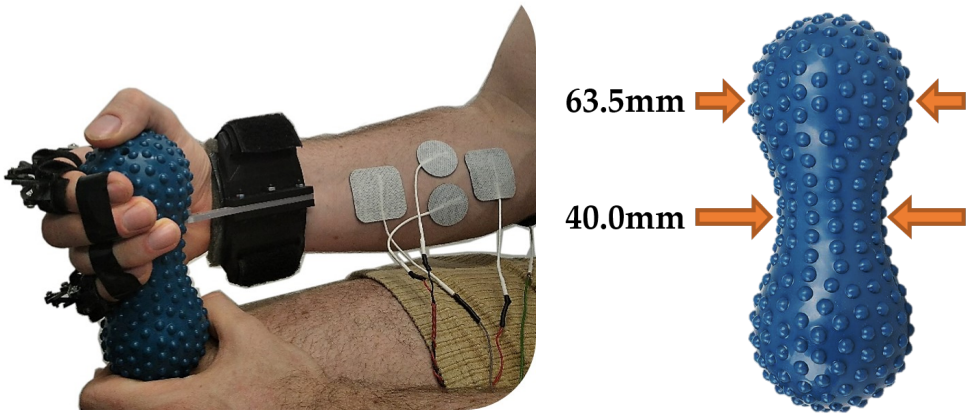

(a) Experimental setup with exoskeleton, wrist brace, and electrode placement.

(b) Object dimensions.

Figure 9.2: Experimental set-up and object dimensions.

The stimulation protocol utilised stimulation to support the flexion portion of each grasp, while the exoskeleton remained passive. Finger extension was completed by the subject, unaided. The hybrid protocol added support from the exoskeleton to assist in both flexion and extension movements. During the hybrid protocol, the stimulation intensity was lowered to 60% of the stimulation protocol.

Prior to the stimulation protocol, the stimulation amplitude was adjusted to a level that would provide tetanic contractions and was comfortable for each subject. Further adjustments were made to the stimulation amplitude and electrode placements to ensure that a clear eEMG waveform was present at full intensity and at 60% intensity. Following this setup, the servo motion-limits were identified for each subject's grasp. These limits corre-

spond to the fully extended and the fully flexed finger positions.

vEMG Control

A dual-threshold control system is utilised in this work (Ambrosini et al., 2014). The controller dictates the position of the servo motors and the timing of stimulation trains based on a volitional intent metric vINT, which is calculated from the subject's estimated vEMG. The vEMG estimate is obtained through an adaptive filter and the vINT is based on a windowed root mean square (RMS) of the vEMG. The data processes to obtain the vEMG estimate and vINT control signal are detailed in Chapter 8, Section 8.2.3.

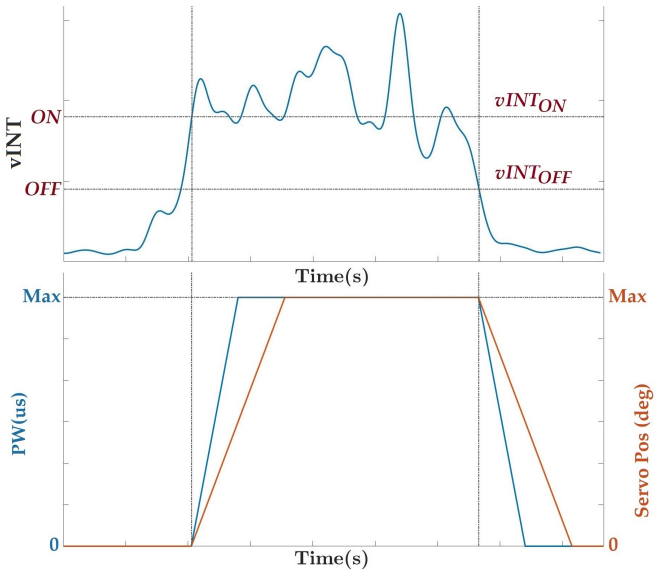

Figure 9.3: Overview of the vEMG based control method used. When $vINT$ rises above the threshold $vINT_{ON}$ the stimulation PW and the servo position is ramped up to its maximum value. When $vINT$ falls below $vINT_{OFF}$ the PW and servo position are ramped down again.

Figure 9.3 shows an overview of the vEMG-based control system, which relies on the vINT signal and two thresholds, $vINT_{ON}$ and $vINT_{OFF}$. The thresholds are subject specific and are adjusted prior to each trial to ensure residual artefacts do not falsely trigger assistance. When vINT rises above the threshold $vINT_{ON}$, the stimulation PW is ramped up to its maximum PW in 100us increments. During the hybrid protocol, the servo positions are incremented until they reach their respective motion-limits. The servo step-sizes are set such that the servo completes the motion range in ten steps. The maximum PW was set to 300us and the servo motion-limits were calibrated prior to each hybrid trial. The

stimulation PW is held at 300us and the servo positions are held at their max positions until vINT drops below the lower threshold $vINT_{OFF}$. Reactivation of the stimulation and exoskeleton is disabled for one second past this point to avoid triggering of the system based on finger extensor activity.

9.3 Results

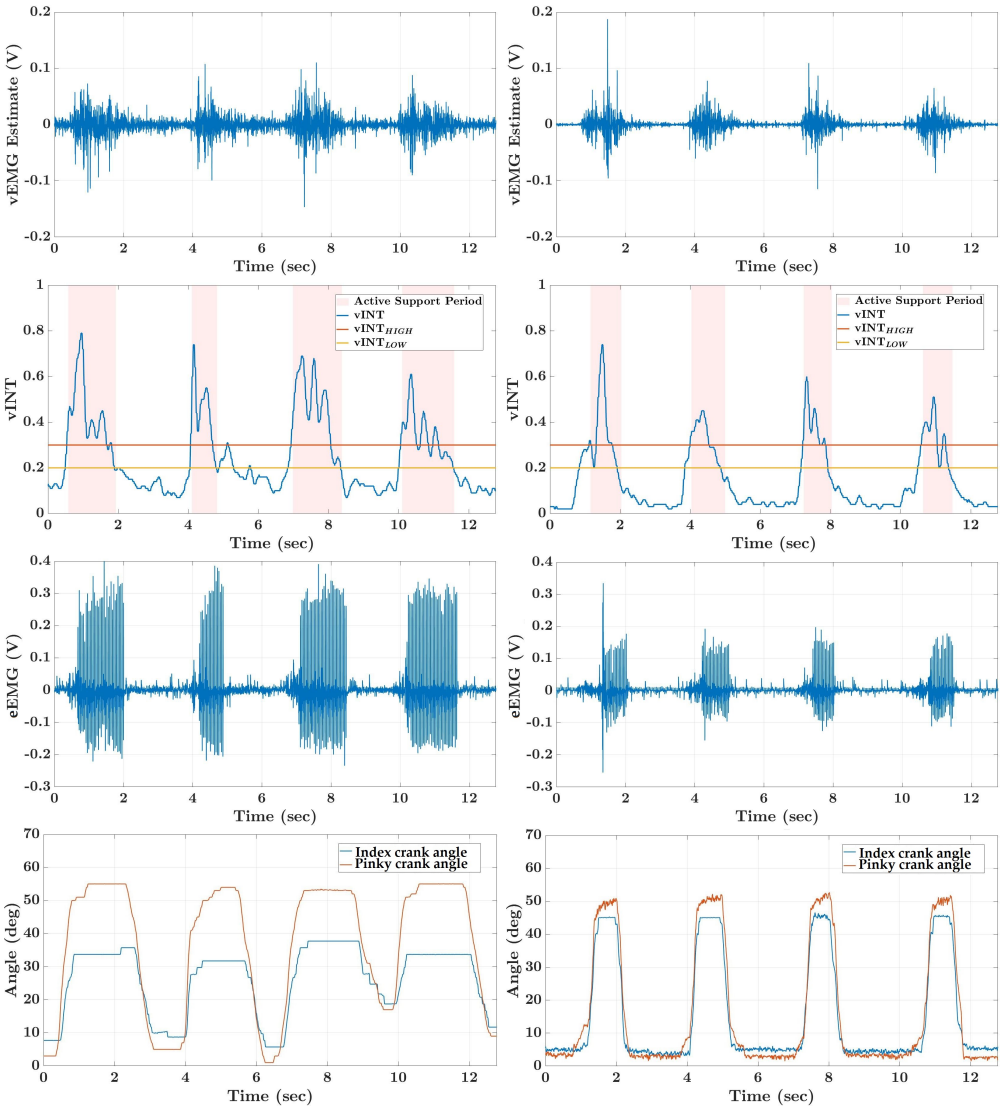

(a) Stimulation only protocol.

(b) Hybrid protocol.

Figure 9.4: The eEMG, vEMG estimate, vINT control signal, and servo positions for Subject 1 over five grasping motions during the (a) stimulation only protocol (b) hybrid protcol. The red portions in the vINT plot represent the periods when stimulation or hybrid support is applied.

Figure 9.4 shows the eEMG, vEMG estimate, vINT, and servo positions, recorded from Subject 1 over four grasping motions. Figure 9.4a shows the data collected during the stimulation protocol and Figure 9.4b shows the data collected during the hybrid protocol.

For each subject, the MDF is calculated from the average eEMG PSD over epochs of two contraction sets. This averaging was used to reduce the effects of changing muscle length and intermittent stimulation, Chapter 8, Section 8.2.3. For each MDF dataset a first order polynomial was fit using linear least squares.

$$y = \alpha X + \beta \tag{9.1}$$

Where y represents the MDF estimate, α represents the gradient of the linear fit, and β represents the y-axis intercept. The gradient and coefficient of determination for each fit are detailed in Table 9.2 and Table 9.3 for the stimulation protocols and hybrid protocols, respectively. The percentage reduction between the MDF gradients of stimulation only and hybrid trials are detailed in Table 9.4 for each subject. The MDF and corresponding linear fits are shown for Subject 1 and Subject 4 in Figure 9.5.

Table 9.2: Gradient (α), initial value (β), and coefficient of determination (R^2) for each subject's linear fit during vEMG controlled stimulation only trial

Subject	***1***	***2***	***3***	***4***	***5***
α $(Hz \cdot Cont^{-1})$	-2.55	-5.48	-1.08	-1.25	-1.21
β (Hz)	131.36	154.43	114.76	119.39	112.78
R^2	0.97	0.93	0.91	0.82	0.74

Table 9.3: Gradient (α), initial value (β), and coefficient of determination (R^2) for each subject's linear fit during vEMG controlled hybrid trial

Subject	***1***	***2***	***3***	***4***	***5***
α $(Hz \cdot Cont^{-1})$	-2.07	-4.59	-1.02	-0.60	-0.97
β (Hz)	124.41	143.76	111.68	122.38	105.00
R^2	0.98	0.88	0.80	0.81	0.55

Table 9.4: Percentage reductions between the MDF gradients for stimulation only and hybrid trials.

Subject	***1***	***2***	***3***	***4***	***5***	***Average***
Stimulation only $\alpha(Hz \cdot Cont^{-1})$	-2.55	-5.48	-1.08	-1.25	-1.21	-2.31
Hybrid $\alpha(Hz \cdot Cont^{-1})$	-2.07	-4.59	-1.02	-0.60	-0.97	-1.85
MDF slope reduction (%)	**18.8**	**16.2**	**5.6**	**52.0**	**20.0**	**20.1**

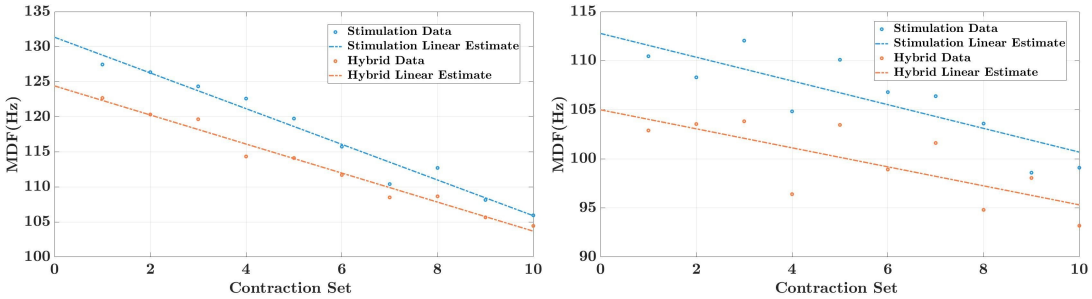

(a) Subject 1 (b) Subject 4

Figure 9.5: MDF calculated per contraction set and corresponding linear fits for Subject 1 and Subject 4 during the stimulation and hybrid support protocols.

After each protocol, the subjects were asked their perceived muscle fatigue on a scale of zero to five. A rating of zero corresponds to no fatigue, as if no stimulation were applied, and a rating of five corresponds to a muscle cramping sensation.

Table 9.5: Subjects' perceived level of fatigue during stimulation and hybrid protocols.

Subject	***1***	***2***	***3***	***4***	***5***	***Average***
Stimulation	3.5	3	3.5	4	4.5	3.6
Hybrid	2	2	2	2	2.5	2.1

9.4 Discussion

This chapter presents the proof-of-concept of a novel hybrid exoskeleton applied towards grasp support. The device integrates a CC stimulator, stimulus-resistant EMG device, and robotic exoskeleton, to provide balanced support using a continuous measure of subject intent. An example is shown in Figure 9.4 where the subject's vEMG, control signal vINT, and ensuing grasping motion are depicted. In comparing Figure 9.4a and Figure 9.4b, the hybrid protocol provides a more consistent finger range of motion (ROM) using 60% stimulation intensity and servo-motor support. This demonstrates the ability for hybrid support to reduce motor torque and stimulation intensity requirements, while providing repeatable motion assistance. This feature can enhance device portability as smaller, less-powerful actuators can be used. For instance, the utilised SG-90 actuators weigh only 10.5g each and can provide 0.18Nm of torque. The motors were capable of actively moving the fingers but could be resisted by the subjects, which acts as a safety mechanism preventing over flexion/extension of the finger joints. However, in a clinical implementation stronger

actuation may be required as patients often suffer from high joint stiffness (Sarac et al., 2019).

The subjects were more comfortable and their perceived levels of fatigue were lower during the hybrid protocol. The average perceived levels of fatigue were 3.6 and 2.1 for stimulation and hybrid protocols, respectively. These levels are on a scale of zero to five, where zero corresponds to no perceived fatigue, and five corresponds to a muscle cramping sensation. This result was expected, as stimulation intensity during the hybrid protocol was lowered to 60% of the stimulation protocol. This demonstrates that a hybrid support profile may be used to increase patient comfort and reduce their perceived rate of fatigue, which in-turn can maximise rehabilitation session-times and enhance therapeutic outcomes.

The eEMG MDF possessed negative gradients for each subject across the stimulation and hybrid support protocols. This result is consistent with the findings of Chapter 8, where the MDF was found to have negative gradients during isometric constant stimulation and during vEMG controlled stimulation. During the stimulation trial, the MDF exhibited gradients in the range of $-1.08Hz \cdot Cont^{-1}$ to $-5.48Hz \cdot Cont^{-1}$, and during the hybrid trials, the MDF gradients ranged from $-0.6 \cdot Cont^{-1}$ to $-4.59Hz \cdot Cont^{-1}$. Linear regression fits were able to capture the fatigue trends, with $R^2 > 0.8$ for Subjects 1-4 over both protocols. The lowest MDF R^2 value was 0.55, corresponding to Subject 5's hybrid protocol dataset. Subject 5 was particularly sensitive to stimulation and therefore could only tolerate low levels of stimulation. The fluctuation of Subject 5's MDF during the hybrid protocol is thought to caused by the unreliability of the eEMG during low-level stimulation (Merletti, Knaflitz, & De Luca, 1990). This suggests that the MDF may become less reliable as a fatigue indicator when applied to stimulation sensitive patients, or when the ratio of FES to robotic support decreases.

The average MDF gradient magnitude reduced by 20.1% between stimulation only and hybrid protocols. This is likely to be caused by the higher stimulation intensities applied during the stimulation protocol. Similar trends have been observed in existing literature, where higher intensity stimulation produces steeper MDF gradients (Farina et al., 2004). Higher stimulation intensities were found to produce more fatigue during isometric stimulation of the tibialis anterior (Merletti et al., 1990), and were found to increase the subjects' perceived fatigue levels recorded in this study. The steeper gradient of the MDF reflects the higher fatiguability of the stimulation protocol. Therefore, the gradient of the MDF can provide useful information on the progression of localised muscle fatigue (Kuthe, Uddanwadiker, & Ramteke, 2018). This finding suggests that the use of the MDF slope as a fatigue measure is feasible, but could benefit from more testing to confirm across a range of different scenarios. In future, this fatigue measure could be used as a feedback tool for therapists. Alternatively, it could be used to guide the support profile between FES and robotic components to provide fatigue compensation during vEMG-based functional assistance.

The MDF variable is affected by the stimulation level. This can be observed in Figure 9.5 by the offset between MDF data-sets for the stimulation and hybrid protocols. For all subjects, with the exception of Subject 4, the lower stimulation intensity applied during the hybrid protocol resulted in a lower initial MDF value. Farina et al. identified the opposite trend during stimulation of the biceps brachii (Farina et al., 2004), and Knaflitz et al. found the change in initial MDF to be less consistent during stimulation of the tibialis anterior muscle (Knaflitz, Merletti, Luca, Iti, & Carlo, 1990). This suggests that the MDF response to stimulation intensity is likely dependant on the muscle of interest and is subject specific. The MDF may not be a reliable fatigue indicator during fully proportional stimulation control as a change in stimulation intensity effects the MDF value independently of fatigue. The control-base used in this work avoids this issue by applying stimulation trains with consistent pulse-width and amplitude for each trial. However, if the MDF slope is used to

modulate stimulation-robotic support profile, the fatigue index would have to account for the associated shift in MDF level.

9.5 Summary

In this chapter the CC stimulator, EMG device, and finger linkages, developed and described in previous chapters, were integrated to form a hybrid hand-exoskeleton. The device was applied towards a functional grasping task, in which the subjects' vEMG was used to modulate FES and robotic assistance. Grasping tasks were completed using two different assistance profiles, stimulation only and a hybrid of stimulation and robotic support. The hybrid support profile utilised lower stimulation intensities, which was found to enhance subject comfort and lower their perceived rate of fatigue. Furthermore, the addition of robotic support was seen to provide more consistent finger ROM.

Linear regression fits were able to characterise the eEMG MDF trends well, with $R^2 > 0.8$ for Subjects 1-4, and $R^2 > 0.55$ for Subject 5. The eEMG MDF linear regression fits possessed negative gradients in the range of $-1.08Hz \cdot Cont^{-1}$ to $-5.48Hz \cdot Cont^{-1}$ during the stimulation protocol and in the range of $-0.6 \cdot Cont^{-1}$ to $-4.59Hz \cdot Cont^{-1}$ during the hybrid protocol. The steeper gradients during the stimulation protocol indicate increased fatigue from higher levels of stimulation. From this observation we suggest that the slope of the eEMG MDF may provide useful information as a fatigue index during vEMG controlled hybrid stimulation. In future applications, the MDF fatigue indicator could be applied to adjust the ratio of FES-robotic support to provide fatigue compensation during rehabilitation.

CHAPTER 10

Conclusions

This thesis details the development of a proof-of-concept hybrid hand-exoskeleton and its application towards assist-as-need support of functional grasping movements. During volitional EMG (vEMG) control of stimulation and robotic modalities, the suitability of electromyography (EMG) based fatigue-indices were explored. The device required the design and integration of a robotic exoskeleton and constant current (CC) stimulator to provide motion support, as well as a novel stimulus-resistant EMG device for volitional intent and fatigue estimation.

The hand exoskeletons comprised of two servo-actuated one-degree of freedom (DOF) Watt I linkages, mounted to the dorsal side of the hand. A parametric model that adapts linkage dimensions to different finger sizes was developed, which allowed fast production of the exoskeletons for a range of different fingers. Parent model linkage dimensions were determined using Differential Evolution (DE) optimisation to minimise angular precision and compactness cost functions over twenty task-positions. The linkage reached the task-positions with a root mean square error (RMSE) of 0.92°. However, its compactness

was limited by the requirement to avoid linkage-finger interference and its placement on the dorsal side of the hand. Through Monte Carlo analysis and experimental testing, the exoskeleton's trajectory was shown to be sensitive to parameter variations. Such variations may be caused by factors such as a shift in coupler placements or error in finger measurements. This means that the exoskeleton cannot fully control the posture of the finger. However, a large range of movement strategies were observed during a set of grasping trials, without the exoskeleton donned. This indicated that the exoskeleton's functional capacity may not be hindered by a lesser degree of posture control, as there are many possible trajectories that result in a successful grasp.

The CC stimulator developed in this work can output current up to ±30mA, given a compliance voltage of ±40V. Stimulation waveform characteristics such as pulse-width, frequency, and amplitude are adjustable using the on-board micro-controller. For most experimental protocols, stimulation was delivered using a biphasic square waveform to help prevent electrode-tissue charge accumulation. A stimulation frequency of 25Hz was typically applied, with adjustable pulse-width and amplitude. Experimental testing of the stimulator was conducted on a set of resistive loads and on one human subject. With a $2k\Omega$ load resistance, the stimulator had a maximum ramp tracking error of 5% and exhibited a linear output transfer function. Across electrode-tissue and resistive load impedances, the stimulator demonstrated its ability to consistently deliver 10mA square-wave output currents.

The EMG device presented in this thesis can record biopotentials of a stimulated muscle through the stimulation electrodes or through separate electrodes. The system blanks stimulation artefacts using pre-amplifier disconnection and a non-linear feedback loop. The design improves upon existing systems which rely on stimulator synchronisation, by using an adjustable Schmitt-trigger artefact detection channel which adapts to different artefact conditions. The design has been made open-source and has a part cost of approximately USD $150 (McKenzie et al., 2021). When recording through separate electrodes,

the device was capable of suppressing the stimulation artefact while the users' elicited EMG (eEMG) and vEMG were captured. In Chapters 8 and 9, the eEMG waveform is used to calculate fatigue metrics while vEMG is used to control stimulation and robotic support levels. When recording through stimulation electrodes the device demonstrated the ability to preserve the vEMG spectra. Pearson's correlation coefficients greater than 0.84 were identified between the normalised power spectral densities (PSDs) of vEMG estimates during stimulation and of stimulation-free vEMG recordings. The device possesses band-pass characteristics of 20-480Hz under both recording conditions. This is an improvement over current same-electrode systems which use elevated high-pass filter cut-off frequencies ($f_c \geq 170Hz$), as the device can sample more of the EMG spectrum's predominant usable energy. The device can access more information on the muscles' state, which creates potential future applications beyond conventional vEMG-based control, such as the monitoring of muscle fatigue.

The CC stimulator, stimulus-resistant EMG device, and robotic exoskeleton developed in this work, were integrated to form a hybrid exoskeleton for functional grasp assistance. Through an EMG-based continuous measure of volitional intent, functional electrical stimulation (FES) and robotic support were delivered in an assist-as-need manner. The device demonstrated the ability for hybrid assistance to provide consistent motion support while lowering stimulation intensities. In turn, the hybrid support profile enhanced the subjects' comfort and lowered their perceived levels of fatigue.

The efficacy of eEMG-based fatigue indices were investigated during vEMG controlled forearm stimulation in Chapter 8 and hybrid exoskeleton support in Chapter 9. During both trials, the subjects performed dynamic movements with assist-as-need support. These conditions more closely represent functional rehabilitation practices, building on current literature which typically examine fatigue under isometric conditions and with fixed stimulation timings. During forearm stimulation in Chapter 8, the eEMG median frequency

(MDF) was found to be a more suitable fatigue indicator than eEMG peak-to-peak amplitude (PTP), as the MDF exhibited negative gradients for all subjects ($R^2 > 0.62$) while the PTP was inconsistent. During the hybrid support profiles in Chapter 9, the MDF gradients exhibited a reduction between 5.6% and 52.0% in response to a 40% reduction in stimulation intensity. The MDF gradients reflected the fatiguability of higher stimulation intensities and therefore may provide useful information as a fatigue index during hybrid vEMG-driven functional assistance. Ultimately, this prompts future research towards the development of the MDF gradient as a fatigue index and its integration with the hybrid-exoskeleton system to guide FES-robotic support balance.

Overall, the objective of this thesis was to develop a hybrid hand-exoskeleton which incorporates stimulation and robotic support for grasp assistance, guided by EMG-based volitional intent and fatigue metrics. The hybrid device was produced through the development and integration of CC stimulator, stimulus-resistant EMG device, and hand-exoskeleton. Hybrid assist-as-need support was provided for a number of subjects, governed by continuous estimates of their vEMG. Lastly, the efficacy of EMG-based fatigue indices were explored during dynamic movements supported by vEMG-controlled hybrid support. This warranted further research into the MDF gradient as a fatigue index, specifically towards guidance of dynamic hybrid support profiles. Ultimately, this will provide a path to more effective rehabilitation practices, in-turn promoting enhanced therapeutic outcomes.

CHAPTER 11

Future Work

There are many avenues of future work that may be pursued to progress the research presented in this thesis. A selection of potential advancements are detailed in the following sections.

Hand-exoskeleton

Future developments for the hand-exoskeleton pertain to the design of the individual finger linkages as well as their integration to provide multi-fingered support. The finger exoskeleton presented in Chapter 5 utilised a novel compactness cost-function to help reduce device volume. However, optimisation was limited by the input four-bar linkage as it was required to avoid interference with the finger in all task-positions. Replacing the input crank with a linear actuator allows its effective length to change during the flexion-extension movements. In turn, this would allow a smaller four-bar volume when the finger is extended, whilst avoiding collision with the finger during flexion.

When integrated into a full hand-exoskeleton in Chapter 9, finger-exoskeletons provided

direct support to the index and pinky fingers, whilst indirect support was transferred to the middle and ring fingers through distal coupling, Figure 9.2a. This coupling method was effective in ensuring a cohesive grasp. However, the hand-exoskeleton could provide a more complete phalanx support-profile with an individual linkage per finger. Through coupling of the finger-linkages' input cranks the number of required actuators can be reduced. Furthermore, achieving such coupling through differential mechanisms would enable the fingers to adapt to objects of different geometries (Mühlbauer, Löhnert, Siegle, Stewart, & Pott, 2020).

During the hybrid trials in Chapter 9 the hand exoskeleton assisted in grasping a cylindrical object with diameter greater than 40mm. However, activities of daily living (ADL) require a larger portfolio of grasping patterns. More extensive testing of the exoskeleton, over a range of grasp topologies, would provide useful information of its functional capacity. For instance, assistance in drinking may require the exoskeleton to grasp at straws, which represents more of a precision grasp topology.

Stimulator

The current stimulator is based on a differential-amplifier based Improved Howland current source (IHCS). The amplifier has a maximum compliance voltage of 40V, which is then passed through an H-bridge to achieve biphasic stimulation within effective $\pm 40V$ rails. This capacity has proved sufficient for forearm stimulation. However, higher voltages may be required for larger muscle groups.

In future designs, the voltage compliance of the differential amplifier can be increased through the use of a bootstrapping network (Cornman et al., 2017). This would allow for lower-compliance, less-expensive amplifiers to be utilised. Additionally, using dual-rails on the IHCS would allow it to output a biphasic current. The H-bridge output can then be omitted, reducing the control complexity of the system.

Currently, the stimulator uses a biphasic current waveform and passive discharging period to prevent charge accumulation in the electrode-skin interface. This method prevented the damage of subjects' skin tissue. However, when electromyography (EMG) was sensed through the stimulation electrodes the remaining charge masked the occurrence of the elicited EMG (eEMG). To enable assessment of the eEMG under these conditions, an active discharge circuit may be a possible solution and should be considered for future designs (Schauer, 2017).

Stimulus-resistant EMG

The EMG device presented in Chapter 7 demonstrated its ability to estimate volitional EMG (vEMG) during stimulation, though stimulation electrodes or through separate electrodes. Currently, the device has only been used to record single-channel EMG. During the vEMG-based support trials in Chapter 8 and Chapter 9, this was mainly due to a lack of space on the forearm that resulted from separate stimulation and EMG electrodes, as required for eEMG monitoring.

With the electrode placement on the forearm, most subjects noted that EMG sensitivity and stimulation-induced contractions were predominately limited to the ring and pinky fingers. In turn, this led to control difficulty for some subjects. Furthermore, single-channel EMG recording restricted the exoskeleton's assistance to simultaneous flexion or extension of all fingers, creating redundant degrees of freedom (DOFs) between its functionality and its application. Future development of the EMG device mostly covers its expansion to multichannel recording which will allow for better coverage of the forearm muscles. Ultimately, this would allow for more selective control of stimulation and robotic-exoskeleton components. Additionally, if the same-electrode functionality demonstrated in Chapter 7 were extended to provide vEMG-based control, the space-efficiency of the system could be enhanced further.

Expansion of the EMG design for multichannel capabilities would most likely be achieved through the addition of parallel amplifier channels. However, the size of the EMG board would significantly increase if the current design was merely replicated, including the artefact detection channel and suppression hardware. A viable option could be to use one artefact detection channel to control the suppression hardware for all channels. This relies on similar stimulation timings for all channels and would also require the accompanying artefacts to be similar. To reduce hardware complexity, another option could be to remove the hardware for artefact detection and suppression, instead relying on the input protection to guard the pre-amplifiers and using an AC-coupler cut-off frequency near zero for DC-offset removal. Software-based removal of motion and stimulation artefacts would then be required to produce vEMG estimates. This approach reduces the size of the board but incurs higher software complexity.

Fatigue

In Chapters 8 and 9, the eEMG median frequency (MDF) was found to be a suitable fatigue indicator during vEMG-based stimulation control. Future integration of the MDF fatigue index into the hybrid-exoskeleton's control system would be a key future development, as it permits dynamic support profiles in which current designs are lacking. Naturally, more extensive testing of the MDF fatigue index would be required to assure its reliability. Further testing would include a larger and more diverse population of subjects, as well as a larger range of stimulation intensities. To provide insight to the fatigue indicator's usefulness in ADL settings, it would also be useful to investigate the influence of recovery intervals.

Current EMG-based studies of stimulation-induced fatigue analyse the shape of the eEMG. However, the repeatability of the eEMG shape is highly dependent on electrode placement, and the appearance of cross-talk could affect fatigue measurements (Merletti, Fiorito, Lo Conte, & Cisari, 1998). Additionally, if EMG recordings are taken from stimulation elec-

trodes, the stimulation artefact masks the eEMG shape. In Chapter 7 the vEMG estimates during stimulation were shown to have similar spectra to stimulation-free EMG recordings. This result prompts future investigation of vEMG estimate-based fatigue indices during stimulation.

Appendices

APPENDIX A

Stimulator Bill of Materials

Description	Reference Designator	Manufacturer	Manufacturer Part Number	Quantity	Supplier	Digi-Key Part Number	Unit Price	Extended Price
Capacitors								
CAP 22 UF 20% 35 V	C8	Würth Elektronik	8.60011E+11	1	Digi-Key	732-8733-1-ND	0.15	0.15
CAP CER 0.1UF 100V X7R 0603	C11, C12, C13, C15, C16, C17, C18, C19, C20, C21, C22, C23, C24	Samsung Electro-	CL10B104KC8NNNC	13	Digi-Key	1276-6807-1-ND	0.109	1.42
CAP CER 10UF 25V X5R 0805	C1, C5	Taiyo Yuden	TMK212BBJ106KG-T	2	Digi-Key	587-2985-1-ND	0.32	0.64
CAP CER 10UF 75V X7R 1210	C9, C10, C26	TDK Corporation	CGA6P1X7R1N106M250AC	3	Digi-Key	445-181609-1-ND	1.64	4.92
CAP CER 1UF 100V X7R 0805	C14	AVX Corporation	08051C105K4T2A	1	Digi-Key	478-12142-1-ND	0.57	0.57
CAP CER 1UF 16V X7R 0603	C3, C6	Samsung Electro-	CL10B105MO8NNWC	2	Digi-Key	1276-6524-1-ND	0.15	0.30
CAP CER 2.2UF 25V X5R 0603	C2	Murata Electroni	GRM188R61E225MA12D	1	Digi-Key	490-12738-1-ND	0.23	0.23
CAP CER 4.7UF 25V X5R 0805	C4	Würth Elektronik	8.85012E+11	1	Digi-Key	732-7628-1-ND	0.26	0.26
CAP CER 470PF 50V X7R 0603	C7	Samsung Electro-	CL10B471JB8NNNC	1	Digi-Key	1276-2058-1-ND	0.15	0.15
CAP CER 820PF 250V C0G/NP0 0603	C25	KEMET	C0603C821JAGAC7867	1	Digi-Key	399-14996-1-ND	0.2	0.20
Diodes								
DIODE SBR 200V 1A POWERDI123	D4	Diodes Incorpora	SBR1U200P1-7	1	Digi-Key	SBR1U200P1-7DICT-ND	0.74	0.74
DIODE SCHOTTKY 100V POWERDI123	D3	Diodes Incorpora	DFLS1100-7	1	Digi-Key	DFLS1100DICT-ND	0.66	0.66
DIODE SCHOTTKY 10V 1A POWERMITE	D1	ON Semiconduct	NRVBM110ET1G	1	Digi-Key	NRVBM110ET1GOSCT-ND	0.75	0.75
DIODE ZENER 24V 1.5W SMA	D2	Central Semicon	CMZ5934B TR13 PBFREE	1	Digi-Key	1514-CMZ5934BTR13PBFREECT-ND	1.41	1.41
DIODE GEN PURP 50V 200MA SOD123	D5	Vishay General S	1N4150W-E3-08	1	Digi-Key	1N4150W-E3-08CT-ND	0.41	0.41
Headers								
CONN HEADER VERT 2POS	SW1, SW2	Sullins Connector	PREC001DAAN-RC	2	Digi-Key	S2012EC-01-ND	0.09	0.18
CONN HEADER VERT 4POS 2.54MM	J3	Sullins Connector	PREC004SAAN-RC	1	Digi-Key	S1012EC-04-ND	0.18	0.18
TERM BLK 2P SIDE ENT 2.54MM PCB	J2	TE Connectivity A	282834-2	1	Digi-Key	A98333-ND	1.95	1.95
Resistors								
RES 0 OHM JUMPER 1/10W 0603	R10, R14, R15, R16, R17, R18, R19, R20, R21, R22, R23, R24	Stackpole Electro	RMCF0603ZT0R00	12	Digi-Key	RMCF0603ZT0R00CT-ND	0.02	0.24
RES 1 OHM 1% 1/8W 0603	R1	Stackpole Electro	RNCP0603FTD1R00	1	Digi-Key	RNCP0603FTD1R00CT-ND	0.15	0.15
RES SMD 10K OHM 0.5% 1/16W 0603	R5	Susumu	RR0816P-103-D	1	Digi-Key	RR08P10.0KDCT-ND	0.15	0.15
RES SMD 121K OHM 0.5% 1/10W 0603	R7	Yageo	RT0603DRE07121KL	1	Digi-Key	311-2410-1-ND	0.15	0.15
RES SMD 15K OHM 1% 1/10W 0603	R4	Yageo	RT0603FRE0715KL	1	Digi-Key	YAG5942CT-ND	0.15	0.15
RES SMD 330 OHM 5% 1/4W 0603	R11	Rohm Semicondu	ESR03EZPJ331	1	Digi-Key	RHM330DCT-ND	0.15	0.15
RES SMD 39 OHM 0.5% 1/10W 0603	R6	Panasonic Electr	ERA-3AHD390V	1	Digi-Key	P123791CT-ND	0.15	0.15
RES SMD 4.7K OHM 1% 1/10W 0603	R8, R12, R13	Yageo	RT0603FRE074K7L	3	Digi-Key	YAG1238CT-ND	0.15	0.45
RES SMD 470K OHM 1% 1/10W 0603	R2	Yageo	RT0603FRE07470KL	1	Digi-Key	YAG5743CT-ND	0.15	0.15
RES SMD 68K OHM 1% 1/10W 0603	R3	Yageo	RT0603FRE0768KL	1	Digi-Key	YAG5967CT-ND	0.15	0.15
POT 10K OHM 1/20W CARBON LINEAR	RV1	Bourns Inc.	PTV09A-2020F-B103	1	Digi-Key	PTV09A-2020F-B103-ND	1.27	1.27
TRIMMER 20 OHM 0.5W PC PIN TOP	R9	Vishay Sfernice	T93YA200KT20	1	Digi-Key	T93YA-20-ND	3	3.00
MISC								
IC SWITCH SPST 48LQFP	U9	Maxim Integrate	MAX14802CCM+	1	Digi-Key	MAX14802CCM+-ND	63.02	63.02
MOSFET N-CH 60V 210MA SOT323	Q1, Q2	Nexperia USA Inc	NX138BKWX	2	Digi-Key	1727-2738-1-ND	0.34	0.68
TEENSY-LC KL2X EVAL BRD	U8	SparkFun Electro	DEV-13305	1	Digi-Key	1568-1233-ND	21.14	21.14
TRANS FLYBACK LT8302	U3	Würth Elektronik	750313457	1	Digi-Key	1297-1136-1-ND	5.94	5.94
PCB and Stencil	PCB	JLCPCB		1	JLCPCB		30.00	30.00
Total Cost							**USD**	**$145.06**

Figure A.1: Stimulator bill of materials

APPENDIX B

Parametric Exoskeleton Finger Measurements

Table B.1: Measurements for eighteen subjects in millimetres (2SF). Hand measurements are defined in Chapter 5, Figure 5.4.

	1	***2***	***3***	***4***	***5***	***6***	***7***	***8***	***9***	***10***	***11***	***12***	***13***	***14***	***15***	***16***	***17***	***18***
L2	42	45	46	39	46	46	44	31	40	46	46	41	36	33	40	35	38	49
L3	25	26	25	20	22	24	22	20	21	17	24	22	16	21	26	17	20	27
W1	26	25	26	27	26	23	26	24	21	26	27	25	20	21	24	20	23	26
W2	16	16	15	18	18	15	17	18	15	17	18	15	14	13	17	14	14	17
W3	11	11	11	13	13	11	13	13	11	12	13	13	11	11	13	11	11	12

APPENDIX C

Stimulus-Resistant EMG Hardware Design Files

C.1 Open Source Hardware Design Files

The EMG device has been made publicly available under the open source license CC BY-NZ-ND 4.0. All design files are accessible through an Open Science Framework repository. A summary of the design files is detailed in Table C.1.

Table C.1: Summary of the open source files and their repository location.

Design filename	File Type	File Location
sEMGArtefactSup.pdf	*PDF Schematic*	*https://doi.org/10.17605/OSF.IO/P5DSW*
sEMG_BOM.csv	*BOM Spreadsheet*	*https://doi.org/10.17605/OSF.IO/P5DSW*
sEMG_Gerber.zip	*Gerber and Drill*	*https://doi.org/10.17605/OSF.IO/P5DSW*
sEMG_Example_Code.ino	*Arduino Script*	*https://doi.org/10.17605/OSF.IO/P5DSW*

The EMG PCB design was developed using KiCad (version 5.0.2). Kicad is an open source software suite for Electronic Design Automation (EDA), licensed under GNU GPL v3. The open source files include a PDF plot of the design schematics and corresponding gerber and drill files. The gerber and drill files are compiled with JLCPCB as the intended PCB manufacturer. A complete bill of materials (BOM) is included in spreadsheet form. Lastly, an Arduino script is provided that contains example code to configure the ADC and capture ADC data, as detailed in (B. Fortune et al., 2019). This script is used to capture the raw EMG data during the experimental testing.

APPENDIX D

Stimulus-Resistant EMG Bill of Materials

Description	Reference Designator	Manufacturer	Manufacturer Part Number	Quantity	Supplier	Digi-Key Part Number	Unit Price	Extended Price
Capacitors								
CAP CER 0.1UF 25V X7R 0603	C1, C2, C3, C4, C5, C7, C8, C9, C12, C13, C14, C15, C21, C22, C25, C26, C31, C32, C33, C34, C35, C36, C37, C38, C39, C40, C41, C42, C44, C45, C50	TDK Corporation	CGA3E2X7R1E104K080AA	31	Digi-Key	445-5667-1-ND	0.057	1.767
CAP CER 0.047UF 50V X7R 0603	C6, C30	Yageo	CC0603KRX7R9BB473	2	Digi-Key	311-1427-1-ND	0.1	0.2
CAP CER 3300PF 50V C0G/NP0 0603	C11	Walsin Technology Corporation	0603N332J500CT	1	Digi-Key	1292-1521-1-ND	0.11	0.11
CAP CER 10UF 25V X5R 0805	C16, C17, C18, C19, C20	Samsung Electro-Mechanics	CL21A106KAYNNNG	5	Digi-Key	1276-6454-1-ND	0.19	0.95
CAP CER 10UF 10V X5R 0603	C23, C27, C29	AVX Corporation	0603ZD106KAT2A	3	Digi-Key	478-10766-1-ND	0.12	0.36
CAP CER 0.27UF 16V X7R 0603	C24, C48	Murata Electronics	GCM188R71C274KA37D	2	Digi-Key	490-16405-1-ND	0.19	0.38
CAP CER 6800PF 10V X7R 0603	C43	Würth Elektronik	8.85012E+11	1	Digi-Key	732-7932-1-ND	0.1	0.1
CAP CER 10000PF 50V X7R 0603	C47	Yageo	CC0603KRX7R9BB103	1	Digi-Key	311-1085-1-ND	0.1	0.1
CAP CER 2.2UF 10V X5R 0603	C46, C49, C51	Samsung Electro-Mechanics	CL10A225KP8NNNC	3	Digi-Key	1276-1085-1-ND	0.1	0.3
CAP CER 47PF 50V C0G/NPO 0603	C10	Yageo	CC0603JRNPO9BN470	1	Digi-Key	311-1065-1-ND	0.1	0.1
CAP TANT 10UF 20% 10V 0805	C28	Vishay Sprague	TMCP1A106MTRF	1	Digi-Key	718-2490-1-ND	0.34	0.34
Diodes								
DIODE GEN PURP 50V 200MA SOD123	D1, D2, D3	Vishay Semiconductor Diodes Division	1N4150W-E3-08	3	Digi-Key	1N4150W-E3-08CT-ND	0.25	0.75
DIODE SCHOTTKY 30V 200MA SOD323	D4	ON Semiconductor	BAT54HT1G	1	Digi-Key	BAT54HT1GOSCT-ND	0.2	0.2
DIODE ZENER 5.1V 300MW SOT23	U7, U8	Vishay Semiconductor Diodes Division	DZ23C5V1-E3-18	2	Digi-Key	DZ23C5V1-E3-18GICT-ND	0.3	0.6
Headers								
CONN HEADER VERT 1POS 2.54MM	J2, J6	Adam Tech	PH1-01-UA	1	Digi-Key	2057-PH1-01-UA-ND	0.1	0.1
CONN HEADER VERT 2POS	J1, J3	Sullins Connector Solutions	PREC001DAAN-RC	2	Digi-Key	S2012EC-01-ND	0.06	0.12
TERM BLK 2P SIDE ENT 2.54MM PCB	J4	TE Connectivity AMP Connectors	282834-2	1	Digi-Key	A98333-ND	1.25	1.25
CONN HEADER VERT 3POS 2.54MM	J5	Sullins Connector Solutions	PREC003SAAN-RC	1	Digi-Key	S1012EC-03-ND	0.09	0.09
CONN HDR 14POS 0.1 GOLD PCB	U20	Sullins Connector Solutions	PPPC072LFBN-RC	2	Digi-Key	S7110-ND	0.97	1.94
Resistors								
RES SMD 68 OHM 0.5% 1/16W 0603	R1, R2	Susumu	RR0816Q-680-D	2	Digi-Key	RR08Q68DCT-ND	0.1	0.2
RES SMD 10K OHM 0.5% 1/16W 0603	R3, R4, R15, R21, R22, R35	Susumu	RR0816P-103-D	6	Digi-Key	RR08P10.0KDCT-ND	0.1	0.6
RES SMD 5.1K OHM 1% 1/10W 0603	R5, R6	Panasonic Electronic Components	ERJ-3EKF5101V	2	Digi-Key	P5.10KHCT-ND	0.1	0.2
RES SMD 510K OHM 1% 1/10W 0603	R7, R9	Yageo	RC0603FR-07510KL	2	Digi-Key	311-510KHRCT-ND	0.1	0.2
RES SMD 1K OHM 0.5% 1/16W 0603	R8, R10, R11, R12	Susumu	RR0816P-102-D	4	Digi-Key	RR08P1.0KDCT-ND	0.1	0.4
RES SMD 49.9KOHM 0.5% 1/16W 0603	R13	Susumu	RR0816P-4992-D-68C	1	Digi-Key	RR08P49.9KDCT-ND	0.1	0.1
RES SMD 4.7K OHM 0.5% 1/16W 0603	R14	Susumu	RR0816P-472-D	1	Digi-Key	RR08P4.7KDCT-ND	0.1	0.1
RES SMD 8.2K OHM 0.5% 1/16W 0603	R16, R19	Susumu	RR0816P-822-D	2	Digi-Key	RR08P8.2KDCT-ND	0.1	0.2
RES SMD 280K OHM 0.5% 1/10W 0603	R17	Yageo	RT0603DRE07280KL	1	Digi-Key	311-2507-1-ND	0.11	0.11
RES SMD 1M OHM 1% 1/10W 0603	R18	Yageo	RT0603FRE071ML	1	Digi-Key	YAG5944CT-ND	0.1	0.1
RES 2K OHM 1% 1/8W 0603	R20	Stackpole Electronics Inc	RNCP0603FTD2K00	1	Digi-Key	RNCP0603FTD2K00CT-ND	0.1	0.1
RES SMD 169K OHM 1% 1/10W 0603	R23, R25	Yageo	RC0603FR-07169KL	2	Digi-Key	311-169KHRCT-ND	0.1	0.2
RES SMD 120 OHM 0.1% 1/10W 0603	R24	Panasonic Electronic Components	ERA-3AEB121V	1	Digi-Key	P120DBCT-ND	0.33	0.33
RES SMD 330 OHM 0.5% 1/16W 0603	R26	Susumu	RR0816P-331-D	1	Digi-Key	RR08P330DCT-ND	0.11	0.11
RES SMD 60.4KOHM 0.5% 1/10W 0603	R29, R30	Yageo	RT0603DRE0760K4L	2	Digi-Key	311-2640-1-ND	0.11	0.22
RES SMD 51K OHM 0.5% 1/16W 0603	R39, R41	Susumu	RR0816P-513-D	2	Digi-Key	RR08P51.0KDCT-ND	0.1	0.2
RES SMD 120 OHM 0.5% 1/16W 0402	R42, R43, R44, R45, R46	Susumu	RR0510P-121-D	5	Digi-Key	RR05P120DCT-ND	0.1	0.5
RES 3.9K OHM 1% 1/10W 0603	R27, R31, R33, R36	Stackpole Electronics Inc	RMCF0603FT3K90	4	Digi-Key	RMCF0603FT3K90CT-ND	0.1	0.4
RES SMD 22K OHM 1% 1/10W 0603	R28, R32, R34, R37	Yageo	RC0603FR-0722KL	4	Digi-Key	311-22.0KHRCT-ND	0.1	0.4
RES 750 OHM 1% 1/8W 0603	R38, R40	Stackpole Electronics Inc	RNCP0603FTD750R	2	Digi-Key	RNCP0603FTD750RCT-ND	0.1	0.2
TRIMMER 20K OHM 0.25W PC PIN TOP	RV1	Bourns Inc.	PV37W203C01B00	1	Digi-Key	490-2976-ND	2.08	2.08
TRIMMER 500K OHM 0.1W J LEAD TOP	RV2	Bourns Inc.	TC33X-2-504E	1	Digi-Key	TC33X-2-504ECT-ND	0.27	0.27
Integrated Circuits (IC)								
IC AUDIO 2 CIRCUIT 8VSSOP	U1, U4, U18	Texas Instruments	OPA1602AIDGKR	3	Digi-Key	296-29166-1-ND	2.86	8.58
IC INST AMP 1 CIRCUIT 8SOIC	U2, U15	Texas Instruments	INA828IDR	2	Digi-Key	296-48914-1-ND	5.01	10.02
IC OPAMP ZER-DRIFT 1CIRC SOT23-5	U3, U13	Microchip Technology	MCP6V51T-E/OT	2	Digi-Key	MCP6V51T-E/OTCT-ND	1.32	2.64
IC DELAY BLOCK 8TAP PROG TSOT23	U5	Analog Devices Inc.	LTC6994CS6-1#TRMPBF	1	Digi-Key	LTC6994CS6-1#TRMPBFCT-ND	3.49	3.49
IC COMPARATOR SNGL 5SOT23	U6	Texas Instruments	TLV1701AIDBVR	1	Digi-Key	296-40599-1-ND	1.1	1.1
IC REG CHARG PUMP -2.5V 8MSOP	U11	Analog Devices Inc.	LTC1550LCMS8-2.5#PBF	1	Digi-Key	LTC1550LCMS8-2.5#PBF-ND	4.75	4.75
IC REG CHARGE PUMP 2.5V SOT23	U12	Texas Instruments	REG710NA-2.5/250	1	Digi-Key	296-12133-1-ND	1.44	1.44
IC SWITCH SPDT DUAL 16TSSOP	U14	Texas Instruments	TMUX6136PWR	1	Digi-Key	296-53265-1-ND	3.31	3.31
IC SWITCH SPDT SINGLE SOT23-8	U16	Texas Instruments	TMUX6119DCNR	1	Digi-Key	296-53446-1-ND	2.65	2.65
IC DGT POT 10KOHM 128TAP 14TSSOP	U17	Analog Devices Inc.	AD5222BRUZ10	1	Digi-Key	AD5222BRUZ10-ND	2.86	2.86
IC ADC 24BIT SIGMA-DELTA 28LFCSP	U19	Analog Devices Inc.	AD7768-1BCPZ	1	Digi-Key	AD7768-1BCPZ-ND	12.83	12.83
Misc								
XTAL OSC XO 2.0480MHZ CMOS SMD	X1	Kyocera International Inc. Electronic Components	KC2016K2.04800C1GE00	1	Digi-Key	1253-1548-1-ND	1.36	1.36
SWITCH TACTILE SPST-NO 0.05A 32V	SW1, SW2	C&K	KSR231GLFS	2	Digi-Key	401-1706-1-ND	0.51	1.02
DC DC CONVERTER 5V 1W	U9	CUI Inc.	PDM1-S12-S5-S	1	Digi-Key	102-2989-5-ND	3.87	3.87
DC-DC ISOLATED, 3 W, 9~18 VDC IN	U10	CUI Inc.	PQP3-D12-D15-D	1	Digi-Key	102-PQP3-D12-D15-D-ND	8.83	8.83
TEENSY 4.0	U20	SparkFun Electronics	DEV-15583	1	PJRC	Teensy4.0	19.95	19.95
TEENSY 4.0 BREAKOUT	U20	OSHPARK	tZbsjC0v	1	OSHPARK	tZbsjC0v	6.3	6.3
PCB and Stencil	PCB	JLCPCB		1	JLCPCB		37.04	37.04
Total Cost							**USD**	**149.017**

Figure D.1: Stimulus-resistant EMG device bill of materials

APPENDIX E

Co-Authorship Forms

The co-authorship forms are below.

Deputy Vice-Chancellor's Office
Postgraduate Research Office

UNIVERSITY OF CANTERBURY
Te Whare Wānanga o Waitaha
CHRISTCHURCH NEW ZEALAND

Co-Authorship Form

This form is to accompany the submission of any thesis that contains research reported in co-authored work that has been published, accepted for publication, or submitted for publication. A copy of this form should be included for each co-authored work that is included in the thesis. Completed forms should be included at the front (after the thesis abstract) of each copy of the thesis submitted for examination and library deposit.

Please indicate the chapter/section/pages of this thesis that are extracted from co-authored work and provide details of the publication or submission from the extract comes:

Section in Thesis: Chapter 7

Publication Type: Journal Paper

Publication: "Low-cost Stimulation Resistant Electromyography." HardwareX

Please detail the nature and extent (%) of contribution by the candidate:

90%

The candidate developed the hardware, conducted the trials, processed the data, and wrote the manuscript

Co-author contributions varied from providing assistance with hardware development, as well as assistance with analysis and interpretation of the results, and revising the paper.

Certification by Co-authors:

If there is more than one co-author then a single co-author can sign on behalf of all

The undersigned certifies that:

- The above statement correctly reflects the nature and extent of the Doctoral candidate's contribution to this co-authored work
- In cases where the candidate was the lead author of the co-authored work he or she wrote the text

Name: *Chris Pretty* Signature: *Chris Pretty* Date: *28/05/2021*

Deputy Vice-Chancellor's Office
Postgraduate Research Office

UNIVERSITY OF CANTERBURY
Te Whare Wānanga o Waitaha
CHRISTCHURCH NEW ZEALAND

Co-Authorship Form

This form is to accompany the submission of any thesis that contains research reported in co-authored work that has been published, accepted for publication, or submitted for publication. A copy of this form should be included for each co-authored work that is included in the thesis. Completed forms should be included at the front (after the thesis abstract) of each copy of the thesis submitted for examination and library deposit.

Please indicate the chapter/section/pages of this thesis that are extracted from co-authored work and provide details of the publication or submission from the extract comes:

Section in Thesis: Chapter 8

Publication Type: Conference Paper

Publication: "Evoked Electromyographic Fatigue Indices During Intermittent Stimulation Towards Dynamic Wrist Contractions." IEEE/ASME International Conference on Mechatronic and Embedded Systems and Applications (MESA 2021)

Please detail the nature and extent (%) of contribution by the candidate:

90%

The candidate conducted trials, developed the analysis algorithms, processed the data, and wrote the manuscript.

Co-author contributions varied from providing as assistance with analysis and interpretation of the results, and revising the paper.

Certification by Co-authors:

If there is more than one co-author then a single co-author can sign on behalf of all

The undersigned certifies that:

- The above statement correctly reflects the nature and extent of the Doctoral candidate's contribution to this co-authored work
- In cases where the candidate was the lead author of the co-authored work he or she wrote the text

Name: *Chris Pretty* Signature: *Chris Pretty* Date: *28/05/2021*

References

Al-ani, T., Cazettes, F., Palfi, S., & Lefaucheur, J. P. (2011). Automatic removal of high-amplitude stimulus artefact from neuronal signal recorded in the subthalamic nucleus. *Journal of Neuroscience Methods*, *198*(1), 135–146. Retrieved from `http://dx.doi.org/10.1016/j.jneumeth.2011.03.022` doi: 10.1016/j.jneumeth.2011.03.022

Alt Murphy, M., Resteghini, C., Feys, P., & Lamers, I. (2015). An overview of systematic reviews on upper extremity outcome measures after stroke. *BMC Neurology*, *15*(1), 29. Retrieved from `http://bmcneurol.biomedcentral.com/articles/10.1186/s12883-015-0292-6` doi: 10.1186/s12883-015-0292-6

Ambrosini, E., Ferrante, S., Gföhler, M., Reichenfelser, W., Karner, J., Schauer, T., ... Pedrocchi, A. (2012). A hybrid assistive system to support daily upper limb activities. , 1–4.

Ambrosini, E., Ferrante, S., Schauer, T., Klauer, C., Gaffuri, M., Ferrigno, G., & Pedrocchi, A. (2014). A myocontrolled neuroprosthesis integrated with a passive exoskeleton to support upper limb activities. *Journal of Electromyography and Kinesiology*, *24*(2), 307–317. Retrieved from `http://dx.doi.org/10.1016/j.jelekin.2014.01.006` doi: 10.1016/j.jelekin.2014.01.006

Ambrosini, E., Ferrante, S., Tibiletti, M., Schauer, T., Klauer, C., & Pedrocchi, A. (2011). Support : a preliminary study. , 4259–4262.

Arora, J. (2012). *Introduction to Optimum Design*. doi: 10.1016/C2009-0-61700-1

Bain, G. I., Polites, N., Higgs, B. G., Heptinstall, R. J., & McGrath, A. M. (2015). The functional range of motion of the finger joints. *Journal of Hand Surgery: European Volume*, *40*(4), 406–411. doi: 10.1177/1753193414533754

Bajd, T., & Munih, M. (2014). Basic functional electrical stimulation (FES) of extremities: An engineer's view. *Technology and Health Care*, *18*(4), 361–369. doi: 10.3233/THC-2010-0588

Basmajian, J. V., & De Luca, C. J. (1979). *Muscles alive: their functions revealed by electromyography*. Williams and Wilkins.

Bataller, A., Cabrera, J. A., Clavijo, M., & Castillo, J. J. (2016). Evolutionary synthesis of mechanisms applied to the design of an exoskeleton for finger rehabilitation. *Mechanism and Machine Theory*, *105*, 31–433. Retrieved from `http://dx.doi.org/10.1016/j.mechmachtheory.2016.06.022` doi: 10.1016/j.mechmachtheory.2016.06.022

Bayona, N. A., Bitensky, J., Salter, K., & Teasell, R. (2005). The Role of Task-Specific Training in Rehabilitation Therapies. *Topics in Stroke Rehabilitation*, *12*(3), 58–65.

Bos, R. A., Haarman, C. J., Stortelder, T., Nizamis, K., Herder, J. L., Stienen, A. H., & Plettenburg, D. H. (2016). A structured overview of trends and technologies used in dynamic hand orthoses. *Journal of NeuroEngineering and Rehabilitation*, *13*(1), 62. Retrieved from `http://jneuroengrehab.biomedcentral.com/articles/10.1186/s12984-016-0168-z` doi: 10.1186/s12984-016-0168-z

Boser, Q. A., Dawson, M. R., Schofield, J. S., Dziwenko, G. Y., & Hebert, J. S. (2020). Defining the design requirements for an assistive powered hand exoskeleton: A pilot explorative interview study and case series. *Prosthetics and Orthotics International*. doi: 10.1177/0309364620963943

Brown, E. a., Ross, J. D., Blum, R. a., Nam, Y., Wheeler, B. C., & Deweerth, S. P. (2008). Stimulus artifact elimination in a multi-electrode system. *IEEE Transactions on Biomedical Circuits and Systems*, *2*(1), 10–21. doi: 10.1109/TBCAS.2008.918285

Burr-Brown. (1990). *Implementations and applications of current sources and current receivers* (Tech. Rep.). Tucson,.

Byl, N., Roderick, J., Mohamed, O., Hanny, M., Kotler, J., Smith, A., ... Abrams, G. (2003). Effectiveness of Sensory and Motor Rehabilitation of the Upper Limb Following the Principles of Neuroplasticity: Patients Stable Poststroke. *Neurorehabilitation & Neural Repair*, *17*(3), 176–191. Retrieved from `http://nnr.sagepub.com/cgi/doi/10.1177/0888439003257137` doi: 10.1177/0888439003257137

Cabrera, J. A., Nadal, F., Muñoz, J. P., & Simon, A. (2007). Multiobjective constrained optimal synthesis of planar mechanisms using a new evolutionary algorithm. *Mechanism and Machine Theory*, *42*(7), 791–806. doi: 10.1016/j.mechmachtheory.2006.07.004

Cabrera, J. A., Ortiz, A., Nadal, F., & Castillo, J. J. (2011). An evolutionary algorithm for path synthesis of mechanisms. *Mechanism and Machine Theory*, *46*(2), 127–141. Retrieved from `http://dx.doi.org/10.1016/j.mechmachtheory.2010.10.003` doi: 10.1016/j.mechmachtheory.2010.10.003

Chantraine, A., Baribeault, A., Uebelhart, D., & Gremion, G. (1999). *Shoulder pain and dysfunction in hemiplegia: effects of functional electrical stimulation* (Vol. 80) (No. 3). doi: 10.1016/S0003-9993(99)90146-6

Chen, J. J., & Yu, N. Y. (1997). The validity of stimulus-evoked EMG for studying muscle fatigue characteristics of paraplegic subjects during dynamic cycling movement. *IEEE Transactions on Rehabilitation Engineering*, *5*(2), 170–178. doi: 10.1109/86.593288

Chen Chen, F., Appendino, S., Battezzato, A., Favetto, A., Mousavi, M., & Pescarmona, F. (2013). Constraint study for a hand exoskeleton: Human hand kinematics and dynamics. *Journal of Robotics*, *2013*. doi: 10.1155/2013/910961

Chester, N. C., & Durfee, W. K. (1997). Surface EMG as a fatigue indicator during FES-induced isometric muscle contractions. *Journal of Electromyography and Kinesiology*, *7*(1), 27–37. doi: 10.1016/S1050-6411(96)00016-8

Chiri, A., Vitiello, N., Member, S., Giovacchini, F., Roccella, S., Vecchi, F., ... Member, A. (2012). Mechatronic Design and Characterization of the Index Finger Module of a Hand Exoskeleton for Post-Stroke Rehabilitation. , *17*(5), 884–894.

Cifu, D. X., & Stewart, D. G. (1999). *Factors affecting functional outcome*

after stroke: A critical review of rehabilitation interventions (Vol. 80) (No. 5). Retrieved from http://www.sciencedirect.com/science/article/pii/S0003999399901016{%}0Ahttp://ac.els-cdn.com/S0003999399901016/1-s2.0-S0003999399901016-main.pdf?{_}tid=7724e78a-6c61-11e6-969e-00000aab0f6c{&}acdnat=1472307834{_}7e1aa600840caba30faa92ba489aa67f doi: 10.1016/S0003-9993(99)90101-6

Cobos, S., Ferre, M., Sánchez-Urán, M., & Ortego, J. (2007). Constraints for Realistic Hand Manipulation. *Proc. Presence 2007*, 369–370. Retrieved from http://www.temple.edu/ispr/prev{_}conferences/proceedings/2007/Cobos,Ferre,Sanchez-Uran,andOrtego.pdf

Connor, A., Douglas, S., & Gilmarti, M. (1995). The kinematic synthesis of path generating mechanisms using genetic algorithms. *Transactions on Information and Communications Technologies, 8*.

Cornman, J., Akhtar, A., & Bretl, T. (2017). A portable, arbitrary waveform, multichannel constant current electrotactile stimulator. *International IEEE/EMBS Conference on Neural Engineering, NER*, 300–303. doi: 10.1109/NER.2017.8008350

Del-Ama, A. J., Gil-Agudo, Á., Pons, J. L., & Moreno, J. C. (2014). Hybrid FES-robot cooperative control of ambulatory gait rehabilitation exoskeleton. *Journal of NeuroEngineering and Rehabilitation, 11*, 27. Retrieved from http://dx.doi.org/10.1186/1743-0003-11-27{%}5Cnhttp://jneuroengrehab.biomedcentral.com/track/pdf/10.1186/1743-0003-11-27?site=jneuroengrehab.biomedcentral.com doi: 10.1186/1743-0003-11-27

Del-Ama, A. J., Moreno, J. C., Koutsou, A. D., & de los Reyes-Guzman, A. (2013). Review of hybrid exoskeletons to restore gait following spinal cord injury. (June 2012). doi: 10.1682/JRRD.2011.03.0043

del Ama Servicio, A. J., Gómez-Soriano, J., Bravo-Esteban, E., & Moreno, J. C. (2013). A comparison of customized strategies to manage muscle fatigue in isometric artificially elicited muscle. *Journal of Automatic Control, 21*, 19–25.

de Luca, C. J. (1979). Physiology and Mathematics of Myoelectric Signals. *IEEE Transactions on Biomedical Engineering*, *BME-26*(6), 313–325. doi: 10.1109/TBME.1979.326534

DeMichele, G., & Troyk, P. (2004). Stimulus-resistant neural recording amplifier. , 3329–3332. doi: 10.1109/iembs.2003.1280857

Dewald, J. P., Sheshadri, V., Dawson, M. L., & Beer, R. F. (2001). Upper-limb discoordination in hemiparetic stroke: implications for neurorehabilitation. *Topics in stroke rehabilitation*, *8*(1), 1–12. doi: 10.1310/WA7K-NGDF-NHKK-JAGD

Dewey, H. M., Sherry, L. J., & Collier, J. M. (2007). Stroke rehabilitation 2007: What should it be? *International Journal of Stroke*, *2*(3), 191–200. doi: 10.1111/j.1747-4949.2007.00146.x

Díez, J. A., Blanco, A., Catalán, J. M., Badesa, F. J., Lledó, L. D., & García-Aracil, N. (2018). Hand exoskeleton for rehabilitation therapies with integrated optical force sensor. *Advances in Mechanical Engineering*, *10*(2), 1–11. doi: 10.1177/1687814017753881

Dimyan, M. A., & Cohen, L. G. (2011). *Neuroplasticity in the context of motor rehabilitation after stroke* (Vol. 7) (No. 2). Retrieved from `http://www.nature.com/doifinder/10.1038/nrneurol.2010.200` doi: 10.1038/nrneurol.2010.200

Dipietro, L., Krebs, H. I., Fasoli, S. E., Volpe, B. T., Stein, J., Bever, C., & Hogan, N. (2007). Changing motor synergies in chronic stroke. *Journal of Neurophysiology*, *98*(2), 757–768. doi: 10.1152/jn.01295.2006

Dobkin, B. H. (2004). *Strategies for stroke rehabilitation* (Vol. 3) (No. 9). doi: 10.1016/S1474-4422(04)00851-8

Doucet, B. M., Lam, A., & Griffin, L. (2012). Neuromuscular Electrical Stimulation for Skeletal Muscle Function. *Yale Journal of Biology and Medicine*, *85*(2), 201–215. doi: 10.1007/BF02371250

Dumitru, L., Iliescu, A., Dumitru, C., Badea, R., Săvulescu, S., Dinu, H., & Berteanu, M. (2014). Physiological considerations on Neuromuscular Electrical Stimulation (NMES) in muscular strength training. , *15*(2), 134–139.

du Plessis, T., Djouani, K., & Oosthuizen, C. (2021). A review of active hand exoskeletons for rehabilitation and assistance. *Robotics*, *10*(1). doi: 10.3390/robotics10010040

Ertas, I. H., Hocaoglu, E., & Patoglu, V. (2014). AssistOn-Finger: An under-actuated finger exoskeleton for robot-assisted tendon therapy. *Robotica*, *32*(08), 1363–1382. Retrieved from `http://www.journals.cambridge.org/abstract{_}S0263574714001957` doi: 10.1017/S0263574714001957

Eser, P. C., Donaldson, N. d. N., Knecht, H., & Stüssi, E. (2003). Influence of different stimulation frequencies on power output and fatigue during FES-cycling in recently injured SCI people. *IEEE Transactions on Neural Systems and Rehabilitation Engineering*, *11*(3), 236–240. doi: 10.1109/TNSRE.2003.817677

Estigoni, E. H., Fornusek, C., Hamzaid, N. A., Hasnan, N., Smith, R. M., & Davis, G. M. (2014). Evoked EMG versus muscle torque during fatiguing functional electrical stimulation-evoked muscle contractions and short-term recovery in individuals with spinal cord injury. *Sensors (Switzerland)*, *14*(12), 22907–22920. doi: 10.3390/s141222907

Estigoni, E. H., Fornusek, C., Smith, R. M., & Davis, G. M. (2011). Evoked EMG and muscle fatigue during isokinetic FES-cycling in individuals with SCI. *Neuromodulation*, *14*(4), 349–355. doi: 10.1111/j.1525-1403.2011.00354.x

Fajardo, J., Neto, A. R., Silva, W., Gomes, M., Fujiwara, E., & Rohmer, E. (2019). A wearable robotic glove based on optical FMG driven controller. *2019 4th IEEE International Conference on Advanced Robotics and Mechatronics, ICARM 2019*, 81–86. doi: 10.1109/ICARM.2019.8834067

Fang, H., Xie, Z., & Liu, H. (2009). An exoskeleton master hand for controlling DLR/HIT hand. *2009 IEEE/RSJ International Conference on Intelligent Robots and Systems, IROS 2009*, 3703–3708. doi: 10.1109/IROS.2009.5354624

Farina, D., Blanchietti, A., Pozzo, M., & Merletti, R. (2004). M-wave properties during progressive motor unit activation by transcutaneous stimulation. *Journal of Applied Physiology*, *97*(2), 545–555. doi: 10.1152/japplphysiol.00064.2004

Ferguson, P. W., Dimapasoc, B., Shen, Y., & Rosen, J. (2019). Design of a hand exoskeleton

for use with upper limb exoskeletons. *Biosystems and Biorobotics*, *22*(July), 276–280. doi: 10.1007/978-3-030-01887-0_53

Ferreira, A., Celeste, W. C., Cheein, F. A., Bastos-Filho, T. F., Sarcinelli-Filho, M., & Carelli, R. (2008). *Human-machine interfaces based on EMG and EEG applied to robotic systems* (Vol. 5) (No. 1). Retrieved from `http://jneuroengrehab.biomedcentral.com/articles/10.1186/1743-0003-5-10` doi: 10.1186/1743-0003-5-10

Fontana, M., Fabio, S., Marcheschi, S., & Bergamasco, M. (2017). Haptic Hand Exoskeleton for Precision Grasp Simulation. , *5*(November 2013), 1–9. doi: 10.1115/1.4024981

Fortune, B., Pretty, C., Chatfield, L., McKenzie, L., & Hayes, M. (2019). Low-cost active electromyography _ Elsevier Enhanced Reader.pdf. *HardwareX*, *6*(1).

Fortune, B. C., Pretty, C. G., Cameron, C. J., McKenzie, L. R., Chatfield, L. T., & Hayes, M. P. (2021). Electrode–skin impedance imbalance measured in the frequency domain. *Biomedical Signal Processing and Control*, *63*(August 2020). doi: 10.1016/j.bspc.2020.102202

Freeman, C. (2016). *Control System Design for Electrical Stimulation in Upper Limb Rehabilitation*. Retrieved from `http://link.springer.com/10.1007/978-3-319-25706-8` doi: 10.1007/978-3-319-25706-8

Frigo, C., Ferrarin, M., Frasson, W., Pavan, E., & Thorsen, R. (2000). EMG signals detection and processing for on-line control of functional electrical stimulation. *Journal of electromyography and kinesiology : official journal of the International Society of Electrophysiological Kinesiology*, *10*(5), 351–360. doi: 10.1016/S1050-6411(00)00026-2

Frisoli, A., Solazzi, M., Loconsole, C., & Barsotti, M. (2016). New generation emerging technologies for neurorehabilitation and motor assistance. *Acta Myologica*, *XXXI*, 141–144 New.

Futami, R., Seki, K., Kawanishi, T., Sugiyama, T., Cikajlo, I., & Handa, Y. (2005). Application of local EMG-driven FES to incompletely paralyzed lower extremities. *10th Annual Conference of the International FES Society July 2005 – Montreal, Canada*(July), 3–5. Retrieved from `http://ifess.org/proceedings/IFESS2005/IFESS2005{_}035{_}Futami`

.pdf

Giggins, O. M., Persson, U., & Caulfield, B. (2013). Biofeedback in rehabilitation. *Journal of NeuroEngineering and Rehabilitation*, *10*(1). Retrieved from http://jneuroengrehab.biomedcentral.com/articles/10.1186/1743-0003-10-60 doi: 10.1186/1743-0003-10-60

Gregory, C. M., & Bickel, C. S. (2005). Recruitment patterns in human skeletal muscle during electrical stimulation. *Phys Ther*, *85*(4), 358–64.

Gregson, J. M., Leathley, M. J., Moore, a. P., Smith, T. L., Sharma, a. K., & Watkins, C. L. (2000). Reliability of measurements of muscle tone and muscle power in stroke patients. *Age and ageing*, *29*(3), 223–228. doi: 10.1093/ageing/29.3.223

Grigoras, A. V., Irimia, D. C., Poboroniuc, M. S., & Popescu, C. D. (2016). Testing of a Hybrid FES-Robot Assisted Hand Motor Training Program in Sub-Acute Stroke Survivors. , *16*(4), 89–94.

Ha, K. H., Murray, S. A., & Goldfarb, M. (2016). An Approach for the Cooperative Control of FES with a Powered Exoskeleton during Level Walking for Persons with Paraplegia. *IEEE Transactions on Neural Systems and Rehabilitation Engineering*, *24*(4), 455–466. doi: 10.1109/TNSRE.2015.2421052

Hall, M. J., Levant, S., & DeFrances, C. J. (2012). Hospitalization for stroke in U.S. hospitals, 1989-2009. *NCHS data brief*(95), 1–8. Retrieved from http://www.ncbi.nlm.nih.gov/pubmed/22617404

Hartopanu, S., & Poboroniuc, M. (2015). New Issues on FES and Robotic Glove Device to Improve the Hand Rehabilitation in Stroke Patients. *Nternational Conference on Modern Power Systems*(May), 18–21.

Heffer, L. F., & Fallon, J. B. (2008). A novel stimulus artifact removal technique for high-rate electrical stimulation. *Journal of Neuroscience Methods*, *170*(2), 277–284. doi: 10.1016/j.jneumeth.2008.01.023

Hennemen, E., Somenm, G., & Carpenter, D. (1965). Functional significance of cell size in spinal motoneurons. *J Neurophysiol*, *28*(3), 560–580.

Hoffmann, U., Cho, W., Ramos-Murguialday, A., & Keller, T. (2011). Detection and removal of stimulation artifacts in electroencephalogram recordings. *Proceedings of the Annual International Conference of the IEEE Engineering in Medicine and Biology Society, EMBS*, 7159–7162. doi: 10.1109/IEMBS.2011.6091809

Hogan, S., & Siddharth, P. (2018). The social and economic costs of stroke. (April). Retrieved from `http://hdl.handle.net/11540/8929`

Hong, H., Rahal, M., Demosthenous, A., & Bayford, R. H. (2007). Floating Voltage-Controlled Current Sources for Electrical Impedance Tomography. (1), 208–211.

Hottowy, P., Skoczeń, A., Gunning, D. E., Kachiguine, S., Mathieson, K., Sher, A., ... Dąbrowski, W. (2012). Properties and application of a multichannel integrated circuit for low-artifact, patterned electrical stimulation of neural tissue. *Journal of Neural Engineering*, *9*(6), 066005. Retrieved from `http://stacks.iop.org/1741-2552/9/i=6/a=066005?key=crossref.90d57b30e604aa6f0351a4c7fa4ee182` doi: 10.1088/1741-2560/9/6/066005

Hu, X., & Tong, R. K. Y. (2014). FES in Rehabilitation Robotics. , 2–4.

Huamani, R. R., Bruno Castillo, S., Marcelo Delgado, D. C., Andrés Montoya, A., Meliza Madueño, T., Suarez, J. T., & Torres, R. R. S. (2019). Design and development of an optimized output stage for electrical stimulation. *6th IEEE Portuguese Meeting on Bioengineering, ENBENG 2019 - Proceedings*. doi: 10.1109/ENBENG.2019.8692535

Huang, H. C., Chung, K. C., Lai, D. C., & Sung, S. F. (2009). The Impact of Timing and Dose of Rehabilitation Delivery on Functional Recovery of Stroke Patients. *Journal of the Chinese Medical Association*, *72*(5), 257–264. Retrieved from `http://dx.doi.org/10.1016/S1726-4901(09)70066-8` doi: 10.1016/S1726-4901(09)70066-8

Huang, Y., Nam, C., Li, W., Rong, W., Xie, Y., Liu, Y., ... Hu, X. (2020). A comparison of the rehabilitation effectiveness of neuromuscular electrical stimulation robotic hand training and pure robotic hand training after stroke: A randomized controlled trial. *Biomedical Signal Processing and Control*, *56*, 101723. Retrieved from `https://doi.org/10.1016/j.bspc.2019.101723` doi: 10.1016/j.bspc.2019.101723

Hume, M. C., Gellman, H., McKellop, H., & Brumfield, R. H. (1990). Functional range of motion of the joints of the hand. *Journal of Hand Surgery*, *15*(2), 240–243. doi: 10.1016/0363-5023(90)90102-W

Ibitoye, M. O., Estigoni, E. H., Hamzaid, N. A., Wahab, A. K. A., & Davis, G. M. (2014). The effectiveness of FES-Evoked EMG potentials to assess muscle force and fatigue in individuals with spinal cord injury. *Sensors (Switzerland)*, *14*(7), 12598–12622. doi: 10.3390/s140712598

Ibitoye, M. O., Hamzaid, N. A., Hasnan, N., Wahab, A. K. A., & Davis, G. M. (2016). *Strategies for rapid muscle fatigue reduction during FES exercise in individuals with spinal cord injury: A systematic review* (Vol. 11) (No. 2). doi: 10.1371/journal.pone.0149024

Ilić, V., Jorgovanović, N., Antić, A., Morača, S., & Ungureanu, N. (2016). A novel fully fast recovery EMG amplifier for the control of neural prosthesis . *Tehnicki Vjesnik*, *23*(4), 1131–1137. Retrieved from https://www.scopus.com/inward/record.uri?eid=2-s2.0-84983059513{&}doi=10.17559{%}2FTV-20150710101906{&}partnerID=40{&}md5=7ea0198b33a15665a117a1cad0fe15e9 doi: 10.17559/TV-20150710101906

Iqbal, J., & Baizid, K. (2015). Stroke rehabilitation using exoskeleton-based robotic exercisers: Mini Review. *Biomedical Research*(December). Retrieved from http://www.biomedres.info/biomedical-research/stroke-rehabilitation-using-exoskeletonbased-robotic-exercisersmini-review.html

Iqbal, J., Khan, H., Tsagarakis, N. G., & Caldwell, D. G. (2014). ScienceDirect A novel exoskeleton robotic system for hand rehabilitation – Conceptualization to prototyping. *Integrative Medicine Research*, *34*(2), 79–89. Retrieved from http://dx.doi.org/10.1016/j.bbe.2014.01.003 doi: 10.1016/j.bbe.2014.01.003

Irimia, D. C., Poboroniuc, M. S., Serea, F., Baciu, A., & Olaru, R. (2016). Controlling a FES-EXOSKELETON rehabilitation system by means of brain-computer interface. *2016 International Conference and Exposition on Electrical and Power Engineering (EPE)*(Epe), 352–355. Retrieved from http://ieeexplore.ieee.org/document/7781361/ doi: 10.1109/ICEPE.2016.7781361

Jo, I., Park, Y., Lee, J., & Bae, J. (2019). *A portable and spring-guided hand exoskeleton for exercising flexion/extension of the fingers* (Vol. 135). doi: 10.1016/j.mechmachtheory.2019.02.004

Johansson, G. (2015). *Clinical and kinematic assessments of upper limb function in persons with post-stroke symptoms.*

Jones, C. L., Wang, F., Morrison, R., Sarkar, N., & Kamper, D. G. (2014). Design and development of the cable actuated finger exoskeleton for hand rehabilitation following stroke. *IEEE/ASME Transactions on Mechatronics*, *19*(1), 131–140. doi: 10.1109/TMECH.2012.2224359

Jubeau, M., Sartorio, A., Marinone, P. G., Agosti, F., Van Hoecke, J., Nosaka, K., & Maffiuletti, N. A. (2008). 75.full.pdf. *J Appl Physiol*, *104*(1), 75–81.

Kamono, A., Muraoka, Y., Tomita, Y., Shimaoka, H., Uchida, S., & Ota, T. (2003). Development of EMG-Controlled Electrical Stimulation System. In *Sice 2002. proceedings of the 41st sice annual conference.* IEEE.

Kamper, D. G., Cruz, E. G., & Siegel, M. P. (2003). Stereotypical fingertip trajectories during grasp. *Journal of neurophysiology*, *90*(6), 3702–3710. doi: 10.1152/jn.00546.2003

Kamper, D. G., Fischer, H. C., Cruz, E. G., & Rymer, W. Z. (2006). Weakness Is the Primary Contributor to Finger Impairment in Chronic Stroke. *Archives of Physical Medicine and Rehabilitation*, *87*(9), 1262–1269. doi: 10.1016/j.apmr.2006.05.013

Kawasaki, H., Ito, S., & Ishigure, Y. (2007). Development of a Hand Motion Assist Robot for Rehabilitation Therapy by Patient Self-Motion Control. , *00*(c), 234–240.

Keller, T., & Veneman, J. (2012). Robotics for Neurorehabilitation: Current State and Future Challenges. *Applied Mechanics and Materials*, *245*(May 2016), 3–8. Retrieved from `http://www.scientific.net/AMM.245.3` doi: 10.4028/www.scientific.net/AMM.245.3

Kessner, S. S., Bingel, U., & Thomalla, G. (2016). Somatosensory deficits after stroke: a scoping review. *Topics in Stroke Rehabilitation*, *23*(2), 136–146. Retrieved from `http://dx.doi.org/10.1080/10749357.2015.1116822{%}5Cnhttp://www.tandfonline.com/doi/full/10.1080/10749357.2015.1116822` doi: 10.1080/

10749357.2015.1116822

Knaflitz, M., Knaflitz, M., Merletti, R., & Merletti, R. (1988). Suppression of Simulation Artifacts from Myoelectric-Evoked Potential Recordings. *IEEE Transactions on Biomedical Engineering*, *35*(9), 758–763. doi: 10.1109/10.7278

Knaflitz, M., Merletti, R., Luca, C. J. D. E., Iti, R. M., & Carlo, J. (1990). Inference of motor unit recruitment order in voluntary and electrically elicited contractions. *Journal of Applied Physiology*, *68*(4), 1657–1667.

Krakauer, J. W. (2005). Arm Function after Stroke From Physiology. , *25*(4), 384–395.

Krenn, M., & Löfler, S. (2013). Current versus voltage controlled electrical stimulation of the anterior thigh. (March 2017).

Kung, P. C., Lin, C. C. K., & Ju, M. S. (2010). Neuro-rehabilitation robot-assisted assessments of synergy patterns of forearm, elbow and shoulder joints in chronic stroke patients. *Clinical Biomechanics*, *25*(7), 647–654. Retrieved from `http://dx.doi.org/10.1016/j.clinbiomech.2010.04.014` doi: 10.1016/j.clinbiomech.2010.04.014

Kuo, C. C., Kung, H. Y., Wu, H. C., & Wang, M. J. (2020). Developing a hand sizing system for a hand exoskeleton device based on the Kansei Engineering method. *Journal of Ambient Intelligence and Humanized Computing*(168). Retrieved from `https://doi.org/10.1007/s12652-020-02354-8` doi: 10.1007/s12652-020-02354-8

Kuthe, C. D., Uddanwadiker, R. V., & Ramteke, A. A. (2018). Surface electromyography based method for computing muscle strength and fatigue of biceps brachii muscle and its clinical implementation. *Informatics in Medicine Unlocked*, *12*(June), 34–43. Retrieved from `https://doi.org/10.1016/j.imu.2018.06.004` doi: 10.1016/j.imu.2018.06.004

Kwakkel, G. (2009a). Intensity of practice after stroke:More is better. *Schweizer Archiv Fur Neurologie und Psychiatrie*, *160*(7), 295–8. doi: 10.1080/09638280500534861

Kwakkel, G. (2009b). Intensity of practice after stroke: More is better. *Schweizer Archiv fur Neurologie und Psychiatrie*, *160*(7), 295–298. doi: 10.1080/09638280500534861

Lalitharatne, T. D., Teramoto, K., Hayashi, Y., & Kiguchi, K. (2013). Towards Hybrid EEG-

EMG-Based Control Approaches to be Used in Bio-robotics Applications: Current Status, Challenges and Future Directions. *PALADYN Journal of Behavioral Robotics*, *4*(2), 147–154.

Lang, C. E., Bland, M. D., Bailey, R. R., Schaefer, S. Y., & Birkenmeier, R. L. (2013). *Assessment of upper extremity impairment, function, and activity after stroke: Foundations for clinical decision making* (Vol. 26) (No. 2). doi: 10.1016/j.jht.2012.06.005

Langzam, E., Isakov, E., & Mizrahi, J. (2006). Evaluation of methods for extraction of the volitional EMG in dynamic hybrid muscle activation. *Journal of neuroengineering and rehabilitation*, *3*, 27. Retrieved from `http://www.pubmedcentral.nih.gov/articlerender.fcgi?artid=1713246{&}tool=pmcentrez{&}rendertype=abstract` doi: 10.1186/1743-0003-3-27

Li, J., Zheng, R., Zhang, Y., & Yao, J. (2011). iHandRehab: An interactive hand exoskeleton for active and passive rehabilitation. *IEEE International Conference on Rehabilitation Robotics*(50975009). doi: 10.1109/ICORR.2011.5975387

Li, M., He, B., Liang, Z., Zhao, C. G., Chen, J., Zhuo, Y., ... Althoefer, K. (2019). An attention-controlled hand exoskeleton for the rehabilitation of finger extension and flexion using a rigid-soft combined mechanism. *Frontiers in Neurorobotics*, *13*(May), 1–13. doi: 10.3389/fnbot.2019.00034

Li, Z., Hayashibe, M., Fattal, C., & Guiraud, D. (2014). Muscle Fatigue Tracking with Evoked EMG via Recurrent Neual Network: Toward Personalized Neuroprosthetics. (April), 38–46.

Lin, J., Wu, Y., & Huang, T. S. (2000). Modeling the constraints of human hand motion. *Proceedings - Workshop on Human Motion, HUMO 2000*, 121–126. doi: 10.1109/HUMO.2000.897381

Liu, J. L. J., & Zhang, Y. Z. Y. (2007). Mapping human hand motion to dexterous robotic hand. *2007 IEEE International Conference on Robotics and Biomimetics (ROBIO)*, 829–834. doi: 10.1109/ROBIO.2007.4522270

Lucas, L., Dicicco, M., & Matsuoka, Y. (2004). An EMG-Controlled Hand Exoskeleton for

Natural Pinching. *Journal of Robotics and Mechatronics*, *16*(5), 1–7. doi: 10.20965/jrm.2004.p0482

Luo, R. (2013). *Can the voluntary drive to a paretic muscle be estimated from the myoelectric signal during stimulation?* (Unpublished doctoral dissertation).

Maciejasz, P., Eschweiler, J., Gerlach-Hahn, K., Jansen-Troy, A., & Leonhardt, S. (2014). A survey on robotic devices for upper limb rehabilitation. *Journal of neuroengineering and rehabilitation*, *11*(1), 3. Retrieved from `http://www.jneuroengrehab.com/content/11/1/3` doi: 10.1186/1743-0003-11-3

Maffiuletti, N. A. (2010). Physiological and methodological considerations for the use of neuromuscular electrical stimulation. *European Journal of Applied Physiology*, *110*(2), 223–234. doi: 10.1007/s00421-010-1502-y

Malesevic, N. M., Popovic, L. Z., Schwirtlich, L., & Popovic, D. B. (2010). *Distributed low-frequency functional electrical stimulation delays muscle fatigue compared to conventional stimulation* (Vol. 42) (No. 4). doi: 10.1002/mus.21736

Mandrile, F., Farina, D., Pozzo, M., & Merletti, R. (2003). Stimulation Artifact in Surface EMG Signal: Effect of the Stimulation Waveform, Detection System, and Current Amplitude Using Hybrid Stimulation Technique. *IEEE Transactions on Neural Systems and Rehabilitation Engineering*, *11*(4), 407–415. doi: 10.1109/TNSRE.2003.819791

Marchis, C. D., Monteiro, T. S., Simon-Martinez, C., Conforto, S., & Gharabaghi, A. (2016). *Multi-contact_functional_electrical_stimulation_fo.pdf.*

McIlroy, W., & Verrier, M. C. (2005). Upper Extremity Functional Electrical Stimulation: Case Study of Neuromuscular Restorative Therapy. In *10th annual conference of the international fes society.* Montreal.

Mckenzie, L. R., Fortune, B. C., Chatfield, L. T., & Pretty, C. G. (2021). Evoked Electromyographic Fatigue Indices During Intermittent Stimulation Towards Dynamic Wrist Contractions. In *Ieee/asme international conference on mechatronic and embedded systems and applications (mesa).*

McKenzie, L. R., Pretty, C. G., Fortune, B. C., & Chatfield, L. T. (2021). Low-cost Stimulation

Resistant Electromyography. *HardwareX*, e00178. Retrieved from https://doi.org/10.1016/j.ohx.2021.e00178 doi: 10.1016/j.ohx.2021.e00178

Mclean, L., Scott, R., & Parker, P. (1996). Stimulus artifact reduction in evoked potential measurements. *Archives of physical medicine and rehabilitation*, *77*(12), 1286–1292. Retrieved from http://linkinghub.elsevier.com/retrieve/pii/S000399939690194X{%}5Cnpapers3://publication/doi/10.1016/S0003-9993(96)90194-X

Megill, K. C., Cummins, K. L., Dorfman, L. J., Berlizot, B. B., Luetkemeyer, K., Nishimura, D. G., & Widrow, B. (1982). On the Nature and Elimination of Stimulus Artifact in Nerve Signals Evoked and Recorded Using Surface Electrodes. *IEEE Transactions on Biomedical Engineering*, *BME-29*(2), 129–137. doi: 10.1109/TBME.1982.325019

Merletti, R., & Farina, D. (2016a). *Surface Electromyography: Physiology, Engineering, and Applications.*

Merletti, R., & Farina, D. (2016b). *Surface Electromyography: Physiology, Engineering, and Applications.* Retrieved from MERLETTI

Merletti, R., Fiorito, A., Lo Conte, L. R., & Cisari, C. (1998). Repeatability of electrically evoked EMG signals in the human vastus medialis muscle. *Muscle and Nerve*, *21*(2), 184–193. doi: 10.1002/(SICI)1097-4598(199802)21:2⟨184::AID-MUS5⟩3.0.CO;2-7

Merletti, R., Knaflitz, M., & De Luca, C. J. (1990). Myoelectric manifestations of fatigue in voluntary and electrically elicited contractions. *Journal of Applied Physiology*, *69*(5), 1810–1820. doi: 10.1152/jappl.1990.69.5.1810

Mesin, L., Merlo, E., Merletti, R., & Orizio, C. (2010). *Investigation of motor unit recruitment during stimulated contractions of tibialis anterior muscle* (Vol. 20) (No. 4). doi: 10.1016/j.jelekin.2009.11.008

Meyer, S., Karttunen, A. H., Thijs, V., Feys, H., & Verheyden, G. (2014). How do somatosensory deficits in the arm and hand relate to upper limb impairment, activity, and participation problems after stroke? A systematic review. *Phys Ther*, *94*(9), 1220–31. Retrieved from http://www.ncbi.nlm.nih.gov/pubmed/24764072 doi:

10.2522/ptj.20130271

Minzly, J., Mizrahi, J., Hakim, N., & Liberson, A. (1993). Stimulus artefact suppressor for EMG recording during FES by a constant-current stimulator. *Medical and Biological Engineering and Computing*, *31*(1), 72–75. doi: 10.1007/BF02446897

Miura, N., & Watanabe, T. (2016). Potential of M-Wave Elicited by Double Pulse for Muscle Fatigue Evaluation in Intermittent Muscle Activation by Functional Electrical Stimulation for Motor Rehabilitation. *Journal of Medical Engineering*, *2016*, 1–12. Retrieved from `http://www.hindawi.com/journals/jme/2016/6957287/` doi: 10.1155/2016/6957287

Mizrahi, J., Levin, O., Aviram, A., Isakov, E., & Susak, Z. (1997). Muscle fatigue in interrupted stimulation: Effect of partial recovery on force and EMG dynamics. *Journal of Electromyography and Kinesiology*, *7*(1), 51–65. doi: 10.1016/S1050-6411(96)00018-1

Moreno-SanJuan, V., Cisnal, A., Fraile, J. C., Pérez-Turiel, J., & De-la Fuente, E. (2021). Design and characterization of a lightweight underactuated RACA hand exoskeleton for neurorehabilitation. *Robotics and Autonomous Systems*, *143*, 103828. Retrieved from `https://doi.org/10.1016/j.robot.2021.103828` doi: 10.1016/j.robot.2021.103828

Mottaghi, S., & Hofmann, U. G. (2015). Dynamically Adjusted , Scalable Electrical Stimulator for Exciteable Tissue. In *Ieee embs conference on neural engineering* (pp. 22–24). Montpellier.

Mozaffari, M. (2013). *Synthesis of Hand Exoskeleton for the Rehabilitation of Post-Stroke Patients* (Doctoral dissertation, Università di Bologna). doi: 10.1007/978-3-7091-1379-0

Mühlbauer, P., Löhnert, L., Siegle, C., Stewart, K. W., & Pott, P. P. (2020). Demonstrator of a Low-Cost Hand Prosthesis. *IFAC-PapersOnLine*, *53*(2), 15998–16003. Retrieved from `https://doi.org/10.1016/j.ifacol.2020.12.398` doi: 10.1016/j.ifacol.2020.12.398

Muraoka, Y. (2002). Development of an EMG recording device from stimulation electrodes for functional electrical stimulation. *Frontiers of medical and biological engineering : the international journal of the Japan Society of Medical Electronics and Biological*

Engineering, *11*(4), 323–333.

Muraoka, Y., Tanabe, S., Yamaguchi, T., & Takeda, K. (2013). Specifications of an electromyogram-driven neuromuscular stimulator for upper limb functional recovery. *Conference proceedings : ... Annual International Conference of the IEEE Engineering in Medicine and Biology Society. IEEE Engineering in Medicine and Biology Society. Annual Conference*, *2013*, 277–280. doi: 10.1109/EMBC.2013.6609491

Nag, S., Sikdar, S. K., Thakor, N. V., Rao, V. R., & Sharma, D. (2015). Sensing of Stimulus Artifact Suppressed Signals From Electrode Interfaces. *IEEE Sensors Journal*, *15*(7), 3734–3742. doi: 10.1109/JSEN.2015.2399248

Nam, C., Rong, W., Li, W., Xie, Y., Hu, X., & Zheng, Y. (2017). The effects of upper-limb training assisted with an electromyography-driven neuromuscular electrical stimulation robotic hand on chronic stroke. *Frontiers in Neurology*, *8*(DEC). doi: 10.3389/fneur.2017.00679

Nef, T., Quinter, G., Müller, R., & Riener, R. (2009). Effects of arm training with the robotic device ARMin i in chronic stroke: Three single cases. *Neurodegenerative Diseases*, *6*(5-6), 240–251. doi: 10.1159/000262444

Neto, A. R., Fajardo, J., Ferman, V., Fujiwara, E., & Rohmer, E. (2019). A hybrid control strategy for tendon-actuated robotic glove and functional electrical stimulation - A preliminary study. *2019 4th IEEE International Conference on Advanced Robotics and Mechatronics, ICARM 2019*, 244–249. doi: 10.1109/ICARM.2019.8834141

Nishida, J., & Suzuki, K. (2016). BioSync: Wearable haptic I/O device for synchronous kinesthetic interaction. *Proceedings - IEEE Virtual Reality*, *2016-July*, 243–244. doi: 10.1109/VR.2016.7504744

Nishida, J., & Suzuki, K. (2017). bioSync. *Proceedings of the 2017 CHI Conference on Human Factors in Computing Systems - CHI '17*, 3316–3327. Retrieved from `http://dl.acm.org/citation.cfm?doid=3025453.3025829` doi: 10.1145/3025453.3025829

Norouzi-Gheidari, N., Archambault, P. S., & Fung, J. (2012). Effects of robot-assisted therapy on stroke rehabilitation in upper limbs: systematic review and meta-analysis

of the literature. *Journal of rehabilitation research and development*, *49*(4), 479–96. Retrieved from http://www.ncbi.nlm.nih.gov/pubmed/22773253 doi: 10.1682/JRRD.2010.10.0210

Obinata, G., Fukada, S., Matsunaga, T., Iwami, T., Shimada, Y., Miyawaki, K., ... Nakayama, A. (2007). Hybrid control of powered orthosis and functional neuromuscular stimulation for restoring gait. *Annual International Conference of the IEEE Engineering in Medicine and Biology - Proceedings*, 4879–4882. doi: 10.1109/IEMBS.2007.4353433

O'Connor, D., Lennon, O., Minogue, C., & Caulfield, B. (2020). Design considerations for the development of neuromuscular electrical stimulation (NMES) exercise in cancer rehabilitation. *Disability and Rehabilitation*, *0*(0), 1–10. Retrieved from https://doi.org/10.1080/09638288.2020.1726510 doi: 10.1080/09638288.2020.1726510

O'Keeffe, D. T., Lyons, G. M., Donnelly, A. E., & Byrne, C. A. (2001). Stimulus artifact removal using a software-based two-stage peak detection algorithm. *Journal of Neuroscience Methods*, *109*(2), 137–145. doi: 10.1016/S0165-0270(01)00407-1

Orlando, M. F., Akolkar, H., Dutta, A., Saxena, A., & Behera, L. (2010). Optimal design and control of a hand exoskeleton. *2010 IEEE Conference on Robotics, Automation and Mechatronics*, 72–77. Retrieved from http://ieeexplore.ieee.org/lpdocs/epic03/wrapper.htm?arnumber=5513211 doi: 10.1109/RAMECH.2010.5513211

Ortiz, A., Cabrera, J. A., Nadal, F., & Bonilla, A. (2013). *Dimensional synthesis of mechanisms using Differential Evolution with auto-adaptive control parameters* (Vol. 64). doi: 10.1016/j.mechmachtheory.2013.02.002

Ortmanns, M. (2007). CHARGE BALANCING IN FUNCTIONAL ELECTRICAL STIMULATORS : A COMPARATIVE STUDY Maurits Ortmanns Department of Microsystems Engineering University of Freiburg , 79110 Freiburg , Germany. *Circuits and Systems, 2007. ISCAS 2007*, 573–576. doi: 10.1109/ISCAS.2007.378802

Osuagwu, B. A., Whicher, E., & Shirley, R. (2020). Active proportional electromyogram controlled functional electrical stimulation system. *Scientific Reports*, *10*(1), 1–15. Retrieved from https://doi.org/10.1038/s41598-020-77664-0 doi: 10.1038/s41598

-020-77664-0

Patriciu, A., Member, S., Yoshida, K., Struijk, J. J., Demonte, T. P., Joy, M. L. G., & Stødkilde-jørgensen, H. (2005). Skin Burns Under Surface Electrodes. *Imaging*, *52*(12), 2024–2031.

Pease, R. (2013). *AN-1515 A Comprehensive Study of the Howland Current Pump* (Tech. Rep. No. April). Retrieved from `www.ti.com/lit/an/snoa474a/snoa474a.pdf`

Peckham, P. H., & Knutson, J. S. (2005). Functional Electrical Stimulation for Neuromuscular Applications. *Annual Review of Biomedical Engineering*, *7*(1), 327–360. Retrieved from `http://www.annualreviews.org/doi/10.1146/annurev.bioeng.6.040803.140103` doi: 10.1146/annurev.bioeng.6.040803.140103

Pertuz, S. A., Llanos, C. H., & Muñoz, D. M. (2016). Bioinspired Optimization of a Robotic Finger Mechanism. *Proceedings - 13th Latin American Robotics Symposium and 4th Brazilian Symposium on Robotics, LARS/SBR 2016*, 199–204. doi: 10.1109/LARS-SBR.2016.40

Phinyomark, A., Thongpanja, S., Hu, H., Phukpattaranont, P., & Limsakul, C. (2012). The Usefulness of Mean and Median Frequencies in Electromyography Analysis. *Computational Intelligence in Electromyography Analysis - A Perspective on Current Applications and Future Challenges*(December 2014). doi: 10.5772/50639

Piast, M., Kustrzeba-Wójcicka, I., Matusiewicz, M., & Banaś, T. (2005). Molecular evolution of enolase. *Acta Biochimica Polonica*, *52*(2), 507–513. doi: 10.1016/S

Pollock, A., Farmer, S., Brady, M., Langhorne, P., Mead, G., Mehrholz, J., & VanWijck, F. (2013). *Interventions for improving upper limb function after stroke (Protocol).* JohnWiley & Sons.

Popovič, D., & Schwirtlich, L. (1993). Design and Evaluation of the Self-Fitting Modular Orthosis (SFMO). *IEEE Transactions on Rehabilitation Engineering*, *1*(3), 165–174. doi: 10.1109/86.279265

Popovic, D., Tomovic, R., & Schwirtlich, L. (1989). Hybrid Assistive System-The Motor Neuroprosthesis. (7).

Popović, D. B., & Popović, M. B. (2006). Hybrid assistive systems for rehabilitation: Lessons learned from functional electrical therapy in hemiplegics. *Annual International Conference of the IEEE Engineering in Medicine and Biology - Proceedings*, 2146–2149. doi: 10.1109/IEMBS.2006.259550

Pouliquen, P., Etienne-cummings, R., & Vogelstein, J. (2008). Practical considerations for the use of a Howland current source for neuro-stimulation. In *Eee biomedical circuits and systems conference* (pp. 33–36). Baltimore. doi: 10.1109/BIOCAS.2008.4696867

Prado-medeiros, C. L., Silva, M. P., Lessi, G. C., Alves, M. Z., Tannus, A., Lindquist, A. R., & Salvini, T. F. (2012). Muscle Atrophy and Functional Deficits of Knee Extensors and Flexors in People With Chronic Stroke. , *92*(3), 429–439.

Prange, G. B., Jannink, M. J. A., Groothuis-Oudshoorn, C. G. M., Hermens, H. J., & IJzerman, M. J. (2006). Systematic review of the effect of robot-aided therapy on recovery of the hemiparetic arm after stroke. *Journal of Rehabilitation Research and Development*, *43*(2), 171–184.

Quandt, F., & Hummel, F. C. (2014). *The influence of functional electrical stimulation on hand motor recovery in stroke patients: a review* (Vol. 6) (No. 1). Retrieved from `http://etsmjournal.biomedcentral.com/articles/10.1186/2040-7378-6-9` doi: 10.1186/2040-7378-6-9

Rajsic, S., Gothe, H., Borba, H. H., Sroczynski, G., Vujicic, J., Toell, T., & Siebert, U. (2019). Economic burden of stroke: a systematic review on post-stroke care. *European Journal of Health Economics*, *20*(1), 107–134. Retrieved from `http://dx.doi.org/10.1007/s10198-018-0984-0` doi: 10.1007/s10198-018-0984-0

Ranzani, R., Lambercy, O., Metzger, J. C., Califfi, A., Regazzi, S., Dinacci, D., ... Gassert, R. (2020). Neurocognitive robot-assisted rehabilitation of hand function: A randomized control trial on motor recovery in subacute stroke. *Journal of NeuroEngineering and Rehabilitation*, *17*(1), 1–14. doi: 10.1186/s12984-020-00746-7

Rätz, R., Conti, F., Müri, R. M., & Marchal-Crespo, L. (2021). A Novel Clinical-Driven Design for Robotic Hand Rehabilitation: Combining Sensory Training, Effortless

Setup, and Large Range of Motion in a Palmar Device. *Frontiers in Neurorobotics*, *15*(December), 1–22. doi: 10.3389/fnbot.2021.748196

Reaz, M. B. I., Hussain, M. S., & Mohd-Yasin, F. (2006). Techniques of EMG signal analysis: detection, processing, classification and applications (Correction). *Biological Procedures Online*, *8*(1), 163–163. Retrieved from `http://www.springerlink.com/index/10.1251/bpo124` doi: 10.1251/bpo124

Refour, E., Asme, M., Tech, V., Sebastian, B., Asme, M., Tech, V., ... Tech, V. (2018). Two-Digit Robotic Exoskeleton Glove Mechanism : Design and Integration. , *10*(April), 1–9. doi: 10.1115/1.4038775

Rijpkema, H., & Girard, M. (1991). Computer animation of knowledge-based human grasping. *ACM SIGGRAPH Computer Graphics*, *25*(4), 339–348. doi: 10.1145/127719.122754

Rong, W., Li, W., Pang, M., Hu, J., Wei, X., Yang, B., ... Hu, X. (2017). A Neuromuscular Electrical Stimulation (NMES) and robot hybrid system for multi-joint coordinated upper limb rehabilitation after stroke. *Journal of NeuroEngineering and Rehabilitation*, *14*(1), 34. Retrieved from `http://jneuroengrehab.biomedcentral.com/articles/10.1186/s12984-017-0245-y` doi: 10.1186/s12984-017-0245-y

Rong, W., Tong, K. Y., Hu, X. L., & Ho, S. K. (2015). Disability and Rehabilitation : Assistive Technology Effects of electromyography-driven robot-aided hand training with neuromuscular electrical stimulation on hand control performance after chronic stroke Effects of electromyography-driven robot-aided han. , *3107*(April 2017). doi: 10.3109/17483107.2013.873491

Ryan, A. S., Dobrovolny, C. L., Smith, G. V., Silver, K. H., & Macko, R. F. (2002). Hemiparetic muscle atrophy and increased intramuscular fat in stroke patients. *Archives of Physical Medicine and Rehabilitation*, *83*(12), 1703–1707. doi: 10.1053/apmr.2002.36399

Sandoval-Gonzalez, O., Jacinto-Villegas, J., Herrera-Aguilar, I., Portillo-Rodiguez, O., Tripicchio, P., Hernandez-Ramos, M., ... Avizzano, C. (2016). Design and development of a hand exoskeleton robot for active and passive rehabilitation. *International Journal*

of Advanced Robotic Systems, *13*(2). doi: 10.5772/62404

Sarac, M., Solazzi, M., & Frisoli, A. (2019). Design Requirements of Generic Hand Exoskeletons and Survey of Hand Exoskeletons for Rehabilitation, Assistive, or Haptic Use. *IEEE Transactions on Haptics*, *12*(4), 400–413. doi: 10.1109/TOH.2019.2924881

Sarac, M., Solazzi, M., Sotgiu, E., Bergamasco, M., & Frisoli, A. (2017). Design and kinematic optimization of a novel underactuated robotic hand exoskeleton. *Meccanica*, *52*(3), 749–761. doi: 10.1007/s11012-016-0530-z

Sarakoglou, I., Brygo, A., Mazzanti, D., Hernandez, N. G., Caldwell, D. G., & Tsagarakis, N. G. (2016). Hexotrac: A highly under-actuated hand Exoskeleton for finger tracking and force feedback. *IEEE International Conference on Intelligent Robots and Systems*, *2016-Novem*, 1033–1040. doi: 10.1109/IROS.2016.7759176

Sathian, K., Buxbaum, L. J., Cohen, L. G., Krakauer, J. W., Lang, C. E., Corbetta, M., & Fitzpatrick, S. M. (2014). Neurological Principles and Rehabilitation of Action Disorders: Common Clinical Deficits. *Neurorehabil Neural Repair*, *19*(6), 431–444. doi: 10.1016/j.cardfail.2013.04.005.Sleep

Schabowsky, C. N., Godfrey, S. B., Holley, R. J., & Lum, P. S. (2010). Development and pilot testing of HEXORR : Hand EXOskeleton Rehabilitation Robot. , 1–16.

Schauer, T. (2017). Sensing motion and muscle activity for feedback control of functional electrical stimulation: Ten years of experience in Berlin. *Annual Reviews in Control*, *44*, 355–374. doi: 10.1016/j.arcontrol.2017.09.014

Schauer, T., Seel, T., Bunt, N. D., Müller, P., & Moreno, J. C. (2016). Realtime EMG analysis for transcutaneous electrical stimulation assisted gait training in stroke patients. *IFAC-PapersOnLine*, *49*(32), 183–187. doi: 10.1016/j.ifacol.2016.12.211

Sennels, S., Biering-Sorensen, F., Andersen, O. T., & Hansen, S. D. (1997). Functional neuromuscular stimulation controlled by surface electromyographic signals produced by volitional activation of the same muscle: Adaptive removal of the muscle response from the recorded EMG-signal. *IEEE Transactions on Rehabilitation Engineering*, *5*(2), 195–206. doi: 10.1109/86.593293

Sennels, S., Biering-Sorensen, F., Hansen, S., & Andersen, O. (1996). Adaptive filters for muscle response suppression. *Proceedings of 18th Annual International Conference of the IEEE Engineering in Medicine and Biology Society*, *2*, 518–520. Retrieved from http://ieeexplore.ieee.org/document/651844/ doi: 10.1109/IEMBS.1996.651844

Serea, F. (2014). Preliminary Tests on a Hybrid Upper Arm Exoskeleton for Upper Arm Rehabilitation for Disabled Patients. (Epe), 16–18.

Shair, E. F., Ahmad, S. A., Marhaban, M. H., Tamrin, S. B., & Abdullah, A. R. (2017). EMG processing based measures of fatigue assessment during manual lifting. *BioMed Research International*, *2017*. doi: 10.1155/2017/3937254

Shalaby, R., Shauer, T., Wolfgang, L., & Raisch, J. (2011). Amplifier design for EMG recording from stimulation electrodes during functional electrical stimulation leg cycling ergometry. *Biomed Tech*, *56*(1), 23–33.

Shao, T., Li, X., Yokoi, H., & Zhang, D. (2016). FESleeve : A Functional Electrical Stimulation System with Multi-electrode Array for Finger Motion Control. , 191–199. doi: 10.1007/978-3-319-43518-3

Sheffler, L. R., & Chae, J. (2007). Neuromuscular electrical stimulation in neurorehabilitation. *Muscle & Nerve*, *35*(5), 562–590. Retrieved from http://doi.wiley.com/10.1002/mus.20758 doi: 10.1002/mus.20758

Shete, S. S., & Kulkarni, S. A. (2015). Dimensional Synthesis of Four Bar Mechanism Using Genetic Algorithm. , *5013*(4), 123–126.

Shiakolas, P. S., Koladiya, D., & Kebrle, J. (2005). On the optimum synthesis of six-bar linkages using differential evolution and the geometric centroid of precision positions technique. *Mechanism and Machine Theory*, *40*(3), 319–335. doi: 10.1016/j.mechmachtheory.2004.07.005

Sidher, A. (2017). Prosthesis Design and Object Recognition Based Grasping of a 3D Printed Anthropomorphic Artificial Hand.

Sonawale, K. H., & McCarthy, J. M. (2014). DETC 2014-35523. In *Proceedings of the asme 2014 international design & engineering technical conferences & computers and*

information in engineering conference idetc/cie (pp. 1–13). Buffalo New York.

Stewart, A. M., Pretty, C. G., Chen, X., & Member, S. (2016). Design And Testing Of A Novel , Low-cost , Low-voltage , Functional Electrical Stimulator.

Stoica, P., & Moses, R. (2005). *Spectral Analysis of Signals* (Vol. 24) (No. 1). PRENTICE HALL. doi: 10.1109/msp.2007.273066

Storn, R., & Price, K. (1997a). Differential Evolution - A simple and efficient adaptive scheme for global optimization over continuous spaces. *Journal of Global Optimization*, *11*(4), 341–359. doi: 10.1023/A:1008202821328

Storn, R., & Price, K. (1997b). Differential Evolution - A Simple and Efficient Heuristic for Global Optimization over Continuous Spaces. *Journal of Global Optimization*, *11*(4), 341–359. doi: 10.1023/A:1008202821328

Stroke Foundation. (2017). Australian Clinical Guidelines for Stroke Management 2017. Chapter 5 of 8: Rehabilitation. , 1–249. Retrieved from `www.informme.org.au`

Stroke Foundation of New Zealand. (2016). *Stroke Foundation campaign going nationwide.* Retrieved 2017-07-25, from `http://www.stroke.org.nz/stroke-foundation-campaign-going-nationwide`

Stroke Foundation of New Zealand. (2017). *Facts about stroke in New Zealand.* Retrieved 2017-07-25, from `http://www.stroke.org.nz/stroke-facts-and-fallacies`

Stroke Foundation of New Zealand. (2020). *Costs of Stroke in New Zealand 2020* (Tech. Rep.).

Strong, K., Mathers, C., & Bonita, R. (2007). Preventing stroke: saving lives around the world. *Lancet Neurology*, *6*(2), 182–187. doi: 10.1016/S1474-4422(07)70031-5

Suhaimi, R., A.R, A., Adnan, N. H., Shahriman, D., & Bakar, J. A. A. (2014). Analysis of EMG-based Muscles Activity for Stroke Rehabilitation. In *2nd international conference on electronic design (iced)* (pp. 167–170).

Sullivan, J. E., & Hedman, L. D. (2008). Sensory Dysfunction Following Stroke: Incidence, Significance, Examination, and Intervention. *Topics in Stroke Rehabilitation*, *15*(3), 200–217. Retrieved from `http://ejournals.ebsco.com/direct.asp`

?ArticleID=43A68F65252FD9249F9C doi: 10.1310/tsr1503-200

Taheri, H., Rowe, J. B., Gardner, D., Chan, V., Gray, K., Bower, C., ... Wolbrecht, E. T. (2014). Design and preliminary evaluation of the FINGER rehabilitation robot: controlling challenge and quantifying finger individuation during musical computer game play. *Journal of NeuroEngineering and Rehabilitation*, *11*(1), 10. Retrieved from http://jneuroengrehab.biomedcentral.com/articles/10.1186/1743-0003-11-10 doi: 10.1186/1743-0003-11-10

Takagi, M., Iwata, K., Takahashi, Y., Yamamoto, S. I., Koyama, H., & Komeda, T. (2009). Development of a grip aid system using air cylinders. *Proceedings - IEEE International Conference on Robotics and Automation*, 2312–2317. doi: 10.1109/ROBOT.2009.5152246

Taylor, P., & Chappell, P. (2003). An investigation of the inhibition of voluntary {EMG} activity by electrical stimulation of the same muscle. *FESnet*, *44*(0). Retrieved from http://www.salisburyfes.com/pdfs/EMGFESNET.PDF

Taylor, P., & Chappell, P. (2004). Variation in system gain when using voluntary EMG to control electrical stimulation of the same muscle. *9th Annnual Conference of the International FES Society*(September), 9–11.

Teasell, R. W., & Kalra, L. (2005). What's new in stroke rehabilitation: Back to basics. *Stroke*, *36*(2), 215–217. doi: 10.1161/01.STR.0000153061.02375.04

Tepavac, D., & Schwirtlich, L. (1997). Detection and prediction of FES-induced fatigue. *Journal of Electromyography and Kinesiology*, *7*(1), 39–50. doi: 10.1016/S1050-6411(96)00008-9

Thorsen, R. (1999). An artefact suppressing fast-recovery myoelectric amplifier. *IEEE Transactions on Biomedical Engineering*, *46*(6), 764–766. doi: 10.1109/10.764955

Tong, K. Y., Ho, S. K., Pang, P. M., Hu, X. L., Tam, W. K., Fung, K. L., ... Chen, M. (2010). An intention driven hand functions task training robotic system. *2010 Annual International Conference of the IEEE Engineering in Medicine and Biology Society, EMBC'10*, 3406–3409. doi: 10.1109/IEMBS.2010.5627930

Triandafilou, K. M., & Kamper, D. G. (2012). Investigation of hand muscle atrophy in stroke survivors. *Clinical Biomechanics*, *27*(3), 268–272. doi: 10.1016/j.clinbiomech.2011.10.002

Trigili, E., Grazi, L., Crea, S., Accogli, A., Carpaneto, J., Micera, S., ... Panarese, A. (2019). Detection of movement onset using EMG signals for upper-limb exoskeletons in reaching tasks. *Journal of NeuroEngineering and Rehabilitation*, *16*(1), 1–16. doi: 10.1186/s12984-019-0512-1

Tu, X., Han, H., Huang, J., Li, J., Su, C., Jiang, X., & He, J. (2017). Upper limb rehabilitation robot powered by PAMs cooperates with FES arrays to realize reach-to-grasp trainings. *Journal of Healthcare Engineering*.

Tu, X., Huang, J., Yu, L., Xu, Q., He, J., & Member, S. (2012). Design of a Wearable Rehabilitation Robot Integrated with Functional Electrical Stimulation. , 1555–1560.

Valtin, M., Werner, C., & Schauer, T. (2016). ONLINE ASSESSMENT OF VOLITIONAL MUSCLE ACTIVITY FROM STIMULATION ELECTRODES IN A DROP FOOT NEUROPROSTHESIS. , 1–4.

Velloso, J. B., & Souza, M. N. (2007). A programmable system of functional electrical stimulation (FES). *Annual International Conference of the IEEE Engineering in Medicine and Biology - Proceedings*, 2234–2237. doi: 10.1109/IEMBS.2007.4352769

Watkins, C. L., Leathley, M. J., Gregson, J. M., Moore, A. P., Smith, T. L., & Sharma, A. K. (2002). Prevalence of spasticity post stroke. *Clinical Rehabilitation*, *16*(5), 515–522. Retrieved from `http://cre.sagepub.com/cgi/doi/10.1191/0269215502cr512oa` doi: 10.1191/0269215502cr512oa

Widjaja, F., Shee, C. Y., Poignet, P., & Ang, W. T. (2009). FES artifact suppression for real-time tremor compensation. *2009 IEEE International Conference on Rehabilitation Robotics, ICORR 2009*, 53–58. doi: 10.1109/ICORR.2009.5209570

Winstein, C. J., Rose, D. K., Tan, S. M., Lewthwaite, R., Chui, H. C., & Azen, S. P. (2004). A randomized controlled comparison of upper-extremity rehabilitation strategies in acute stroke: A pilot study of immediate and long-term outcomes. *Archives of Physical*

Medicine and Rehabilitation, *85*(4), 620–628. doi: 10.1016/j.apmr.2003.06.027

Wolbrecht, E. T., Reinkensmeyer, D. J., & Perez-Garcia, A. (2011). Single degree-of-freedom exoskeleton mechanism design for finger rehabilitation . *2011 IEEE International Conference on Robotic Rehabilitation*, 1–6.

Woldag, H., Waldmann, G., Heuschkel, G., & Hummelsheim, H. (2003). Is the repetitive training of complex hand and arm movements benefi cial for motor recovery in stroke patients? *Clinical Rehabilitation*, *17*(7), 723–730. Retrieved from `http://journals.sagepub.com/doi/10.1191/0269215503cr669oa` doi: 10.1191/0269215503cr669oa

Wood, D., & Swain, I. (2013). Functional Electrical Stimulation. In P. W. Azzam F G Taktak, Paul Ganney, David Long (Ed.), *Clinical engineering: A handbook for clinical and biomedical engineers* (1st ed., pp. 275–283). Oxford: Elsevier. Retrieved from `https://books.google.co.nz/books?id=ikV9CWAbNLgC{&}dq=physiological+principles+surface+electrical+stimulation{&}source=gbs{_}navlinks{_}s`

World Stroke Organisation, S. (2017). *Face the Facts: Stroke is Treatable.* Retrieved 2017-07-25, from `http://www.worldstrokecampaign.org/learn.html`

Yang, J., Xie, H., & Shi, J. (2016). A novel motion-coupling design for a jointless tendon-driven finger exoskeleton for rehabilitation. *Mechanism and Machine Theory*, *99*, 83–102. Retrieved from `http://dx.doi.org/10.1016/j.mechmachtheory.2015.12.010` doi: 10.1016/j.mechmachtheory.2015.12.010

Ye, T. (2013). *Precision Full-Wave Rectifier, Dual-Supply* (Tech. Rep. No. 1). Dallas: Texas Instruments. Retrieved from `https://www.ti.com/lit/ug/tidu030/tidu030.pdf?ts=1608802393793{&}ref{_}url=https{%}253A{%}252F{%}252Fwww.google.com{%}252F`

Yeom, H., & Chang, Y.-H. (2011). Autogenic EMG-Controlled Functional Electrical Stimulation for Ankle Dorsiflexion Control. , *193*(1), 118–125. doi: 10.1016/j.jneumeth.2010.08.011.Autogenic

Yi, X., Jia, J., Deng, S., Shen, S. G., Xie, Q., & Wang, G. (2013). A Blink Restoration System With Contralateral EMG Triggered Stimulation and Real-Time Artifact Blanking.

IEEE Transactions on Biomedical Circuits and Systems, *7*(2), 140–148.

Yili, F., Wang, P., Wang, S., Liu, H., & Zhang, F. (2007). Design and Development of a Portable Exoskeleton Based CPM Machine for Rehabilitation of. In *2007 ieee international conference on robotics and biomimetics* (pp. 1476–1481).

Yochum, M., Bakir, T., Lepers, R., & Binczak, S. (2012). Electromyostimulation using CWT. *IEEE Transactions on Biomedical Engineering*, *59*(12), 3372–3378.

Yochum, M., & Binczak, S. (2015). A wavelet based method for electrical stimulation artifacts removal in electromyogram. *Biomedical Signal Processing and Control*, *22*(October), 1–10. Retrieved from `http://www.sciencedirect.com/science/article/pii/S1746809415001093` doi: 10.1016/j.bspc.2015.06.007

Yu, N.-y., Chen, J.-j. J., & Ju, M.-s. (1999). Study of the Electrically Evoked EMG and Torque Output During the Muscle Fatigue Process in FES-Induced Static and Dynamic Contractions. (1).

Zhang, D., & Ang, W. T. (2007). Reciprocal EMG controlled FES for pathological tremor suppression of forearm. *Annual International Conference of the IEEE Engineering in Medicine and Biology - Proceedings*(1), 4810–4813. doi: 10.1109/IEMBS.2007.4353416

Zhang, Q., Hayashibe, M., & Guiraud, D. (2011). Muscle fatigue tracking based on stimulus evoked EMG and adaptive torque prediction. *Proceedings - IEEE International Conference on Robotics and Automation*, 1433–1438. doi: 10.1109/ICRA.2011.5980087

Zhang, X., Lee, S. W., & Braido, P. (2003). Determining finger segmental centers of rotation in flexion-extension based on surface marker measurement. *Journal of Biomechanics*, *36*(8), 1097–1102. doi: 10.1016/S0021-9290(03)00112-X